

# MODELLING AND ANALYSIS OF PHASOR MEASUREMENT UNITS FOR WAMS APPLICATIONS

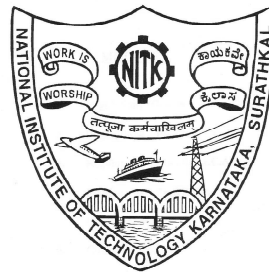
Thesis

Submitted in partial fulfillment of the requirements for the degree of

DOCTOR OF PHILOSOPHY

by

**MIR KHADIM AALAM**



DEPARTMENT OF ELECTRICAL AND ELECTRONICS ENGINEERING

NATIONAL INSTITUTE OF TECHNOLOGY KARNATAKA

SURATHKAL, MANGALORE -575025

JULY 2023



## DECLARATION

*by the Ph.D. Research Scholar*

I hereby ***declare*** that the Research Thesis entitled **MODELLING AND ANALYSIS OF PHASOR MEASUREMENT UNITS FOR WAMS APPLICATIONS** which is being submitted to the *National Institute of Technology Karnataka, Surathkal* in partial fulfillment of the requirement for the award of the Degree of *Doctor of Philosophy* in **Department of Electrical and Electronics Engineering** is a *bonafide report of the research work carried out by me*. The material contained in this Research Thesis has not been submitted to any University or Institution for the award of any degree.



177024EE008, MIR KHADIM AALAM

(Register Number, Name & Signature of the Research Scholar)

Department of Electrical and Electronics Engineering

Place: NITK-Surathkal.

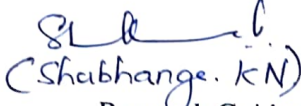
Date: 07/07/2023





# CERTIFICATE

This is to certify that the Research Thesis entitled **MODELLING AND ANALYSIS OF PHASOR MEASUREMENT UNITS FOR WAMS APPLICATIONS** submitted by MIR KHADIM AALAM, (Register Number: 177024EE008) as the record of the research work carried out by him, is *accepted as the Research Thesis submission* in partial fulfillment of the requirements for the award of degree of **Doctor of Philosophy**.

  
(Shabhanje. KN) 7/7/2023  
Research Guide (s)

(Name and  
Signature with Date  
and Seal)

  
(Dattabaja N. Gowder)  
7/7/2023  
Chairman-DRPC

ASSOC. PROFESSOR & HEAD  
(Signature with Date and Seal)  
DEPT. OF ELECTRICAL & ELECTRONICS ENGINEERING  
NATIONAL INSTITUTE OF TECHNOLOGY KARNATAKA  
SURATHKAL SRINIVASNAGAR P.O., MANGALORE-575025



## Acknowledgements

I am eternally thankful to my guide Prof. K. N. Shubhanga for giving me the opportunity of working under him. His patience, encouragement and constant guidance are the only reasons for the completion of this work. The ready availability of power system stability-related programs developed by him over the decades has simplified my work a great deal, enabling me to focus on the core research objectives.

I am also thankful to the learned members of my Research Progress Assessment Committee, Prof. K. P. Vittal and Dr. Ramesh Kini M for their practical suggestions.

Electrical Engineering Department of NITK has provided me a conducive atmosphere and excellent facilities for conducting this research. For this, I thank Prof. B. Venkatesa Perumal, Prof. K. N. Shubhanga, Prof. G. S. Punekar and Dr. Dattatraya N. Gaonkar who have successively headed the department during the tenure of my doctoral research.

I would like to give a special mention to two of my best friends, Zubair and Waleed, who were there for me consistently, encouraging me, making me laugh, even during the worst of the times. I ought to place on record my gratitude to my lab-mates and friends—Krishna Rao, Rashmi, Vikas Singh, Anvit Khare and Ravikiran Hiremath. I also thank my fellow research scholars at the Electrical Engineering Department, particularly for adjusting my duties related to teaching assistance.

I will forever be thankful to my family, especially my father, my uncle and my aunt for their unwavering support and encouragement during the duration of my research.

To conclude, I thank God Almighty for providing me with good health and patience to successfully complete this research work.

NITK-Surathkal

Mir Khadim Aalam



---

## Abstract

Wide Area Measurement Systems (WAMS) which cover an extensive geographical area help in better monitoring, control and protection of power systems. Hence, the conventional Supervisory Control and Data Acquisition System (SCADA) is being replaced or augmented by WAMS across all modern power grids. The time-stamped WAMS data obtained at high sampling frequencies provides information related to both the static and dynamic behaviour of the power systems, in contrast to the SCADA systems which provide data at a very low frame rate. The primary measuring device in the WAMS architecture is the Phasor Measurement Unit (PMU) which outputs synchrophasors, frequency and rate-of-change of frequency (ROCOF). The estimation capabilities of PMU algorithms are verified using test signals recommended by the IEEE standard for synchrophasor measurements in power systems. Over the last two decades, PMU algorithms and the application of PMUs in WAMS have been a focal point of research for power system engineers. In this regard, a detailed discussion with respect to the standard based PMU testing is provided using a DFT-based PMU in a tutorial manner. Various methods to time-tag phasors are demonstrated in order to show the importance of the placement of the phasor sample at different points in an observation window.

Varieties of static and dynamic models-based PMU algorithms are implemented and tested in an integrated PMU architecture environment. This architecture provides both causal and non-causal outputs in a single module which can be used for different power system applications. Various phase-angle compensation schemes have been suggested for a causal-PMU to show the superiority of the bus voltage-signal frequency against the line current-signal frequency as the input for compensation. A power system stabilizer (PSS) is designed based on the Phase Angle Difference (PAD) signals to illustrate the influence of causal and non-causal PMUs on the small-signal stability of a power system.

A single-phase frequency estimation technique which involves signal-reconstruction process is proposed. From the reconstructed time-domain signals, the frequency is obtained using the Convolution Average Filter (CAF) and a single-phase demodulation technique employing Hilbert filter (HF). The proposed

method provides an M-class compliant frequency estimator when augmented with a conventional P-class algorithm. Accuracy of the reconstruction-based approach is verified through test signals recommended by the IEEE standard, as well as by using signals obtained from the ISO-New England (ISO-NE) power system and simulation based studies. The use of ROCOF as a potential candidate signal in addition to frequency signal for mode identification is explored. It is also noted through a lab experimentation that an accurate frequency estimation during an out-of-step (OOS) condition is not straightforward.

Further, an event detection and localization tool is developed to illustrate an application of WAMS signals. Events in power system signals are detected using the wavelet transform and the standard deviation based methods. The effectiveness of these methods is demonstrated using practical signals from the ISO-NE power system as well as signals obtained from a simulation based 4-machine, 10-bus power system. A new event localization algorithm based on the number of PMUs involved in the event detection stage is also presented. Effect of threshold computation methods on the event detection and localization results is explored. As a part of the event analysis, a scheme to detect an OOS condition, is developed using PAD signals obtained from across transmission lines. This is found to enable the supervisory Power Swing Blocking (PSB) function for a relay during OOS condition to avoid unintentional tripping of lines.

**Keywords:** WAMS; PMU; DFT; Prony; IEEE standards for synchrophasor measurements in power systems; Event detection; Frequency estimation; Integrated PMU architecture.



---

# Contents

List of figures . . . . .	viii
List of tables . . . . .	xv
Nomenclature . . . . .	xix
Abbreviations . . . . .	xxii
<b>1 INTRODUCTION</b>	<b>1</b>
1.1 Background . . . . .	1
1.2 Components of a Typical WAMS Architecture . . . . .	3
1.2.1 Phasor Measurement Unit . . . . .	4
1.2.1.1 Phasor computing module . . . . .	5
1.2.1.2 PMU Placement . . . . .	5
1.2.1.3 Micro PMU ( $\mu$ -PMU) . . . . .	6
1.2.2 Communication Links . . . . .	7
1.2.3 Phasor Data Concentrators . . . . .	7
1.3 Applications of WAMS . . . . .	8
1.3.1 Off-line applications of WAMS data . . . . .	8
1.3.2 Online application of WAMS data . . . . .	10
1.3.3 Real-time applications . . . . .	13
1.4 Problems With the Present WAMS Architecture and Applications . . . . .	14
1.5 Literature review . . . . .	15
1.5.1 IEEE Standard Based Testing of PMU Algorithms . . . . .	15
1.5.1.1 Static-Model Based Algorithms . . . . .	17
1.5.1.2 Dynamic-Model Based Algorithms . . . . .	22
1.5.1.3 Adaptive Algorithms . . . . .	23
1.5.2 Handling of Group delays in PMU Algorithms . . . . .	23
1.5.3 Frequency Estimation Methods in PMUs . . . . .	25



---

1.5.4	Event Analysis Employing WAMS Signals . . . . .	26
1.5.4.1	Non-Training Based Methods . . . . .	27
1.5.4.2	Training-Based Methods . . . . .	28
1.5.4.3	Loss-of-Synchronism Condition Detection . . . . .	29
1.6	Research Gap and Major Contributions . . . . .	33
1.6.1	Research Gap and Motivation for the Thesis . . . . .	33
1.6.1.1	Implementation and Testing of PMU Algorithms Based on an Integrated PMU Architecture . . . . .	33
1.6.1.2	Improved Single-Phase Based Frequency Estimation . . .	35
1.6.1.3	Development of an Event Detection and Localization Tool	35
1.6.2	Objectives and Major Contribution of the Thesis . . . . .	36
1.7	Organization of the Thesis . . . . .	38
<b>2</b>	<b>SYNCHROPHASOR STANDARDS AND PMU ALGORITHMS</b>	<b>41</b>
2.1	INTRODUCTION . . . . .	41
2.2	Phasor Estimation Using DFT . . . . .	42
2.3	IEEE Standard Based Tests and Latency . . . . .	43
2.4	Error Metrics for PMUs . . . . .	44
2.5	Steady-State Tests . . . . .	45
2.5.1	Static off-nominal frequency test . . . . .	45
2.5.2	Harmonic distortion test . . . . .	47
2.5.3	Out-of-band interference test / Interharmonic test . . . . .	47
2.6	Dynamic Tests . . . . .	49
2.6.1	Bandwidth test . . . . .	49
2.6.2	Ramp test . . . . .	51
2.6.3	Step test . . . . .	53
2.6.3.1	Computation of delay . . . . .	53
2.6.3.2	Response time . . . . .	53
2.7	PMU Algorithms . . . . .	55
2.7.1	DFT with 3PF (PMU-A) . . . . .	56
2.7.2	DFT with IEEE P-Class Filter (PMU-B and PMU-B1) . . . . .	57
2.7.3	Maximally Flat Differentiators (PMU-C) . . . . .	58
2.7.4	Improved Weighted Least Squares-Taylor Fourier (PMU-D) . . . . .	60
2.7.5	Clarke Transformation based-DFT (PMU-E) . . . . .	62

---

---

2.7.6	DFT with IEEE M-Class Filter (PMU-F)	65
2.7.7	Interpolated DFT (PMU-G)	65
2.8	Group delay computation of PMUs	67
2.9	Time-Tag of Phasors	69
2.9.1	Performance evaluation of PMUs based on RE-approach	70
2.10	Summary of the Presented Work	73
<b>3</b>	<b>AN INTEGRATED PMU ARCHITECTURE</b>	<b>75</b>
3.1	INTRODUCTION	75
3.2	Causality in PMUs: An Integrated PMU Architecture	76
3.2.1	Basic PMU Block	76
3.2.1.1	Non-Causal Compensation	77
3.2.1.2	Causal PMUs	80
3.2.2	Modelling of PMUs	82
3.3	Synchrophasor Standard Based Tests	83
3.3.1	Static off-nominal test	84
3.3.1.1	Effect of sampling frequency on PMU performance	85
3.3.2	Harmonics test	86
3.3.3	Inter-harmonic test/Out-of-band interference test	87
3.3.4	Bandwidth Compliance test	89
3.3.4.1	Amplitude modulation test	89
3.3.4.2	Phase Modulation test	90
3.3.5	Ramp Test	91
3.3.6	Step test	92
3.3.6.1	Amplitude Step test	92
3.3.6.2	Phase Step test	93
3.4	Different Schemes for Angle-Compensation in an Integrated Architecture for Causal PMU	95
3.4.1	Effect of schemes of compensation on power calculations	96
3.4.2	Case-1 : Small-Signal Stable Condition	97
3.4.2.1	Voltage and Current TVE calculations	98
3.4.2.2	Power calculation: Small-signal stable case	102
3.4.3	Case-2 : Small-Signal Unstable Condition	104
3.4.3.1	TVE and Power Error calculations	106

---

---

3.4.3.2	A Large Disturbance Condition . . . . .	106
3.4.4	Impedance calculations . . . . .	108
3.4.4.1	Small-signal stable case . . . . .	109
3.4.4.2	Small-signal unstable case . . . . .	109
3.5	Role of Causality in Power System Stability . . . . .	110
3.5.1	Local versus WAMS based frequency input to PSS . . . . .	110
3.5.2	Angle input based PSS . . . . .	112
3.5.3	Performance evaluation using Causal and Non-Causal PSS inputs . . . . .	115
3.5.3.1	Case Studies for Additional Delays of 0.1 s and 0.12 s. . . . .	115
3.6	Summary of the Presented Work . . . . .	117
<b>4</b>	<b>FREQUENCY ESTIMATION USING SIGNAL RECONSTRUCTION AP- PROACH</b>	<b>121</b>
4.1	INTRODUCTION . . . . .	121
4.2	Signal Reconstruction Using DFT-Based Phasors . . . . .	122
4.2.1	Off-nominal frequency performance . . . . .	122
4.2.2	Time- Domain Signal Reconstruction Procedure . . . . .	125
4.3	Frequency Measurement . . . . .	126
4.3.1	Reconstruction based frequency estimation . . . . .	126
4.3.1.1	Convolution Averaging Filter (CAF)-based Method . . . . .	128
4.3.1.2	Hilbert Filter-Demodulation (HFD) method . . . . .	129
4.3.2	ROCOF Computation . . . . .	131
4.4	Latency Computation . . . . .	132
4.5	Testing of the Reconstruction Method Using IEEE Standard Signals . . . . .	133
4.5.1	Off-Nominal Frequency Test . . . . .	134
4.5.2	Inter-harmonic test . . . . .	136
4.5.3	Bandwidth Compliance Test . . . . .	137
4.5.4	Step in Phase test . . . . .	139
4.6	Case Studies Using a 4-Machine Power System . . . . .	140
4.6.1	Case-1: Small-Signal Oscillatory Performance . . . . .	140
4.6.2	Case-2: A Large-Disturbance Unstable Performance . . . . .	144
4.6.3	Mode estimation using frequency and ROCOF signals . . . . .	147
4.7	Case Studies Using ISO New-England Power System Signals . . . . .	149
4.7.1	Construction of time-domain sinusoidal signals from phasor samples . . . . .	149

---

---

4.7.2	Mode estimation using frequency signals . . . . .	157
4.7.3	Time-Window/Piece-Wise Prony analysis of ISO-NE signals . . . .	158
4.7.3.1	Case-1 . . . . .	159
4.7.3.2	Case-3 . . . . .	161
4.7.4	Effect of initial value of the order of linear predictor (OLP) on execution time . . . . .	163
4.7.4.1	An approach to avoid iteration in the Prony algorithm . .	164
4.7.5	Effect of window length on mode estimation . . . . .	165
4.7.5.1	Case-1 . . . . .	165
4.7.5.2	Case-3 . . . . .	166
4.7.5.3	Case-1 and Case-3 with 40 s window . . . . .	168
4.7.6	Effect of starting point of the data window on mode estimation . . .	170
4.7.6.1	Inclusion of Pre-Event Signal for Prony Analysis . . . . .	172
4.7.7	Mode estimation using ROCOF signals . . . . .	172
4.8	Frequency Estimation During Loss-of-Synchronism of a Lab Machine . . .	175
4.9	Summary of the Presented Work . . . . .	176

**5 POWER SYSTEM EVENT DETECTION AND LOCALIZATION-A NEW APPROACH** **179**

5.1	INTRODUCTION . . . . .	179
5.2	Stages Involved in Event Detection and Localization . . . . .	180
5.3	Wavelet Transform . . . . .	182
5.3.1	Discrete Wavelet Transform . . . . .	184
5.3.2	Event Detection Using Wavelet Transform . . . . .	186
5.4	Standard Deviation . . . . .	189
5.5	Steps Involved in Event Detection and Localization Using WE and SD Methods . . . . .	191
5.6	WE-based Detection Using ISO-NE Power System Signals . . . . .	194
5.6.1	Event Detection Using Case-1 Signals . . . . .	198
5.6.1.1	Event detection in voltage signals . . . . .	198
5.6.1.2	Event detection in frequency signals . . . . .	199
5.6.1.3	Event detection in ROCOF signals . . . . .	201
5.6.2	Event Detection Using Case-3 Signals . . . . .	202
5.6.2.1	Event-1 in voltage signal . . . . .	202

---

---

5.6.2.2	Event-2 in voltage signal . . . . .	203
5.6.2.3	Event-2 in frequency signal . . . . .	203
5.6.2.4	Event-3 in frequency signal . . . . .	204
5.6.2.5	Event-2 in ROCOF signal . . . . .	206
5.6.2.6	Event-3 in ROCOF signal . . . . .	206
5.7	SD-based Detection Using ISO-NE Power System Signals . . . . .	208
5.7.1	Event Detection Using Case-1 Signals . . . . .	208
5.7.1.1	Event-1 in voltage signal . . . . .	208
5.7.1.2	Event-1 in frequency and ROCOF signals . . . . .	208
5.7.2	Event Detection Using Case-3 Signals . . . . .	210
5.8	Event Detection in a 4-Machine 10-Bus Power System . . . . .	212
5.8.1	Case-1 : Fault at bus-7 . . . . .	213
5.8.1.1	Event detection using voltage magnitude signals . . . . .	214
5.8.1.2	Event detection employing frequency and ROCOF signals . . . . .	216
5.8.2	Case-2 : Disconnection of Load-C (Purely Q-type) . . . . .	218
5.9	Methods for Estimating Threshold Values . . . . .	220
5.9.1	Percentile-Based Threshold Calculation . . . . .	221
5.9.1.1	Event detection based on voltage magnitude signal using percentile threshold (Case-1) . . . . .	222
5.9.1.2	Event detection based on frequency signal using percentile threshold (Case-1) . . . . .	222
5.9.1.3	Event detection based on ROCOF signal using percentile threshold (Case-1) . . . . .	222
5.9.2	3-SD-Based Threshold Calculations . . . . .	224
5.10	Utilization of PAD-Signals for Out-Of-Step Condition Detection . . . . .	227
5.10.1	Large-signal unstable system (Case-3) . . . . .	228
5.10.2	Small-signal unstable case (Case-4) . . . . .	231
5.11	Summary of the Presented Work . . . . .	234
<b>6</b>	<b>CONCLUSIONS</b> . . . . .	<b>237</b>
6.1	Work Carried Out and Inferences . . . . .	237
6.2	Major Contributions . . . . .	239
6.3	Future Work . . . . .	240
<b>A</b>	<b>PMU numbering for ISO-NE data</b> . . . . .	<b>242</b>

---



---

# List of Figures

1.1	A generalized WAMS structure. . . . .	4
1.2	Structure of a typical PMU. . . . .	5
1.3	A typical PMU algorithm. . . . .	6
1.4	Functions of a PDC. . . . .	8
1.5	Application of WAMS. . . . .	9
2.1	TVE plot for off-nominal frequency signals . . . . .	46
2.2	TVE plot for a signal with 10 Hz interharmonic . . . . .	48
2.3	TVE plot for amplitude modulated signals . . . . .	50
2.4	TVE plot for M class ramp test . . . . .	52
2.5	Phase angle plot for step in phase . . . . .	54
2.6	TVE plot for step in phase . . . . .	54
2.7	(a) Time domain signal with zeroes appended. (b) Corresponding phasors referred to different positions of the window. . . . .	70
2.8	RE-based phasor magnitude plots for different PMUs. . . . .	71
2.9	Frequency using different PMUs for bandwidth compliance test with $f_m = 2$ Hz. . . . .	71
2.10	ROCOF using different PMUs for bandwidth compliance test with $f_m = 2$ Hz. . . . .	72
2.11	TVE response for magnitude step using different PMUs. . . . .	72
3.1	Integrated PMU architectures . . . . .	77
3.2	Non-Causal PMU block . . . . .	78
3.3	(a) Time domain signal with a DFT window. (b)Time-tag setting in a DFT based PMU with a 3-point filter. . . . .	79
3.4	Causal PMU block . . . . .	81

---

3.5	Amplitude computation using causal and non-causal PMU-A. . . . .	82
3.6	Model representation of PMU-B1 . . . . .	83
3.7	Model representation of PMU-D . . . . .	83
3.8	Different schemes of compensation for causal PMU architecture. . . . .	95
3.9	A 4-machine 10-bus power system. . . . .	97
3.10	Rotor angle plots for case-1. . . . .	98
3.11	Time-domain plots for instantaneous voltage at bus-9 and current through line-1 for case-1. . . . .	99
3.12	Frequency using voltage and current phasor for case-1. . . . .	99
3.13	TVE for current and voltage at Bus-9 using Scheme-1 for case-1. . . . .	100
3.14	TVE for current and voltage at Bus-9 using Scheme-2 for case-1. . . . .	101
3.15	TVE for current and voltage at Bus-9 using Scheme-3 for case-1. . . . .	101
3.16	Active power flowing through line-1 using different schemes of compensa- tion for case-1. . . . .	102
3.17	Reactive power flowing through line-1 using different schemes of compen- sation for case-1. . . . .	103
3.18	Error in active and reactive power flow through line-1 using Scheme-1 and Scheme-3 based compensations for case-1. . . . .	104
3.19	Rotor angle plots for case-2. . . . .	104
3.20	Instantaneous voltage for bus-9 and current through line-1 for case-2. . . .	105
3.21	Current and Voltage based frequency for case-2. . . . .	105
3.22	Instantaneous voltage for bus-9 and current through line-1 for a large dis- turbance. . . . .	107
3.23	Frequency using voltage and current phasor for a large disturbance. . . . .	108
3.24	Impedance using Scheme-1 based compensation for case-1. . . . .	109
3.25	Impedance using Scheme-1 based compensation for case-2. . . . .	110
3.26	Frequency deviation (Hz), frequency difference and angular difference (ra- dians) plot obtained using causal PMU-B1 V2. . . . .	111
3.27	Slip COI signal for generator 3 using local frequency ( $\Delta f_3$ ) and WAMS based frequency ( $\Delta f_{10} - \Delta f_9$ ) input to the PSS, obtained using causal PMU- B1 V2 and PMU-D. . . . .	112
3.28	Transfer function representation of an angle input based PSS. . . . .	113
3.29	Slip COI for gen 3 using causal and non-causal angle input for PSS. . . . .	114
3.30	Methodology of introducing artificial delay at the phasor level . . . . .	115

---



---

3.31	Comparing Slip COI of gen 3 obtained using causal compensated and non-causal inputs to PSS (additional delay $t_d = 0.1s$ ). . . . .	116
3.32	Comparing Slip COI of gen 3 obtained using causal compensated and non-causal inputs to PSS (additional delay $t_d = 0.12s$ ). . . . .	117
4.1	A functional block diagram for frequency measurement using reconstructed signals. . . . .	127
4.2	A 4-machine 10-bus power system . . . . .	140
4.3	Frequency measurements for Case-1 using PMU-1. . . . .	141
4.4	Frequency errors for Case-1 using PMU-1. . . . .	142
4.5	ROCOF measurements for Case-1 using PMU-1. . . . .	142
4.6	Rate-of-change of frequency errors for Case-1 using PMU-1. . . . .	143
4.7	Frequency errors for Case-1 using PMU-2. . . . .	143
4.8	Rate-of-change of frequency errors for Case-1 using PMU-2. . . . .	144
4.9	Frequency measurements for Case-2 using PMU-1. . . . .	145
4.10	Frequency errors for Case-2 using PMU-1. . . . .	145
4.11	ROCOF measurements for Case-2 using PMU-1. . . . .	146
4.12	Rate-of-change of frequency errors for Case-2 using PMU-1. . . . .	146
4.13	Slip excursions during $V_{ref}$ perturbation of gen-1. . . . .	148
4.14	Frequency deviation at bus-1 for $V_{ref}$ perturbation of gen-1. . . . .	148
4.15	ROCOF at bus-1 for $V_{ref}$ perturbation of gen-1. . . . .	149
4.16	Schematic approach for construction of sinusoidal signals from phasor data. 150	
4.17	Area map of the ISO-NE power system with Area-1 denoting the internal area of the ISO-NE power system, whereas Area-2 and Area-3 denoting the surrounding areas, (EECS, 2022), (Maslennikov et al., 2016). . . . .	151
4.18	Frequency estimates for case-1 from ISO-NE PMU data. . . . .	152
4.19	Frequency estimates for case-1 using PMU-2. . . . .	152
4.20	Frequency estimates for case-1 using PMU-3. . . . .	153
4.21	Frequency error for case-1 using PMU-2 and PMU-3. . . . .	153
4.22	ROCOF for Case-1 using PMU-3. . . . .	154
4.23	Frequency estimates for case-3 from ISO-NE PMU data. . . . .	155
4.24	Frequency estimates for Case-3 using PMU-2. . . . .	155
4.25	Frequency estimates for Case-3 using PMU-3. . . . .	156

---

---

4.26	Frequency error for Case-3 using PMU-2 and PMU-3. . . . .	156
4.27	ROCOF for Case-3 using PMU-3. . . . .	157
4.28	Four 10 s data windows for case-1 for Prony Analysis. . . . .	159
4.29	Four 10 s data windows for case-3 for Prony Analysis. . . . .	161
4.30	Prony based mode estimation for case-1 using 20 s data windows . . . . .	166
4.31	Prony based mode estimation for case-3 using 20 s data windows . . . . .	167
4.32	Fitment for 40 s data windows for case-1 and case-3. . . . .	169
4.33	Change of starting point of 10 s frequency window for case-1 . . . . .	171
4.34	Change of starting point of 10 s frequency window for case-3 . . . . .	171
4.35	CAF-based ROCOF vs frequency for case-1 . . . . .	173
4.36	CAF-based ROCOF vs frequency for case 3 . . . . .	173
4.37	(a) Voltage signal during loss of synchronism. (b) Frequency computed during loss of synchronism. . . . .	175
5.1	A generalized representation of PMU data based event detection, localiza- tion and classification. . . . .	181
5.2	Different transformations comparison . . . . .	183
5.3	Complementary filters used in discrete wavelet transform . . . . .	185
5.4	Downsampling in discrete wavelet transform . . . . .	186
5.5	Wavelet decomposition tree . . . . .	186
5.6	Normalized wavelet energy for voltage magnitude signal case-3. . . . .	188
5.7	Normalized wavelet energy for frequency signal case-3 . . . . .	188
5.8	SD for voltage magnitude signal case-3. . . . .	190
5.9	SD for frequency signal case-3 . . . . .	190
5.10	Event detection and localization flow chart . . . . .	193
5.11	ISO-NE case-1 all voltage magnitude signals. . . . .	194
5.12	ISO-NE case-1 all frequency signals. . . . .	195
5.13	ISO-NE case-1 all ROCOF signals. . . . .	195
5.14	ISO-NE case 3 all voltage magnitude signals. . . . .	196
5.15	ISO-NE case 3 all frequency signals. . . . .	196
5.16	ISO-NE case-3 all ROCOF signals. . . . .	197
5.17	WE for voltage magnitude across all PMUs for ISO-NE case-1. . . . .	198
5.18	Maximum values for voltage magnitude WE across all PMUs for ISO-NE case-1. . . . .	199

---

---

5.19	WE for frequency signal across all PMUs for ISO-NE case-1. . . . .	200
5.20	Maximum values for frequency signal WE across all PMUs for ISO-NE case-1. . . . .	200
5.21	WE for ROCOF signal across all PMUs for ISO-NE-case-1. . . . .	201
5.22	Maximum values for ROCOF signal WE across all PMUs for ISO-NE-case-1. . . . .	202
5.23	WE for voltage magnitude data across all PMUs for ISO-NE case-3. . . . .	203
5.24	Maximum values for voltage magnitude WE across all PMUs for ISO-NE case-3. . . . .	204
5.25	WE for frequency data across all PMUs for ISO-NE case-3. . . . .	205
5.26	Maximum values for frequency WE across all PMUs for ISO-NE case-3. . . . .	205
5.27	WE for ROCOF data across all PMUs for ISO-NE case-3. . . . .	206
5.28	Maximum values for ROCOF WE across all PMUs for ISO-NE case-3. . . . .	207
5.29	SD for voltage magnitude across all PMUs for ISO-NE case-1. . . . .	209
5.30	Maximum values of voltage magnitude SD across all PMUs for ISO-NE case-1. . . . .	209
5.31	SD for PMU-3, 4, 5 and 8 for case-3, a) voltage magnitude b) frequency c) ROCOF. . . . .	210
5.32	SD for frequency across all PMUs for ISO-NE case-3. . . . .	211
5.33	Maximum value of frequency SD across all PMUs for ISO-NE case-3. . . . .	212
5.34	Modified 4-machine 10-bus system with an additional $P + jQ$ load at bus-11.	213
5.35	Voltage magnitude at all generator buses for a fault case. . . . .	214
5.36	SD for voltage magnitude data across all PMUs for a fault case. . . . .	215
5.37	Maximum values for voltage magnitude SD across all PMUs for a fault case.	215
5.38	Frequency at all generator buses for a fault case. . . . .	216
5.39	SD for frequency data across all PMUs for a fault case. . . . .	217
5.40	Maximum values for frequency SD across all PMUs for a fault case. . . . .	217
5.41	Voltage magnitude at all generator buses for line trip case-2. . . . .	218
5.42	Maximum values for voltage magnitude SD across all PMUs for load trip case ( $0 + jQ$ load only). . . . .	219
5.43	Frequency at all generator buses for line trip case-2. . . . .	220
5.44	Frequency at all generator buses for case-3. . . . .	225
5.45	Maximum value of Frequency WE with PMU-9 (case-3). . . . .	226
5.46	Phase angles across transmission lines for Case-1. . . . .	228

---

---

5.47 Rotor angle excursions for large-signal unstable case (Case-3). . . . .	229
5.48 Phase angles across transmission lines for Case-3. . . . .	230
5.49 Apparent impedance trajectory of line 9-10 (Case-3). . . . .	230
5.50 R-X plot of apparent impedance of line 9-10 (Case-3). . . . .	231
5.51 R-X plot of apparent impedance of line 8-7 (Case-3). . . . .	232
5.52 Phase angle across transmission lines for small signal unstable case (Case-4).	233
5.53 Apparent impedance trajectory of line 9-10 for small-signal unstable case (Case-4). . . . .	233
5.54 R-X plot of apparent impedance of line 9-10 for small signal unstable case (Case-4). . . . .	234



---

# List of Tables

1.1	SCADA vs WAMS-A comparison . . . . .	3
1.2	Evolution of the IEEE standard for synchrophasor measurement . . . . .	17
1.3	Static-Model based PMU algorithms (Part-1). . . . .	20
1.4	Static-Model based PMU algorithms (Part-2). . . . .	21
1.5	Time-Domain based frequency estimation methods. . . . .	27
1.6	Frequency-Domain based frequency estimation methods. . . . .	28
1.7	Non-Training based event detection methods. . . . .	31
2.1	Comparison of IEEE benchmarks for steady-state tests ( $F_{rr} > 20$ fps). . . . .	46
2.2	Comparison of IEEE benchmarks for bandwidth compliance test ( $F_{rr} > 20$ fps). . . . .	49
2.3	Comparison of IEEE benchmarks for ramp test. . . . .	52
2.4	Comparison of IEEE benchmarks for response time and delay time in case of step test. . . . .	54
2.5	List of three-phase and single-phase PMUs. . . . .	67
2.6	Latency for different PMUs. . . . .	68
2.7	TVE response time for different PMUs for a step in magnitude. . . . .	73
3.1	Window length details for different PMUs . . . . .	84
3.2	Error values for the static off-nominal test . . . . .	85
3.3	Effect of sampling rate on PMU performance. . . . .	86
3.4	Error values for the Harmonics test . . . . .	86
3.5	Error values for inter-harmonic frequency of 10 Hz. . . . .	87
3.6	Error values for inter-harmonic frequency of 25 Hz . . . . .	88
3.7	Error values for inter-harmonic frequency of 75 Hz . . . . .	88
3.8	Error values for inter-harmonic frequency of 100 Hz . . . . .	88

---

3.9	Error values for the amplitude modulation test . . . . .	90
3.10	Error values for the phase modulation test . . . . .	91
3.11	Error values for the P-class ramp test . . . . .	92
3.12	Error values for the M-class ramp test . . . . .	92
3.13	Response time values for Amplitude step test . . . . .	93
3.14	Response time values for Phase step test . . . . .	94
3.15	Compliance verification for all PMUs based on the integrated architecture using IEEE synchrophasor standard signals. . . . .	94
3.16	Maximum error value comparison for stable Case 1 . . . . .	103
3.17	Error value comparison for Unstable Case 2 . . . . .	106
3.18	The Prony analysis of slip COI signals of generator 3 obtained employing different PSS input signals. . . . .	112
3.19	List of dominant modes obtained using the Prony analysis with cascading compensators ( $\phi_m = 35^\circ$ each) . . . . .	114
3.20	List of dominant modes for non-causal and causal based slip signals (addi- tional delay of 0.1 s. . . . .	116
3.21	List of dominant modes for non-causal and causal based slip signals (addi- tional delay of 0.12 s). . . . .	117
4.1	Frequency error for static off-nominal signals . . . . .	135
4.2	ROCOF Error for static off-nominal signals . . . . .	135
4.3	Frequency Error for inter-harmonic test ( $F_{rr} = 50$ fps) . . . . .	137
4.4	Frequency error for phase modulation test ( $k_a = 0.1$ ). . . . .	138
4.5	ROCOF error for phase modulation test ( $k_a = 0.1$ ). . . . .	138
4.6	Response time for FE and RFE . . . . .	139
4.7	Prony analysis for case-1 frequency and ROCOF signals obtained using PMU-2 . . . . .	143
4.8	Maximum frequency and ROCOF errors for case-1, case-2. . . . .	147
4.9	Prony analysis of case-3 signals obtained using PMU-2 . . . . .	149
4.10	List of Events in ISO-NE power system (EECS, 2022), (Maslennikov et al., 2016). . . . .	151
4.11	Prony analysis of different frequency signals . . . . .	158
4.12	List of dominant modes obtained using Prony analysis for $F_{R1}$ frequency. . . . .	158

---

---

4.13	Prony analysis of different 10 s windows for case-1 using theoretical and PMU-3 CAF signal at 30 fps. . . . .	160
4.14	Prony analysis of different 10 s windows for case-1 using PMU-3 CAF signals at 60 fps and 120 fps. . . . .	160
4.15	Prony analysis of different 10 s windows for case-3 using theoretical and PMU-3 CAF signal at 30 fps. . . . .	162
4.16	Prony analysis of different 10 s windows for case-3 using PMU-3 CAF signals at 60 fps and 120 fps. . . . .	162
4.17	Prony results of different 10 s windows for case-3 using PMU-3 HFD signals (30 fps) . . . . .	163
4.18	Effect of base initial value of $n$ on execution time . . . . .	164
4.19	Effect of high initial value of $n$ on execution time . . . . .	164
4.20	Prony analysis of different 20 s windows for case-1 using PMU-3 CAF signals (30 fps) . . . . .	166
4.21	Prony analysis of different 20 s windows for case-3 using PMU-3 CAF signals (30 fps) . . . . .	168
4.22	Prony analysis of a 40 s window for case-1 using PMU-3 CAF signal (30 fps)	168
4.23	Prony analysis of a 40 s window for case-3 using PMU-3 CAF signal (30 fps)	168
4.24	Prony analysis for Case-1 CAF-based (30 fps) frequency signals using 10 s windows with a delay of 5 s . . . . .	170
4.25	Prony analysis for Case-3 CAF-based (30 fps) frequency signals using 10 s windows with an advancement of 5 s . . . . .	172
4.26	Inclusion of pre-event signal in Prony time window for case-3 . . . . .	172
4.27	Modal performance comparison of ROCOF and frequency signals for case-1 (30 fps) . . . . .	174
4.28	Modal performance comparison of ROCOF and frequency signals for case-3 (30 fps) . . . . .	174
5.1	Localization decision based on wavelet energy computation of ISO-NE data for case-1 for event at 40 s. . . . .	202
5.2	Event localization decision based on Wavelet energy estimates for ISO-NE power system . . . . .	207
5.3	Event localization decision based on SD estimates for case-1 ISO-NE power system . . . . .	210

---



---

5.4	Event detection and localization procedure for case-3 based on SD estimates.	212
5.5	Event detection results for case-1, 4-machine, 10-bus power system . . . .	218
5.6	Case-2 using trail and error thresholds . . . . .	219
5.7	Case-1 using percentile based threshold . . . . .	223
5.8	Case-2 using percentile based threshold . . . . .	223
5.9	Event detection and localization for the unstable case with PMU-9 estimates.	225
5.10	Event detection and localization for the unstable case without PMU-9 estimates. . . . .	226
5.11	Pre and post fault $Z_{app}$ for Case-3. . . . .	231
A.1	PMU No and the associated substation and line for the ISO-NE system. . .	243

---

---

---

## Nomenclature

$\Delta t$	:	Sampling period (s)
$f_m$	:	Modulation frequency (Hz)
$\omega_m$	:	Angular frequency (rad/s)
$X_m$	:	Maximum amplitude of time-domain signal (p.u.)
$f_{ih}$	:	Interharmonic frequency (Hz)
$\phi$	:	Initial phase angle (rad or degree)
$f_0$	:	Nominal frequency in Hertz
$\Delta f$	:	Deviation from nominal frequency in Hertz
$f_b$	:	Base frequency (Hz)
$f_R$	:	Frequency resolution in Hertz
$N$	:	Number of samples per cycle of the fundamental
$L_{dft}$	:	Number of samples used for phasor computation
$L_{RF}$	:	Number of samples used for ROCOF computation
$M$	:	Number of samples used for frequency computation
$f_0$	:	Nominal frequency in Hertz
$\omega_0$	:	Nominal frequency in rad/s
$\bar{X}_T$	:	Theoretical phasor
$k_H$	:	Harmonic distortion factor (p.u)
$F_{rr}$	:	Phasor reporting rate (fps)
$k_a$	:	Phase modulation/step factor (p.u)
$k_x$	:	Amplitude modulation/step factor (p.u)
$u(t)$	:	Step function
$c_{uc}$	:	Uncompensated phasor
$c_{nc}$	:	Non-causal compensated phasor
$c_c$	:	Causal compensated phasor
$t_a$	:	Actual time (s)
$t_{PMU}$	:	PMU time (s)
$x_{aR}(t)$	:	Reconstructed time-domain signal (p.u)
$R_f$	:	Frequency ramp rate (Hz/s)
$Z_{app}$	:	Apparent impedance (p.u)
$WE_{th}$	:	Wavelet Energy threshold (p.u)
$SD_{th}$	:	Standard Deviation threshold (p.u)

---

## Abbreviations

$\mu$ -PMU	:	Micro PMU
3PF	:	Three Point Filter
ADC	:	Analog to Digital Converter
BPA	:	Bonneville Power Administration
BWC	:	Bandwidth Compliance Test
CT	:	Current Transformer
CT-DFT	:	Clarke Transform based Discrete Fourier Transform
COI	:	Center of Inertia
CAF	:	Convolution Averaging Filter
DFT	:	Discrete Fourier Transform
DTFT	:	Digital Taylor-Fourier Transform
DWT	:	Discrete Wavelet Transform
EMD	:	Empirical Mode Decomposition
FFT	:	Fast Fourier Transform
FE	:	Frequency Error
FF	:	Fourier Filter
fps	:	Frames Per Second
FIR	:	Finite Impulse Response
GPS	:	Global Positioning System
HFD	:	Hilbert Filter Demodulation
IEEE	:	Institute of Electrical and Electronics Engineers
I/O	:	Input/Output
IpDFT	:	Interpolation based Discrete Fourier Transform
IIR	:	Infinite Impulse Response
LS	:	Least Squares
LOS	:	Loss of Synchronism
MAPE	:	Mean Absolute Percentage Error
M-class	:	Measurement class
MAF	:	Moving Average Filter
NASPI	:	North American Synchro-Phasor Initiative
NWE	:	Normalized Wavelet Energy
NE	:	New England
OLP	:	Order of Linear Prediction
OOB	:	Out of Band Interference
OOS	:	Out of Step
OPP	:	Optimum PMU Placement
PMU	:	Phasor Measurement Unit
PDC	:	Phasor Data Concentrator
PSS	:	Power System Stabilizer
PT	:	Potential Transformer

---

## Abbreviations (Continued)

p.u.	:	Per Unit
P-class	:	Protection class
PAD	:	Phase Angle Difference
QP-DFT	:	Quasi positive sequence discrete fourier transform
RPAD	:	Relative Phase Angle Difference
RS	:	Referred to the start
RC	:	Referred to the center
RE	:	Referred to the end
rms	:	Root Mean Square
RTU	:	Remote Terminal Unit
ROCOF	:	Rate of change of frequency
RFE	:	Rate of Change of Frequency Error
SCADA	:	Supervisory Control And Data Acquisition System
SNR	:	Signal-to-Noise Ratio
SE	:	State estimation
Std	:	Standard
SVA	:	Sample Value Adjustment
SD	:	Standard Deviation
T-F	:	Taylor-Fourier
TVE	:	Total Vector Error
USA	:	United States of America
UTC	:	Universal Time Coordinated
WAMPAC	:	Wide Area Monitoring Protection And Control
WAMS	:	Wide Area Measurement (Monitoring) System (Systems)
WSCC	:	Western Systems Coordinating Council
WT	:	Wavelet Transform
WE	:	Wavelet Energy
WLS	:	Weighted Least Squares

---

# Chapter 1

## INTRODUCTION

### 1.1 Background

Conventional power systems primarily include remote generation units supplying electrical energy to load centers using highly interconnected long AC lines and limited high-voltage direct current (HVDC) links. The fast depleting non-renewable resources, environmental concerns and the growing need for sustainable energy have led to the increased integration of Renewable Energy Sources (RES) with the power system. The seamless addition of low-inertia and inverter-based RES to the existing power system have posed new challenges which can be overcome via the *smart grid* architecture. The smart grid uses cutting-edge technologies, equipment, and controls that communicate and work together to provide enhanced monitoring and control of the power system.

Such a smart grid is built on the foundations of a reliable and resilient power system which can be ensured by continuously monitoring and controlling the generation, transmission as well as the distribution network of the power system. In 1970's, to achieve this task, the Supervisory Control and Data Acquisition (SCADA) system was introduced. SCADA systems gather data asynchronously by polling remote terminal units (RTUs). The data collected by SCADA systems includes, voltage magnitude signals, active power, reactive power and system topology via breaker status (Kumar et al., 2010). SCADA systems obtain steady-state grid data every 2-6 seconds. Due to such a low sampling rate, short term transient events with high frequencies are not captured and therefore fast changing dynamics in power system signals go undetected. In addition, the data provided using SCADA systems lacks time-synchronization and due to its high latency is not applicable for online or real-time applications. The state estimation (SE) process run based on SCADA data has

a delay of around 70 s, which may not be problematic during normal operating conditions but can lead to inconsistent results during system incidents (Ashton et al., 2013), (Phadke et al., 1986). Phase angles in SCADA systems are not directly measured but rather computed using SE algorithms. This information is only available at a central location and therefore cannot be used for local applications. Blackout occurrences in U.S.A, parts of Europe and several other countries due to the lack of availability of real-time system information emphasized the need for improving on SCADA technology. This led to the evolution of Wide Area Monitoring/Measurement Systems (WAMS) which provide better wide-area visualization and control, compared to SCADA systems (Gomez and Abur, 2013), (Sharma and Dhole, 2016).

WAMS were introduced in the 1980's by the Bonneville Power Administration (BPA) to enable operators to acquire dynamic data for power systems (NERC, 2010), (Phadke, 1990). The first test bed for WAMS implementation was the Western Interconnection of the North American power system (NERC, 2010). The definition of a wide area measurement system as given by the U.S Department of Energy (U.S DOE) is as follows “*A wide area measurement system consists of advanced measurement technology, information tools, and operational infrastructure tools that facilitate the understanding and management of the increasingly complex behaviour exhibited by the large power systems*” (Hadley et al., 2007).

WAMS use high sampling rates for measurement and also time stamp each sample value using a GPS based clock whose time is traceable to Universal Time Coordinated (UTC) (PGCL, 2012), (De La Ree et al., 2010) (Usman and Faruque, 2019). The highly granular nature of WAMS data enables real-time system protection and control functions, much better than SCADA estimates (Kumar et al., 2010), (Martinez and Serna, 2015), (De la Serna, and Rodriguez-Maldonado, J, 2011). The WAMS architecture provides time-stamped phasor samples of voltage and current, frequency and Rate-of-Change of Frequency (ROCOF) at different locations in a power system during steady-state nominal and dynamic conditions as well, (Dai and Tate, 2021), (Zhang et al., 2018), (Jiang et al., 2019). This helps in better monitoring, control and protection of grids covering an extensive geographical area (Ivanković and Brnobić, 2021). A brief comparison of SCADA and WAMS is presented in Table. 1.1. WAMS primarily carries out three tasks, which include:

1. Data metering and collection.

2. Data transmission.
3. Data monitoring and control.

**Table 1.1:** SCADA vs WAMS-A comparison

Feature	SCADA	WAMS
Frame rate	1 frame per 2-6 sec	10-120 frames per sec
Data flow latency	High	Negligible
Observability	Steady-state	Steady-state and Dynamic
Measurements	V, I	V, $\phi_v$ , I, $\phi_i$ , $f$ , ROCOF
Universal time synchronization	No	Yes
Local estimation of phase angles	No	Yes
Communication method	Serial communication	Network communication
Objective	Local monitoring and control	Wide area monitoring and control

Phasor Measurement Units (PMUs) installed all over the grid are used as the primary data metering devices in a WAMS architecture (Monti et al., 2016). PMUs employ signal-processing based techniques to compute the fundamental phasor and other associated quantities. These quantities are transmitted to control centers via a low latency, high speed communication network. The monitoring and control provided by the WAMS predominantly refers to the energy management system which carries out a variety of power system functions. Data acquired using WAMS is integrated into wide-area visualization tools and improved state estimators to elevate grid reliability and situational awareness.

## 1.2 Components of a Typical WAMS Architecture

A typical wide area measurement system as shown in Fig. 1.1 consists of the following components

1. Phasor Measurement Units (PMU)
2. Communication Links
3. Phasor Data Concentrators (PDC)



### 1.2.1 Phasor Measurement Unit

A PMU is the primary measuring device in the WAMS architecture, (Phadke and Thorp, 2010), (Agarwal et al., 2013), (Shi et al., 2020), (Liu et al., 2021), (Shahraeini and Javidi, 2012), (Thorp et al., 1988), (Ree et al., 2010). PMUs use digital signal processing techniques to compute phasors, frequency and ROCOF from 50 or 60 Hz AC waveforms (voltages and currents) after the analog AC waveforms are converted into digital samples form using analog to digital converters for each phase, (Phadke and Thorp, 2010).

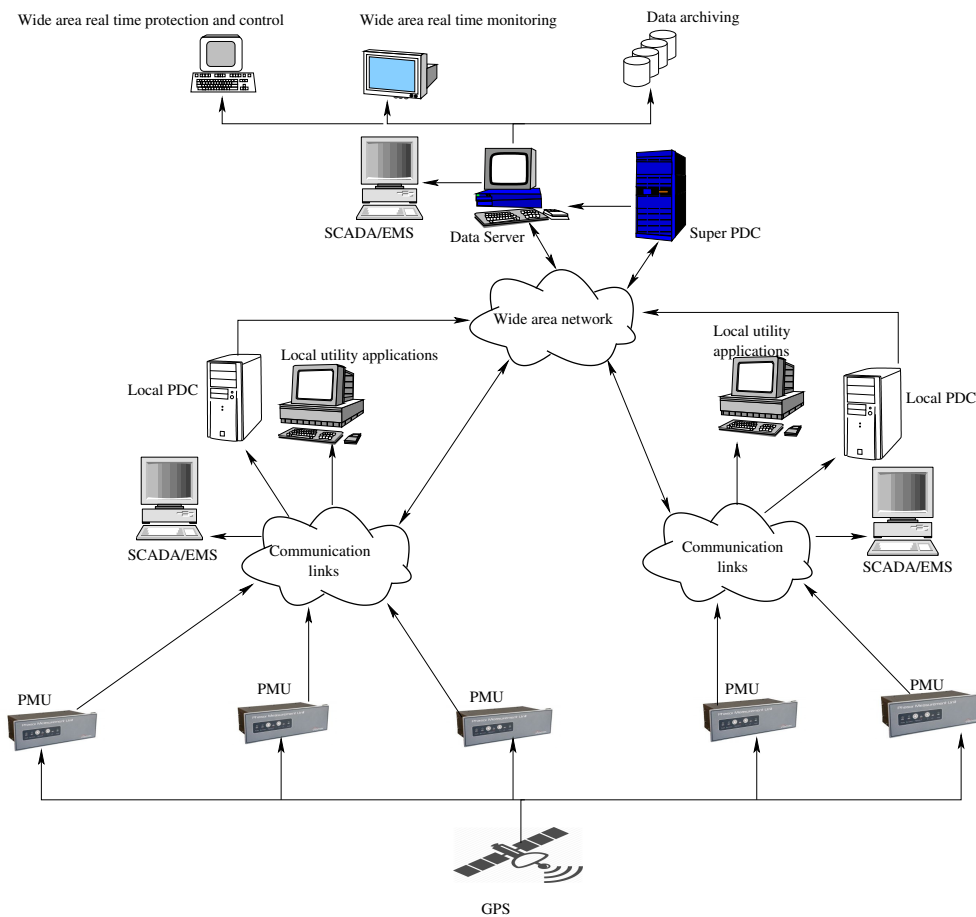
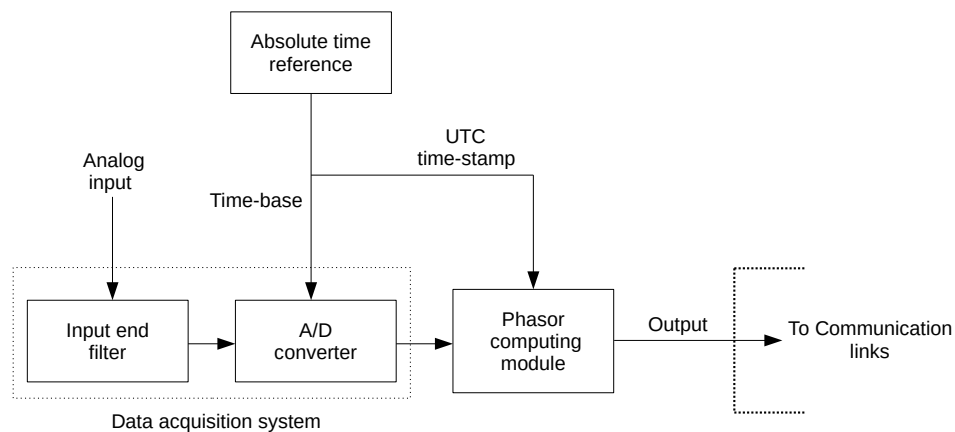


Figure 1.1: A generalized WAMS structure.

Phasors computed by a PMU have an associated time-tag which is obtained via a highly synchronized time source. Such a time tagged phasor is labelled as a *synchrophasor*, which is available at the output end of a phasor measurement unit (Dagle, 2018). Along with the

synchrophasor, time-tagged frequency and ROCOF signals are also available at the output end of the PMU module. These signals are transmitted at high frame rates via communication links to control centers for further processing. For example, PMUs installed in the ISO-New England power system transmit data at a frame rate of 30 frames per second, for a 60 Hz system (EECS, 2022). The synchrophasor, frequency and ROCOF values must meet the minimum accuracy requirements given in the IEEE standard for synchrophasor measurements in power systems (IEEE Std, 2011), (IEEE Std, 2014), (IEEE Std, 2018). The essential components of a phasor measurement unit are shown in Fig. 1.2 (Monti et al., 2016),



**Figure 1.2:** Structure of a typical PMU.

### 1.2.1.1 Phasor computing module

Most phasor computing modules work on three-phase systems and therefore output positive sequence estimates. These estimates are further used for frequency and ROCOF computation -see Fig. 1.3. PMU algorithms such as (Derviškadić et al., 2017), (Belega and Petri, 2013), inherently provide frequency estimates without the requirement of an additional computing module.

### 1.2.1.2 PMU Placement

A power system is deemed to be observable, when all the measurements obtained from different sources yield enough information for state estimation. Since it is not cost-effective

to install a PMU on each bus, it is required to determine the least set of PMUs necessary to make the entire system observable. This is the aim of the optimal PMU placement problem (OPP), (Yuill et al., 2011), (Manousakis, 2011). OPP, (Nazari-Heris et al., 2015) is an active research topic and several methods have been suggested over the years. These methods are primarily categorized as conventional and non-conventional techniques. Conventional techniques include, greedy search, graph theory, linear programming, non-linear programming etc. Alternatively, non-conventional techniques can be divided further into two sub-categories, i.e., heuristic and meta-heuristic. Fuzzy decision making, unified algorithm, monte-carlo simulation can be labelled as heuristic approaches, whereas genetic algorithm, particle swarm optimization, tabu search, simulated annealing can be categorized as meta-heuristic techniques (Ahmed et al., 2022). However, in most cases, PMUs are installed in a phased manner in order to cover major transmission lines and critical buses with an objective to make the whole power system visible (Gajjar et al., 2021).

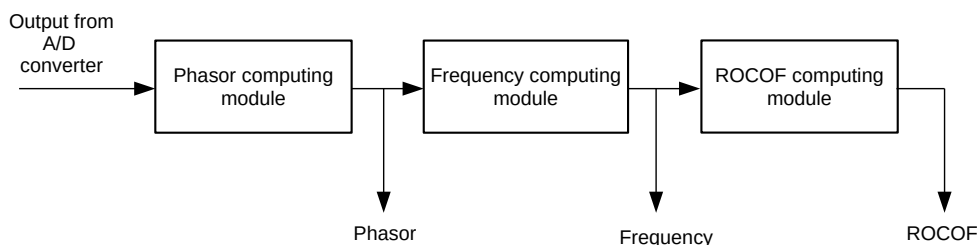


**Figure 1.3:** A typical PMU algorithm.

### 1.2.1.3 Micro PMU ( $\mu$ -PMU)

The need for installation of PMUs at the transmission level rather than at distribution level is justified due to its high installation costs. The intricate nature of the distribution network including numerous nodes, faster dynamics, low amplitude and phase angle differences demand for the design of advanced measuring systems with high accuracy and precision (Dusabimana and Yoon, 2020), (Von Meier et al., 2017). This led to the development of micro-PMUs ( $\mu$ -PMU), which is a measurement device that accurately obtains the synchronized voltage and current values from complex distribution networks.  $\mu$ -PMUs or distribution-PMUs (D-PMU) as they are also known as, were developed by Power Sensors Limited (PSL), with the University of California and Lawrence Berkley National Lab (LBNL) in 2015 (Usman and Faruque, 2019). Compared to the current commercial PMUs (transmission level), these devices ( $\mu$ -PMU) can be produced more affordably and pro-

vide ultra-accurate synchronised measurements of voltage and or current magnitudes and phase angles. Some of the notable applications of a  $\mu$ -PMU include, distribution-network reconfiguration, phase identification, high-impedance fault detection, etc.

### **1.2.2 Communication Links**

The PMU is designed as a measurement point in a coordinated architecture for wide-area monitoring. To link to the rest of the infrastructure and transmit measurement data to the rest of the monitoring network, each PMU has its own communication system. One or more network adapters, often using both copper wire and optical fibre Ethernet technologies, are used for communication by the PMUs. In (IEEE Std C37.118.2, 2011) methods for transferring synchronized phasor samples over a network are described. This standard defines different data formats, contents and messaging types for synchrophasor transmission. The standard also introduces a new configuration message which is intended to process multiple data streams from PMUs and PDCs designed by different manufacturers, ensuring interoperability (Louis et al., 2021).

### **1.2.3 Phasor Data Concentrators**

Synchrophasor data obtained from many PMUs over the entire network is combined using a Phasor Data Concentrator (PDC) into a single data stream for further processing. Some of the most notable PDC functions are listed below,

1. Processing and storage of PMU data which are sent as continuous streams in real-time.
2. Checking the healthiness of the overall measurement system.
3. Protection, control and monitoring of power systems.

Within a connected system, PDCs can exchange data with other PDCs situated at different locations. Primarily PDCs can be divided into two categories based on the way that they have been implemented, a) Software based PDCs, b) Hardware based PDCs (Annakage et al., 2017). A software based PDC is a software package installed in approved commercial hardware, the size of which is dependent on the area covered and the number of PMUs installed in the network. The hardware PDC on the other hand is installed to handle a system with limited number of PMUs, such as at a substation. PDCs, similar to PMUs are

associated with a synchronized time source for proper functioning. They get assigned with a fixed amount of waiting time to receive data from all PMUs connected to it. In case a PMU sends data later than the fixed waiting time, a PDC replaces the missing data with filler data. As described in (IEEE Std C37.244, 2013), the main functions of a PDC are summarized in Fig. 1.4.

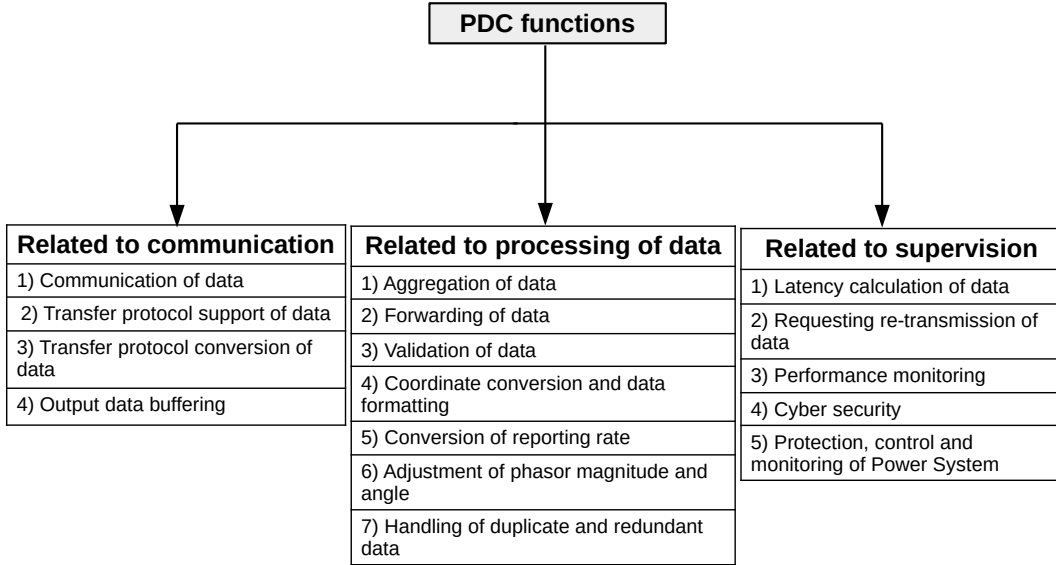


**Figure 1.4:** Functions of a PDC.

## 1.3 Applications of WAMS

Time-stamped and high sample rate data available from WAMS has numerous applications in power systems (PGCL, 2012). Depending on the time-scale involved while using WAMS data, these applications are primarily segregated into off-line, online and real-time categories as indicated in Fig. 1.5.

### 1.3.1 Off-line applications of WAMS data

1. **Model validation, tuning and parameter estimation:** The measured PMU signals, such as the voltage phasors at the generator terminals, are used as inputs to the simulation models of a generator in a hybrid simulation, (De La Ree et al., 2010), (Padiyar and Kulkarni, 2019). The output of the simulation model (currents or power

flows) is compared with the signals measured from the generator. Such an analysis is carried out for various disturbance scenarios. In case the simulation and the measured responses vary within a set threshold the model can be considered as accurate. Similarly power system inertia is also estimated using WAMS signals acquired from geographically dispersed PMUs as shown in (Ashton et al., 2014). WAMS data can also be used to rectify Instrument Transformer systematic errors as well as estimate transmission line parameters as shown in (Goklani et al., 2020).

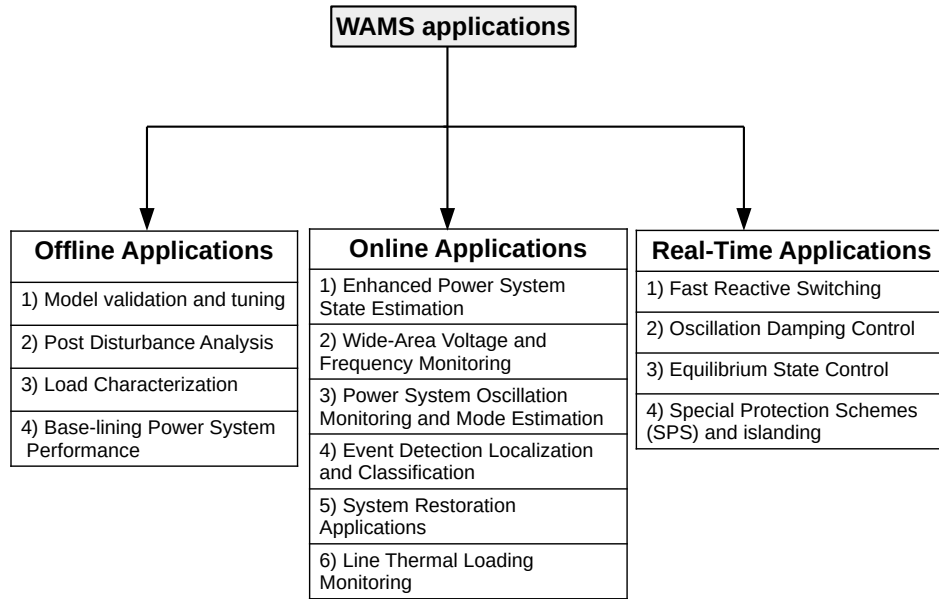


**Figure 1.5:** Application of WAMS.

2. **Post disturbance analysis:** After the occurrence of a disturbance, data from WAMS can be used for post-mortem analysis (Shaw and Jena, 2020), (Wang et al., 2019), (Ge et al., 2015). The cause for the occurrence of a disturbance can be pin-pointed and corrective schemes to prevent any such events in the future can be suggested. Synchronized PMU data is crucial in order to backtrack and reconstruct the sequence of events mostly when multiple disturbances occur in a short time-span (Salunkhe and Kulkarni, 2015).
3. **Load characterization:** Data obtained from WAMS is helpful in understanding and modelling loads for power system studies. Certain loads can be identified on a power system and their responses to variations in frequency can be collected using PMUs in-

stalled at sub-transmission levels to improve load modeling (Annakage et al., 2017), (Hadley et al., 2007). System load's sensitivity to changes in frequency due to small generation trips is one aspect of WAMS based high-level load model characterization. Sensitivity of loads to voltage can also be evaluated using WAMS data.

4. **Base-lining power system performance:** Data accumulated from different PDCs/PMUs in a WAMS architecture over a long period of time can be used for baselining studies which involves a variety of tasks, (De la Serna and Martinez, 2015), as listed below:
  - (a) Building accurate system state prediction and trend detection tools.
  - (b) Tracing power system performance over time.
  - (c) Detecting major changes in power system performance.
  - (d) Validating models which help in setting system limits.
  - (e) Calculate thresholds for event detection algorithms
  - (f) Calculate security margins of the system

### 1.3.2 Online application of WAMS data

1. **Enhanced power system state estimation :** Online synchrophasors obtained from PMUs installed over a WAMS network are used to estimate the state of a power system. Fast and accurate state estimation can be achieved using WAMS data which is obtained at a high reporting rate as compared to SCADA data, (Ashton et al., 2014), (Monti et al., 2016), (Ghiocel et al., 2013). State estimation based on synchrophasor data can provide the following functionalities as well,
  - (a) Topology processing: Which includes building the present topology of the whole power system together with the states of the circuit breakers and switches.
  - (b) Observability analysis: To evaluate the observability of the whole network based on the gathered WAMS data.
  - (c) Bad data detection: Allowing identification and rejection of unusable data obtained because of possible communication errors or instrument failure, or other reasons.
  - (d) Topology error identification: Which is similar to bad data identification where estimation results in topology processing are analyzed to recognize any possible errors in the accepted topology of the system.

2. **Wide-area voltage and frequency monitoring:** WAMS are used to control, observe and foresee voltage and frequency in large power systems. Trend of voltage signals at key load centers or transmission lines can be predicted using the high frame rate data provided by the WAMS network. Instability prediction based on the trend of a voltage signal is a very useful application of WAMS data (Gomez and Abur, 2013). Phasor measurement units enable operators to monitor voltage sensitivities, MVar margins, voltage profiles at different buses in real-time whereas a trend monitoring function can provide a timely indication for power system instability, (Hatziaargyriou et al., 2020). Wide Area Monitoring Protection and Control Systems (WAMPACS) are also supplemented with WAMS data in order to provide better visualization and control of the power system. Positive sequence voltage phasor angles obtained using WAMS can also be used as a power system health indicator. Relative phase angle difference (RPAD or PAD) signals across major transmission lines can be monitored online in order to identify a potential Out-Of-Step (OOS) condition, (McDonald et al., 2005), (Dagle, 2018),(Lavand and Soman, 2016), (PGCL, 2012).

Power system frequency is another primary indicator of load-generation balance. The extent of the frequency deviation and the magnitude of the generation loss are closely related. During system events involving separation or islanding, system frequency provides an excellent measure of the integrity of an interconnection (Salunkhe et al., 2014). An overview of the bus frequencies across the entire wide area power system helps the power system operator to identify the system separation points and the islands.

3. **Power system oscillation monitoring and mode estimation :** One of the major applications of high frame rate data provided by the WAMS network is the identification of frequency and damping of power system oscillations, (Jiang et al., 2019), (Liu et al., 2021), (De la Serna et al., 2016), (Zhang et al., 2018). These include local and inter-area oscillations which are a result of electromechanical swings of machines. The frequency and the damping associated with an oscillation can be extracted from either synchrophasors (magnitude and angle) or frequency or ROCOF signals. In case an oscillation is associated with a low/negative damping, preventive action may be initiated in order to improve the security of a power system.
4. **Event detection localization and classification :** Data streams from different PMUs



installed over a wide area network can be processed using event detection algorithms to identify the occurrence of an event (Brahma et al., 2016), (Yadav et al., 2018), (Yadav et al., 2019), (Allen et al., 2013). This can be achieved via any of the PMU signals, i.e., phasor magnitude, phase angle, frequency and ROCOF. Events in the PMU data can be identified using statistical/signal-processing or artificial intelligence based techniques. Events can be localized based on the amplitude of excursions exhibited by different PMUs. Events occurring in a power system can also be classified by identifying the signatures left on different PMU output signals. For example, a real power event leaves its imprints on the frequency and ROCOF signals, whereas a reactive power event is seen to affect the voltage signal dominantly. Upon the detection and localization of an event, alarm or alert indicators are used to notify the operator about the occurrence of an event.

5. **System restoration applications** : When systems are restored after separation (islanding scenarios) and black-started, frequency information available from phasor measurement units is crucial. Phasor data can be utilised to restart equipment without endangering stability or wasting time on ineffective reclosing attempts (Liu et al., 2016).
6. **Line thermal loading monitoring** : Transmission line loadings can be tracked using phasor data and line ratings can be updated instantly. Online phasor data for chosen transmission lines along with local weather conditions can be used to compute the actual ampacity of the transmission line (Annakage et al., 2017). This rating can vary compared to the conservative seasonal rating assigned by power system operators. Such online estimation of line ratings using synchrophasor data can enhance power transfer across transmission lines and relieve congestion along key lines.
7. **Other applications**: As per, PGCL (2012), some of the other online applications of WAMS data include,
  - (a) Vulnerability test on relay characteristics.
  - (b) Dynamic state measurements.
  - (c) Load control and load shedding techniques such as demand response to manage the power system.

### **1.3.3 Real-time applications**

Real-time applications of WAMS include wide-area stability control applications. Due to the vast observability of the state of the system, intelligent decisions can be taken to ensure system stability. Using the high resolution nature of the phasor data local or centralized control of power system can be executed. In order to prevent the spread of major disturbances, the wide-area monitoring, protection, and control (WAMPAC) functions make use of system-wide data and specific local data which is communicated to a centralized location. Some important real-time applications of WAMS data are as follows,

1. **Fast reactive switching** : Due to a strong correlation between the voltage phasor and the reactive power reserves in a power system, shunt capacitors are introduced to increase reactive power reserves. Control schemes have been employed involving synchrophasor based monitoring of reactive power output at important power plants to enable quick reactive switching of shunt reactors or capacitors for voltage support (NERC, 2010).
2. **Oscillation damping control** : Inter-area or wide-area oscillations can be damped effectively employing high-speed low latency PMU data. WAMS based signals have been used as an input to power system stabilizers for damping unstable power swings in (Wang et al., 2011), (Meng et al., 2017).
3. **Equilibrium state control** : After a disturbance the power system must return to a stable state, which is also labelled as a target state. The more stable the target state, the more likely will the system oscillations be damped and robust oscillation control will not be necessary. Real-time WAMS data can help in balancing the network load and the transfer demands to ensure that there is optimal power flow (stable equilibrium condition), (Annakage et al., 2017), (Hadley et al., 2007).
4. **Special protection schemes and islanding** : Special protection schemes/systems (SPS) are control systems that are activated as soon as the occurrence of an event is detected (Phadke and Thorp, 2009). These are also known as System Integrity Protection Schemes (SIPS) or Remedial Action Schemes (RAS). System-wide WAMS data acquired in real-time is gathered at control centers to identify which RAS should be used to navigate the power system to a stable state, if needed. These systems respond to various pre-identified set of disturbances which are recognized through

extensive dynamic simulation studies. The implementation of an SPS logic is expensive and complicated, especially if WAMS based remote signals are involved (De La Ree et al., 2010), (Ivanković and Brnobić, 2021). Unintentional tripping of transmission lines during stable recoverable swings can be prevented using SPS such as the power swing blocking (PSB) logic. This is done by identifying vulnerable transmission lines which are likely to trip during power swing conditions and issuing a block command to the relay. Islanding at pre-selected locations is executed to maintain load-generation balance and system integrity (SPCS, 2013), (Zhang and Zhang, 2016), (Raj and Soman, 2020), (Gajjar et al., 2021).

## **1.4 Problems With the Present WAMS Architecture and Applications**

WAMS and PMUs have been the center of research for most power system engineers over the last two decades. As discussed in the previous sections WAMS/PMUs are effectively being deployed all over major grids across the world. The deployment of PMUs is on the rise especially in developing countries such as India, where rural electrification is on the ascendant. Also, the continuous integration of renewable sources with the main grid in order to decarbonize electricity generation requires frequent monitoring and visualisation. With the substantial advances in signal processing and communication technology, both in terms of hardware and software solutions, the required synchrophasor standard compliance criteria with regards to PMUs is expected to become even more strict in the upcoming years. In order to be well prepared for such eventualities, several major steps can be taken beforehand so as to make sure that PMUs and different WAMS applications are not overwhelmed by the demands of the growing and evolving power grids. A few problems which have been identified with the established WAMS architecture and its components are listed below:

1. The IEEE synchrophasor standards, (IEEE Std, 2011), (IEEE Std, 2018) are flexible with regards to compliance of either three-phase positive sequence or single-phase phasors. With the advent of micro-PMUs, there needs to be a major update to the existing synchrophasor standards such that tests and limits with regards to single-phase systems are exclusively included. This is due to the fact that micro-PMUs

which are predominantly deployed in distribution networks work mostly on single-phase systems which are more prone to harmonics and noise.

2. Wide area monitoring of power systems is one of the key aspects of WAMS applications. This includes monitoring phasors, frequency and ROCOF at key locations across the power system. Prevalent literatures in the field of WAMS based monitoring concern themselves with voltage phasors and its associated quantities. On the other hand, current based phasors, frequency and ROCOF are not monitored as frequently as their voltage counterparts.
3. Group delay of phasor estimation algorithms and the latency associated with the phasor computation process has not been discussed thoroughly in the literature. No particular emphasis has been given in the literature apart from Meng et al. (2017) to help the reader understand exactly the group delay compensation aspect of PMUs. This information in turn affects the design and the application aspect of a PMU in the WAMS architecture.
4. The highly granular nature of WAMS data and the ever improving communication technology open up possibilities for even more refined applications of WAMS data. Several online and real-time applications of WAMS data are still in the development stage, and once deployed will enable an elevated wide area visualization of the grid. One such application is event detection and localization, which uses data from WAMS in order to identify anomalies representing power system disturbances. Majority of the research has been dedicated towards identifying anomalies using PMU data available only at critical points of the power system such as in Gajjar and Soman (2014), Shaw and Jena (2020), thus defeating the purpose of wide-area monitoring and visualization.

## **1.5 Literature review**

### **1.5.1 IEEE Standard Based Testing of PMU Algorithms**

PMUs are the primary measuring device in WAMS, as discussed previously. According to the IEEE Std (2011), PMUs are broadly classified as Protection (P) class and Measurement (M) class. This distinction is predominantly based on the application of the PMUs. P-class

PMUs are used for protection applications which require data at high reporting speed. M-class PMUs are used for measurement applications, postmortem analysis etc, which require high accuracy values but do not require low reporting delay, (Agarwal et al., 2013) (Shi et al., 2020), (Liu et al., 2021). The accuracy of estimates provided by both P and M class PMU algorithms must meet the requirements set by the latest IEEE standards, in order to be deemed fit for practical applications. These standards were first introduced in Power System Relaying Committee (1995), and an updated version was released in IEEE Std (2005). Tests such as the step test, steady-state test, ramp test etc, were introduced along with Total Vector Error (TVE) to measure the precision of the synchrophasor algorithms. A major change to the IEEE standard was proposed in IEEE Std (2011), which included treatment for dynamic phasors, as put forward for the first time by De la Serna (2007). An updated version of the the 2011 standard was published in IEEE Std (2014), with several notable changes such as,

1. Removal of the combined amplitude and phase modulation test.
2. Variation of the base frequency and the removal of the ROCOF requirements for the inter-harmonic test.
3. Decrease in the passband attenuation and increase in the stop-band attenuation of M class filters.

The reasons for the amendments made to IEEE Std (2011), have been explained in detail in Martin (2015) and Roscoe et al. (2015). For example, one of the changes includes the variation of the base frequency as per the reporting rate, in case of the inter-harmonic test. Such a requirement was added to ensure that the filtering is good enough to handle inter-harmonic conditions when the power system is operating at an off-nominal frequency. Similarly, due to the simultaneous interactions between the phase and amplitude modulated signals the performance of PMU algorithms could not be properly evaluated, therefore IEEE Std (2014) revised the procedure into respective amplitude and phase modulation tests. In Table. 1.2, salient features of all the released versions of the IEEE standards for synchrophasor measurements in power systems are listed.

**Table 1.2:** Evolution of the IEEE standard for synchrophasor measurement

IEEE Standards	Salient Features
IEEE Std 1344-1995 (Power System Relaying Committee, 1995)	<ul style="list-style-type: none"> <li>• Time-tagging of phasors is introduced</li> </ul>
IEEE Std C37.118-2005 (IEEE Std, 2005)	<ul style="list-style-type: none"> <li>• Magnitude step, Phase step and Frequency step test are introduced for the first time.</li> <li>• TVE evaluation is also described.</li> </ul>
IEEE Std C37.118.1-2011 (IEEE Std, 2011)	<ul style="list-style-type: none"> <li>• Most major update to the standard till date.</li> <li>• Included treatment of dynamic phasors.</li> <li>• Amplitude modulation, phase modulation, frequency ramp tests are included.</li> <li>• P and M class PMU models were also suggested.</li> </ul>
IEEE Std C37.118.1a-2014 (IEEE Std, 2014)	<ul style="list-style-type: none"> <li>• Several test procedures were removed.</li> <li>• Error limits for various tests are altered.</li> <li>• M-class PMU model was re-designed to meet the accuracy requirements.</li> </ul>
IEC/IEEE 60255-118-1 (IEEE Std, 2018)	<ul style="list-style-type: none"> <li>• No changes were made to the error limits or the test procedures.</li> </ul>

**Classification of PMU algorithms:** Due to the constant updation of the IEEE synchrophasor standards resulting in stricter accuracy requirements, several PMU algorithms have been proposed over the years. These algorithms can be categorized as (Castello et al., 2012):

1. Static-model based algorithms
2. Dynamic-model based algorithms
3. Adaptive algorithms

### 1.5.1.1 Static-Model Based Algorithms

The static-model based algorithms employ the popular Discrete Fourier Transform (DFT) for phasor estimation, (Adhikari et al., 2019), (Ghafari, 2016). This method uses a fixed sampling rate based on the nominal frequency. The static-model based algorithms assume that the amplitude as well as the phase of the time-domain signal is fixed in an observation window. Hence, such algorithms fail during off-nominal frequency and modulation conditions because of spectral leakage which is caused due to incoherent sampling. Under these conditions, the second harmonic frequency component is seen to dominate the amplitude as well as the phase estimates provided by the static-model based methods. This high frequency content if not dealt with leads to poor frequency and ROCOF estimates. Several modifications have been suggested to improve the phasor estimates provided by the static model. Some of the techniques include,

- Using a three-point averaging filter as described in Phadke and Thorp (2010), Guardado and Guardado (2015). This technique averages three synchrophasors computed at nominal frequency which are  $60^\circ$  apart. For off-nominal frequency signals, this corresponds to second harmonic component phasors which are  $120^\circ$  apart for one-cycle DFT. Such a technique reduces the amplitude of the second harmonic component which otherwise dominates traditional DFT based phasor estimates.
- Using PMU models for P and M-class measurements IEEE Std (2011). These models involve FIR filters based on different windows and with different filtering capabilities. The P-class model uses a triangular window spanning over 2-cycles of the fundamental frequency. Low latency estimates provided by the P-class models are useful for protection applications. The M-class filter involves a more complex design based on the reporting rate required. A “sinc” and a hamming functions are used in conjunction in order to obtain the filter coefficients. Modifications to the M-class filters and an empirical relation between the phasor reporting rate and filter order required for designing the M-class filters are presented in Roscoe et al. (2013) and Roscoe et al. (2015).
- The absence of an amplitude correction factor for the M-class PMUs hampered the IEEE compliance requirements for frequency deviations close to  $\pm 5$  Hz. Authors in Gurusinghe et al. (2014) have presented a correction factor based on the measured signal frequency for the M-class filter in order to be compliant around extreme frequency deviations. Authors have also modified the existing M-class filter and suggested improved frequency estimation techniques to provide compliant estimates.
- Authors in Thilakarathne et al. (2017) have proposed major modifications to the synchrophasor algorithms suggested in IEEE Std (2011). An input-end anti-aliasing filter, Blackman-gaussian window and Parks and McClellan window are suggested for improving synchrophasor estimation during frequency deviation conditions. Compensation factors for amplitude, based on frequency estimates are also provided by the authors.
- Authors in Dotta and Chow (2013) have compared the effects of windowing on the amplitude of the second harmonic component of the phasors at off-nominal frequencies. Authors have used the Blackman-Harris window and compared the results with a three-point averaging filter as well as the least squares method.

- A pre-processing or a pre-DFT method known as sample value adjustment is used in Akke and Thorp (2010), Ghafari et al. (2016), Maharjan et al. (2016) for accurate phasor estimation. This technique requires accurate frequency information in order to be able to correct for the drifting of the sample values at off-nominal frequencies. Sample values at off-nominal frequencies are adjusted and the processed signals are passed as nominal frequency signals resulting in accurate phasor estimation.
- In Xia and Liu (2009) an accurate single-phase phasor and frequency estimation technique is proposed. Authors construct quasi-three-phase signals from a single-phase signal in order to naturally eliminate the second harmonic component, by computing the positive sequence estimate. The quasi-three-phase signals are constructed by simply shifting the data-windows in the single-phase signals by  $\pm N/3$  samples, depending on the phase required.
- An artificial signal with DFT equal and opposite to the signal to be measured is constructed using the Clarke's transform, in Zhan et al. (2016). This is done in order to totally cancel out the second harmonic component present during frequency deviation conditions. For single-phase systems, three-phase signals are artificially constructed using the method presented by Xia and Liu (2009), in order to obtain the Clarke transformed signals. This method of phasor computation also involves input-end averaging filters, amplitude adjustments based on least squares technique as well as Blackman-Harris window based DFT.
- Authors in Belega and Petri (2013), Macci et al. (2011), Barchi et al. (2013), Jin and Zhang (2020), Frigo et al. (2018) employ the popular interpolated DFT (IpDFT) method for phasor estimation. This method solves the problem of spectral leakage during frequency excursion scenarios by interpolating the maximum amplitudes of the DFT spectrum to obtain a correction term. Any number of points can be interpolated to obtain the correction term e.g, 2p-*IpDFT*, 3p-*IpDFT*, 4p-*IpDFT* etc. The correction term is further used to correct for the amplitude error and phase error introduced during frequency excursion scenarios. An improved version of *IpDFT* namely iterative *IpDFT* is introduced in Derviškadić et al. (2017), (Romano and Paolone, 2014), which provides P-as well as M class compliant estimates.

The discussed PMU algorithms employing the static-model are summarized in Tables. 1.3 and 1.4.



**Table 1.3: Static-Model based PMU algorithms (Part-1).**

Methodology used	Performance Class (P or M)	Salient features
<b>DFT with filtering</b>	Three-Point filter Phadke and Thorp (2010) Guardado and Guardado (2015)	<ul style="list-style-type: none"> <li>Averages three synchrophasors computed at nominal frequency which are <math>60^\circ</math> apart.</li> <li>For off-nominal frequency signals synchrophasors with angle difference of <math>120^\circ</math> are used, i.e., phasors which are separated by <math>N/3</math> samples.</li> </ul>
	IEEE P-Class filter IEEE Std (2011)	<ul style="list-style-type: none"> <li>Uses DFT in conjunction with a triangular window spanning over two cycles of the fundamental frequency.</li> <li>Amplitude compensation factor is provided by the standard.</li> </ul>
	IEEE M-Class filter IEEE Std (2011)	<ul style="list-style-type: none"> <li>A "sinc" and a hamming function are used for designing a M-class filter.</li> <li>The order of the filter is directly related to the reporting rate required for the PMU.</li> <li>Amplitude compensation factor is absent.</li> </ul>
	Modified IEEE M-Class filter Roscoe et al. (2013) Roscoe et al. (2015)	<ul style="list-style-type: none"> <li>IEEE recommended M-class filters are modified and an empirical relation between the phasor reporting rate and the filter order is presented.</li> </ul>
	Modified IEEE M-class filter Gurusinghe et al. (2014)	<ul style="list-style-type: none"> <li>Modified IEEE-M class filter proposed</li> <li>Amplitude correction factor for the IEEE M-class filter is given.</li> <li>Adjustments to the performance of the M-class filter are also mentioned, thus enabling its compliance around extreme frequency deviations.</li> </ul>
	Modified P-type Thiakarathne et al. (2017)	<ul style="list-style-type: none"> <li>IEEE P-class filters are improved upon using half cycle averaging technique.</li> <li>Amplitude compensation factors are provided.</li> </ul>
	Modified M-type Thiakarathne et al. (2017)	<ul style="list-style-type: none"> <li>IEEE M-class filters are improved by using Parks McClellan and Blackman Harris window .</li> <li>Amplitude compensation factors are provided.</li> </ul>
	Windowing Dotia and Chow (2013)	<ul style="list-style-type: none"> <li>Amplitude of the second harmonic component is reduced using windowed DFT.</li> <li>Blackman-Harris window is compared against three-point averaging filter and LS method.</li> </ul>

**Table 1.4:** Static-Model based PMU algorithms (Part-2).

Methodology used	Performance Class (P or M)	Salient features
<b>DFT with pre-processing</b>	P	<ul style="list-style-type: none"> <li>Drifting of sample values is accounted for by pre-processing the input time-domain signal.</li> <li>Pre-processing adjusts the sample values such that a signal is passed on as a nominal frequency signal.</li> <li>Recursive least squares (RLS) method is employed in order to extract frequency information required for sample value adjustment.</li> <li>Computationally light nature of the algorithm makes it appealing for use in real-time.</li> </ul>
	P	<ul style="list-style-type: none"> <li>Adjusts the sample values in order to generate samples whose frequency matches the power system frequency thus resulting in accurate synchrophasor estimation.</li> <li>Simulation results, conducted for the method show compliance as per the latest IEEE Standard.</li> </ul>
	P	<ul style="list-style-type: none"> <li>Involves the construction of an artificial three-phase signal from a single-phase system.</li> <li>This enables the computation of positive sequence estimates thus lowering error.</li> <li>Has been used in Frequency disturbance recorders.</li> <li>Can be implemented for both three-phase and single-phase systems.</li> </ul>
<b>DFT with quasi-positive sequence</b>	M	<ul style="list-style-type: none"> <li>Uses QP-DFT logic for single-phase systems.</li> <li>Constructs in-phase and phase-quadrature signals in order to eliminate DFT imposed error.</li> <li>Least squares technique, averaging filters and Blackman-Harris window also involved in the overall phasor estimation process.</li> </ul>
	P	<ul style="list-style-type: none"> <li>Interpolates DFT estimates with maximum amplitudes to obtain a correction term.</li> <li>The correction term is further used to modify for the amplitude and the phase values in order to eliminate the error encountered during frequency excursion scenarios.</li> <li>The evaluation of the correction term varies based on the window used for DFT estimation.</li> <li>Any number of points can be interpolated to obtain the correction term, e.g. 2p-lpDFT, 3p-lpDFT, 4p-lpDFT etc.</li> </ul>
<b>DFT with interpolation</b>	M	<ul style="list-style-type: none"> <li>Improves upon the basic lp-DFT logic.</li> <li>Is implemented in an iterative manner.</li> </ul>
	M	<ul style="list-style-type: none"> <li>Clarke's Transform based DFT Zhan et al. (2016)</li> </ul>
		<ul style="list-style-type: none"> <li>Interpolation-based DFT (lpDFT) Belega and Peiri (2013) Maeci et al. (2011) Frigo et al. (2018) Jin and Zhang (2020)</li> </ul>
		<ul style="list-style-type: none"> <li>Iterative lpDFT (IlpDFT) Derviškić et al. (2017)</li> </ul>

### 1.5.1.2 Dynamic-Model Based Algorithms

The dynamic phasor models are used when an improved accuracy is needed, at the cost of speed and computational efficiency. The signal model in such algorithms assumes the amplitude and phase of the time-domain signal to be varying in nature which resembles realistic power system signals. The varying amplitudes and phases are then expressed using Taylor series polynomials of certain degrees. The degree of the polynomial is based on the accuracy level of the estimates required. Some of the notable methods in this category include :

- Authors in Premerlani et al. (2007) introduce two methods namely the 4 parameter and 6 parameter phasor estimation technique. These methods compensate for the errors introduced at off-nominal frequencies by calculating the first and the second derivatives of the time-varying phasor.
- The well known Prony method is suggested for P-class phasor estimation in De la Serna (2013). Due to the flexible nature of the Prony method, estimates obtained during power system oscillation conditions are significantly better compared to static-model based algorithms such as the one-cycle DFT method. Additionally, the Prony filter offers instantaneous values of damping and frequency, which correspond to the first derivative of amplitude and phase. These instantaneous estimates are highly helpful for evaluating the stability of the power system.
- A least square estimation technique is used in De la Serna (2010) where Taylor based Fourier Filter is employed. A hamming window is used by the authors to minimize the error between the actual and the estimated signals. This technique is further improved upon in Zhan and Liu (2014) by including the second harmonic component in the polynomial approximation of the time-domain signal in order to provide M-class compliant estimates.
- Another P-class dynamic phasor model based method using the least squares technique is presented in Vejdani et al. (2015). The PMU algorithm in addition to phasor values also provides additional estimates such as swing frequency without any increased computational burden.
- For handling out-of-band interfering signals primarily, a *Dynamic Phasor Estimation Algorithm considering OBI (DSEA-OBI)* is proposed by authors in Fu et al. (2021).

In this method the Taylor series time-domain signal model used by authors includes the fundamental as well as the out-of-band interference component to provide M-class compliant estimates.

- In order to provide M-class compliant estimates, authors in Narduzzi et al. (2018) propose a compressive sensing based Taylor Fourier method, namely fast-TFM for accurate harmonic and inter-harmonic phasor computation. This method provides estimates at a high frame rate, even while computing phasors at multiple frequencies.

### **1.5.1.3 Adaptive Algorithms**

Adaptive techniques for phasor estimation which use feedback in any form to improve the phasor estimates are also present in the literature. In, Castello et al. (2014) frequency feedback has been used to constantly adjust the model of the Taylor Fourier Transform. Similarly, in Bansal and Sodhi (2019), frequency feedback is provided to a PMU to generate reference signals with the same frequency as the input time-domain signal. In Kamwa et al. (2014) the center frequency of FIR bandpass filters is constantly tuned on-line as per the input signal frequency. In order to effectively eliminate the majority of the off-nominal frequency leakage in the computed magnitudes and phase angles, especially under steady state conditions, a frequency corrected three-point averaging filter (F3P) is suggested in Novak (2021). Authors in Khodaparast et al. (2022) use the Empirical Mode Decomposition (EMD) method in conjunction with the Prony algorithm to estimate phasors. The input time-domain signals are projected onto a set of  $L$  exponentially damped sine functions, where  $L$  is the Prony order. To reduce the computation time, the order of the Prony algorithm is adaptively adjusted using EMD method. The empirical wavelet transform is employed for phasor estimation in Chauhan et al. (2018). Here, M-class compliant estimates are obtained for distribution level signals polluted with noise and under dynamic conditions. The wavelet filters for phasor estimation are designed based on frequency information extracted using the DFT method. Signals are pre-processed using the sample value adjustment technique before being subjected to frequency spectrum analysis via DFT.

## **1.5.2 Handling of Group delays in PMU Algorithms**

In most of the above mentioned literature the implications of positioning the obtained phasor samples relative to a data window is not thoroughly discussed. The Power System

Relaying Committee (1995) and IEEE Std (1998), explicitly mention three positions in the data window to which the computed phasor can be referred to, namely, the start of an observation window, the center of an observation window or to the end of an observation window. As mentioned in Annex. C of the Power System Relaying Committee (1995), referring an obtained phasor to any point in the data window is largely a matter of preference. The Power System Relaying Committee (1995) clearly mentions that no particular referring technique shall be given preference over the other. In the IEEE Std (2005) it is found that referring a phasor to the end of an observation window leads to high values of phase angle error during dynamic and static off-nominal frequency conditions. Further, referring the estimated phasors to the center of the observation window is seen to cancel out the group delay introduced during varying frequency conditions which in-turn lead to low values of the phase angle error. The 2005 standard also mentions that whenever the TVE associated with a PMU under a certain set of conditions is to be calculated, all delays should be compensated for, so that the theoretical and the computed phasors are aligned with each other. The IEEE Std (2011), IEEE Std (2014), IEEE Std (2018), again prefer that the phasor estimated at the end of the window should be referred to the center of the window. Methods used for referring phasor samples in an observation window result in different values of latency which has led to the classification of PMUs as indicated by Meng et al. (2017) as following :

1. Causal PMUs
2. Non-Causal PMUs

Latency with regards to power system can be defined as the time interval between when an event occurs on the power system and when it is reported in data at the PDC. It is noted that in the current literature the effects of latency, mostly due to communication links in wide-area monitoring and control on power system stability during contingencies have been extensively studied. With the help of a flexible AC transmission system and a wide area controller, latency issues are studied in Musleh et al. (2018). In, Sharma and Tyagi, B (2014), the effect of latency on wide area damping controllers used in large power grids to minimise small-signal oscillations is investigated. In Chaudhuri et al. (2010), the authors showed that if damping controllers are operated under measurement latency, oscillations may be triggered in tie-line. The impact of measurement latency on wide-area control operations in a power grid was investigated in Stahlhut et al. (2008). Here, the latency was modelled as a stochastic process, and the impact on the inter-area mode was investigated

using the damping ratio. The case studies revealed that the damping ratio decreases sharply with time delay. Latency obtained due to causal and non-causal PMUs has been discussed with regard to stability issues in Meng et al. (2017), Zhu et al. (2010) and Thomas et al. (2014).

### **1.5.3 Frequency Estimation Methods in PMUs**

WAMS provide time-stamped estimates via PMUs which include phasors (magnitude and phase angle), frequency and the rate-of-change of frequency (ROCOF) (IEEE Std, 2011), (IEEE Std, 2014). Among these estimates, frequency is one of the most critical health indicators of a highly interconnected grid (Kirkham et al., 2018). Continuous monitoring and regulation of frequency is necessary in order to achieve load-generation balance in a system while maintaining synchronous operation of interconnected power systems (Milano and Manjavacas, 2020). Numerous power-system protection and control applications such as frequency relaying and Power System Stabilizers necessitate precise and quick frequency estimates (Kundur, 1994), (Padiyar, 2008). Rapid-response applications, such as load shedding, generator protection, and renewable energy regulation also require accurate prediction of the power system frequency in real-time (Nam et al., 2014). Frequency estimation is even more important in the context of smart grid, where frequent switching from the main grid to microgrids, electricity islands, and dual natures of some loads, such as plug-in hybrid electric vehicles (PHEVs), all cause imbalance in the power generation-load chain, and thus frequency variations (Rahmann and Castillo, 2014), (Xia et al., 2012). In conventional synchronous generator-based power systems the frequency regulation is achieved using speed governors, (Padiyar and Kulkarni, 2019), (Shubhanga, 2018). However, due to the integration of low-inertia based Renewable Energy Sources (RES) into the existing power grid in order to decarbonize energy generation, the ability to regulate frequency in transmission and distribution networks after a transient disturbance has degraded (Zarifakis et al., 2019). Therefore, to maintain grid integrity despite its ever expanding nature and continuous integration of RES, accurate frequency regulation and estimation is essential. Online or off-line event detection, inertia estimation and control of power system oscillations using power system stabilizers (PSS) can also benefit from precise frequency measurements, (Shaw and Jena, 2020), (Ashton et al., 2014), (Rao and Shubhanga, 2018). With the help of accurate frequency knowledge smart grids can control the power flow between generation nodes and loads, increase power delivery efficiency, enhance equipment

utilisation, and maintain system stability, (Dai and Tate, 2021).

Most of the modern power grids utilize PMU based time-stamped frequency estimation. Frequency estimation in PMUs is typically achieved using an additional module which deals with the phase angle estimates provided by the phasor computing module (Dai and Tate, 2021). Some PMU algorithms even directly compute frequency without the requirement of additional modules (Belega and Petri, 2013). It is seen that the PMU-based frequency estimation methods are highly dependent on the accuracy levels of the synchrophasor computing algorithms. The literature broadly classifies frequency estimation techniques as time-domain based and frequency-domain based methods some of which are summarized in Tables. 1.5 and 1.6, respectively.

#### **1.5.4 Event Analysis Employing WAMS Signals**

Power system monitoring is a primary feature of WAMS. Due to the geographically diverse nature of the PMUs and a high sampling rate employed for synchrophasors, the PMU data reveals the state of a power system, much better than conventional SCADA based methods. With the continuous increase in PMU numbers, the visualization ability of WAMS has improved exponentially. Therefore, the regular inspection of all the PMU data-streams manually in order to pin point anomalies in the data, has become a very tedious and an error prone task. Till date around 1800 PMUs have been installed in the United States of America and around 1400 have been installed in India (Raj et al., 2019). Scanning the synchrophasor data provided by these many PMUs either off-line or in real-time is near impossible if manual approaches are employed. A single phasor data concentrator (PDC) gathering data from say 100 PMUs with a sampling rate of 20 measurements per second creates about 50 GB of data in a single day (Xie et al., 2014). Such a massive volume of data must be thoroughly analysed and intelligently presented to system operators in order for them to understand the current condition of the system, as well as to detect abnormal events at various locations in a large power system and enable them to take appropriate decisions to initiate control actions.

Thus, in order to detect anomalies in the synchrophasor data provided by numerous PMUs installed in a WAMS, event detection is necessary. Event detection in power systems is the process of analyzing PMU data streams in order to discover sets of data points which do not match with the ambient or normal values. Any irregular patterns or signatures left on a power system signal define the type of an event. If any disturbance pattern is discovered

**Table 1.5:** Time-Domain based frequency estimation methods.

S.No	Reference	1- $\phi$	3- $\phi$	Salient features
1	Carcelen-Flores et al. (2012) Kulkarni (2014)	Yes	No	<ul style="list-style-type: none"> <li>• Uses the Zero-Crossing method to compute frequency.</li> <li>• Very poor performance during noise, harmonics and inter-harmonics.</li> <li>• Computationally Light.</li> </ul>
2	Seyedi and Pasand (2012)	Yes	No	<ul style="list-style-type: none"> <li>• Uses Consecutive samples for frequency estimation.</li> <li>• Accuracy is directly dependent on the number of samples used.</li> <li>• Poor performance in presence of noise, harmonics and inter-harmonics.</li> <li>• Computationally light.</li> </ul>
3	Seo and Kang (2017) Moore et al. (1994)	No	Yes	<ul style="list-style-type: none"> <li>• Uses time-derivative of in-phase and quadrature components for frequency computation.</li> <li>• Derivative calculations lead to errors in such a technique.</li> <li>• Poor harmonic and inter-harmonic performance.</li> <li>• Computationally light.</li> </ul>
4	Akke (1997)	No	Yes	<ul style="list-style-type: none"> <li>• Uses complex demodulation technique to compute frequency.</li> <li>• Requires all three phases.</li> <li>• Performance degrades during unbalanced conditions.</li> <li>• Computationally light.</li> </ul>
5	Canteli et al. (2006) Xia et al. (2012)	No	Yes	<ul style="list-style-type: none"> <li>• Uses an improved complex demodulation technique to compute frequency.</li> <li>• Effects of unbalance on the <math>\alpha\beta</math> signals are corrected.</li> <li>• Requires all three phases.</li> </ul>
6	Li et al. (2019)	Yes	No	<ul style="list-style-type: none"> <li>• Uses averaging filters in convolution to estimate frequency.</li> <li>• Harmonic and inter-harmonic performance not provided.</li> <li>• Computationally light.</li> </ul>
7	Xia et al. (2014)	No	Yes	<ul style="list-style-type: none"> <li>• Uses the complex least squares based technique to estimate frequency.</li> <li>• Performance during unbalanced conditions is improved.</li> <li>• Excellent performance in presence of harmonics and inter-harmonics.</li> </ul>
8	Ahmed et al. (2021)	No	Yes	<ul style="list-style-type: none"> <li>• Uses gradient method on delayed Clarke's transform based signals to estimate frequency.</li> <li>• Limited details with respect to performance under different signal conditions are provided.</li> </ul>
9	Zečević et al. (2016)	No	Yes	<ul style="list-style-type: none"> <li>• Uses an iterative technique based on the Orthogonal Constant Modulus.</li> <li>• Performance during fault scenarios in power systems is excellent.</li> <li>• Performance metrics during harmonic and inter-harmonic conditions not provided.</li> </ul>
10	Jafarpisheh et al. (2018)	Yes	No	<ul style="list-style-type: none"> <li>• Uses Adaptive Accelerated Multiple Signal Classification algorithm for frequency estimation.</li> <li>• Excellent performance in presence of noise and d.c offsets.</li> <li>• No performance comparison during inter-harmonic conditions is provided.</li> </ul>
11	Sun et al. (2019)	Yes	Yes	<ul style="list-style-type: none"> <li>• Uses the Harmonics Aboutanios Mulgrew (HAM) method for frequency estimation.</li> <li>• Frequency values are refined using a weighted least squares estimator.</li> <li>• Excellent harmonic and inter-harmonic performance.</li> </ul>
12	Kim et al. (2020)	No	Yes	<ul style="list-style-type: none"> <li>• Uses an iterative based approach employing a modified periodogram.</li> <li>• Very similar to the iterative interpolated DFT based approach</li> <li>• Excellent performance during three-phase unbalanced conditions.</li> </ul>
13	Ahmed et al. (2018)	Yes	No	<ul style="list-style-type: none"> <li>• Uses an adaptive sliding mode observer for phase as well as frequency estimation.</li> <li>• Provides excellent results during phase jump scenarios.</li> <li>• Poor performance during the presence of harmonics and d.c offsets.</li> </ul>
14	Verma et al. (2020)	Yes	Yes	<ul style="list-style-type: none"> <li>• Uses Enhanced Lyapunov Demodulation (ELD) method to obtain frequency.</li> <li>• Other signal parameters such as amplitude and phase are also estimated.</li> <li>• Uses a moving average filter to improve harmonic performance.</li> <li>• Excellent performance in presence of d.c offsets.</li> <li>• Performance in the presence of inter-Harmonic signals not presented.</li> </ul>

during an event analysis, then an appropriate preventive control action may be initiated by the operator. Numerous event detection algorithms are available in the literature and can be broadly classified as non-training based and training-based.

#### 1.5.4.1 Non-Training Based Methods

Non-training based methods include the use of statistical or signal-processing techniques to identify irregular or anomalous patterns in PMU data obtained from WAMS. These methods predominantly include, principal component analysis, wavelet transform, discrete fourier transform, standard deviation, etc. Some of the popular state-of-the-art non-training



**Table 1.6:** Frequency-Domain based frequency estimation methods.

S.No	Reference	1- $\phi$	3- $\phi$	Salient features
1	Phadke and Thorp (2010)	Yes	Yes	<ul style="list-style-type: none"> <li>• Uses Least Squares based technique for frequency estimation.</li> <li>• Poor performance for single-phase signals.</li> <li>• Excellent harmonic performance, poor inter-harmonic performance.</li> <li>• Computationally Light</li> </ul>
2	Macci et al. (2011) Derviškadić et al. (2017)	Yes	Yes	<ul style="list-style-type: none"> <li>• Uses frequency domain interpolation for frequency estimation.</li> <li>• Harmonic performance is poor compared to DFT.</li> <li>• Poor inter-harmonic frequency.</li> <li>• Poor performance for single-phase signals.</li> </ul>
3	IEEE Std (2011) IEEE Std (2014)	Yes	Yes	<ul style="list-style-type: none"> <li>• Uses time-derivative approach for frequency estimation.</li> <li>• Susceptible to noise.</li> <li>• Poor inter-harmonic performance using P-class filter.</li> <li>• Poor single phase performance.</li> <li>• Computationally light.</li> </ul>
4	Gurusinghe et al. (2014) Vejan et al. (2015)	Yes	Yes	<ul style="list-style-type: none"> <li>• Uses improved time-derivative based approach for frequency estimation.</li> <li>• Average of frequency estimates computed over two reporting rates is used.</li> <li>• Improved inter-harmonic performance, yet inadequate to meet M-class requirements</li> <li>• Poor single-phase performance</li> </ul>
5	Xia and Liu (2009)	Yes	No	<ul style="list-style-type: none"> <li>• Uses quasi positive sequence synthesis for frequency estimation.</li> <li>• Used in frequency disturbance recorders.</li> <li>• Computationally light.</li> <li>• Poor inter-harmonic performance.</li> </ul>
6	Zhan et al. (2016)	Yes	Yes	<ul style="list-style-type: none"> <li>• Uses Least squares approximation for frequency estimation.</li> <li>• Poor dynamic performance.</li> <li>• Excellent harmonic and inter-harmonic performance.</li> <li>• Computationally heavy</li> </ul>
7	De la Serna (2010) Castello et al. (2014)	Yes	Yes	<ul style="list-style-type: none"> <li>• Uses instantaneous signal coefficients for frequency estimation.</li> <li>• Excellent harmonic and inter-harmonic performance.</li> <li>• Poor single-phase performance.</li> <li>• Computationally heavy.</li> </ul>
8	Zhan and Liu (2014)	Yes	Yes	<ul style="list-style-type: none"> <li>• Uses Least squares approximation to obtain frequency.</li> <li>• Poor single phase estimates.</li> <li>• Excellent harmonic and inter-harmonic performance.</li> <li>• Computationally heavy.</li> </ul>
9	Reza et al. (2014)	Yes	No	<ul style="list-style-type: none"> <li>• Uses three DFT based filters with constant coefficients to estimate frequency.</li> <li>• Other parameters such as amplitude and phase are also computed using this method.</li> <li>• Tuning of parameters required.</li> <li>• Harmonic performance excellent, inter-harmonic performance not mentioned.</li> </ul>
11	Xia et al. (2016) Xia et al. (2015)	Yes	No	<ul style="list-style-type: none"> <li>• Uses a complex Least Square based Smart DFT method to estimate frequency.</li> <li>• Provides excellent results in the presence of frequency modulations, harmonics and noise.</li> <li>• Performance during the presence of inter-harmonic frequencies not mentioned.</li> </ul>
10	Grebla et al. (2019)	Yes	Yes	<ul style="list-style-type: none"> <li>• Uses an adaptive Kalman filter to estimate frequency.</li> <li>• Kalman gain is adapted to be less sensitive during fault scenarios.</li> <li>• Limited performance comparisons provided.</li> </ul>
11	Reza et al. (2014)	Yes	No	<ul style="list-style-type: none"> <li>• Uses an adaptive demodulation method to estimate single-phase signal parameters.</li> <li>• Provides excellent results in the presence of harmonics.</li> <li>• Performance during the presence of inter-harmonic frequencies not mentioned.</li> </ul>

based methods currently available in the literature are presented in Table. 1.7.

#### 1.5.4.2 Training-Based Methods

Typically, training-based event detection techniques use artificial intelligence (AI), machine learning (ML), or deep learning (DL) methods for real-time event detection and categorization. The challenge of real-time detection of dynamic events is investigated utilising data-driven and physics-based models in Brahma et al. (2016). In Yadav et al. (2019) and Wang et al. (2019), a deep neural network (DNN) and a convolution neural network based real-time event classification method is discussed, respectively. Authors in Wang et al.

(2020) use a Convolution Neural Network (CNN) model using gray scale images to detect anomalies in power system signals. Authors in Ahmed et al. (2021), introduce the concept of event detection during data drifting scenarios. The authors define drifting as the variations in data statistics over a data stream, due to power grid dynamics. The authors point to the fact that the performance of previously trained machine learning algorithms may degrade during conditions of data drift. To overcome such scenarios, the authors propose a framework called as the PMUNET which trains machine learning algorithms online, in order to enable detection of anomalies during drifting data conditions. In Cui et al. (2018), a dynamic programming based Swinging Door Trending (DPSDT) method is used for compressing large PMU data and identifying events using the magnitude and the slope rate rule. A few of the above-mentioned techniques necessitate complete grid monitoring using PMU measurements at each bus which is not practical. Furthermore, Machine Learning based classifiers have low accuracy and require a large amount of historical data for training purposes.

#### **1.5.4.3 Loss-of-Synchronism Condition Detection**

Synchronous operation of AC generators is a major requirement of an interconnected power system. When disturbances such as generation loss, load loss, line tripping or faults etc, occur it leads to rotor angle oscillations in synchronous machines which may be stable or unstable depending on the nature and the severity of the disturbance, the response of the protective relays and other power system controls. An unstable swing will generally result in significant fluctuations in power flows, voltages and currents, and finally leads to loss-of-synchronism. This is also known as an out-of-step (OOS) condition. An OOS or loss-of-synchronism condition occurs when one or a number of generators in the power system fail to maintain synchronism with the rest of the grid. Such a condition must be detected in order to,

1. Help the operator to initiate emergency control actions.
2. Prevent uncontrolled separation of the power system which may result in the formation of unstable islands, and even a blackout, (SPCS, 2013).

During an OOS condition system separation at pre-determined locations is desirable/necessary in order to maximize the generation load balance in an island and to minimize the system restoration process, (Zhang and Zhang, 2016), (Raj et al., 2019), (Raj and Soman, 2020).

The idea behind a supervisory Power Swing Blocking (PSB) function is to identify relays which are prone to operate during unstable swing conditions and issues a block command to stop the relay operation if an OOS condition is identified, (McDonald et al., 2005), (SPCS, 2013). This technique of blocking relays is also known as the transfer trip operation or out-of-step tripping (OST), or controlled islanding, (Raj et al., 2019). The coherency of the generators and the balance between the generation and load on the constructed islands must both be taken into account while creating islands.

Some of the popular approaches present in the literature for detecting power swings (stable or unstable) are described below,

1. **Concentric characteristic scheme:** The distinction between a fault and a swing is traditionally made by calculating the rate-of-change of apparent impedance seen by a relay. To achieve this differentiation, a timer is used to time the duration of the impedance locus as it moves between two concentric impedance characteristics separated by  $\Delta Z$  impedance on the impedance plane, (McDonald et al., 2005), (Tziouvaras and Hou, 2004). The relay declares the event as a system fault if the measured impedance crosses the concentric characteristics before the timer expires. Otherwise, the relay qualifies the event as a power swing if the timer runs out before the impedance crosses both impedance characteristics.
2. **Two-Blinder scheme:** The two blinder method works on the same premise of timing the passage of an impedance vector through a particular  $\Delta Z$ . When the impedance vector reaches the outer blinder, the time measurement begins, and it ends when it crosses the inner blinder, (Elmore, 2003). A power swing condition is detected if the measured time exceeds the time setting.
3. **Continuous Impedance calculation:** This technique uses continuous impedance calculation to determine a power swing. An impedance calculation is made at a time say, " $t$ " s and compared to the impedance calculation made at " $t - 0.05$ " s. If there is a deviation between the two measured impedance values a power swing state is presumed but not yet established, (Blumschein et al., 2014). Based on the deviation between the previous measured impedance the following impedance at " $t + 0.05$ " s is predicted. If the prediction is correct, a power swing condition is detected.
4. **Rdot scheme:** The primary benefit of this relaying scheme is to initiate early controlled tripping for non-recoverable swings, whereas avoiding tripping for stable/recoverable

**Table 1.7:** Non-Training based event detection methods.

Methodology Used	Reference	Salient Features
<b>Principal Component Analysis (PCA)</b>	Ge et al. (2015)	<ul style="list-style-type: none"> <li>• PCA is used to compute the trend of a data stream in order to identify abnormal data due to sudden changes.</li> <li>• Events are classified as real-power events or voltage events.</li> </ul>
	Xu and Overbye (2015)	<ul style="list-style-type: none"> <li>• Partitional PCA (PPCA) is used for improved real-time anomaly detection.</li> <li>• Voltage magnitude, phase angle and frequency signals are used.</li> </ul>
	Cai et al. (2018)	<ul style="list-style-type: none"> <li>• <math>k^{th}</math> Nearest Neighbor (<math>kNN</math>) is used in conjunction with PCA.</li> <li>• Author applies <math>kNN</math> on the Hotellings <math>T^2</math> and <math>Q</math> to obtain two new monitoring statistics for detecting disturbances.</li> <li>• Focus of this method is primarily on events of oscillatory nature.</li> </ul>
	Guo et al. (2015)	<ul style="list-style-type: none"> <li>• Recursive Principal Component Analysis (RPCA) is used for detection.</li> <li>• Focus of this method is primarily on islanding detection for power systems with high level of renewable energy integration.</li> <li>• Suitable for online applications and involves updation of training data and monitoring thresholds adaptively.</li> </ul>
	Liu et al. (2015)	<ul style="list-style-type: none"> <li>• Modified PCA is used for creating early warnings during islanding conditions.</li> <li>• Long term historic data is used for threshold computation.</li> <li>• Only frequency signals are used for event detection.</li> </ul>
	Gajjar and Soman (2014)	<ul style="list-style-type: none"> <li>• Method of ellipsoids based on PCA is used for auto event detection.</li> <li>• Frequency measurements from critical buses on the power system are used for detecting oscillatory events.</li> </ul>
	Xie et al. (2014) Barocio et al. (2013)	<ul style="list-style-type: none"> <li>• Event detection is performed using a reduced number of PMUs.</li> <li>• Simulation data from a transient stability model of a New-England power system is used for demonstration.</li> </ul>
<b>Wavelet Transform Based</b>	Gao and Ning (2011)	<ul style="list-style-type: none"> <li>• Detail coefficients obtained using the wavelet transform are used to pin-point the occurrence of an event.</li> <li>• The amplitude of the detail coefficients reflects the proximity of the PMU closest to the fault location.</li> <li>• The use of "db2" wavelet with level 5 decomposition is suggested.</li> </ul>
	Kim et al. (2015)	<ul style="list-style-type: none"> <li>• Modified Wavelet Energy (MWE) and Normalized Wavelet Energy (NWE) values for voltage magnitude and frequency are computed.</li> <li>• Normalization is performed to eliminate risks of false alarms due to high variability PMU/PDC data.</li> <li>• Authors have employed "db1" wavelet with level 3 decomposition.</li> </ul>
	Vaz et al. (2021)	<ul style="list-style-type: none"> <li>• Low voltage data from the Brazilian and the Chilean power system is analysed for event detection using NWE.</li> </ul>
	Thomas et al. (2020)	<ul style="list-style-type: none"> <li>• Authors use NWE to detect events such as generator trip, three-phase fault and capacitor outages.</li> <li>• Event categorization is obtained using, a) Support Vector Machines b) <math>k^{th}</math> Nearest Neighbor (<math>kNN</math>) c) Decision tree techniques.</li> </ul>
<b>Standard Deviation Based</b>	Pandey et al. (2020)	<ul style="list-style-type: none"> <li>• Authors propose a synchrophasor anomaly detection tool (SynAD).</li> <li>• Location of events is narrowed down by calculating "scores" for an event for each PMU.</li> <li>• Events are classified as, active power, reactive power or fault events.</li> </ul>
	Shaw and Jena (2020)	<ul style="list-style-type: none"> <li>• Frequency signals obtained from WAFMS are used for event detection.</li> <li>• Raw frequency signals are denoised using wavelet transform.</li> <li>• Phase angle difference (PAD) and ROCOF are computed using frequency.</li> <li>• Standard deviation of PAD and ROCOF signals is evaluated and compared against thresholds for event detection.</li> </ul>
	Allen et al. (2013)	<ul style="list-style-type: none"> <li>• Relative Phase Angle Difference (RPAD) signals are used for detection.</li> <li>• Standard deviation of "transformed" RPAD signals is compared against a threshold for event detection.</li> </ul>
<b>Other methods</b>	Shaik and Mahela (2018)	<ul style="list-style-type: none"> <li>• Authors employ the S-transform for event detection.</li> <li>• Negative sequence voltage signal is used for detecting events such as islanding, outage of PV or wind generators, etc.</li> </ul>
	Yadav et al. (2018)	<ul style="list-style-type: none"> <li>• Detection and localization of events is performed using Teager-Kaiser Energy operator (TKEO).</li> <li>• Author focuses on multiple event detection and the super imposition of sequential events on candidate signals.</li> </ul>
	Ashton et al. (2013)	<ul style="list-style-type: none"> <li>• Root mean square of fluctuations of detrended signals is calculated for event detection.</li> <li>• This is done in order to remove the normal portion of the signal and to focus on the captured transient part.</li> </ul>

swings. This relaying scheme consists of a typical resistance based out-of-step relay augmented with the rate-of-change of apparent resistance module. For a severe disturbance, the rate-of-change of measured resistance will be large indicating an upcoming instability (SPCS, 2013). Therefore, the Rdot scheme based relay will trip even at a high resistance if the value of rate-of-change of resistance is high.

5. **Synchrophasor based schemes:** Synchrophasor estimates can also be used to detect an OOS condition in a power system network. If a power system is represented as a two machine equivalent, the phase angle between the voltages behind the transient reactance is calculated. After the occurrence of a disturbance the new phase angle is computed and the stability of the system is verified using the equal area criteria (Liu et al., 2014). The bus voltage phase angle trajectory is monitored for OOS condition detection in Zhang and Zhang (2016). The phase angle difference between the two latest synchrophasor samples, i.e.,  $|\theta_i - \theta_{i-1}|$ , as well as the rate-of-change of the phase angle difference, i.e.,  $d|\theta_i - \theta_{i-1}|/dt$ , are compared against a set threshold value for detection of an OOS condition.
6. **Energy function based scheme :** Authors in Padiyar and Krishna (2005), use energy function analysis for power system instability detection. During a disturbance scenario, a power system gains both potential as well as kinetic energy. This kinetic energy must be completely absorbed by the system in order to be categorized as large signal stable. Hence, if the value of kinetic energy is zero when the potential energy is maximum, a swing is categorized as a stable swing, whereas if the value of kinetic energy is non-zero when the potential energy is at its peak, the resultant swing is unstable in nature, (Padiyar and Krishna, 2005). This method of instability detection requires angular separation and potential energy values. The former requires voltage and current measurements with prior knowledge of line impedance.
7.  **$\delta_{SR} - V$  based scheme :** Coordinate system with angular separation as “x-axis” and voltage magnitude as “y-axis” is introduced in (Lavand and Soman, 2016) for detecting OOS conditions in power system. This is also labelled as the  $\delta_{SR} - V$  plane. At the instant of an electrical center creation the values of voltage magnitude and the angular separation are 0 and  $\pm 180^\circ$ , respectively. These quantities are computed for each synchrophasor sample, therefore enabling the constant monitoring of the power swing in the  $\delta_{SR} - V$  plane. Due to the large inertia of the power system, it is shown that the development of an electrical center in the plane has a smooth trajectory, as

compared to a 3-phase fault. By extrapolating the oscillation trajectory in the  $\delta_{SR} - V$  plane, the occurrence of an electrical center and an OOS condition can be predicted.

## **1.6 Research Gap and Major Contributions**

### **1.6.1 Research Gap and Motivation for the Thesis**

Over the last three decades, WAMS technology has been one of the key subjects of research for power system engineers. The countless applications and improved control and visibility of power systems provided by WAMS have led to its emergence as a visualization tool around the globe. The revision of the 2005 IEEE synchrophasor standard, (IEEE Std, 2005), which was published in 2011, (IEEE Std, 2011), for the first time included a treatment of dynamic power system signals. This update to the synchrophasor standard highlighted the need for improving upon the conventional PMU algorithms used in WAMS. Test procedures indicated in the synchrophasor standards published after 2005 ensured that commercial PMUs are capable of providing accurate synchrophasor estimates even during adverse signal conditions. These conditions include frequency deviations, amplitude modulations, phase modulations, harmonics, inter-harmonics, frequency ramps, and amplitude or phase step. Such features can be identified in power system signals during disturbance scenarios and must not hamper the performance of the PMU beyond a certain limit as dictated by the standard. Also, the performance of several WAMS based power system protection, control and monitoring functions is closely related to the speed and accuracy of the estimates obtained via PMUs. Therefore, an extensive survey of the PMUs, including the algorithms employed by them and their applications in WAMS has indicated that there are quite a few issues yet to be explored in this area, which are highlighted below.

#### **1.6.1.1 Implementation and Testing of PMU Algorithms Based on an Integrated PMU Architecture**

Updates to the IEEE standard for synchrophasor measurements in power systems have demanded continuous improvements to the phasor computing capabilities of PMU algorithms. A balance between the accuracy levels of the PMU estimates and the latency must be achieved, in order for a PMU algorithm to be used for practical WAMS applications. To attain this compliance, the error values of the estimated signals must be less than as prescribed by the latest standards. Errors in the phasor computation process are mostly

introduced due to varying frequency conditions or the presence of harmonics in the input time-domain signal. The errors due to group delays are eliminated by properly referring the estimated phasor samples to recommended points in an observation window, which involves a certain latency. Clarity with respect to referring of phasor samples in an observation window is scarcely available in the current literature and must be explored further. Some of the shortcomings of the existing literature are summarized below :

- It is seen from the literature that latency due to group delay compensation has not been studied until Meng et al. (2017). Here, authors have presented an off-line and online method to handle the group delay which has resulted in the evolution of causal and non-causal PMUs, as two separate entities. This way of handling PMUs, as two individual entities, is not only difficult to understand but also fails to clarify their usage for control and measurement applications.
- Differences between actual-time and other time vectors such as the PMU-time, frequency time and ROCOF time have not been clarified.
- PMUs that compute both current and voltage phasors have been used in power systems such as in Guardado and Guardado (2015), Dotta et al. (2013), without much understanding of the TVE computations and phasor compensation. With the advent of causality in PMUs, (Meng et al., 2017), the compensations now have a significant impact on the PMU outputs. In these, different compensation schemes can be applied for a 3-phase, 6-input PMU by using voltage or current signal-based frequency. These possibilities are not discussed in the literature.
- Effect of these different compensation schemes on TVE and other measurements such as complex power and impedance has not been clarified.
- An extensive comparison of PMU performance based on their causal and non-causal versions has not been presented in the literature.
- Stability assessment of power systems using causal and non-causal PMU estimates has not been well explored, (Roy et al., 2013), (Kulkarni and Ballal, 2020).

To address the above concerns an integrated architecture for PMUs has been proposed in this work.

### 1.6.1.2 Improved Single-Phase Based Frequency Estimation

Due to the advent of micro-PMUs, -see section.1.2.1.3, (Dusabimana and Yoon, 2020), (Von Meier et al., 2017), which are cheap alternatives for the current commercial PMUs, the use of PMUs in distribution networks has gained importance. Although, considering the present synchrophasor landscape, the majority of PMUs are installed on transmission networks. Therefore, most PMUs process three-phase signals and obtain positive sequence phasor estimates. The computation of positive sequence phasors naturally eliminates the second harmonic component which is dominant in the single-phase phasor estimates, (Phadke and Thorp, 2010). The use of such single-phase phasor signals for frequency computation results in the amplification of the second harmonic component due to the differential nature of the estimates, thus making them unusable as per the standard.

In order to achieve M-class PMU compliance, frequency estimates must satisfy the requirements dictated by the inter-harmonic test given in the IEEE Std (2018). Several PMU algorithms satisfy such requirements when the positive-sequence estimates are used, but fail when tested on a single-phase basis. Compliance for such a test is achieved by the use of additional filters in the phasor computing module or by using long windows with excellent harmonic rejection, such as in Castello et al. (2014). From the literature it is noted that for either single-phase or three-phase systems, which employ time-domain frequency estimation methods, the IEEE standard based compliance requirements (especially the inter-harmonic test) are not generally explored. Very few methods are described in the literature which retain the simplicity and computationally light nature of the traditional algorithms such as the DFT and yet provide frequency and ROCOF estimates which are compatible with the latest IEEE standards especially for single-phase signals. This aspect therefore deserves further investigating which is one of the objectives of this thesis.

### 1.6.1.3 Development of an Event Detection and Localization Tool

Due to the extensive installation of WAMS all over the globe, segregation and proper channelization of PMU data has become necessary. A single PDC which collects a massive volume of data *from a number of PMUs* must be thoroughly analysed and intelligently given to system operators in order for them to understand the current condition of the system, as well as abnormal behaviour at various locations. Based on the analysed data, power system operators can take appropriate decisions to bring the system back to normalcy in



case of a disturbance scenario. Therefore, in order to detect, localize and classify anomalies from the synchrophasor data provided by numerous PMUs installed in WAMS, event analysis is necessary. Event detection, which is the first step in event analysis identifies the onset of power system disturbances. This can be performed in an offline or an online manner using time-stamped PMU estimates such as phasors, frequency and ROCOF. Once an event detection algorithm flags the occurrence of an event, the next step is to zero in on the exact location of the disturbance. This can be a portion of the grid where the event has originated or where the events effects are observed. This process is known as event localization. Identification of the affected portion of the power system as quickly as possible enables the operators to separate out the portion of the grid (if necessary) in order to avoid cascading outages. Compared to event detection, the event localization problem has not been keenly pursued in the literature. This can be seen in Shaw and Jena (2020), Gajjar and Soman (2014), where the authors use wide area frequency data from limited sources (two or three PMUs/FDRs) for the event detection process, disregarding the state of the rest of the grid. Therefore, in order to fully utilize the wide-area visualization capability of the WAMS, data obtained from *multiple PMUs* installed throughout the power system must be examined in order to accurately identify the occurrence of an event. Hence, this aspect of event analysis deserves more attention.

## **1.6.2 Objectives and Major Contribution of the Thesis**

The extensive literature survey undergone has helped identify several research gaps based on which the objectives of the thesis are formulated as follows:

1. *A study of the IEEE synchrophasor based standards:* Before declaring a PMU to be fit for practical applications, it has to pass the IEEE synchrophasor standard based tests by providing error values less than those recommended by the latest standard. Therefore, it is of utmost importance to compare the changes made to the IEEE synchrophasor standard over the years and the requirements for P and M-class compliance. In this regard, test procedures for static and dynamic conditions are clarified including the steps for calculating the error values. PMU based on the one-cycle DFT algorithm is used for the demonstration of compliance/non-compliance verification. Special emphasis is given to time-tagging methods for synchrophasor samples and their effects on the overall synchrophasor quality and end usage is studied.

2. *Development of a generalized integrated PMU architecture:* A generalized architecture also known as an “Integrated PMU architecture” is proposed which simplifies the understanding and implementation of PMU modules. Different types of outputs can be chosen from the Integrated architecture, depending on the requirement of the power system operator. These outputs primarily differ according to the method used for their group delay compensation. Several static and dynamic model based PMU algorithms are implemented based on the integrated PMU architecture. Performance comparison of different PMU algorithms implemented in the integrated architecture environment, is conducted using the IEEE synchrophasor standard based tests. A 6-input PMU based on the mentioned architecture is used in a 4-machine 10-bus power system. Impact of different compensation methods on direct measurements (voltage, current) and pseudo measurements (complex power, impedance) from the power system is also demonstrated. Influence of the integrated PMU architecture estimates on power system oscillation damping is also presented.
3. *Improvement of frequency estimation using signal-reconstruction approach:* In order to achieve M-class frequency compliance, whilst retaining simple and computationally light phasor computing modules, a signal-reconstruction based approach is proposed. This method helps to improve the frequency estimation performance of DFT based methods even during frequency deviation and harmonic conditions. The algorithm is implemented on a single-phase basis unlike the most PMU based frequency estimation techniques. Despite that, the signal-reconstruction based method provides estimates which are compliant with the stricter M-class limits. This makes the approach even more appealing since precise single-phase frequency estimation in PMUs is difficult to achieve especially during off-nominal frequency and out-of-band interfering conditions due to the lack of natural elimination of the second harmonic component. The signal-reconstruction block has been added as an augmented module to several single-phase static and dynamic PMU algorithms thus keeping the core structure of PMUs intact. Different IEEE based tests are conducted showing the improved frequency and ROCOF estimation using the newly developed approach.
4. *Application of WAMS in power system operation and control:* Numerous applications of WAMS/PMU data are demonstrated which include:
  - (a) *Real-time application of WAMS data for power system control:* WAMS data obtained from across the power system is used as an input to a power system

stabilizer in order to compare the damping performance during an oscillation scenario. Pros and cons of different integrated PMU architecture outputs as control signals is demonstrated. Several frequency and ROCOF based phase angle compensation schemes are proposed for a causal PMU and their impact on direct and pseudo measurements is also investigated.

- (b) *Application of different PMU signals for power system mode identification:* A rigorous analysis is conducted comparing the effectiveness of different signals for mode identification. Effect of window length, start time and the data frame rate on mode identification using PMU signals is studied. Comparison studies between frequency and ROCOF signals as potential candidates for mode identification are conducted.
- (c) *Development of an event detection and localization tool:* Data obtained from *multiple* PMUs/PDCs spread over a wide area is analyzed using an event detection and localization tool for identification of different types of power system events. Signal-processing based methods are employed for examining such a massive volume of WAMS data at a time for event occurrences. An algorithm is proposed to enable the operator to localize the area/substation at which the event has occurred or which is affected the most, based on the number of PMUs exhibiting anomalous behaviour. Effect of the threshold values on the event detection and localization process is examined. A methodology to preemptively identify a loss-of-synchronism scenario is devised. The technique is based on monitoring the phase angle difference (PAD) signals across transmission lines. Such a technique can be used to initiate PSB logic for distance relays in order to avoid uncontrolled tripping across the power system leading to blackout condition.

## 1.7 Organization of the Thesis

This thesis is divided into six chapters and are detailed below:

1. **Chapter 2:** elaborates on the static and dynamic test procedures required for the IEEE synchrophasor standard compliance verification. A one-cycle DFT based PMU is subjected to different test signals and its compliance is verified with respect to

the latest standard. Several other static and dynamic PMU algorithms are also described in this chapter including their group delay computation procedure. Three time-tagging methods for phasor samples are also illustrated in this chapter.

2. **Chapter 3:** presents an integrated PMU architecture which provides synchrophasor estimates useful for multiple WAMS applications. PMUs are implemented based on the integrated architecture in a multi-machine transient stability environment as SIMULINK models (".mdl") as well as MATLAB script files (".m"). The implemented PMUs are subjected to the IEEE synchrophasor standard based tests. Also, a comparison between causal and non-causal estimates is made using standard test signals. A three-phase six-input PMU based on the integrated architecture is used in a 4-machine 10-bus power system to demonstrate the effect of compensation on the PMU estimates. A power system stabilizer is designed based on the PAD signals to illustrate the influence of causal and non-causal PMUs on the small-signal stability of a power system.
3. **Chapter 4:** describes a signal-reconstruction based frequency estimation technique. Phasor samples obtained employing different PMUs are used to reconstruct back the time-domain signals. These reconstructed signals are used for obtaining frequency using a Convolution Averaging filter and a Hilbert filter. Compatibility of these estimates with the latest synchrophasor standards is also verified. Frequency and ROCOF estimates obtained via the reconstruction-based methods are employed for mode identification via Prony analysis and relevant specifications such as the damping ratio, frequency, order of the linear predictor, execution time, are also explored. Some practical signals obtained from the ISO-New England power systems are used to test the performance of the new frequency estimation technique.
4. **Chapter 5:** describes the development of an event analysis tool, focusing on the detection and localization aspect. Non-training based signal processing methods such as the wavelet transform and the standard deviation are applied to signals obtained from multiple PMUs/PDCs to detect data outliers. An event localization logic is proposed based on the output of the event detection process. Effect of the threshold computing methods on the event localization aspect of event analysis is demonstrated. A method for detection of an out-of-step condition using PAD signals is also presented.
5. **Chapter 6:** summarizes the contribution of the work presented in this thesis. In this

chapter the future research work which can be undertaken related to the thesis is also discussed.

---

## Chapter 2

# SYNCHROPHASOR STANDARDS AND PMU ALGORITHMS

### 2.1 INTRODUCTION

PMUs are subjected to a series of tests before they are deployed in wide area measurement systems. Estimates provided by PMUs during these test scenarios must have error values less than those prescribed by the IEEE standards for synchrophasor measurements in power systems. The continuous integration of renewable energy sources (RES) has worsened the self-regulating capability of the power system, thereby increasing its vulnerability to disturbances. This has led to more frequency fluctuations in the power systems along with increased harmonic penetration due to the converters associated with RES. During such conditions, accurate synchrophasor estimation is a challenging task which a conventional PMU algorithm such as the Discrete Fourier Transform (DFT) cannot accomplish. Hence, over the last two decades several state-of-the-art PMU algorithms have been suggested which improve upon the conventional phasor estimation methods. Accuracy of the estimates provided by these algorithms has been evaluated using the IEEE synchrophasor measurement standard and its updates.

In this chapter, the IEEE synchrophasor measurement standard based test procedures are detailed in such a way that they can be readily applied to test any PMU algorithm. For illustration purpose, the DFT is presented as a PMU algorithm and its compliance is verified with respect to the latest standard, (IEEE Std, 2018). Updates to the error limits required for the protection : P-class and the measurement : M-class compliance are also

highlighted for all the test cases. Several well known PMU algorithms are introduced including details with respect to their synchrophasor, frequency and ROCOF estimation modules. Various methods used to time-tag phasors are also illustrated using the one-cycle DFT algorithm. Group delay associated with different PMU algorithms is also highlighted. A basic comparison of PMU algorithms using different input signals is also presented.

## 2.2 Phasor Estimation Using DFT

Consider a sinusoidally varying signal,  $x(t)$  with nominal frequency  $\omega_0$  and phase angle  $\phi$  as

$$x(t) = X_m \cos(\omega_0 t + \phi) \quad (2.1)$$

where  $X_m$  denotes the peak amplitude of the signal. Assuming a sampling frequency pertaining to the nominal value given by  $f_0 N$  we get

$$x(n\Delta t) = X_m \cos(2\pi n\Delta t f_0 + \phi) \quad (2.2)$$

where  $\Delta t = 1/(f_0 N)$  and  $n = 0, 1, 2, 3, \dots$ . The number of samples per cycle of the nominal frequency  $f_0$  Hz is given by  $N$ . Now, the Fourier components of (2.2) are obtained as,

$$X_c = a_1 = \frac{2}{N} \sum_{n=0}^{N-1} x(n\Delta t) (\cos(2\pi n/N)) \quad (2.3)$$

$$X_s = b_1 = \frac{2}{N} \sum_{n=0}^{N-1} x(n\Delta t) (\sin(2\pi n/N)) \quad (2.4)$$

Using (2.3) and (2.4), the phasor for a cosine signal is given by,

$$\bar{c}_1 = a_1 - jb_1 = X_c - jX_s \quad (2.5)$$

The phasors given by (2.5) are denoted by a constant phasor for a nominal and a constant amplitude input signal (Phadke and Thorp, 2010).

For illustration purpose, the deviation from the nominal frequency is evaluated from phasors by estimating the rate-of-change of the phase angle obtained from (2.5) as follows,

$$\Delta\omega = \frac{d\phi}{dt} = \frac{b_1 \frac{d}{dt}(a_1) - a_1 \frac{d}{dt}(b_1)}{a_1^2 + b_1^2} \quad (2.6)$$

The derivatives in (2.6) are obtained by using the following approximate derivative function,

$$H(s) = \frac{s}{1 + sT} \quad (2.7)$$

where  $T$  is assigned a very small value (say 0.01 s) so that  $sT \ll 1$  in (2.7). The rate-of-change of frequency (ROCOF) is calculated similarly by solving for the derivative of (2.6) i.e.,  $d(\Delta\omega)/dt$  using the same procedure.

## 2.3 IEEE Standard Based Tests and Latency

To assess the correctness of measurements of PMUs during different conditions in a power system, the IEEE standard (IEEE Std, 2011) has presented a list of tests that are to be performed. These tests demonstrate the estimating, tracking and filtering ability of an algorithm during various conditions in a power system. These tests are primarily divided into two categories, namely steady-state and dynamic which are further divided as following:

- Steady-State tests: Which include, Off-nominal frequency test, Harmonic test and Inter-Harmonic test.
- Dynamic tests: Which include, Measurement Bandwidth test, Ramp test and Step test.

In IEEE Std (2005), IEEE Std (2011) it has been suggested that while computing the errors all delays imparted by the PMU algorithm or its associated modules should be compensated for, so that the theoretical and the computed quantities are in alignment with each other when calculating the errors. In this regard, the phasor obtained using (2.5) is referred to the center of the data window, so that these periodic delays are compensated. The phasor  $\bar{X}$  referred to the center can be computed directly as,

$$\bar{X} = \frac{2}{N} \sum_{n=-N/2}^{N/2} x(n)e^{-j2\pi n/N} \quad (2.8)$$

However, this process introduces a time delay known as latency. The value of latency depends on the size of the data window used by the algorithm and can be calculated as follows:

$$L_T = (N_a) \times \Delta t \quad (2.9)$$



where  $L_T$ , is the latency in seconds and  $N_a$  is the group delay associated with the algorithm in terms of samples. In this chapter the procedures for all the IEEE based tests are provided and the tests are conducted for a sampling frequency of 5050 Hz in order to have  $N = 101$ . Thus,  $N_a = N/2$ , considering an integer value.

## 2.4 Error Metrics for PMUs

The accuracy of the estimates provided by a PMU is determined primarily using the following three metrics,

1. **Total Vector Error:** The computed synchrophasor values differ from the theoretical values in both amplitude as well as phase. In order to merge the two differences, i.e. the amplitude difference and the phase difference, the IEEE standard for synchrophasor measurements, (IEEE Std, 2005), (IEEE Std, 2011), suggested a quantity called as the Total Vector Error (TVE). This parameter indicates the difference between a theoretical synchrophasor and the estimated synchrophasor, for the same time-instant. The Total Vector Error value is normalized and expressed as per unit of the theoretical phasor. TVE can be computed as,

$$\text{TVE (\%)} = \frac{\bar{c}_1 - \bar{X}_T}{\bar{X}_T} \times 100 \quad (2.10)$$

where  $c_1$  represents the computed phasor and  $\bar{X}_T$  represents its corresponding theoretical counterpart. Synchrophasor measurement accuracy of PMUs is evaluated primarily using the TVE criteria.

2. **Frequency Error:** The accuracy of the frequency estimates provided by a PMU is evaluated using the frequency error metric. If  $f_T$  is the theoretical value of the frequency, the frequency error can be computed as

$$\text{FE} = f_T - f_c \quad (2.11)$$

where FE represents the error in frequency estimates given in Hz, and  $f_c$  represents the frequency values computed by the PMU.

3. **Rate-of-Change of Frequency Error:** Similar to the frequency error estimates the Rate-of-Change of Frequency Error (RFE) is computed as follows,

$$\text{RFE} = \text{ROCOF}_T - \text{ROCOF}_c \quad (2.12)$$

where RFE is the error in ROCOF given in Hz/s.  $\text{ROCOF}_T$  represents the theoretical values while as the computed ROCOF is given by  $\text{ROCOF}_c$ .

The above mentioned values are obtained for all the IEEE synchrophasor standard tests for each PMU and are compared with the set limits. The required error limits vary depending on the test involved and the class of PMU in question (whether the PMU being tested is P or M class compliant). The tests required for compliance verification along with their respective error limits are described in the following section.

## 2.5 Steady-State Tests

The three major steady state tests include the :

1. Static-off-nominal test
2. Harmonic test
3. Inter-harmonic test

The acceptable error limits for these tests as per the IEEE Std (2011) and the updated IEEE Std (2014) are given in Table. 2.1. Several changes to the frequency and ROCOF error limits can be seen, comparing the 2011 and the 2014 versions of the standard. The TVE limits for the steady-state tests over the two updates have remained unchanged.

### 2.5.1 Static off-nominal frequency test

The following are the steps involved in the static off-nominal frequency test :

1. **Step 1:** Generate a time-domain signal with an off-nominal frequency (IEEE Std, 2018), such as

$$x(t) = X_m \cos(2\pi(f_0 + \Delta f)t) \quad (2.13)$$

where  $X_m$  represents the peak value of the signal and  $\Delta f$  represents the frequency deviation in Hz.

2. **Step 2:** Compute phasors of (2.13) using the PMU algorithm.
3. **Step 3:** Subject phasor samples to frequency and ROCOF estimations.
4. **Step 4:** Construct a theoretical phasor pertaining to the off-nominal frequency deviation as

$$\bar{X}_T = X_m e^{j(2\pi \times \Delta f)t} \quad (2.14)$$

5. **Step 5:** Here the theoretical frequency is  $f_0 + \Delta f$  and ROCOF is zero.
6. **Step 6:** Compute the Total Vector Error, frequency error and RFE using the computed and the theoretical values obtained using the above steps.

**Table 2.1:** Comparison of IEEE benchmarks for steady-state tests ( $F_{rr} > 20$  fps).

Test type	FE Limit (Hz)				RFE Limit (Hz/s)				TVE Limit (%)
	2011 Std		2014 Std		2011 Std		2014 Std		2011/2014
	P Class	M Class	P Class	M Class	P Class	M Class	P Class	M Class	P/M Class
Off-nominal test	0.005	0.005	0.005	0.005	0.01	0.01	0.4	0.1	1
Harmonic test	0.005	0.025	0.005	0.025	0.01	6	0.4	Suspended	
Inter Harmonic test	-	0.01	-	0.01	-	0.1	-	Suspended	1.3

Observations: The TVE plots for a single phase 52 Hz and a 55 Hz off-nominal frequency signal using the DFT are shown in Fig. 2.1, with the maximum values being equal to 2.21% and 6.32%, respectively. The frequency and ROCOF are calculated using the DFT based phasor samples and the respective maximum errors for a 52 Hz off-nominal signal are 0.341 Hz and 31.16 Hz/s which can be compared with those given in Table. 2.1 for compliance verification.

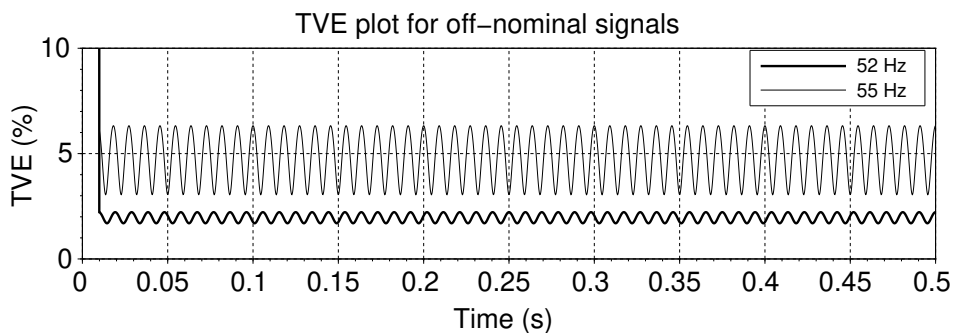


**Figure 2.1:** TVE plot for off-nominal frequency signals

### 2.5.2 Harmonic distortion test

In this test the harmonic filtering capabilities of a PMU algorithm are put to test. The following are the steps:

1. **Step 1:** Generate a time-domain signal polluted with harmonics of order ranging from  $2^{nd}$  to  $50^{th}$ , one at a time, (IEEE Std, 2018), as shown below,

$$x(t) = X_m \cos(\omega_0 t + \phi) + (k_H \times X_m \cos(n\omega_0 t + n\phi)) \quad (2.15)$$

where  $n = 2, 3, 4, \dots, 50$ ,  $\phi$  is the initial phase angle of the time-domain signal and  $k_H$  is 0.01 for P class and 0.1 for M class.

2. **Step 2:** Subject the signal in (2.15) to the PMU algorithm.
3. **Step 3:** Phasor samples are used to obtain the frequency and ROCOF estimations.
4. **Step 4:** Construct a theoretical phasor pertaining to the nominal frequency signal as,

$$\bar{X}_T = X_m e^{j\phi} \quad (2.16)$$

5. **Step 5:** The theoretical frequency is  $f_0$  and ROCOF is zero.

Since the DFT method inherently filters out all the integral multiples of the nominal frequency components, the value of TVE, the frequency error and ROCOF error are zero.

### 2.5.3 Out-of-band interference test / Interharmonic test

This test is performed to demonstrate the behaviour of PMU algorithms during the presence of out-of band frequency signals. A frequency  $f_{ih}$  can be called as out-of-band or interharmonic if,

$$|f_{ih} - f_0| \geq F_{rr}/2 \quad (2.17)$$

where  $f_0$  denotes the nominal frequency and  $F_{rr}$  denotes the phasor reporting rate. This test is to be done only for M class PMUs (IEEE Std, 2011), (IEEE Std, 2018). The following are the steps :

1. **Step 1:** Generate a time-domain signal polluted with interharmonic frequencies calculated in (2.17), as shown below,

$$x(t) = X_m \cos(2\pi f_b t) + 0.1 \times X_m \cos(2\pi f_{ih} t) \quad (2.18)$$

where  $f_b$  denotes the base frequency of the signal.

2. **Step 2:** Vary the interharmonic frequency  $f_{ih}$ , from the lower limit, i.e., 10 Hz to the upper limit  $2f_0$ , (IEEE Std, 2018), with the injection of one interharmonic frequency at a time. The base frequency  $f_b$  used for this test is also supposed to be varied in the range given by (2.19), as per (IEEE Std, 2011),

$$f_0 - 0.1(F_{rr}/2) \leq f_b \leq f_0 + 0.1(F_{rr}/2) \quad (2.19)$$

where  $F_{rr}/2$  represents the Nyquist frequency of the reporting rate (IEEE Std, 2011). For example, if  $F_{rr} = 50$ , then  $47.5 < f_b < 52.5$  Hz.

3. **Step 3:** Compute the phasor of the signal given in (2.18) using the PMU algorithm.
4. **Step 4:** From phasor samples obtain the frequency and ROCOF estimation.
5. **Step 5:** The theoretical frequency is  $f_b$  and ROCOF is zero.

For  $f_b = 50$ Hz and  $f_{ih} = 10$ Hz, the TVE plot is given in Fig. 2.2, with the error limits for this test given in Table. 2.1. The TVE value for this test is 3.89% which is clearly greater than the permissible limits, showing that the DFT method is incapable of filtering out interharmonic frequencies.

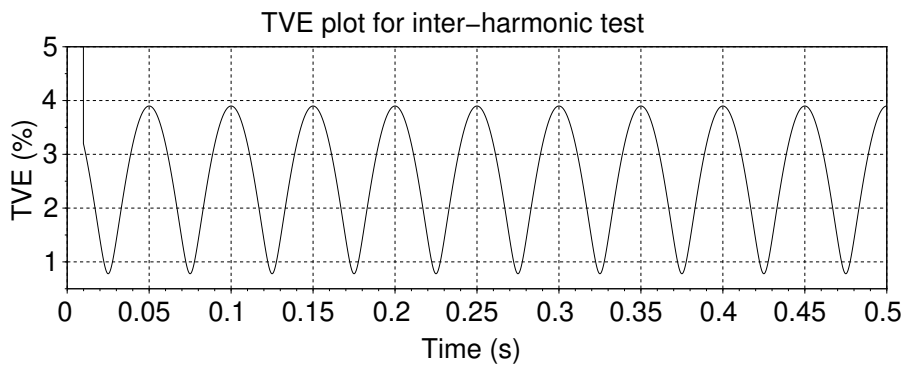


**Figure 2.2:** TVE plot for a signal with 10 Hz interharmonic

The frequency and the ROCOF errors gave the maximum values as 0.567 Hz and 53.61 Hz/s, respectively.

## 2.6 Dynamic Tests

The major tests involving dynamic signals include,

1. Bandwidth test
2. Ramp test
3. Step test

Comparison of the error limits across the IEEE Std (2011) and the IEEE Std (2014) for all these tests is listed in Tables. 2.2-2.4.

**Table 2.2:** Comparison of IEEE benchmarks for bandwidth compliance test ( $F_{rr} > 20$  fps).

Modulation Type	Modulation Level	FE Limit (Hz)				RFE (Hz/s)				TVE limit (%)
		2011 Std		2014 Std		2011 Std		2014 Std		2011/2014
		P Class	M Class	P Class	M Class	P Class	M Class	P Class	M Class	P/M class
Amplitude+Phase	$k_x = k_a = 0.1$	0.06	0.3	-	-	3	30	-	-	3
Amplitude only	$k_x = 0.1, k_a = 0$	-	-	0.06	0.3	-	-	2.3	14	
Phase only	$k_x = 0, k_a = 0.1$	0.06	0.3	0.06	0.3	3	30	2.3	14	

### 2.6.1 Bandwidth test

This test checks the estimation capabilities of an algorithm during modulations in amplitude as well as in the phase. As per the 2011 standard (IEEE Std, 2011), two variants of this test are given, one is the combined amplitude and phase modulation, and one is the phase modulation alone. But in the latest update of the standard (IEEE Std, 2014), (IEEE Std, 2018), the combined amplitude and phase modulation test has been removed and replaced by only amplitude modulation due to reasons mentioned in (Martin, 2015), (Roscoe et al., 2015). The following are the steps to perform bandwidth compliance test:

1. **Step 1:** Generate a time-domain signal as given below

$$x(t) = X_m [1 + k_x \cos(\omega_m t)] \times \cos[\omega_0 t + k_a \cos(\omega_m t - \pi)] \quad (2.20)$$

where  $k_x, k_a$ , denote the amplitude and the phase modulation index respectively, the values of which are fixed by the standard as 0.1 and  $\omega_m = 2\pi f_m \text{rad/s}$  denotes the modulation frequency (IEEE Std, 2018).

2. **Step 2:** Start the modulation frequency from a lower value and increase it in steps of 0.2 Hz till the upper limit for the class of PMUs is reached (2 Hz for P class and 5 Hz for M class) (IEEE Std, 2018).
3. **Step 3:** Obtain the phasors for the signal generated using step 1 and step 2.
4. **Step 4:** Using the phasor samples calculate the frequency and ROCOF.
5. **Step 5:** Construct the theoretical phasor pertaining to the signal given in step 1 as shown below,

$$\bar{X}_T = X_m(1 + k_x \cos(\omega_m n \Delta t)) \angle k_a \cos(\omega_m n \Delta t - \pi) \quad (2.21)$$

6. **Step 6:** Calculate the theoretical frequency and ROCOF using the derivatives of the phase angle of the theoretical phasor given in step 5 as follows:

$$f_T = (\omega_0/2\pi) - k_a(\omega_m/2\pi) \sin(\omega_m n \Delta t) \quad (2.22)$$

$$ROCOF_T = -k_a(\omega_m^2/2\pi) \cos(\omega_m n \Delta t - \pi) \quad (2.23)$$

The maximum value of TVE calculated for a 2 Hz and 5 Hz amplitude modulation is 0.2% and 0.52% respectively as shown in Fig. 2.3.

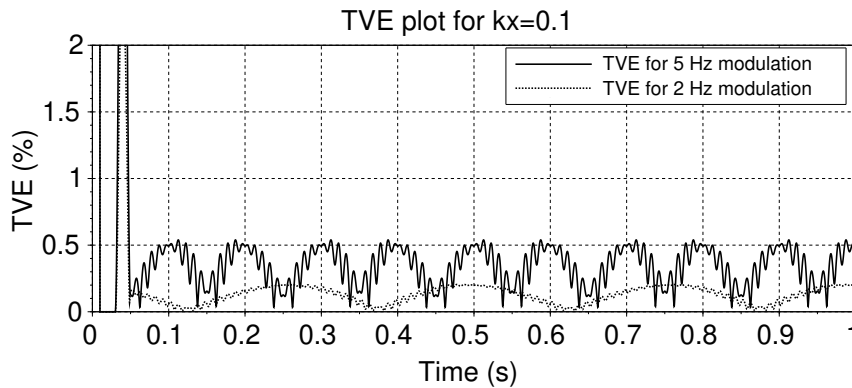


**Figure 2.3:** TVE plot for amplitude modulated signals

The frequency and the ROCOF errors for a 5 Hz amplitude modulation are 0.08 Hz and 7.90 Hz/s, even though the value of  $k_a$  is zero. These values can be compared with the error limits given in Table. 2.2.

### 2.6.2 Ramp test

The following are the steps to perform a frequency ramp test:

1. **Step 1:** Generate a time-domain signal as given below

$$x(t) = X_m \cos(\omega_0 t + \pi R_f t^2) \quad (2.24)$$

where  $R_f$  denotes the ramp rate in Hz/s.

2. **Step 2:** Set the initial frequency  $f_0$ , ( $\omega_0 = 2\pi f_0$ ), in (2.24) to a lower value (45 or 48 Hz) depending on the class of PMU in question, and then ramp up the frequency at a ramp rate of +1Hz/s till the upper limit (55 or 52 Hz) is reached, where it is held for some time, (IEEE Std, 2018). The reverse is done for a negative ramp in frequency.
3. **Step 3:** Construct the theoretical phasor pertaining to the signal given in step 1 as shown below,

$$\bar{X}_T = X_m \angle \pi R_f t^2 \quad (2.25)$$

4. **Step 4:** Calculate the theoretical frequency and ROCOF using the derivatives of phase angle of the theoretical phasor given by (2.25), these values are given by the following equations,

$$f_T = f_0 + R_f n \Delta t \quad (2.26)$$

$$ROCOF_T = R_f \quad (2.27)$$

Whenever a ramp is initiated in time domain signal the FE and the RFE values may increase and cross the permissible limits, this happens immediately after a ramp is applied. The values of error around this time are discarded and not used for compliance verification. The time period for which the values of error cannot be used is called as the exclusion time interval and the frequency pertaining to that interval is called as the exclusion frequency



deviation which is given as, (IEEE Std, 2011),

$$F_{ex} = R_f \times \frac{n_1}{F_{rr}} \quad (2.28)$$

where  $n_1=2$  (P-class) or  $7$  (M-class),  $R_f$ =Ramp rate and  $F_{rr}$ =Reporting rate.

For example, for a 50 Hz system, with a reporting rate of 50 frames per second and a uniform ramp rate of +1Hz/s, the exclusion frequency deviation as calculated using (2.28) for a M-class PMU is 0.14 Hz, and hence the exclusion frequency is 45.14 Hz and 54.86 Hz for the lower and the upper limits, respectively. This means that the measurements below 45.14 Hz and above 54.86 Hz are excluded for compliance verification. TVE for this case is plotted in Fig. 2.4 with the error limits given in Table. 2.3.

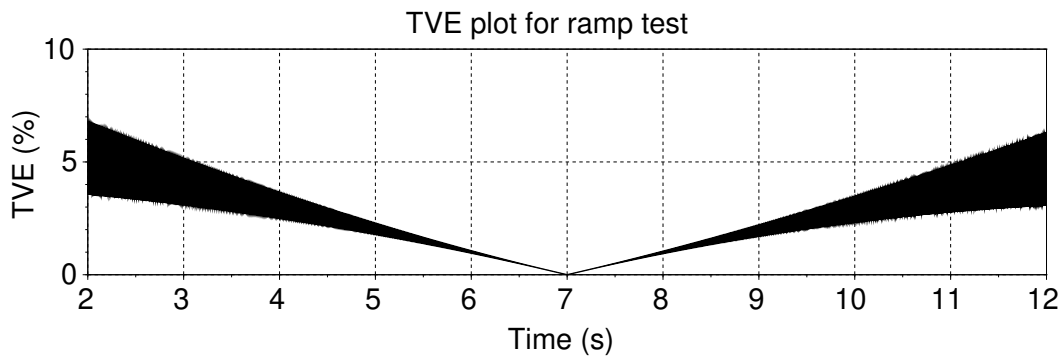


**Figure 2.4:** TVE plot for M class ramp test

The TVE values are highest immediately after the ramp is applied, equal to 6.56%. The value of TVE reaches zero once the frequency attains a value of 50 Hz at  $t = 7$  s in the figure. Similar observations are true for frequency and ROCOF errors with maximum values of 1.13 Hz and 73.85 Hz/s, respectively.

**Table 2.3:** Comparison of IEEE benchmarks for ramp test.

FE Limit (Hz)				RFE Limit (Hz/s)				TVE Limit (%)
2011 Std		2014 Std		2011 Std		2014 Std		2011/2014
P Class	M Class	P Class	M Class	P Class	M Class	P Class	M Class	P/M Class
0.01	0.005	0.01	0.01	0.1	0.1	0.4	0.2	1

### 2.6.3 Step test

This test verifies the tracking capabilities of PMU algorithms to sudden changes in amplitude or phase. The following are the steps to perform a step test:

1. **Step 1:** Generate a time-domain signal as given below

$$x(t) = X_m[1 + k_x u(t)] \times \cos[\omega_0 t + k_a u(t)] \quad (2.29)$$

where  $k_x, k_a$  denote the step size of magnitude and phase respectively, whereas  $u(t)$  denotes the step function, (IEEE Std, 2011).

2. **Step 2:** Initiate step in amplitude of 10% or a step in phase of  $\pi/18$  rad (one at a time), using the step function given in (2.29) at any time  $t$ .
3. **Step 3:** Construct the theoretical phasor pertaining to the signal given in step 1 as shown below,

$$\bar{X}_T = X_m[1 + k_x u(n\Delta t)] \angle k_a u(n\Delta t) \quad (2.30)$$

4. **Step 4:** The theoretical frequency is  $f_0$  and the ROCOF is zero.

#### 2.6.3.1 Computation of delay

The delay time ( $t_d$ ) is described as the time required by the output to reach half (50%) of the final value after the application of a step (IEEE Std, 2011). For example, as shown in Fig. 2.5, if the phase of a signal is stepped from 0 to  $\pi/18$  rad at time  $t_s$  s, and the output signal attains a value of  $\pi/36$  rad, say at time  $t_e$  s, the delay time can be given by  $t_d = t_e - t_s$ . For DFT based step test, the delay time as calculated from Fig. 2.5 is 0.01 s. This is also treated as the periodic delay for the DFT.

#### 2.6.3.2 Response time

On the other hand the response time ( $t_r$ ) is defined as the time interval between the time instant when an error parameter, e.g, TVE, leaves the permissible limit mark, and then enters back and remains within the limit (IEEE Std, 2011). The response time for the TVE obtained for a step in phase (0 to  $\pi/18$  rad) via the DFT method is shown in Fig. 2.6. The response times obtained using the DFT method are 0.075 s for FE, 0.097 s and 0.113 s for RFE (P and M class respectively) and 0.018 s for TVE.

Values of maximum allowable response time and delay time as per the IEEE standards for a nominal frequency of 50 Hz and a reporting rate of 50 fps are given in Table. 2.4.

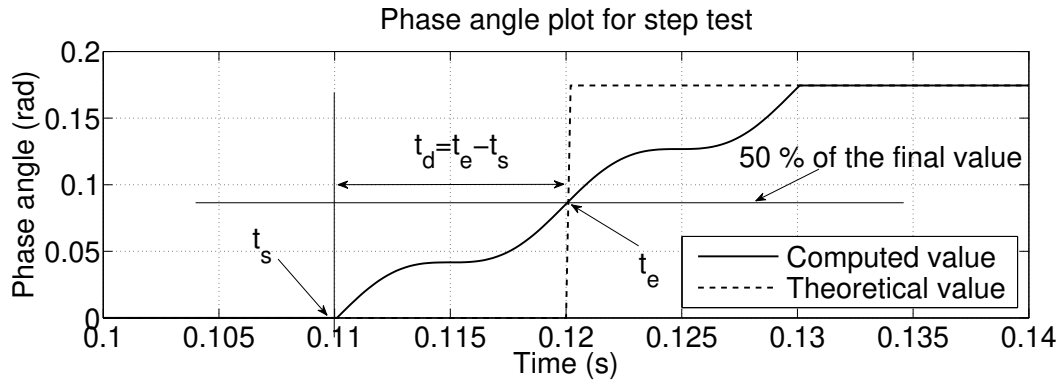


Figure 2.5: Phase angle plot for step in phase

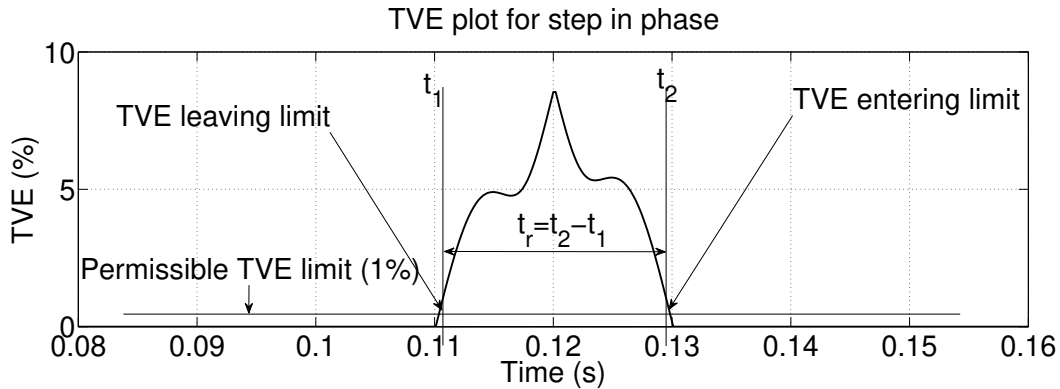


Figure 2.6: TVE plot for step in phase

Table 2.4: Comparison of IEEE benchmarks for response time and delay time in case of step test.

Parameters	Response time $t_r$ (s)			
	2011 Std		2014 Std	
	P-Class	M-Class	P-Class	M-Class
TVE	0.034	0.199	0.04	0.14
FE	0.07	0.130	0.09	0.28
RFE	0.08	0.134	0.12	0.28
Delay time $t_d$ (s)				
Magnitude/Phase	0.005	0.005	0.005	0.005

## 2.7 PMU Algorithms

The DFT is a conventional algorithm that was used for phasor measurement during the initial stages of the synchrophasor revolution. The computationally light nature and excellent integral harmonic performance made it appealing for phasor computation in power systems (Phadke et al., 1983). But due to the introduction of the IEEE standard and its updates the requirements for accuracy expected from PMUs have become more strict over the years, (IEEE Std, 2011), (IEEE Std, 2018). This has rendered the basic DFT algorithm less suitable for modern PMU applications. Therefore, in order to comply with the latest IEEE synchrophasor standard requirements, several PMU algorithms have been proposed based on different phasor computing techniques. These algorithms are categorized based of the models used for phasor estimation. These include,

1. Static-model based algorithms
2. Dynamic-model based algorithms
3. Adaptive algorithms

In this section static and dynamic model based PMU algorithms are discussed. The static model based algorithms include,

1. **PMU-A (P-class)**: Employs DFT with a three-point filter for phasor estimation. Phasor samples are computed using the nominal frequency based one-cycle DFT and the output phasor samples are filtered using a three-point averaging filter (Akke and Thorp, 2010), (Phadke and Thorp, 2010).
2. **PMU-B and PMU-B1 (P-class)**: Utilizes DFT with the IEEE P-class filter for synchrophasor estimation. The IEEE P-class FIR filter is based on a triangular window as recommended by the IEEE synchrophasor standard (IEEE Std, 2011), (IEEE Std, 2014), (IEEE Std, 2018). Frequency and ROCOF are computed using a time-difference based approach.
3. **PMU-E (M-class)**: This PMU is based on the Clarke transformation based DFT. This method includes the use of quasi-positive sequence approach (Xia and Liu, 2009) as well as the improved weighted least squares approach (Zhan and Liu, 2014) for phasor estimation (Zhan et al., 2016).

4. **PMU-F (M-class)**: This PMU is based on the IEEE M-class filter. Phasor estimates are obtained using a Hamming window based DFT, whose length varies according to the reporting rate (IEEE Std, 2018).
5. **PMU-G (P-class)**: This PMU employs the Interpolation based DFT technique in conjunction with the Hanning window. Three highest magnitude estimates obtained from the DFT spectrum are used to obtain a magnitude and phase angle correction term (Derviškadić et al., 2017).

The dynamic phasor models used here include,

1. **PMU-C (P-class)**: This PMU utilizes the weighted least squares technique to estimate phasors. Amplitude and phase angle values are approximated using second order Taylor series polynomials in order to account for the dynamic behaviour of the power system signals (De la Serna, 2010).
2. **PMU-D (M-class)**: An improved weighted least squares technique is employed for phasor estimation in this PMU. In addition to the fundamental, the second harmonic component is also included in the Taylor-series approximation of the time-domain amplitude and phase angle (Zhan and Liu, 2014). Frequency and ROCOF are computed using a polynomial-based least squares approach.

### **2.7.1 DFT with 3PF (PMU-A)**

Here, the phasor estimation module employs the conventional one cycle DFT given by (2.3), (2.4) followed by a three-point averaging filter (Phadke and Thorp, 2010). The output of the three-point averaging filter is computed as follows,

$$\bar{V}_{3PF} = \frac{1}{3} \left( \bar{V}(n) + \bar{V}(n + N/6) + \bar{V}(n + 2N/6) \right) \quad (2.31)$$

where  $\bar{V}_{3PF}$  represents the filtered phasor and  $\bar{V}(n)$  is the  $n^{th}$  phasor sample. It is to be noted that  $N$  must be a multiple of 6 for the three point filter to work.

A 3rd order least square based technique is used to estimate the frequency and ROCOF (Phadke and Thorp, 2010), (Guardado and Guardado, 2015), given as follows:

$$\begin{bmatrix} \phi(\Delta t) \\ \phi(2\Delta t) \\ \phi(3\Delta t) \\ \cdot \\ \cdot \\ \cdot \\ \phi(N\Delta t) \end{bmatrix} = \begin{bmatrix} 1 & \Delta t & (\Delta t)^2 & (\Delta t)^3 \\ 1 & 2\Delta t & (2\Delta t)^2 & (2\Delta t)^3 \\ 1 & 3\Delta t & (3\Delta t)^2 & (3\Delta t)^3 \\ \cdot & \cdot & \cdot & \cdot \\ \cdot & \cdot & \cdot & \cdot \\ \cdot & \cdot & \cdot & \cdot \\ 1 & N\Delta t & (N\Delta t)^2 & (N\Delta t)^3 \end{bmatrix} \begin{bmatrix} a_0 \\ a_1 \\ a_2 \\ a_3 \end{bmatrix} \quad (2.32)$$

or

$$[\phi] = [H][A] \quad (2.33)$$

or

$$[A] = [H] \setminus [\phi] \quad (2.34)$$

**Note:** The backslash command in MATLAB environment is used for solving a system of linear equations.

Where,  $\phi(N\Delta t)$  represents the phase angle at a time instant  $N\Delta t$ . The value of  $[A]$  can be found using (2.34) in the least squares sense to yield the values of frequency and ROCOF given by  $a_1$  and  $a_2$  respectively.

### 2.7.2 DFT with IEEE P-Class Filter (PMU-B and PMU-B1)

Here, the phasor estimation module employs the conventional one cycle DFT and a P-class IEEE C-37 filter. To estimate frequency and ROCOF a sample-based approach is realized (IEEE Std, 2018). The reference PMU structure given by the IEEE Std (2011), and its updated version (IEEE Std, 2014), (IEEE Std, 2018), includes two variants of linear phase FIR filters. These two filters are designed separately for P-class and the M-class compliance. The P class filter is a fixed length filter using a 2-cycle triangular window. Equation for evaluating the filter coefficients for P class filter is given in (IEEE Std, 2011), (IEEE Std, 2014), (IEEE Std, 2018), as follows,

$$W(k) = 1 - \left( \frac{2}{N+2} \right) \times |k| \quad (2.35)$$

where,  $k = -N$  to  $N$  and  $W(k)$  represents the filter coefficients.

The frequency and ROCOF estimation methods are as given below (IEEE Std, 2018).

$$\Delta f(i) = \frac{(\phi(i+1) - \phi(i-1))}{4\pi \times \Delta t} \quad (2.36)$$

$$ROCOF(i) = \frac{(\phi(i+1) + \phi(i-1) - 2\phi(i))}{2\pi \times \Delta t^2} \quad (2.37)$$

Two implementation techniques for P-class filtering have been mentioned in IEEE Std (2018). The first one involves one-cycle of DFT followed by 2-cycles of filtering (PMU-B), while as in the other technique the triangular window of two fundamental cycle length is directly used in conjunction with the phasor computation equation (PMU-B1). This leads to a single stage for phasor computation and filtering. The equation used for PMU-B1 is given in IEEE Std (2011), IEEE Std (2018), and is repeated here in the form of (2.38).

$$\bar{X}(i) = \frac{\sqrt{2}}{G} \sum_{k=-N/2}^{N/2} x(i+k)W(k)e^{-j(i+k)\Delta t\omega_0} \quad (2.38)$$

$G$  represents the sum of the P-Class filter coefficients.

### 2.7.3 Maximally Flat Differentiators (PMU-C)

This PMU is only P-class compatible but is an improvement over the previously mentioned static-model based PMUs which do not take into account the dynamic behaviour of the phasor. The details of the PMU algorithm are given as follows.

Let  $s(t)$  be a time domain signal with an amplitude  $a(t)$  and phase  $\phi(t)$ ,

$$s(t) = a(t) \cos(2\pi f_0 t + \phi(t)) \quad (2.39)$$

$s(t)$  can also be expanded as,

$$s(t) = \frac{1}{2}(p(t)e^{j2\pi f_0 t} + \bar{p}(t)e^{-j2\pi f_0 t}) \quad (2.40)$$

where  $p(t) = a(t)e^{j\phi(t)}$ , the nominal frequency is given by  $f_0$  and  $\bar{p}$  represents the complex conjugate of  $p$ .

For the purpose of phasor computation  $p$  can be approximated using a Taylor polynomial of varying degrees. In De la Serna (2010) the authors suggest that using a 2nd degree

polynomial leads to acceptable measurement accuracy, hence  $p(t)$  can be written as,

$$p(t) = p_0 + p_1t + p_2t^2 \quad (2.41)$$

Hence, the signal  $s(t)$  can be approximated as,

$$\mathbf{S} = \mathbf{B}\mathbf{M} \quad (2.42)$$

where  $\mathbf{S} = [s(-N_h), \dots, s(0), \dots, s(N_h)]$  with  $N_h$  being the sample index and  $\mathbf{M} = [\bar{p}_2, \bar{p}_1, \bar{p}_0, p_0, p_1, p_2]$ .  $\mathbf{B}$  is the relation matrix, relating the time-domain signal to the coefficients which is given in (2.43).

$$\mathbf{B} = \begin{bmatrix} (-N_h)^2 e^{jN_h\omega_1} & (-N_h) e^{jN_h\omega_1} & (-N_h)^0 e^{jN_h\omega_1} & (-N_h)^0 e^{-jN_h\omega_1} & (-N_h) e^{-jN_h\omega_1} & (-N_h)^2 e^{-jN_h\omega_1} \\ (-n)^2 e^{jn\omega_1} & (-n) e^{jn\omega_1} & (-n)^0 e^{jn\omega_1} & (-n)^0 e^{-jn\omega_1} & (-n) e^{-jn\omega_1} & (-n)^2 e^{-jn\omega_1} \\ 0 & 0 & 1 & 1 & 0 & 0 \\ (n)^2 e^{-jn\omega_1} & (n) e^{-jn\omega_1} & (n)^0 e^{-jn\omega_1} & (n)^0 e^{jn\omega_1} & (n) e^{jn\omega_1} & (n)^2 e^{jn\omega_1} \\ (N_h)^2 e^{-jN_h\omega_1} & (N_h) e^{-jN_h\omega_1} & (N_h)^0 e^{-jN_h\omega_1} & (N_h)^0 e^{jN_h\omega_1} & (N_h) e^{jN_h\omega_1} & (N_h)^2 e^{jN_h\omega_1} \end{bmatrix} \quad (2.43)$$

Hence the coefficients can be estimated as,

$$\hat{\mathbf{M}} = (\mathbf{B}'\mathbf{B})^{-1}\mathbf{B}'\mathbf{S} \quad (2.44)$$

For better approximation of the polynomial coefficients the matrix  $\mathbf{B}$  is weighted by an appropriate window, such as Hamming, Hanning, Blackman etc, denoted here by matrix  $\mathbf{W}$ . The dimensions of the window matrix are same as that of the window length ( $L_{dft}$ ) chosen for phasor computation,

$$\mathbf{W} = \text{diag}(L_{dft}) \quad (2.45)$$

where  $\text{diag}(L_{dft})$  is the diagonal matrix with diagonal elements as window weights. It can be used in (2.44) as follows,

$$\hat{\mathbf{M}}_{WLS} = (\mathbf{B}'\mathbf{W}'\mathbf{W}\mathbf{B})^{-1}\mathbf{B}'\mathbf{W}'\mathbf{W}\mathbf{S} \quad (2.46)$$

The final estimates are then given by the matrix  $\hat{\mathbf{M}}_{WLS} = [\bar{p}_2, \bar{p}_1, \bar{p}_0, p_0, p_1, p_2]$ . The amplitude, phase, frequency and ROCOF are finally computed as follows (De la Serna, 2007), (Petri et al., 2014), (Radulović et al., 2019).



$$\begin{aligned}
 A &= 2 \times |p_0| \\
 \phi &= \angle p_0 \\
 f_F &= \frac{\mathbf{Im}(p_1 \bar{p}_0)}{2\pi\Delta t \times |p_0|^2} \\
 \text{ROCOF} &= \frac{1}{\pi\Delta t^2} \times \left( \frac{\mathbf{Im}(p_2 \bar{p}_0)}{|p_0|^2} - \frac{\mathbf{Re}(p_1 \bar{p}_0)\mathbf{Im}(p_1 \bar{p}_0)}{|p_0|^4} \right)
 \end{aligned} \tag{2.47}$$

### 2.7.4 Improved Weighted Least Squares-Taylor Fourier (PMU-D)

This phasor measurement method is a direct improvement over the previous method. This method as given by Zhan and Liu (2014), improves over the harmonic performance of PMU-C by including the second harmonic component in the polynomial approximation. The inter-harmonic performance of this method proves that this PMU is M-class compatible. The improved weighted least squares Taylor Fourier method is described in detail in the following text.

Standard nominal signal is given by (2.39), whereas a nominal signal along with a second harmonic component can be written as,

$$s(t) = a(t) \cos(2\pi f_0 t + \phi(t)) + b \cos(2\pi(2f_0)t + \theta) \tag{2.48}$$

or

$$s(t) = \frac{1}{2}(p(t)e^{j2\pi f_0 t} + \bar{p}(t)e^{-j2\pi f_0 t}) + \frac{1}{2}(qe^{j2\pi 2f_0 t} + \bar{q}e^{-j2\pi 2f_0 t}) \tag{2.49}$$

where  $p(t) = a(t)e^{j\phi(t)}$  and  $q = be^{j\theta}$ ,  $f_0$  is the nominal frequency and  $\bar{p}, \bar{q}$  represent the complex conjugates of  $p, q$  respectively. Approximating  $p(t)$  using a 2nd order Taylor polynomial

$$p(t) = p_0 + p_1 t + p_2 t^2 \tag{2.50}$$

Approximation based on (2.42) can be used here as well with  $\mathbf{M} = [\bar{p}_2, \bar{p}_1, \bar{p}_0, \bar{q}, q, p_0, p_1, p_2]$ .  $\mathbf{B}$  for this PMU is given as follows.

$$\mathbf{B} = \begin{bmatrix}
 (-N_h)^2 e^{jN_h \omega_1} & (-N_h) e^{jN_h \omega_1} & (-N_h)^0 e^{jN_h \omega_1} & e^{jN_h 2\omega_1} & e^{-jN_h 2\omega_1} & (-N_h)^0 e^{-jN_h \omega_1} & (-N_h) e^{-jN_h \omega_1} & (-N_h)^2 e^{-jN_h \omega_1} \\
 (-n)^2 e^{jn\omega_1} & (-n) e^{jn\omega_1} & (-n)^0 e^{jn\omega_1} & e^{jn2\omega_1} & e^{-jn2\omega_1} & (-n)^0 e^{-jn\omega_1} & (-n) e^{-jn\omega_1} & (-n)^2 e^{-jn\omega_1} \\
 0 & 0 & 1 & 1 & 1 & 1 & 0 & 0 \\
 (n)^2 e^{-jn\omega_1} & (n) e^{-jn\omega_1} & (n)^0 e^{-jn\omega_1} & e^{-jn2\omega_1} & e^{jn2\omega_1} & (n)^0 e^{jn\omega_1} & (n) e^{jn\omega_1} & (n)^2 e^{jn\omega_1} \\
 (N_h)^2 e^{-jN_h \omega_1} & (N_h) e^{-jN_h \omega_1} & (N_h)^0 e^{-jN_h \omega_1} & e^{-jN_h 2\omega_1} & e^{jN_h 2\omega_1} & (N_h)^0 e^{jN_h \omega_1} & (N_h) e^{jN_h \omega_1} & (N_h)^2 e^{jN_h \omega_1}
 \end{bmatrix} \tag{2.51}$$

The values of the coefficients given using  $\mathbf{M}$  can be evaluated in the least squares sense

$$\hat{M}_{WLS} = (\mathbf{B}' \mathbf{W}' \mathbf{W} \mathbf{B})^{-1} \mathbf{B}' \mathbf{W}' \mathbf{W} \mathbf{S} \quad (2.52)$$

where  $\mathbf{W}$  represents the diagonal window matrix. The amplitude  $a(t)$  and phase  $\phi(t)$  are given using the coefficients in  $\hat{M}_{WLS}$ . The amplitude and the angle can be calculated as  $a(t) = 2|\bar{p}_0|$  and  $\phi(t) = \angle \bar{p}_0$ , respectively.

**Frequency Estimation:** Angles as computed previously can be interpolated using a second degree polynomial given by

$$\phi(t) = \phi_0 + \phi_1 t + \phi_2 t^2 \quad (2.53)$$

or

$$\phi(i) = \phi_{F0} + \phi_{F1} \left(i - \frac{(M+1)}{2}\right) + \phi_{F2} \left(i - \frac{(M+1)}{2}\right)^2 \quad (2.54)$$

where  $M$  is the number of angles used for frequency estimation. A window of angle estimates represented using (2.54) can be written in a compact form given by (2.55).

$$\phi = M_f \phi_{coef} \quad (2.55)$$

where  $\phi_{coef} = [\phi_{F0}, \phi_{F1}, \phi_{F2}]$  and

$$M_f(i, j) = \left(i - \frac{(M+1)}{2}\right)^{(j-1)} \quad (2.56)$$

where  $i = 1, 2, \dots, M$ ,  $j = 1, 2, 3$  and  $\phi = [\phi(1), \phi(2 \times \phi_{step}), \dots, \phi(M \times \phi_{step})]$ , where  $\phi_{step}$  is the number of samples by which the frequency computing window is shifted. Using least square fitting method, we can obtain the following,

$$\phi_{coef} = (M_f' M_f)^{-1} M_f' \phi \quad (2.57)$$

The final frequency can be computed as follows,

$$f_F = \frac{f_0 N}{2\pi \phi_{step}} \phi_{F1} \quad (2.58)$$

The same method is used for ROCOF computation, with frequency being approximated using a second order polynomial, similar to that in (2.54).

### 2.7.5 Clarke Transformation based-DFT (PMU-E)

In this method the emphasis is laid on totally eliminating the error caused by the second harmonic component present in simple DFT based phasor analysis in order to obtain M-class estimates. This error is primarily encountered when dealing with off-nominal or amplitude modulated signals. Several algorithms such as Xia and Liu (2009) focus on reducing the angle error caused by nominal DFT, while as Clarke Transformation based DFT (PMU-E) eliminates this error completely (Zhan et al., 2016). As given in Phadke and Thorp (2010), an off-nominal phasor computed using full-cycle DFT can be represented as,

$$\bar{X}_r = \bar{P}\bar{X}e^{jr(\omega-\omega_0)\Delta t} + \bar{Q}\bar{X}^*e^{-jr(\omega+\omega_0)\Delta t} \quad (2.59)$$

where,  $\bar{X}_r$  is the value of the off-nominal phasor at a frequency  $\omega = 2\pi f = 2\pi(f_0 + \Delta f)$ , where  $\Delta f$  is the deviation in Hertz from the nominal value,  $\bar{X}$  is the value of the phasor when the frequency is at nominal value i.e.,  $\omega = \omega_0 = 2\pi f_0$ .  $\bar{P}$  and  $\bar{Q}$  are complex functions of the frequency deviation  $\Delta f$ .

CT-DFT constructs an artificial signal with a DFT equal and opposite to that given in (2.59), such that the error primarily due to the second harmonic component (given as  $\bar{Q}$ ) is totally eliminated. The required DFT is given as below,

$$\bar{Y}_r = \bar{P}\bar{X}e^{jr(\omega-\omega_0)\Delta t} - \bar{Q}\bar{X}^*e^{-jr(\omega+\omega_0)\Delta t} \quad (2.60)$$

Adding (2.59) and (2.60), we get,

$$\bar{Z} = 2 \times \bar{P}\bar{X}e^{jr(\omega-\omega_0)\Delta t} \quad (2.61)$$

The  $\bar{Q}$  term has been eliminated as seen in (2.61). The crucial step involved in this method is the construction of a signal with a DFT as given by (2.60), such that the  $\bar{Q}$  terms cancel out each other and result in a second harmonic free phasor. The details of the CT-DFT algorithm are described further in the following steps :

1. **Step 1:** The time-domain signal is first filtered using a simple moving average filter of length equal to  $L_{maf}$ . For single phase measurements the quasi-positive sequence method is used to generate three phase signals in order to further increase the algorithm accuracy Xia and Liu (2009). No such thing is done when all the three phases

are available. This method of artificially constructing the two phases leads to errors in amplitude of the phasors, which is corrected later on.

2. **Step 2:** As previously discussed a signal whose DFT cancels out the  $\bar{Q}$  component has to be devised in order to eliminate the angle error completely. This is done using the Clarke's transformation which computes two signals orthogonal to each other, as given in (2.62).

$$X_{\alpha\beta\gamma} = [C_k] \times [x_{abc}] \quad (2.62)$$

where  $C_k$  is the Clarke's transformation matrix given by

$$C_k = \begin{bmatrix} 2/3 & -1/3 & -1/3 \\ 0 & 1/\sqrt{3} & -1/\sqrt{3} \\ 1/3 & 1/3 & 1/3 \end{bmatrix} \quad (2.63)$$

and  $[x_{abc}]$  is as a set of three phase signals. The value of  $X_\gamma$  is zero if the system is balanced and  $X_\alpha$  and  $X_\beta$  have a phase difference of  $90^\circ$ .

3. **Step 3:** In case phase  $b$  and  $c$  are artificially created the amplitudes of  $X_\alpha$ ,  $X_\beta$  are not ideal and need correction. This is done using the weighted least squares algorithm.

$$X_{cor} = 2 \left| \sum_{k=1}^{L_m} w_k \times X_\alpha \right| \quad (2.64)$$

where  $w_k$  is the complex matrix employed for amplitude correction same as that given in Zhan and Liu (2014),  $X_\alpha$  is the signal in question and  $L_m$  is the length of the window. This step is by-passed in case of a three phase system.

4. **Step 4:** The amplitude corrected signals, say  $X_{cor1}$ ,  $X_{cor2}$ , have a phase difference of  $90^\circ$  as originally intended. These two signals are now subjected to DFT employing the Blackman Harris window. The final phasor is then given by

$$\bar{Z} = (\bar{X}_{c1} + e^{j\pi/2}\bar{X}_{c2})/2 \quad (2.65)$$

where  $\bar{X}_{c1}$  and  $\bar{X}_{c2}$  correspond to the DFT of signals  $X_{cor1}$  and  $X_{cor2}$  respectively.

5. **Step 5:** The magnitude attenuation due to the noise filter and the Blackman Harris

window are accounted at the end as follows,

$$\bar{Z}_F = \frac{\bar{Z}}{L_{MAF}|H_1(e^{j\omega_1})||H_2(e^{j\omega_2})|} \quad (2.66)$$

where,  $\bar{Z}_F$  represents the magnitude compensated phasor,  $|H_1(e^{j\omega_1})|$  and  $|H_2(e^{j\omega_2})|$  represent the magnitude attenuation caused by the noise filter and the window respectively.

**Frequency and ROCOF estimation:** Polynomial approximations for the phase angle in the second degree as given previously in case of PMU-D in (2.54) are slightly modified in this method, shown as follows,

$$\phi(i) = \phi_{F0} + \phi_{F1}\left(i - \frac{(M+1)}{2}\right)(\phi_{step}\Delta t) + \phi_{F2}\left(i - \frac{(M+1)}{2}\right)^2(\phi_{step}\Delta t)^2 \quad (2.67)$$

The modified  $M_f$  in this method is given as follows,

$$M_f(i, j) = \left(i - \frac{(M+1)}{2}\right) \times \phi_{step}^{(j-1)} \quad (2.68)$$

Similar to the previous PMU, using the least squares method, we obtain

$$[\phi_{coef}] = (M'_f M_f)^{-1} M'_f [\phi] \quad (2.69)$$

which gives the values of frequency. Similar technique is used for ROCOF computation, where in (2.69),  $[\phi_{coef}]$  is replaced by  $[F_{RF}] = [F_{R1}, F_{R2}, F_{R3}]$ ,  $M_f$  is replaced by  $M_{rf}$ , calculated as below,

$$M_{rf}(i, j) = \left(i - \frac{(L_{RF} + 1)}{2}\right) \times f_{step}^{(j-1)} \quad (2.70)$$

where  $i = 1, 2, \dots, L_{RF}$  and  $j = 1, 2, 3$ . Where  $L_{RF}$  is the number of samples used for ROCOF computation and  $f_{step}$  is the step size used in the frequency window. Finally the ROCOF is given by

$$R_F = |R \times f_R| \quad (2.71)$$

where  $R_F$  is the ROCOF,  $R$  is the second row of the matrix  $(M'_{rf} M_{rf})^{-1} M'_{rf}$  and  $f_R = [f_F(1), f_F(2 \times f_{step}) \dots f_F(L_{RF} \times f_{step})]$ .

### 2.7.6 DFT with IEEE M-Class Filter (PMU-F)

PMU-F is based on the IEEE recommended M-class filter. This PMU is specifically designed to provide measurement class compliant estimates. The trade off being the increased window lengths and consequently the latency associated with it. The filter coefficients  $W(k)$  for this PMU are computed as given by the IEEE standard (IEEE Std, 2018),

$$W(k) = \frac{\sin\left(\frac{2\pi 2F_{fr}k}{F_{sampling}}\right)}{2\pi \frac{2F_{fr}k}{F_{sampling}}} \times h(k) \quad (2.72)$$

where,  $F_{fr}$  is the filter reference frequency,  $F_{sampling}$  is the sampling frequency and  $h(k)$  is the hamming function. The filter order, as well as the filter reference frequency  $F_{fr}$ , used for designing a M-class filter depend on the reporting rate of the PMU. Filter parameters for different values of reporting rates (for both 50 and 60 Hz fundamental) are mentioned in IEEE Std (2018). Authors in Roscoe et al. (2013) have provided methods for designing M-class filters for any arbitrary reporting rate, based on the IEEE Std (2011).

The magnitude compensation term for the M-class filter is not provided in any iteration of the synchrophasor standards till date. Without proper magnitude compensation during frequency deviation conditions, the PMU fails to limit the TVE values to less than 1% for deviations close to  $\pm 5$  Hz. Authors in Gurusinge et al. (2014) have provided a correction term which compensates for the magnitude attenuation due to the M-class filter, the term is denoted as  $M_{com}$  and is computed as follows,

$$M_{com}(i) = \frac{1}{\sin\left(\frac{\pi(f_0 + 1.15\Delta f(i))}{2f_0}\right)} \quad (2.73)$$

**Note:** Frequency and ROCOF for PMU-F are computed using the polynomial based least squares method as described for PMU-D.

### 2.7.7 Interpolated DFT (PMU-G)

The performance of most DFT based algorithms deteriorates during frequency excursion scenarios due to the incoherent sampling which is a result of fixed length windows. The spectral leakage problem encountered during static and dynamic off-nominal frequency conditions is resolved by using interpolated DFT (PMU-G) in combination with suitable windows thus enabling P-class compliance, (Derviškić et al., 2017). For IpDFT imple-

mentation a window length of at least two cycles is required. In case of incoherent sampling the peak value of the fundamental component is situated between two consecutive DFT bins (Derviškadić et al., 2017) and the signal frequency can be computed as,

$$f = (k_m + \delta)f_R \quad (2.74)$$

where  $\delta$  is a fractional term, the value of which is between  $\pm 0.5$ . The other term i.e.,  $k_m$  represents the index of the highest DFT bin which is  $\geq 2$ , while as  $f_R$  represents the frequency resolution. For example, for a 50 Hz nominal frequency signal, ( $\delta = 0$ ), if a window length of 2-cycles is used for the IpDFT computation, the frequency resolution, i.e.,  $f_R = 1/(2 \times 0.02) = 25$  Hz. The highest DFT bin,  $k_m = 2$  (since a window length of 2-cycles is used), and therefore  $f = (2 + 0) \times 25 = 50$  Hz. For hanning window based IpDFT the value of the fractional term  $\delta$  can be computed using the three highest DFT bins of the spectrum as follows, (Macci et al., 2011), (Belega and Petri, 2013), (Derviškadić et al., 2017), (Barchi et al., 2013)

$$\delta = 2\varepsilon \frac{|X(k_m + \varepsilon)| - |X(k_m - \varepsilon)|}{|X(k_m + \varepsilon)| + 2|X(k_m)| + |X(k_m - \varepsilon)|} \quad (2.75)$$

where  $|X(k_m)|$  is the magnitude of the fundamental DFT bin and the value of  $\varepsilon$  depends on the following conditions,

$$\varepsilon = +1 \quad \text{when} \quad |X(k_m + 1)| > |X(k_m - 1)|$$

or

$$\varepsilon = -1 \quad \text{when} \quad |X(k_m + 1)| < |X(k_m - 1)|$$

The amplitude and phase of the fundamental is corrected using the value of  $\delta$  as follows

$$X_c = |X(k_m)| \left| \frac{\pi\delta}{\sin(\pi\delta)} \right| |\delta^2 - 1| \quad (2.76)$$

$$\phi_0 = \angle X(k_m) - \pi\delta \quad (2.77)$$

The formula for computing,  $\delta$ , varies depending on the window used for DFT computation.

**Note:** The frequency and ROCOF values are computed using the method given in PMU-D.

The PMUs discussed in the previous section are summarized in Table. 2.5.

**Table 2.5:** List of three-phase and single-phase PMUs.

Three phase/Single phase	Model used	Performance class	Algorithm used
PMU-A/PMU-1	Static	P	DFT with three point filter (Phadke and Thorp, 2010)
PMU-B	Static	P	IEEE P-class filter (IEEE Std, 2011)
PMU-B1/PMU-2	Static	P	IEEE P-class filter version 2 (IEEE Std, 2011)
PMU-C	Dynamic	P	Weighted Least squares (De la Serna, 2010)
PMU-D/PMU-3	Dynamic	M	Improved Weighted Least squares (Zhan and Liu, 2014)
PMU-E	Static	M	Clarke's Transform based DFT (Zhan et al., 2016)
PMU-F/PMU-4	Static	M	IEEE M-class filter (IEEE Std, 2011)
PMU-G/PMU-5	Static	P	Interpolation based DFT (Belega and Petri, 2013)

## 2.8 Group delay computation of PMUs

The group delays for different PMUs detailed earlier are listed below :

1. PMU-A : Group delay for phasor computation in case of PMU-A is  $N/2$  corresponding to the 1-cycle DFT, followed by  $N/6$  for the three-point filter. The delay involved in frequency and ROCOF computation is  $N$  samples.
2. PMU-B : For phasor computation the group delay is  $N/2$  samples, followed by the 2-cycle P-Class filter with a group delay of  $N$  samples. The frequency and the ROCOF delay is approximately zero since IEEE sample based method is used.
3. PMU-B1 : Single stage is used for phasor computation and filtering hence the group delay is given by  $N$  samples. Same frequency and ROCOF method is used as in PMU-B.
4. PMU-C : In this PMU four cycles are employed for phasor computation i.e.  $4N + 1 = L_{dft}$ , the group delay hence is given by  $(L_{dft} - 1)/2$ . Frequency and ROCOF are obtained simultaneously via the elements of the  $[\mathbf{M}]$  matrix, hence both do not exhibit any delay for this PMU.
5. PMU-D : Similar to the previous PMU the group delay is given by  $(L_{dft} - 1)/2$ . Frequency delay is given by  $M \times \phi_{step}/2$  and the ROCOF delay is given by  $L_{RF} \times f_{step}/2$ .



6. PMU-E : For a 3-phase based PMU-E, the group delay exhibited by the averaging filter is giving by  $(L_{MAF} - 1)/2$ , followed by the group delay of the phasor computing module given by  $(L_{dft} - 1)/2$ . Frequency delay is given by  $M \times \phi_{step}/2$  and the ROCOF delay is given by  $L_{RF} \times f_{step}/2$ . For a single-phase based PMU-E an additional delay is added to the phasor computational module given by  $N/3$  samples, corresponding to the quasi-three phase signal construction process.
7. PMU-F : Single stage is used for phasor computation and filtering. The group delay is given by  $L_{Mdfi}/2$  samples, which is dependent on the phasor reporting rate. The frequency and ROCOF delay is similar to PMU-D.
8. PMU-G : Four cycles of the fundamental frequency signal are used for phasor estimation hence a total group delay of  $(L_{dft} - 1)/2$  samples is associated with the IpDFT algorithm. The frequency and ROCOF delay is similar to PMU-D.

**Table 2.6:** Latency for different PMUs.

PMU	Phasor Latency (s)	Frequency Latency (s)	ROCOF Latency (s)
<b>DFT with 3PF (PMU-A)</b>	$((N/2) + (N/6)) \times \Delta t$ = 0.0133	$N \times \Delta t$ = 0.02	$N \times \Delta t$ = 0.02
<b>DFT with IEEE P-Class Filter Two-Stage (PMU-B)</b>	$((N/2) + (N)) \times \Delta t$ = 0.03	0	0
<b>DFT with IEEE P-Class Filter Single-Stage (PMU-B1)</b>	$N \times \Delta t$ = 0.02	0	0
<b>Max-Flat Differentiators (PMU-C)</b>	$((L_{dft} - 1)/2) \times \Delta t$ = 0.04	0	0
<b>Improved WLS-TF (PMU-D)</b>	$((L_{dft} - 1)/2) \times \Delta t$ = 0.04	$((M \times \phi_{step})/2) \times \Delta t$ = 0.0225	$((L_{RF} \times f_{step})/2) \times \Delta t$ = 0.0088
<b>Clarke Transform based DFT (PMU-E)</b>	$((L_{maf} - 1)/2 + (L_{dft} - 1)/2 + (N/3)) \times \Delta t$ = 0.052	$((M \times \phi_{step})/2) \times \Delta t$ = 0.0225	$((L_{RF} \times f_{step})/2) \times \Delta t$ = 0.0088
<b>DFT with IEEE M-class filter (PMU-F)</b>	$(L_{Mdfi})/2 \times \Delta t$ = 0.0473	$((M \times \phi_{step})/2) \times \Delta t$ = 0.007	$((L_{RF} \times f_{step})/2) \times \Delta t$ = 0.018
<b>Interpolated DFT (PMU-G)</b>	$(L_{dft} - 1)/2 \times \Delta t$ = 0.04	$((M \times \phi_{step})/2) \times \Delta t$ = 0.0225	$((L_{RF} \times f_{step})/2) \times \Delta t$ = 0.0088

The latency (group delay  $\times$  sampling interval) associated with all the PMUs is summarized in Table. 2.6. Also, as an example, values of latency for arbitrary values of sampling rate, window length, etc, such as,  $f_0 = 50$  Hz,  $N = 24$ ,  $\Delta t = 1/(f_0 N) = 8.3 \times 10^{-4}$  s,  $L_{dft} = 4N + 1$ ,  $L_{maf} = 31$ ,  $M = 9$ ,  $\phi_{step} = 6$ ,  $L_{RF} = 7$ ,  $f_{step} = 3$ , are given in Table. 2.6. For PMU-F, since the filter length employed for phasor estimation depends on the reporting rate, the parameters for latency calculation are slightly modified. For this PMU, the

value of  $N = 30$  and a reporting rate  $F_{rr} = 50$  fps is chosen, resulting in a window length  $L_{Mdf_t} = 142$  samples (IEEE Std, 2018).

## 2.9 Time-Tag of Phasors

Synchrophasors can be computed either for single-phase or three-phase systems using any of the previously described PMU algorithms. As given in (2.5) a single-phase phasor can be represented as

$$\bar{c}_1 = a_1 - jb_1 = V_c - jV_s \quad (2.78)$$

From the single-phase estimates the positive sequence phasor can be obtained as (Phadke and Thorp, 2010),

$$\bar{c}_{1p} = \frac{1}{3} \times (\bar{c}_{1a} + \alpha \bar{c}_{1b} + \alpha^2 \bar{c}_{1c}) \quad (2.79)$$

where  $\alpha$  is equal to  $-0.5 + j0.866$  or  $e^{j2\pi/3}$  and  $\bar{c}_{1a}, \bar{c}_{1b}$  and  $\bar{c}_{1c}$  are phasors pertaining to individual phases, with  $abc$ -phase sequence.

In order to obtain a single phasor estimate, a window of data is used, say  $N$  samples, as can be seen in (2.3), (2.4). As per Power System Relaying Committee (1995), the use of a window of data provides an option to place the obtained phasor samples relative to the window as follows:

1. **Referred to the end (RE) approach:** The phasor estimates are positioned at the end of a window as when they are obtained without shifting. For example in Fig. 2.7(a), a time-domain signal is sampled at a rate of 1 kHz ( $f_0=50$  Hz), and is appended with  $N = 20$  zeroes at the beginning. Gradually as the window moves and starts accounting the data points from the original input signal, the corresponding phasor magnitude plot given by Fig. 2.7 (b) can be seen growing and eventually reaching unity at 0.02 s when the rectangular data window given by  $W_N$  is completely filled up with samples from the input nominal frequency signal. Hence, appending a time-domain signal with zeros is equivalent to referring the phasor estimate to the end of the window, and is labelled here as RE (Referred to the end) approach.
2. **Referred to the center (RC) approach:** Most of the authors use this approach in which the phasor estimate, though obtained at the end of a window, is placed at the center of the data window as shown in Fig. 2.7 (b).

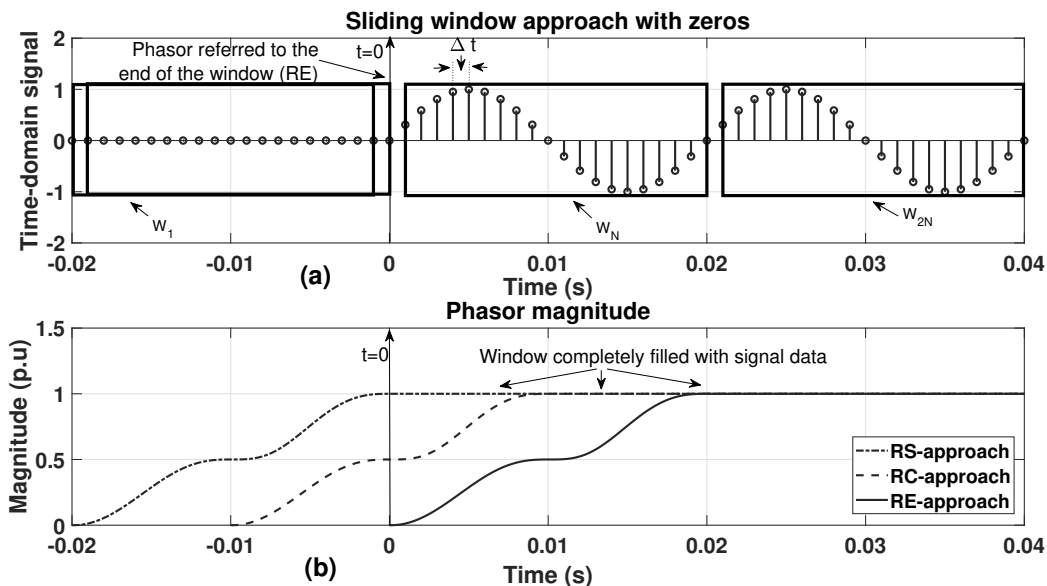


**Figure 2.7:** (a) Time domain signal with zeroes appended. (b) Corresponding phasors referred to different positions of the window.

3. **Referred to the start (RS) approach:** Here, the phasor estimate which is determined at the end of a window, is referred to the beginning of the data window as shown in Fig. 2.7 (b). Hence, the phasor magnitude is seen to be of unity magnitude from the start itself.

### 2.9.1 Performance evaluation of PMUs based on RE-approach

For the PMU specifications employed in Table. 2.6, the phasor magnitudes for a 50 Hz pure sinusoidal signal obtained using different PMUs are shown in Fig. 2.8. These phasor estimates are referred to the end of the observation window based on the RE-approach. Since the phasors are referred to the end of the window, the settling-time of the magnitude estimates depict the exact observation window lengths required by each of the PMUs.

For example, for PMU-A, the DFT module uses a single cycle followed by a three-point filter which uses one-third of the fundamental cycle, this amounts to a total of  $(0.02+0.02/3) = 0.0267$  s, approximately. The same time can be seen associated with the settling-time of the magnitude plot corresponding to PMU-A in Fig. 2.8. Similar observations can be made for the other remaining PMUs.

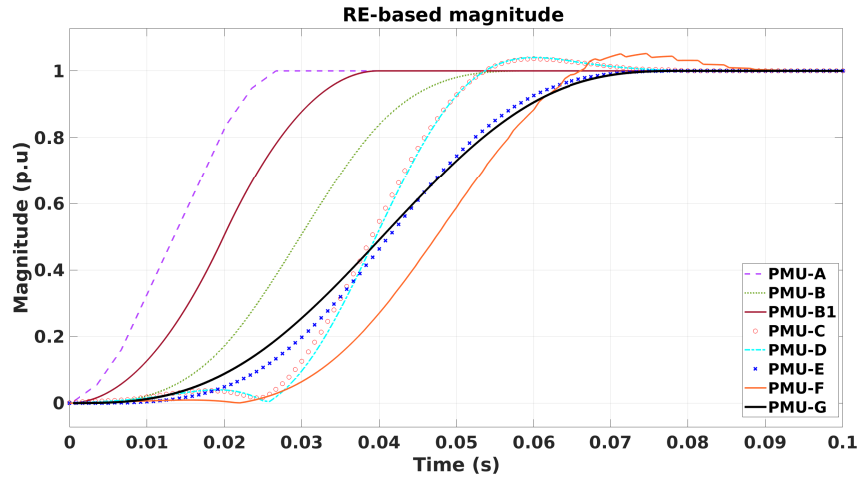


**Figure 2.8:** RE-based phasor magnitude plots for different PMUs.

Based on the RE-approach, the frequency and ROCOF estimates obtained using some of the PMUs have been shown here for the bandwidth compliance test. The phase of the time-domain signals is modulated according to the IEEE Std (2018) using a modulation frequency equal to 2 Hz. The frequency deviations and ROCOF obtained using these PMUs are shown in Figs. 2.9 and 2.10, respectively.

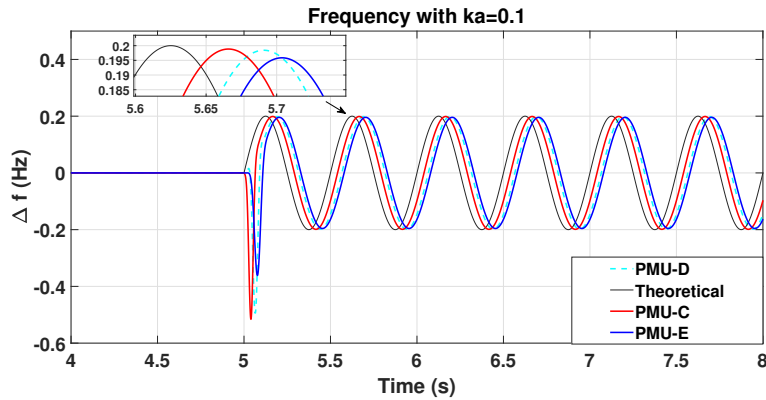


**Figure 2.9:** Frequency using different PMUs for bandwidth compliance test with  $f_m = 2$  Hz.

For example, in case of PMU-C, the frequency latency is approximately zero, given in Table. 2.6. Therefore, the RE-based frequency estimates obtained using PMU-C are delayed by approximately 0.04 s from the theoretical as can be seen from Fig. 2.9. A

similar observation can be made for ROCOF estimated using PMU-C which also is seen to be delayed by 0.04 s, compared to the theoretical, -see Fig. 2.10.

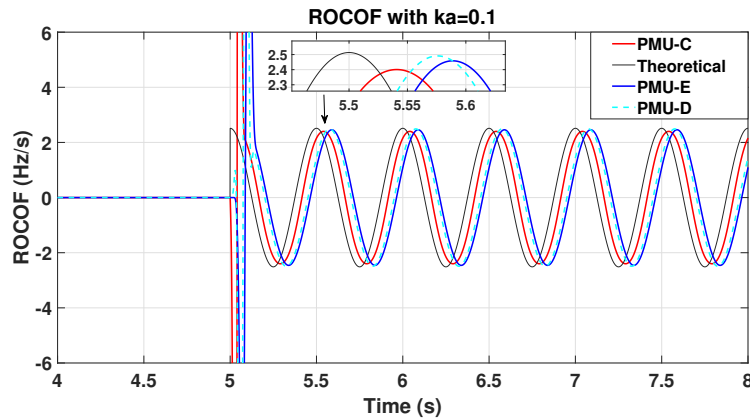


**Figure 2.10:** ROCOF using different PMUs for bandwidth compliance test with  $f_m = 2$  Hz.

The TVEs for the magnitude step test obtained for different PMUs are plotted in Fig. 2.11 and the response times for the same are given in Table. 2.7.

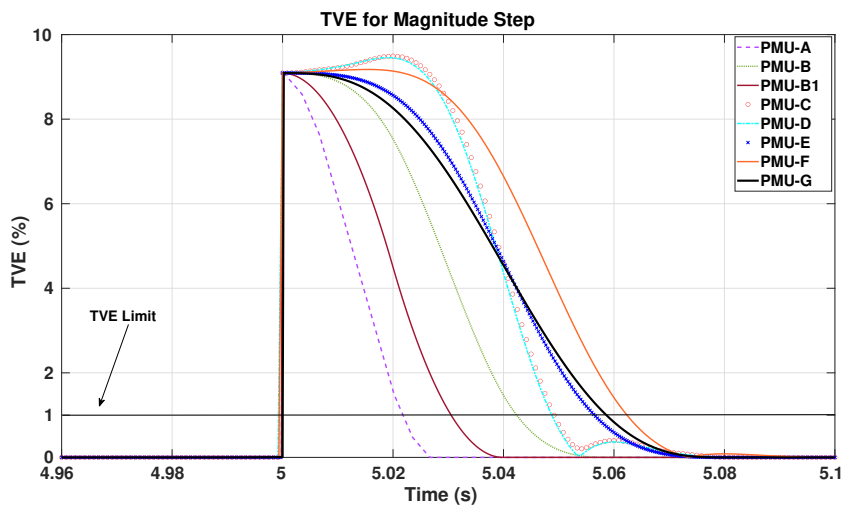


**Figure 2.11:** TVE response for magnitude step using different PMUs.

It can be noted that as the observation window length for the PMU increases, the response time also increases. For example, PMU-B1 employs a single-stage DFT using 2-cycles of the fundamental for phasor computation, whereas PMU-B involves two stages,

one-cycle DFT followed by two cycles of filtering. This increases the overall observation window length in case of PMU-B, which in-turn results in higher values of response time, as can be seen from Table. 2.7.

**Table 2.7:** TVE response time for different PMUs for a step in magnitude.

TVE response time $t_r$ (s)							
PMU-A	PMU-B	PMU-B1	PMU-C	PMU-D	PMU-E	PMU-F	PMU-G
0.022	0.0426	0.031	0.0494	0.0494	0.0568	0.062	0.0587

## 2.10 Summary of the Presented Work

This chapter provides a thorough insight into the static as well as the dynamic tests and their respective error limits, required for compliance verification. The two most recent updates of the standards (IEEE Std, 2011), (IEEE Std, 2014), are compared side by side in order to emphasize the changes made to the TVE, FE and RFE requirements for P or M class compliance. The following are the other topics discussed in this chapter,

1. Performance of the single-phase, one-cycle DFT algorithm is evaluated using the latest IEEE synchrophasor standard. Both static and dynamic test signals are used as inputs to the algorithm and the different error values are compared against the limits set by the standard.
2. Further, a variety of PMU algorithms, based on both the static as well as the dynamic model are described.
3. The techniques employed for phasor, frequency and ROCOF estimation by each of these PMUs are elaborated upon. The group delay associated with each PMU is also computed for arbitrary values of window length.
4. The RC, RS and RE based approaches for referring phasors in an observation window are also discussed, with emphasis primarily on the RE-approach.
5. Phasor magnitude, frequency and ROCOF are obtained for various PMUs based on the RE-approach employing different test signals.

An integrated PMU architecture for implementing phasor algorithms based on the RE-approach is presented in the next chapter. Based on this architecture, PMU-A to PMU-G, have been implemented employing causal and a non-causal compensation and tested following the IEEE synchrophasor standards. Application of the estimates obtained using the integrated PMU architecture for power system protection and control purposes are also demonstrated.

---

## Chapter 3

# AN INTEGRATED PMU ARCHITECTURE

### 3.1 INTRODUCTION

As discussed in the previous chapter, section. 2.9, the three methods used for time-tagging phasors associate the computed PMU quantities to different points in an observation window. Most PMU algorithms compensate the group delay by simply using the RC-approach which involves a certain latency. Such a latency can limit the use of synchrophasor estimates for control applications requiring a fast response time. Recently, a latency free method for delay compensation was proposed in, Meng et al. (2017), resulting in the categorization of PMUs as causal and non-causal.

In this chapter, an integrated architecture for PMUs has been presented which accommodates both the causal and non-causal variants in a single PMU module. This enables easy understanding of a causal PMU which involves real-time phase compensation, there by preferring such PMUs for control applications over the non-causal option. It is also brought out clearly that in the non-causal PMUs, both the phase and amplitude group delay issues are handled by time-tag adjustments in an off-line fashion. This also facilitates easy analysis of causal and non-causal methods for a given PMU algorithm. Using this approach, multiple applications of a PMU can be illustrated in a single module. PMU algorithms have been implemented based on the integrated architecture and tested as per the IEEE standards. Various phase-angle compensation schemes have been suggested for a causal-PMU to show the superiority of the bus voltage-signal frequency against the line



current-signal frequency as the input for compensation. The influence of these schemes on the line power flows and impedance measurements has been demonstrated. Further, a causal and non-causal PMU-based PSS has been designed to illustrate the control application of a WAMS system using a 4-machine power system. Stability of a power system is assessed using causal and non-causal estimates, reflecting the effect of latency due to group delay compensation on the small-signal stability.

## **3.2 Causality in PMUs: An Integrated PMU Architecture**

A system which computes output at a certain time using inputs from the past and the present is said to be causal in nature, while a system which uses future samples as well is referred to as non-causal. Causality in PMUs is primarily introduced by group delay compensation (Meng et al., 2017) and hence PMUs are generally considered as either causal or non-causal type. However, in reality, all PMUs are actually of causal type with the RE based approach for phasor estimation as shown in Fig. 3.1. The uncompensated output from a PMU can be further processed in order to obtain causal or non-causal phasor estimates as per requirement. Thus, a causal or a non-causal PMU results only at the group delay compensation stage of the processing. This provides an integrated PMU architecture for phasor estimation.

### **3.2.1 Basic PMU Block**

In this block the estimation algorithm uses the RE approach, where it employs a window of data consisting of  $N$  samples with a sampling interval equal to  $\Delta t$  to obtain a single phasor estimate at the end of the window when the time is equal to  $t_a$ . Thus the RE approach provides the fundamental scheme for phasor estimation in the basic PMU block. For an observation window consisting of  $N$  samples, the phasor estimation process naturally offers a group delay given by  $N/2$  samples. This applies not only to algorithms but also to filters with symmetrical parameters across the observation window. Therefore, the outputs of the basic PMU block are inherently uncompensated with respect to group delays. In order to compensate this group delay the following two procedures are generally employed, which in-turn gave rise to the corresponding types of PMUs :

1. Non-Causal PMUs or Non-Causal Compensation

## 2. Causal PMUs or Causal Compensation

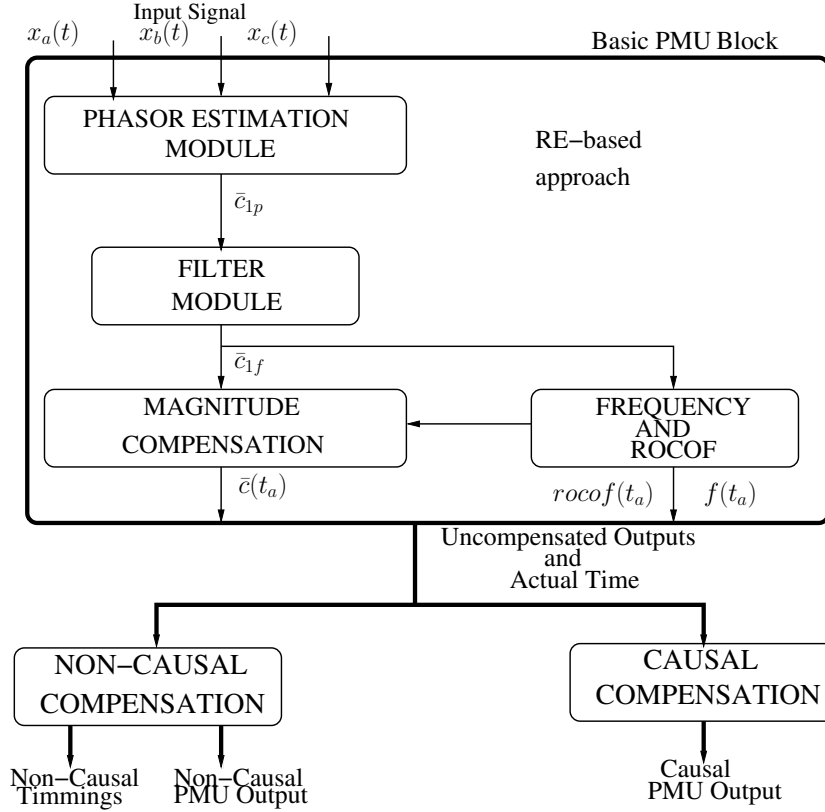


**Figure 3.1:** Integrated PMU architectures

### 3.2.1.1 Non-Causal Compensation

In this case, the group delay associated with the phasor is compensated simply by shifting only the time-tag of a phasor sample as follows (see Fig. 3.2):

$$\bar{c}_{nc}(t_{PMU}) = \bar{c}(t_a - t_L) \quad (3.1)$$

where  $\bar{c}_{nc}$  and  $\bar{c}$  represent the non-causal compensated and the uncompensated phasor estimates respectively,  $t_{PMU}$  is the PMU-time,  $t_a$  is the actual time and  $t_L = \Delta t \times N_L$ , is the group delay in seconds (Meng et al., 2017).  $N_L$  is the lumped group delay of the PMU in terms of samples. It consists of  $N_a$ , the algorithm group delay and  $N_f$ , the filter group delay.

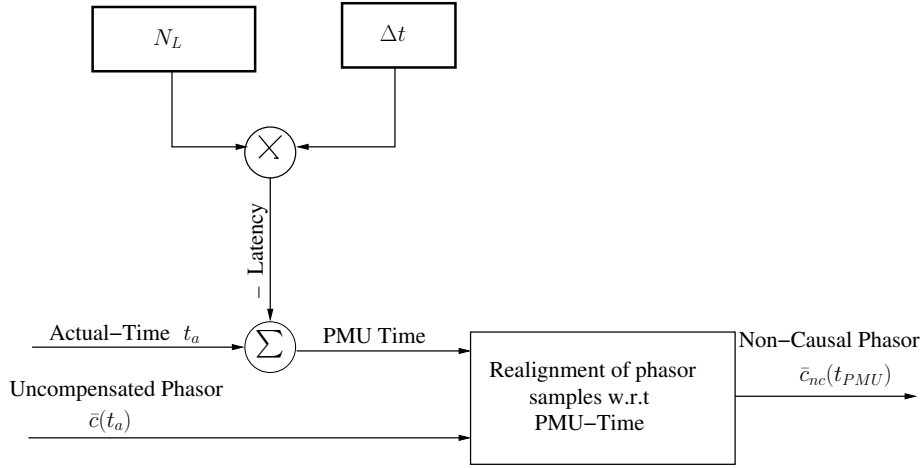


**Figure 3.2:** Non-Causal PMU block

The above time-advancement just denotes the scheme of the RC-approach, where it appears as if a phasor is computed using future signal samples signifying a non-causal behavior. Hence in a non-causal PMU phasors are manipulated with a time-tag which represents the center of the estimation window. When this manipulated time-tag variant of the phasor is communicated in real-time, one observes that at a time  $t_a$  a phasor sample with a time-tag of  $t_{PMU}$  is available, which represents an apparent delay in a PMU measurement which is known as latency. The time-tag shifting surely does compensate for the group delay but it also introduces the above mentioned latency which can render the PMU phasor samples less applicable for real-time control.

This is demonstrated for a one-cycle DFT based PMU with a three-point filter (3PF) (Akke and Thorp, 2010), (Phadke and Thorp, 2010), as shown in Fig. 3.3. The nominal frequency  $f_0$  is 50 Hz, with one cycle of data in 0.02 s. The initial DFT algorithm based observation window of  $N$  data samples is shown in Fig. 3.3(a). The calculated phasor samples are then filtered using a 3PF, which has a window span of  $N/3$  samples, as shown in Fig. 3.3(b). The  $t_{PMU}$  instant for a certain  $t_a$  is also shown in the figure.

The total latency due to the algorithm along with a filter can be calculated as follows,

$$t_L = N_L \times \Delta t = (N_a + N_f) \Delta t \quad (3.2)$$

Where  $N_a = N/2$ , is due to the one-cycle DFT and for the three-point filter the latency is  $N_f = N/6$ , Therefore,

$$t_L = \left( \frac{N}{2} + \frac{N}{6} \right) \Delta t \quad (3.3)$$

Hence,

$$t_{PMU} = t_a - t_L \quad (3.4)$$

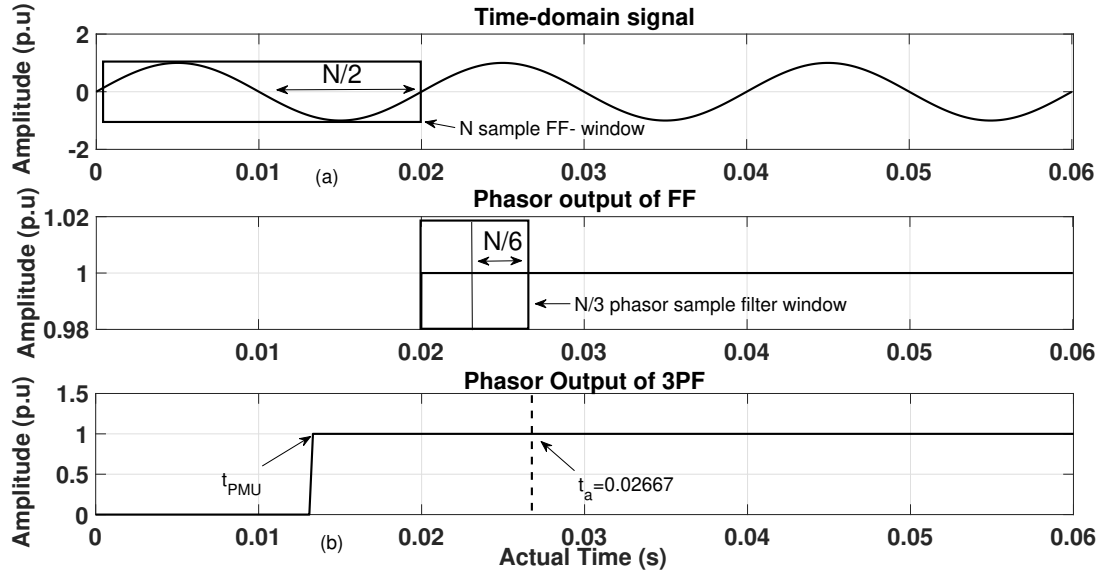


**Figure 3.3:** (a) Time domain signal with a DFT window. (b) Time-tag setting in a DFT based PMU with a 3-point filter.

The uncompensated phasor from the Basic PMU block in Fig. 3.1 is then realigned according to this newly created time vector using (3.1). This process of realignment using PMU-time compensates for the group delay introduced by the algorithm and/or filter, and provides a non-causal phasor.

- Such a time-tag shift for the phasors not only compensates the phase angle delay, but also compensates the periodic delay associated with the amplitude if there is any modulation in the amplitude of the phasor.
- The frequency and ROCOF available at the end of the basic PMU block as shown in Fig. 3.1, are computed using phasors which are available at the immediate output of the filter module. These phasor estimates being uncompensated in nature lead to frequency and ROCOF estimates which are adrift from the theoretical values. Additional delay is then introduced depending on the frequency and ROCOF estimation algorithms. This delay can be compensated by accounting for the value of latency

introduced via these frequency/ROCOF estimation algorithms (in addition to the previous delay introduced by the algorithm and the filter). This leads to the introduction of another time vector known as frequency time given as,

$$t_F = t_{af} - t_L - t_{LF} \quad (3.5)$$

where,  $t_F$  denotes the frequency time vector,  $t_{af}$  denotes the actual time at the end of the frequency estimation module employing the RE approach, and  $t_{LF}$  denotes the latency introduced by the frequency estimation method. Similarly, the ROCOF time can be evaluated as

$$t_{RF} = t_{arf} - t_L - t_{LF} - t_{LR} \quad (3.6)$$

where,  $t_{RF}$  denotes the ROCOF time vector,  $t_{arf}$  denotes the actual time at the end of the ROCOF estimation module employing the RE approach, and  $t_{LR}$  denotes the latency introduced by the ROCOF estimation technique.

### 3.2.1.2 Causal PMUs

In this type of PMU the group delay is compensated by means of a complex exponential function (Meng et al., 2017) without manipulating the time-tag of the input uncompensated phasor as shown below,

$$\bar{c}_c(t_a) = \bar{c}(t_a) \times e^{j\Delta\omega_c\Delta t \times (N_L)} \quad (3.7)$$

where

$$\Delta\omega_c = 2\pi[\Delta f(t_a) + (ROCOF(t_a) \times N_L \times \Delta t/2)] \quad (3.8)$$

and  $\bar{c}$  and  $\bar{c}_c$  represent the uncompensated and the compensated causal phasor estimates respectively.

It is clear that (3.7) with (3.8) are ideally valid during conditions when both the value of frequency and ROCOF remains constant. In Fig. 3.4, we can see that a complex exponential factor is evaluated and is multiplied with the uncompensated phasor which is the output of the Basic PMU block. The output of the causal compensation block is a causal phasor with time-tag same as that of the RE approach. Referring to Fig. 3.3,  $t_a$  is the time-tag of the phasor which is not manipulated in the causal compensation process. This leads to zero latency. Further note that:

- Compensation of only phase angle delay: The exponential term given by (3.7) multiplied with the uncompensated phasor without any time-tag shift, is seen to only compensate the phase angle delay and not the periodic delay associated with the amplitude of the phasor.
- Latency in frequency and ROCOF estimates: In causal PMUs the time at the end of the frequency and ROCOF estimation window is used as the time-tag of the frequency and ROCOF estimates. For example in case of a DFT-based PMU using a three point filter, if the actual time at the end of the filter window as shown in Fig. 3.3 is  $t_a$  s and  $N$  filtered phasors are used for frequency and ROCOF estimation, the time-tag of the frequency and ROCOF estimates obtained using the causal PMU architecture will be given by,  $t_a + N\Delta t$ . Similar to the phasor samples, the frequency and ROCOF samples obtained via causal PMUs are free from latency.

**NOTE:** In case of PMU algorithms, when real-time implementation is carried out there is no way to perform non-causal computations. Non-causal nature is introduced basically due to time-tag shifting. The definition of a non-causal PMU stems from the logic that in order to obtain a phasor with a time-tag  $t_{PMU}$ , samples of the signal pertaining to  $t_a$  have to be used, which represent the future samples (when compared with  $t_{PMU}$ ). The conclusion is that the causal and non-causal behaviors of PMU algorithms are solely as a result of time-tag manipulation. Also in case of non-causal phasor estimates the time-tag shifted version of the phasor is used for TVE calculations, hence TVE in case of non-causal PMUs is given with respect to the PMU-time axis. In case of causal PMUs, since the time-tag is not manipulated, the actual time itself is the PMU-time.

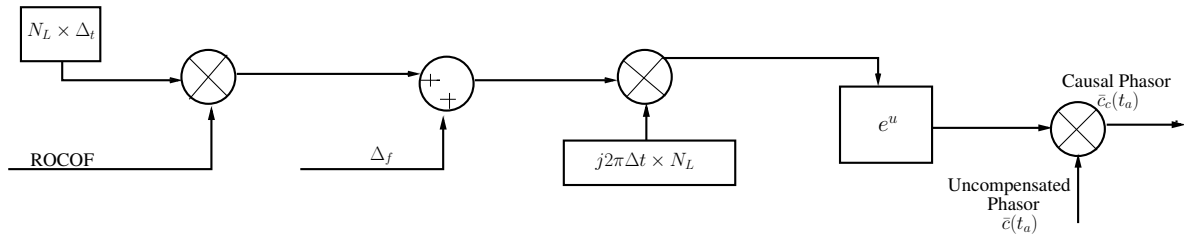


Figure 3.4: Causal PMU block

This can be better visualized using the bandwidth compliance test as recommended by the IEEE Std (2018), -see Section. 2.6.1. An amplitude modulated signal is used with

a modulation factor of  $k_x = 0.1$  p.u and a modulation frequency of 2 Hz. The amplitude computed using both the causal and the non-causal variants of DFT with 3PF (PMU-A) is shown in Fig. 3.5. It can be seen that the amplitude periodic delay gets compensated for the non-causal variant. However, for the causal PMU, the amplitude plot shows a delay in the PMU output with respect to the theoretical value.

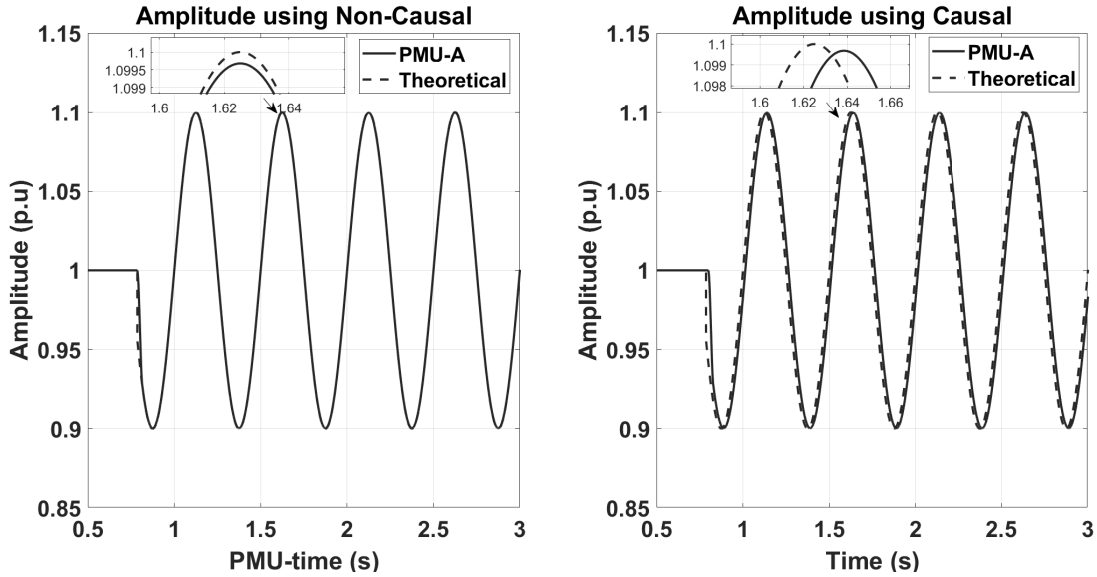


Figure 3.5: Amplitude computation using causal and non-causal PMU-A.

### 3.2.2 Modelling of PMUs

For the purpose of illustration, the model representation of PMU-B1 (a P-type) and PMU-D (M-type) are given in Figs. 3.6 and 3.7, respectively.

Note that in both the models the causal and non-causal phasor estimates are available demonstrating the integrated PMU architecture. In PMU-D, the relation matrix given by  $(\mathbf{B}'\mathbf{W}'\mathbf{W}\mathbf{B})^{-1}\mathbf{B}'\mathbf{W}'\mathbf{W}$  is precalculated as its value does not change. Based on the same architecture, other PMUs (PMU-A to PMU-G) as described in Chapter. 2 have been implemented. Causal and non-causal outputs obtained using these PMUs are checked for compliance using the IEEE synchrophasor standard, (IEEE Std, 2011), (IEEE Std, 2014), (IEEE Std, 2018), in the following section.

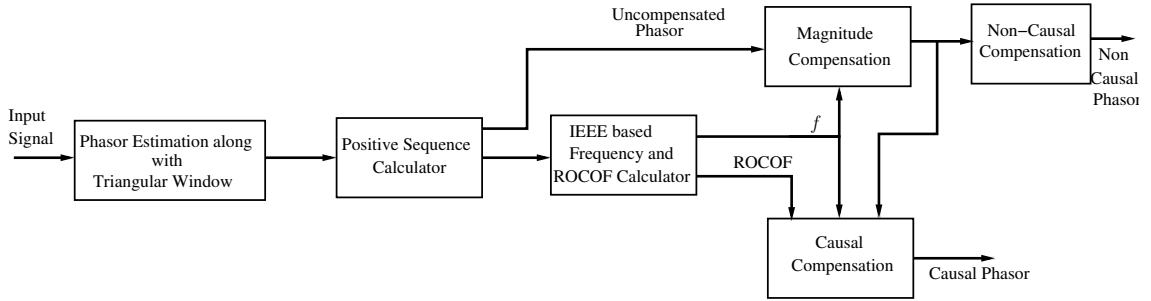


Figure 3.6: Model representation of PMU-B1

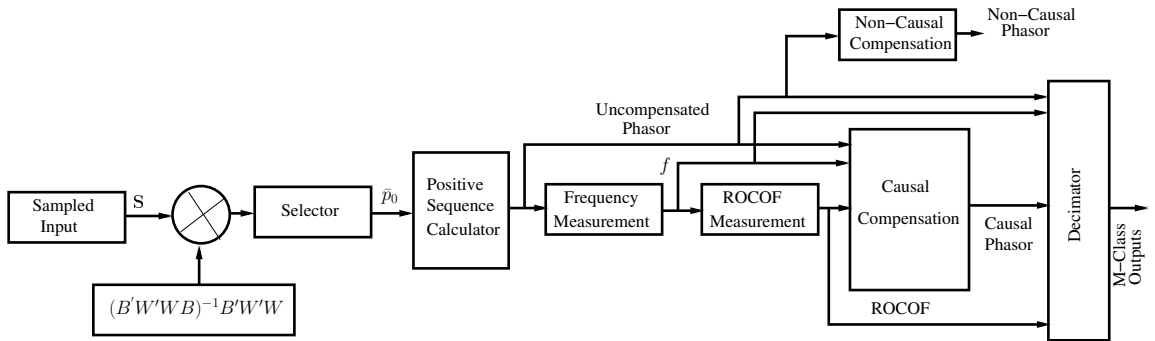


Figure 3.7: Model representation of PMU-D

### 3.3 Synchrophasor Standard Based Tests

In this section, different PMU algorithms are tested as recommended by the IEEE standard for synchrophasors, (IEEE Std, 2014) in the integrated PMU architecture environment. Causal and non-causal phasor outputs, along with frequency and ROCOF values are compared with the theoretical signals for TVE, FE and RFE computations. It must be noted that while for a particular test case the causal and non-causal TVE values might differ, (Meng et al., 2017), the FE and RFE for both the variants are same since no on-line compensation is applied for frequency and ROCOF estimates.

The tests in this section are performed for a nominal frequency of 50 Hz and the rest of the PMU specifications are given in Table. 3.1. The number of samples per cycle as denoted by  $N$  is chosen to be 90, for PMU-A to PMU-E and PMU-G. In case of PMU-F, which is based on the IEEE M-class filter, value of  $N=30$  is chosen, in order to avoid excessively long length filters. PMU-F is designed for a reporting rate of 50 fps with a filter reference



frequency,  $F_{fr}$  of 7.75 Hz and a filter order of 142 samples as given by IEEE Std (2018). In case of PMUs which use time-difference based methods (similar to the one suggested in IEEE Std (2018)) to estimate frequency and ROCOF, such as PMU-B, PMU-B1 and PMU-C, the window length for frequency and ROCOF estimation is considered as zero, see-Table. 3.1. This is because phasor values which are a few samples apart are used to calculate frequency and ROCOF which results in a window length of just 2 or 3 samples. The frequency and ROCOF window lengths in case of PMU-D, PMU-E, PMU-F and PMU-G are given by  $\phi_{step} \times M$  and  $f_{step} \times L_{RF}$  respectively. For example, in case of PMU-D, four cycles of the fundamental are used for phasor estimation, i.e.,  $L_{dft} = (4 \times 90) + 1 = 361$  samples, as given in Table. 3.1. Similarly, for frequency estimation the the number of phase angle samples used are 20 ( $M$ ) with a step size of 15 ( $\phi_{step}$ ), resulting in a window length of 300 samples. In case of ROCOF computation, the number of frequency samples used is 7 ( $L_{RF}$ ) with a step of 3 ( $f_{step}$ ), resulting in a window length of 21 samples, -see Table. 3.1. These parameters can be adjusted accordingly in order to provide P-class or M-class compliant estimates. All the tests are performed on positive sequence signals obtained from a three-phase system. These tests are performed using PMUs implemented in the MATLAB environment on an Intel core i7-4770, 3.4 GHz, 8 GB RAM computer.

**Table 3.1:** Window length details for different PMUs

Parameters → PMU↓	Samples per cycle (N)	Phasor Est Window Length (samples)	Frequency/ROCOF Est Window Length (samples)
PMU-A	90	120	90
PMU-B	90	270	0/0
PMU-B1	90	180	0/0
PMU-C	90	361	0/0
PMU-D	90	361	300/21
PMU-E	90	361	375/21
PMU-F	30	142	100/21
PMU-G	90	361	54/21

### 3.3.1 Static off-nominal test

The input time-domain signal used for this test is given by (2.13). Signal frequency is varied from the nominal by  $\pm 2$  Hz for P-class testing and  $\pm 5$  Hz for M-class testing, (IEEE Std, 2011), (IEEE Std, 2018). The error values for phasor, frequency and ROCOF estimates for this test are given in Table. 3.2, with compliant estimates shown using grey color.

1. It is observed that both the causal and non-causal variants of the PMUs provide exactly the same TVE results. This demonstrates the successful group delay compensation in the causal PMUs, especially during such static conditions resulting in the same estimation accuracy as the non-causal PMUs.
2. Both static as well as dynamic model based PMU algorithms provide TVE values which are well below the 1% limit, (IEEE Std, 2018), required for both P and M class compliance.
3. Frequency errors obtained for all the PMUs are also less than 0.005 Hz ensuring compliance with both the PMU classes.
4. Similarly, RFE values below 0.4 Hz/s (P-class) and 0.1 Hz/s (M-class) limits set by the latest standard (IEEE Std, 2018) are obtained using all the PMUs.

**Table 3.2:** Error values for the static off-nominal test

$f_{sig} \rightarrow$	$\pm 2$ Hz				$\pm 5$ Hz			
	TVE (%) (1%)		FE (Hz)	RFE (Hz/s)	TVE (%) (1%)		FE (Hz)	RFE (Hz/s)
	Causal	Non-Causal	(0.005 Hz)	(0.4 Hz/s)	Causal	Non-Causal	(0.005 Hz)	(0.1 Hz/s)
PMU- $\downarrow$								
PMU-A	0.05	0.05	6.5e-12	1.6e-9	0.12	0.12	1.2e-11	2.4e-9
PMU-B	0.14	0.14	5.3e-12	9.2e-8	0.35	0.35	1.36e-11	3.7e-7
PMU-BI	4.5e-3	4.5e-3	2e-10	3.5e-6	6.7e-3	6.7e-3	2.1e-10	3.7e-6
PMU-C	5.7e-3	5.7e-3	2.54e-10	6e-6	0.22	0.22	2.6e-10	6.2e-6
PMU-D	5.6e-3	5.6e-3	1.6e-11	3.8e-9	0.22	0.22	1.6e-11	4e-9
PMU-E	2.5e-7	2.5e-7	2.8e-9	3.5e-7	5.4e-7	5.4e-7	3.6e-8	8.2e-6
PMU-F	0.169	0.169	7.3e-13	1.3e-11	0.3	0.3	6.8e-13	1.4e-11
PMU-G	0.05	0.05	2e-9	6e-8	0.121	0.121	3.7e-8	8e-7

### 3.3.1.1 Effect of sampling frequency on PMU performance

The effect of sampling frequency on the performance of the PMU algorithms is shown here for the static off-nominal test. The frequency is varied by  $\pm 2$  Hz from the nominal 50 Hz and the maximum TVE is noted for different PMUs employing a range of sampling frequencies. The results are given in Table. 3.3. Slight performance improvement can be seen in PMUs-A, B, F and G, when a higher sampling rate is used. Even though increased sampling rate provides better estimation accuracy it substantially increases the computational burden on the system.

**Table 3.3:** Effect of sampling rate on PMU performance.

TVE (%) for $\pm 2$ Hz (1%)				
$f_s$	2.1 kHz	3 kHz	4.5 kHz	6 kHz
PMU-A	0.11	0.071	0.05	0.036
PMU-B	0.29	0.21	0.14	0.105
PMU-B1	$4.5 \times 10^{-3}$	$4.4 \times 10^{-3}$	$4.4 \times 10^{-3}$	$4.4 \times 10^{-3}$
PMU-C	$5.647 \times 10^{-3}$	$5.62 \times 10^{-3}$	$5.6 \times 10^{-3}$	$5.59 \times 10^{-3}$
PMU-D	$5.64 \times 10^{-3}$	$5.62 \times 10^{-3}$	$5.6 \times 10^{-3}$	$5.59 \times 10^{-3}$
PMU-E	$2.362 \times 10^{-8}$	$2.32 \times 10^{-8}$	$2.3 \times 10^{-8}$	$2.28 \times 10^{-8}$
PMU-F	0.672	0.484	0.183	0.03787
PMU-G	0.105	0.0743	0.05	0.0373

### 3.3.2 Harmonics test

The input time-domain signal used for this test is given in (2.15). The amplitude of the added harmonic is recommended to be 1% or 10% ( $k_H$ ) of the fundamental signal amplitude, for P and M class PMUs, respectively, (IEEE Std, 2018). The results for this test are given in Table. 3.4 for M-class compliance verification. Maximum values of TVE, FE and RFE over a range of harmonics (2 to 50) are noted. Harmonics close to the fundamental i.e., the first three (2nd, 3rd and 4th), primarily affect the performance of the PMU algorithms, however the compliance is verified up to the 50th harmonic.

**Table 3.4:** Error values for the Harmonics test

Harmonic test $k_H = 0.1, h = 2$ to 50				
PMU	Max TVE (%) (1%)		FE (Hz) (5e-3 Hz)	RFE (Hz/s) (-)
	Causal	Non-Causal		
PMU-A	6.7e-11	3.5e-11	6.2e-12	1.3e-9
PMU-B	6.5e-10	2.8e-11	1.6e-12	2.4e-9
PMU-B1	4.4e-7	3.7e-11	2e-10	3.5e-6
PMU-C	0.0533	0.0032	0.0015	0.0784
PMU-D	0.005	0.0023	4.1e-12	0.0077
PMU-E	1.5e-4	1.2e-4	3.5e-7	9e-5
PMU-F	0.0033	0.0032	2.6e-5	1.4e-4
PMU-G	1.9e-3	2.73e-4	3.3e-5	3.5e-4

1. All the PMUs are seen to comply with the latest standard limits for the harmonics test with TVE values less than 1% for both causal as well as non-causal architectures.
2. PMUs such as PMU-A, B, B1, E, F and G provide accurate estimates for the integer harmonics test since these PMUs are based on the DFT algorithm.
3. The frequency error values for all the PMUs are less than 0.005 Hz, which ensures M-class compliance.

4. It is noted that even though the RFE limits for the M-class harmonics test have been suspended in IEEE Std (2014), the estimates provided via these PMUs are very accurate.

Since all the PMUs comply with the stricter M-class requirements, they also comply with the P-class requirements, hence the results are not presented in this report.

### 3.3.3 Inter-harmonic test/Out-of-band interference test

This test is performed for a reporting rate  $F_{rr}$  of 50 fps and the input time-domain signal used is given by (2.18). The base frequency values obtained for the selected reporting rate are 47.5, 50 and 52.5 Hz. Inter-harmonic frequencies ( $f_{ih}$ ) of 10,  $f_0 \pm F_{rr}/2, 2f_0$  Hz are used to perform this test. As per IEEE Std (2018), this test is only recommended for M-class PMUs and no RFE limits are prescribed. This test is the most demanding test and requires dynamic PMU algorithms or traditional algorithms with additional filtering in order to meet the recommended accuracy levels. The TVE and frequency error values for this test for different of out-of band signals are given in Tables. 3.5-3.8.

**Table 3.5:** Error values for inter-harmonic frequency of 10 Hz.

$f_{ih} \rightarrow$	10 Hz		
$f_{base} \rightarrow$	47.5/50/52.5 Hz		
Error $\rightarrow$	TVE (%) (1.3%)		FE (Hz) (0.01 Hz)
PMU $\downarrow$	Causal	Non-Causal	
PMU-A	12/12.5/13.1	2.2/1.94/2.24	1.32/1.46/1.63
PMU-B	3.5/3.65/4.3	0.29/0.13/0.29	0.05/0.052/0.055
PMU-B1	6.3/7/7.9	0.68/0.56/0.56	0.21/0.22/0.24
PMU-C	4.4/3.7/4.7	0.35/0.34/0.35	0.033/0.01/0.05
PMU-D	0.36/0.37/0.38	0.36/0.34/0.355	0.003/0.001/5.6e-4
PMU-E	0.27/6.2e-3/0.27	0.27/4.4e-3/0.27	1.5e-5/2.3e-5/1.1e-5
PMU-F	0.32/0.002/0.32	0.32/0.002/0.32	2.7e-5/2.1e-5/4.9e-6
PMU-G	35/38/43	0.46/0.42/1.3	0.12/0.13/0.15

1. It is observed that only the non-causal versions of PMU-D, PMU-E and PMU-F provide estimates which comply with the latest IEEE standards for all the given inter-harmonic frequencies, since they are basically designed for M-class compliance.
2. Causal versions of PMUs-D, E and F fail to provide M-class compliant TVE estimates for  $f_{ih}$  values of 25 Hz and 75 Hz. This can be attributed to the role of frequency and ROCOF estimates involved in causal based phase-angle compensation.

**Table 3.6:** Error values for inter-harmonic frequency of 25 Hz

$f_{ih} \rightarrow$	25 Hz		
$f_{base} \rightarrow$	47.5/50/52.5 Hz		
Error $\rightarrow$	TVE (%) (1.3%)		FE (Hz) (0.01 Hz)
PMU $\downarrow$	Causal	Non-Causal	
PMU-A	22.6/25/28	5.93/6.2/7.4	1.76/2.06/2.42
PMU-B	24.2/29.6/36.2	3.3/2.67/2.8	0.61/0.67/0.74
PMU-B1	18.3/21.9/26.3	4.8/4.2/4.09	0.96/1.06/1.18
PMU-C	29/34.3/41.5	4.8/4.74/4.75	0.35/0.43/0.55
PMU-D	1.37/3.2/4.03	0.73/0.67/0.73	0.0043/0.009/0.009
PMU-E	1.85/1.28/1.14	1.21/0.93/1.21	0.007/0.006/7.9e-4
PMU-F	0.33/0.02/0.33	0.33/0.019/0.33	1.9e-4/3.4e-5/2e-4
PMU-G	200/200/202	10.3/10.7/12.8	2.1/2.4/2.9

**Table 3.7:** Error values for inter-harmonic frequency of 75 Hz

$f_{ih} \rightarrow$	75 Hz		
$f_{base} \rightarrow$	47.5/50/52.5 Hz		
Error $\rightarrow$	TVE (%) (1.3%)		FE (Hz) (0.01 Hz)
PMU $\downarrow$	Causal	Non-Causal	
PMU-A	27.8/25/22.6	7.4/6.2/6	2.42/2.06/1.76
PMU-B	36.2/29.6/24.2	2.8/2.67/3.3	0.74/0.67/0.61
PMU-B1	26.3/21.9/18.3	4.09/4.2/4.8	1.18/1.06/0.96
PMU-C	41.5/34.3/29	4.75/4.74/4.75	0.55/0.43/0.35
PMU-D	4.03/3.02/1.37	0.74/0.67/0.74	0.0009/0.0009/0.0043
PMU-E	1.14/1.28/1.83	1.22/0.94/1.22	7.9e-4/0.006/0.0075
PMU-F	0.33/0.02/0.33	0.33/0.019/0.33	2e-4/3.4e-5/1.87e-4
PMU-G	202/201/201	12.8/10.7/10.3	2.9/2.4/2.1

**Table 3.8:** Error values for inter-harmonic frequency of 100 Hz

$f_{ih} \rightarrow$	100 Hz		
$f_{base} \rightarrow$	47.5/50/52.5 Hz		
Error $\rightarrow$	TVE (%) (1.3%)		FE (Hz) (0.01 Hz)
PMU $\downarrow$	Causal	Non-Causal	
PMU-A	0.05/5.2e-11/0.05	0.05/5.2e-11/0.05	7e-12/5.4e-12/7.2e-12
PMU-B	0.15/6e-10/0.15	0.15/2.3e-11/0.15	1.2e-11/1.2e-11/1.2e-11
PMU-B1	5.4e-3/4.4e-7/5.4e-3	5.4e-3/3.2e-11/5.4e-3	2e-10/2e-10/2e-10
PMU-C	1.55/0.66/1.33	0.07/0.06/0.07	0.04/7.3e-3/0.03
PMU-D	0.009/5e-10/0.009	0.009/1e-10/0.009	1.5e-12/4.1e-12/3.8e-12
PMU-E	0.26/6.8e-4/0.26	0.26/6.6e-4/0.26	6.5e-7/1.9e-6/3e-6
PMU-F	0.33/0.012/0.33	0.33/0.012/0.33	6e-5/9.1e-5/7.1e-5
PMU-G	0.94/0.52/0.91	0.77/0.006/0.77	0.001/0.001/0.001

3. The TVE values for non-causal PMUs-D, E and F across all the inter-harmonic frequencies are strictly less than 1.3%, as recommended by the standard (IEEE Std, 2018).
4. The frequency errors exhibited by these PMUs do not cross the 0.01 Hz standard limit, (IEEE Std, 2018), hence validating their M-class compliance.
5. Most causal PMUs, such as A, B, B1, C and G, exhibit errors well above the permissible limits due to poor frequency and ROCOF estimates which are used for angle compensation in causal PMUs.

### **3.3.4 Bandwidth Compliance test**

#### **3.3.4.1 Amplitude modulation test**

The time-domain signal prescribed by the IEEE Std (2018) for this test is given by (2.20). The amplitude of the time-domain signal is modulated using a modulation factor  $k_x = 0.1$  p.u and a modulation frequency ( $f_m$ ) of 2 Hz and 5 Hz for P-class and M-class testing, respectively, (IEEE Std, 2018).

1. In case of causal PMUs, due to the absence of an amplitude compensation scheme, the TVE values are high, as can be seen in Table. 3.9.
2. On the other hand, since the amplitude delay in case of non-causal PMUs is compensated, it results in very low TVE values. An observation which can be made from Table. 3.9 is that, higher the group delay associated with a PMU, higher is the causal TVE in case of signals involving amplitude modulation. For example, PMU-F which employs the IEEE-M class filter (IEEE Std, 2018) for phasor estimation with reporting rate of 50 fps, a FIR filter of order 142 and a sampling frequency of 1.5 kHz results in a poor performance for amplitude modulation if causal estimates are considered.
3. Due to the absence of phase angle excursions involved in the amplitude modulation test the frequency and ROCOF errors exhibited by all the PMUs are well within the required limits, see Table. 3.9.

4. To summarize, all the non-causal PMUs meet the prescribed limits for both the PMU classes. In case of causal PMUs, only PMU-A and PMU-B1 satisfy the requirement limits for P class compliance, due to smaller window lengths.

**Table 3.9:** Error values for the amplitude modulation test

$f_m \rightarrow$	Amplitude Modulation $k_v = 0.1$							
	2 Hz (P-class)				5 Hz (M-class)			
	TVE (%) (3%)		FE (Hz)	RFE (Hz/s)	TVE (%) (3%)		FE (Hz)	RFE (Hz/s)
PMU ↓	Causal	Non-Causal	(0.06 Hz)	(2.3 Hz/s)	Causal	Non-Causal	(0.3 Hz)	(14 Hz/s)
PMU-A	1.74	0.036	6.5e-12	1.6e-9	4.4	0.22	6e-12	1e-9
PMU-B	3.9	0.09	1.2e-12	3e-9	9.5	0.54	1.2e-12	3e-9
PMU-B1	2.6	0.06	2e-10	2e-6	6.5	0.37	2e-10	2e-6
PMU-C	5.2	6.3e-4	3e-8	5e-5	12.6	0.025	1.2e-6	8e-4
PMU-D	5.2	6.3e-4	3.7e-8	4.5e-7	12.6	0.024	1.3e-6	3.8e-5
PMU-E	5.2	0.145	8e-12	1e-9	12.3	0.88	8e-12	1.5e-9
PMU-F	7.1	1.5e-3	8e-13	1.3e-11	16.5	0.094	8e-13	1.3e-11
PMU-G	5.2	0.2	2e-9	5e-8	12.1	1.1	2e-8	1e-6

### 3.3.4.2 Phase Modulation test

The input signal to the PMUs for this test is given in (2.20). The amplitude modulation factor is set to zero, while  $k_d$  which represents the phase modulation factor, is set to 0.1 p.u. Similar to the amplitude modulation test, the phase modulation frequency ( $f_m$ ) is taken as 2 Hz for P-class compliance and 5 Hz for M-class compliance (IEEE Std, 2018).

1. For causal PMUs, if phase modulated signals are used as inputs, the group delay of the computed phasor is compensated using the frequency and ROCOF values, via the complex exponential term given in (3.7). The precision of the compensation depends on the accuracy of the frequency and ROCOF estimates provided by the PMU.
2. The error values for both P and M class compliance verification are summarized in Table. 3.10. Compared to the amplitude modulation test, the causal PMUs perform significantly better, albeit not as accurate as their non-causal counterparts. All non-causal PMUs provide TVE estimates less than 3% for both 2 Hz and 5 Hz modulation frequencies.
3. FE exhibited by all the PMUs is less than 0.06 Hz and 0.3 Hz as required for P and M-class compliance, respectively (IEEE Std, 2018).

4. The RFE values for all the PMUs are also less than 2.3 Hz/s and 14 Hz/s, thus satisfying both P and M class requirements, as can be seen in Table. 3.10.
5. To summarize, several causal and most non-causal versions of the PMUs satisfy the IEEE standard imposed limits for TVE, frequency and ROCOF for both the classes in case of the phase modulation test.

**Table 3.10:** Error values for the phase modulation test

$f_m \rightarrow$	Phase Modulation $k_a = 0.1$							
	2 Hz (P-class)				5 Hz (M-class)			
	TVE (%) (3%)		FE (Hz) (0.06 Hz)	RFE (Hz/s) (2.3 Hz/s)	TVE (%) (3%)		FE (Hz) (0.3 Hz)	RFE (Hz/s) (14 Hz/s)
PMU ↓	Causal	Non-Causal			Causal	Non-Causal		
PMU-A	0.4	0.033	9.4e-4	0.011	2.44	0.198	0.011	0.31
PMU-B	0.048	0.08	1.6e-3	0.021	0.27	0.49	0.025	0.77
PMU-B1	0.048	0.054	1.2e-3	0.015	0.36	0.33	0.017	0.53
PMU-C	0.16	6e-4	2.2e-3	0.26	2.35	0.022	0.034	0.98
PMU-D	0.54	6.4e-4	1.3e-4	1.8e-3	5.45	0.023	2.9e-3	0.1
PMU-E	0.6	0.13	3e-3	0.04	5.6	0.8	0.043	1.38
PMU-F	0.8	2.2e-3	5.6e-3	0.14	7.5	0.09	0.084	4.8
PMU-G	1.92	0.85	0.021	0.25	6.2	0.95	0.24	7

### 3.3.5 Ramp Test

The time-domain signal used for the ramp test is given by (2.24) as recommended by the IEEE Std (2018). For P-class testing, the frequency is set to 48 Hz and is then ramped up to 52 Hz at a ramp rate of 1 Hz/s. The opposite is done for a negative ramp rate (IEEE Std, 2018).

1. The results compiled in Table. 3.11 show that the TVE values for all the PMUs are well below the 1% limit set by the standard.
2. Both the causal as well as the non-causal PMUs provide similar estimates since the phasor magnitude and ROCOF of the signals are constant for the frequency ramp test.
3. Frequency estimates for the ramp test provided by all the PMUs also satisfy the P-class criteria with FE values being less than 0.01 Hz.
4. RFE values are also less than 0.4 Hz/s for all the mentioned PMUs.



In case of M-class testing, frequency of the input signal is started from 45 Hz and ramped up till 55 Hz at a rate of 1 Hz/s. The results for this test are given in Table. 3.12. TVE values for both the causal and the non-causal versions are less than 1%, thereby ensuring M-class compatibility for phasor estimates. FE and RFE values obtained for all the PMUs are less than the 0.01 Hz and 0.2 Hz/s limits set by the standard. It should be noted that the error values from the exclusion interval for all the parameters are exempted for the ramp test as suggested by IEEE Std (2014), IEEE Std (2018).

**Table 3.11:** Error values for the P-class ramp test

P-Class ramp (48 – 52) Hz				
Error →	TVE (1%)		FE (0.01 Hz)	RFE (0.4 Hz/s)
PMU ↓	Causal	Non-Causal		
PMU-A	0.05	0.05	3.72e-5	9.7e-8
PMU-B	0.15	0.15	1.2e-4	3.3e-7
PMU-B1	4.5e-3	4.5e-3	2.3e-4	1e-6
PMU-C	5.6e-3	5.6e-3	2e-4	3e-3
PMU-D	5.7e-3	5.7e-3	9.7e-6	5.5e-6
PMU-E	0.025	0.025	1.69e-4	8.9e-7
PMU-F	0.169	0.169	4.25e-4	4.8e-6
PMU-G	0.48	0.48	4.5e-3	2e-6

**Table 3.12:** Error values for the M-class ramp test

M-Class ramp (45 – 55) Hz				
Error →	TVE (1%)		FE (0.01 Hz)	RFE (0.2 Hz/s)
PMU ↓	Causal	Non-Causal		
PMU-A	0.122	0.122	3.8e-5	2e-7
PMU-B	0.36	0.36	1.2e-4	4.5e-7
PMU-B1	6.8e-3	6.8e-3	2.3e-4	3.4e-6
PMU-C	0.2	0.2	3.8e-3	0.02
PMU-D	0.211	0.211	1.8e-5	6e-6
PMU-E	0.046	0.046	1.72e-4	9.7e-7
PMU-F	0.41	0.41	4.4e-4	5e-6
PMU-G	0.567	0.567	4.5e-3	3.8e-6

### 3.3.6 Step test

#### 3.3.6.1 Amplitude Step test

The time-domain signal used for this test is given by (2.29), where  $u(t)$  represents the step function and  $k_x (= \pm 0.1 \text{ p.u})$  is the magnitude of the amplitude step. In case of the step test the result of concern is the response time. It denotes the time-difference between the

instants when the error leaves the prescribed limit and returns back and stays within the limit (1% for TVE, 0.05 Hz for FE, 0.4 Hz/s (for P) and 0.1 Hz/s (for M) in case of RFE) (IEEE Std, 2018). The values of response time for the amplitude step test as obtained for different PMUs are listed in Table. 3.13.

1. All the PMUs (causal as well as the non-causal) are seen to satisfy the M-class response time requirements.
2. On the other hand, P-class requirements are fulfilled by all non-causal PMUs except PMU-G.
3. Based on the causal architecture only PMU-A and B1 satisfy the P-class requirements for the TVE response time.
4. All the frequency and ROCOF response times for this test are zero since no frequency excursions occur when an amplitude step is initiated.

**Table 3.13:** Response time values for Amplitude step test

Amplitude step response time $t_r$ (s)					
PMU ↓	TVE (0.04 s (P) and 0.14 s (M))		FE 0.09 s (P) / 0.28 s (M)	RFE	
	Causal	Non-Causal		P (0.12 s)	M (0.28 s)
PMU-A	0.022	0.0169	0	0	0
PMU-B	0.0426	0.0257	0	0	0
PMU-B1	0.0307	0.0217	0	0	0
PMU-C	0.0494	0.0186	0	0	0
PMU-D	0.0494	0.0186	0	0	0
PMU-E	0.0568	0.0329	0	0	0
PMU-F	0.062	0.029	0	0	0
PMU-G	0.059	0.059	0	0	0

### 3.3.6.2 Phase Step test

Similar to the amplitude step test, the input signal to the PMU in case of the phase step test is given by (2.29). The value of angle step,  $k_a$ , as prescribed by the standard is  $\pm\pi/18$  radians. The TVE, FE and RFE response time values for this test are presented in Table. 3.14. It should be noted that the response time values are computed for a 50 Hz nominal system with a reporting rate of 50 fps.

1. TVE response time requirements for M-class compliance are satisfied by all non-causal PMUs.

- Similarly, the TVE response time requirements for P-class compliance are also fulfilled by all non-causal PMUs except PMU-G.

**Table 3.14:** Response time values for Phase step test

Phase step response time $t_r$ (s)					
PMU	TVE (0.04 s (P) and 0.14 s (M))		FE 0.09 s (P) / 0.28 s (M)	RFE	
	Causal	Non-Causal		P (0.12 s)	M (0.28 s)
PMU-A	0.043	0.0198	0.0458	0.0461	0.0462
PMU-B	0.0591	0.032	0.0566	0.0598	0.0599
PMU-B1	0.0404	0.0264	0.0399	0.0402	0.0402
PMU-C	0.0748	0.0221	0.0738	0.0782	0.0797
PMU-D	0.0983	0.0221	0.089	0.0994	0.1026
PMU-E	0.1804	0.04	0.159	0.1697	0.1821
PMU-F	0.146	0.0364	0.102	0.116	0.152
PMU-G	0.0902	0.0663	0.079	0.092	0.095

- For frequency error, response time limits for P-class PMUs are satisfied by all the PMUs except PMU-E and F, see Table.3.14. On the other hand, M-class limits for FE are satisfied by all the PMUs with response time values less than 0.28 s.
- PMU-E also fails to satisfy the response time limits for P-class compliance, for RFE signals. M-class compliance for RFE signals is achieved using all the PMUs with response time values less than 0.28 s.

The results for all the tests are summarized in Table. 3.15.

**Table 3.15:** Compliance verification for all PMUs based on the integrated architecture using IEEE synchrophasor standard signals.

Test case	Compensation method	PMU-A		PMU-B		PMU-B1		PMU-C		PMU-D		PMU-E		PMU-F		PMU-G	
		P	M	P	M	P	M	P	M	P	M	P	M	P	M	P	M
Static Off-nominal	Causal	✓	✓	✓	✓	✓	✓	✓	✓	✓	✓	✓	✓	✓	✓	✓	✓
	Non-Causal	✓	✓	✓	✓	✓	✓	✓	✓	✓	✓	✓	✓	✓	✓	✓	✓
Harmonic	Causal	✓	✓	✓	✓	✓	✓	✓	✓	✓	✓	✓	✓	✓	✓	✓	✓
	Non-Causal	✓	✓	✓	✓	✓	✓	✓	✓	✓	✓	✓	✓	✓	✓	✓	✓
Inter-harmonic	Causal	-	X	-	X	-	X	-	X	-	X	-	X	-	X	-	X
	Non-Causal	-	X	-	X	-	X	-	X	-	✓	-	✓	-	✓	-	X
Amplitude mod	Causal	✓	X	X	X	✓	X	X	X	X	X	X	X	X	X	X	X
	Non-Causal	✓	✓	✓	✓	✓	✓	✓	✓	✓	✓	✓	✓	✓	✓	✓	✓
Phase mod	Causal	✓	✓	✓	✓	✓	✓	✓	✓	✓	X	✓	X	✓	X	✓	X
	Non-Causal	✓	✓	✓	✓	✓	✓	✓	✓	✓	✓	✓	✓	✓	✓	✓	✓
Ramp	Causal	✓	✓	✓	✓	✓	✓	✓	✓	✓	✓	✓	✓	✓	✓	✓	✓
	Non-Causal	✓	✓	✓	✓	✓	✓	✓	✓	✓	✓	✓	✓	✓	✓	✓	✓
Amplitude step	Causal	✓	✓	X	✓	✓	✓	X	✓	X	✓	X	✓	X	✓	X	✓
	Non-Causal	✓	✓	✓	✓	✓	✓	✓	✓	✓	✓	✓	✓	✓	✓	✓	✓
Phase step	Causal	X	✓	X	✓	X	✓	X	✓	X	✓	X	✓	X	✓	X	✓
	Non-Causal	✓	✓	✓	✓	✓	✓	✓	✓	✓	✓	✓	X	✓	X	✓	✓

### 3.4 Different Schemes for Angle-Compensation in an Integrated Architecture for Causal PMU

PMUs computing both current as well as voltage phasors have been applied to power systems in Dotta et al. (2013), Guardado and Guardado (2015), without much insight into the TVE calculations and the compensation aspect of the phasors. Now, with the introduction of causality in PMUs, (Meng et al., 2017), the compensations have notable influence on the PMU outputs. In a six input PMU (three-phase voltages and three-phase currents), two frequencies and ROCOFs are available based on the positive-sequence voltage phasor and the current phasor. Here, the voltage phasor denotes a bus voltage and the current phasor represents the current flowing in a line associated with that bus. Since the presented work mainly deals with the power swings related slow dynamic phenomena, the network transients are not modelled in the power system stability program and hence the DC components in the input signal which decays quickly, are neglected in the analysis.

Voltage and current-based frequencies and ROCOFs can be used for magnitude and phase compensation in a causal PMU, (Meng et al., 2017). Thus, availability of multiple frequencies and ROCOFs leads to different schemes of compensation in the integrated PMU architecture given in Fig. 3.8. These are listed as follows,

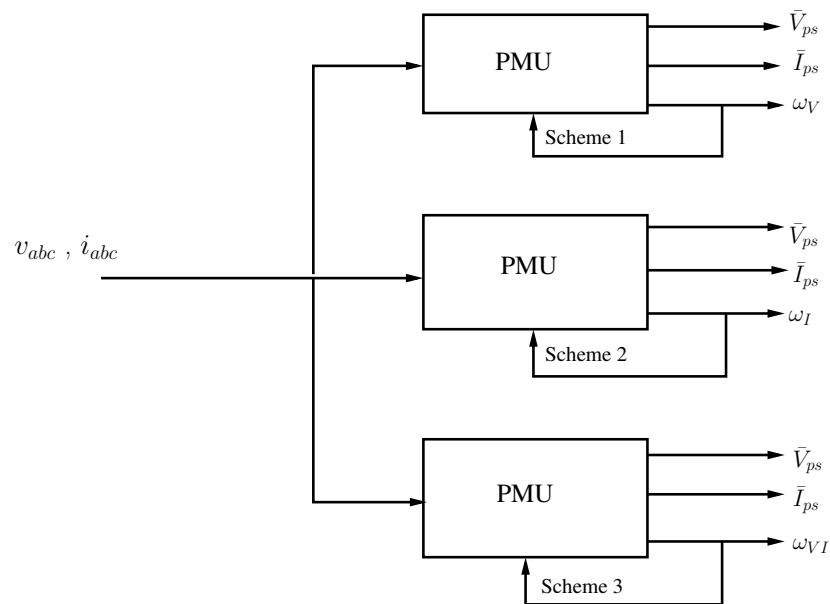


**Figure 3.8:** Different schemes of compensation for causal PMU architecture.

1. Scheme-1: Only the voltage-based frequency and ROCOF estimates are used for magnitude and phase compensation of both the voltage as well as the current phasors.
2. Scheme-2: Only the current-based frequency and ROCOF estimates are used for magnitude and phase compensation of both the voltage as well as current phasors.
3. Scheme-3: Here, both the current and voltage-based frequencies and ROCOFs are employed in the PMU. The current and voltage phasors are compensated for magnitude and angle using their respective frequencies and ROCOFs.

For each of the above schemes, in addition to voltage and current phasors, real and reactive powers are estimated to obtain the line flows.

### 3.4.1 Effect of schemes of compensation on power calculations

Following Scheme-3, the phase angle compensation is applied as follows:

The causal voltage,  $\bar{V}_c$  and the uncompensated voltage estimate  $\bar{V}_{uc}$  are related as,

$$\bar{V}_c = \bar{V}_{uc} \times e^{j\omega_v \Delta t N_L} \quad (3.9)$$

Similarly, the causal current,  $\bar{I}_c$  and the uncompensated current estimate  $\bar{I}_{uc}$  are related as,

$$\bar{I}_c = \bar{I}_{uc} \times e^{j\omega_i \Delta t N_L} \quad (3.10)$$

Hence, the complex power,  $\bar{S}_c$  calculated using the causal estimates is given by,

$$\bar{S}_c = \bar{V}_c \times \bar{I}_c^* \quad (3.11)$$

where \* represents the complex conjugate operation. The compensated voltages and currents can be expanded in-terms of their respective magnitudes and phase angles as,

$$\bar{S}_c = |\bar{V}_{uc}| e^{j\theta_v} e^{j\omega_v \Delta t N_L} \times (|\bar{I}_{uc}| e^{j\theta_i} e^{j\omega_i \Delta t N_L})^* \quad (3.12)$$

or

$$\bar{S}_c = |\bar{V}_{uc}| |\bar{I}_{uc}| e^{j(\phi + (\omega_v - \omega_i) \Delta t N_L)} \quad (3.13)$$

where  $\phi = \theta_V - \theta_I$ . Using (3.13) the active and reactive power can be written as,

$$Re(S_c) = P_c = |\bar{V}_{uc}| |\bar{I}_{uc}| \cos(\phi + (\omega_V - \omega_I)\Delta t N_L) \quad (3.14)$$

$$Im(S_c) = Q_c = |\bar{V}_{uc}| |\bar{I}_{uc}| \sin(\phi + (\omega_V - \omega_I)\Delta t N_L) \quad (3.15)$$

**Note :** In Scheme-1 and Scheme-2 the argument of the trigonometric functions in (3.14) and (3.15) reduces to  $\phi$ . Hence, the active and reactive power obtained using the causal PMU is exactly identical to that in the non-causal PMU given by  $S_{nc}$ , as follows,

$$S_c = S_{nc} = |\bar{V}_{uc}| |\bar{I}_{uc}| e^{j\phi} \quad (3.16)$$

In order to analyse the phase compensation effects in causal PMU following different schemes of frequency/ROCOF usage, case studies are carried out which include a small-signal stable case, small-signal unstable case and a large disturbance condition.

### 3.4.2 Case-1 : Small-Signal Stable Condition

In this case a three-phase fault is simulated at 0.1 s at bus-10 of a 4-machine 10-bus power system shown in Fig. 3.9. The fault is cleared after 0.05 s, without any line tripping, (Shubhanga, 2018). The power system modelling details are enumerated below:

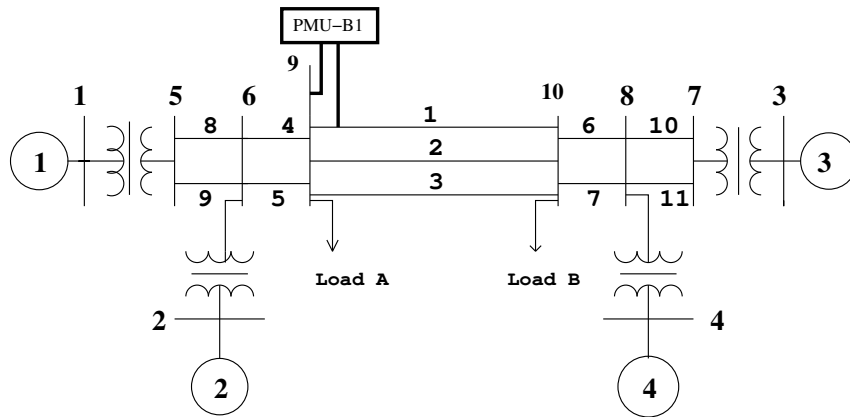


**Figure 3.9:** A 4-machine 10-bus power system.

- Generators are modeled pertaining to the 2.2 model with single time-constant static exciters.

- Load is modeled as constant impedance type.
- The network transients are neglected by representing the network by an admittance matrix.
- The simulation is carried out in MATLAB/SIMULINK.
- PMUs are implemented in the multi-machine transient stability environment as SIMULINK models (".mdl") as well as script files (".m").

The rotor angle plots for such a small duration fault are shown in Fig. 3.10. The figure shows that generators in area 1 (G1 and G2) oscillate together against the other two generators in area 2 (G3 and G4) of the system. For this case, PMU-B1 with six inputs has been placed at Bus-9 with the arrangement as shown in Fig. 3.9.

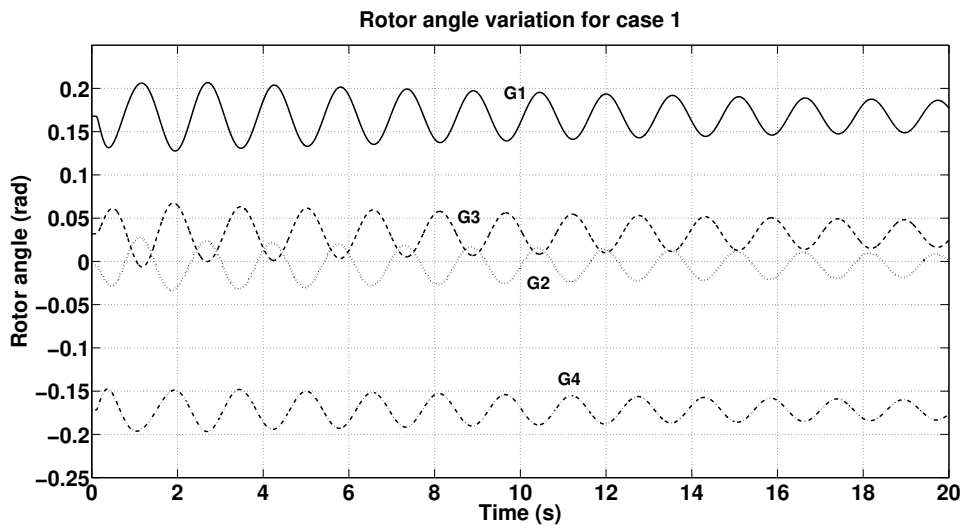


**Figure 3.10:** Rotor angle plots for case-1.

The time-domain plots for instantaneous voltage and currents used as inputs by PMU-B1 have been given in Fig. 3.11 for phase a. From Fig. 3.12 it can be clearly seen that the frequency of the voltage and current signals is different under dynamic conditions.

### 3.4.2.1 Voltage and Current TVE calculations

Due to the availability of two frequencies and ROCOFs, based on the voltage and the current signals, three compensation schemes as described previously, have been used and

TVE are computed. Effects of these compensation schemes on the power calculations are also estimated.

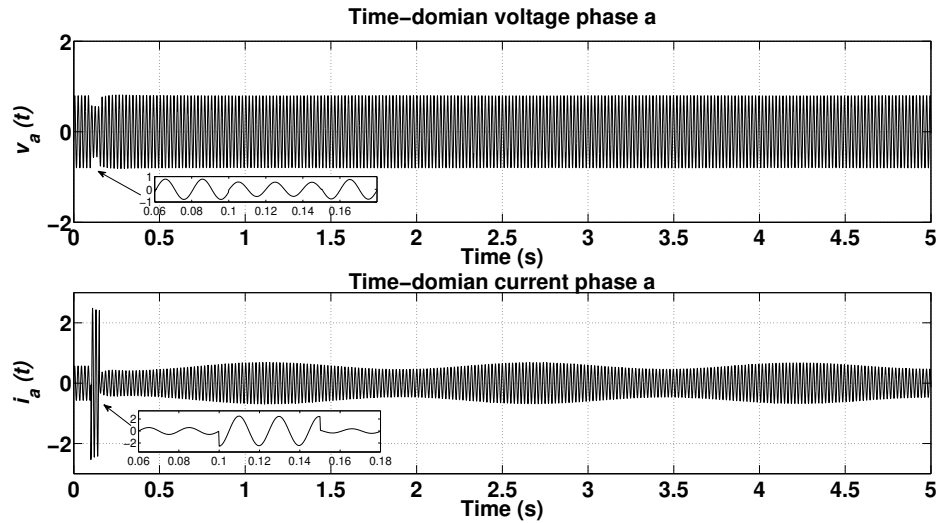


**Figure 3.11:** Time-domain plots for instantaneous voltage at bus-9 and current through line-1 for case-1.

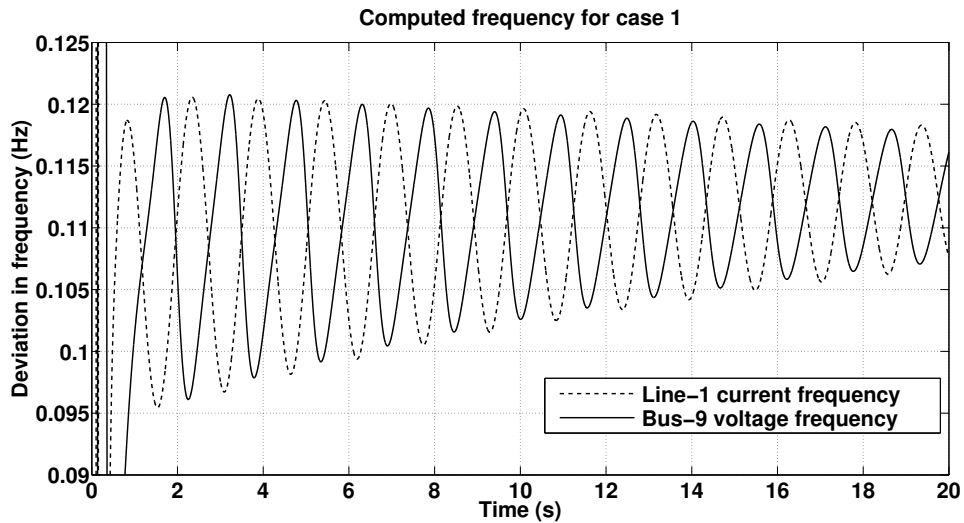


**Figure 3.12:** Frequency using voltage and current phasor for case-1.

1. **Scheme-1:** This scheme leads to lower values of voltage TVE at the cost of increased current TVE, since voltage-based frequency and ROCOF are used for magnitude



and causal phase compensation even for current phasors. The causal and non-causal TVEs for voltage and current using this scheme of compensation are given in Fig. 3.13.

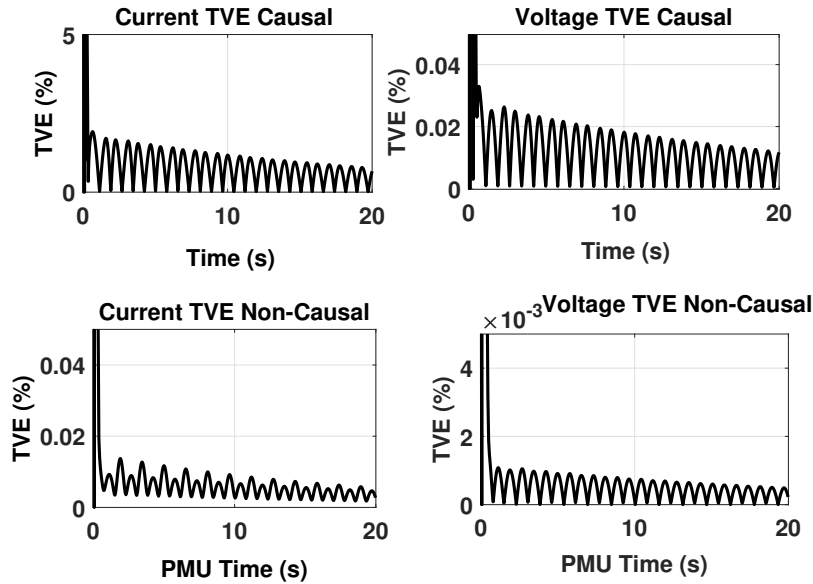


**Figure 3.13:** TVE for current and voltage at Bus-9 using Scheme-1 for case-1.

2. **Scheme-2:** This scheme of compensation leads to lower values of current TVE at the cost of increased voltage TVE, since current-based frequency and ROCOF are used for magnitude and causal phase compensation of voltage phasors. The causal and non-causal TVEs for voltage and current using this scheme of compensation are given in Fig. 3.14. Note that, the voltage TVE is nearly ten times greater than that obtained using the previous scheme (see Fig. 3.13), whereas the current TVE is more or less similar to that obtained using the previous scheme.
3. **Scheme-3:** In this scheme, since both the voltage and current based frequency and ROCOF are used, the lowest possible TVE is obtained for both the phasors, as can be seen in Fig. 3.15. The TVE obtained for the current phasor is identical to that obtained using Scheme-2, while, the TVE obtained for the voltage phasor is equal to that obtained using Scheme-1. In all three schemes, the TVEs for the voltage and current phasors are the lowest for the non-causal PMU version. With Scheme-2, the

TVE of the voltage phasor suffers to a greater extent than that of the current phasor in Scheme-1 for the causal PMU.

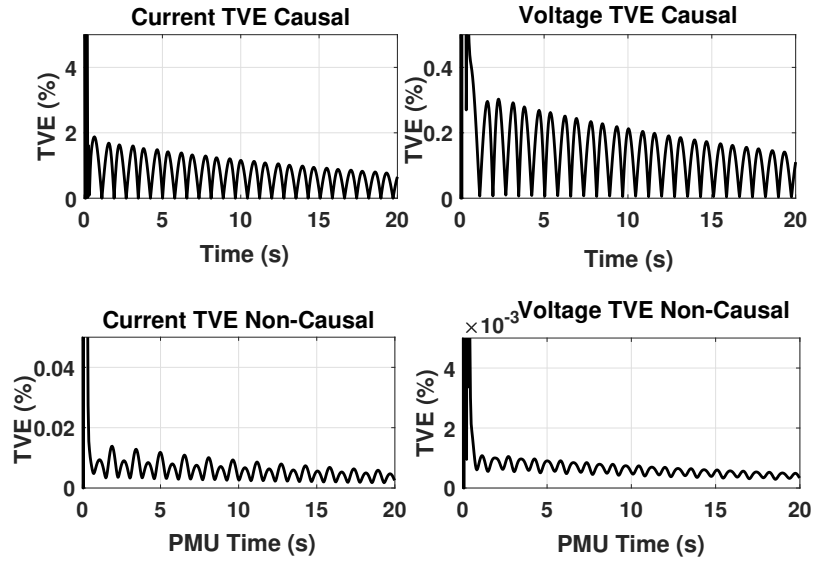


Figure 3.14: TVE for current and voltage at Bus-9 using Scheme-2 for case-1.

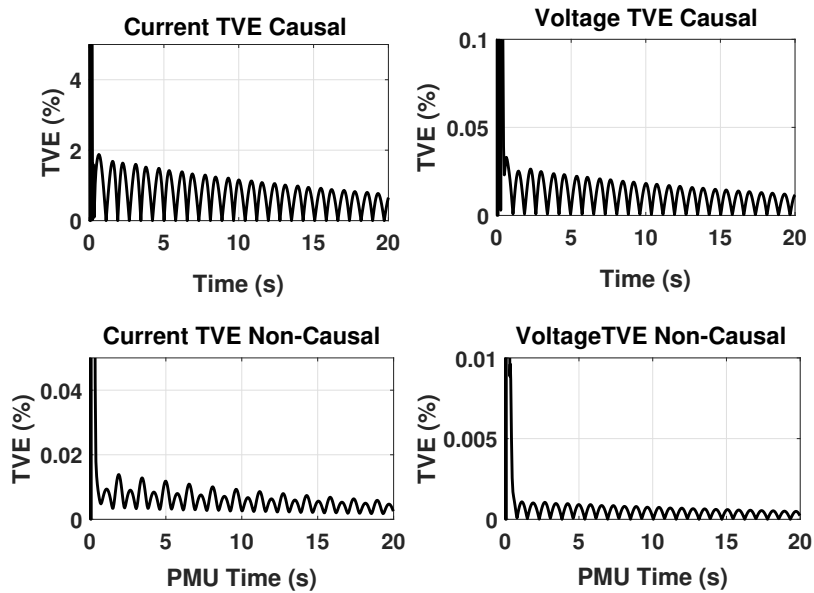
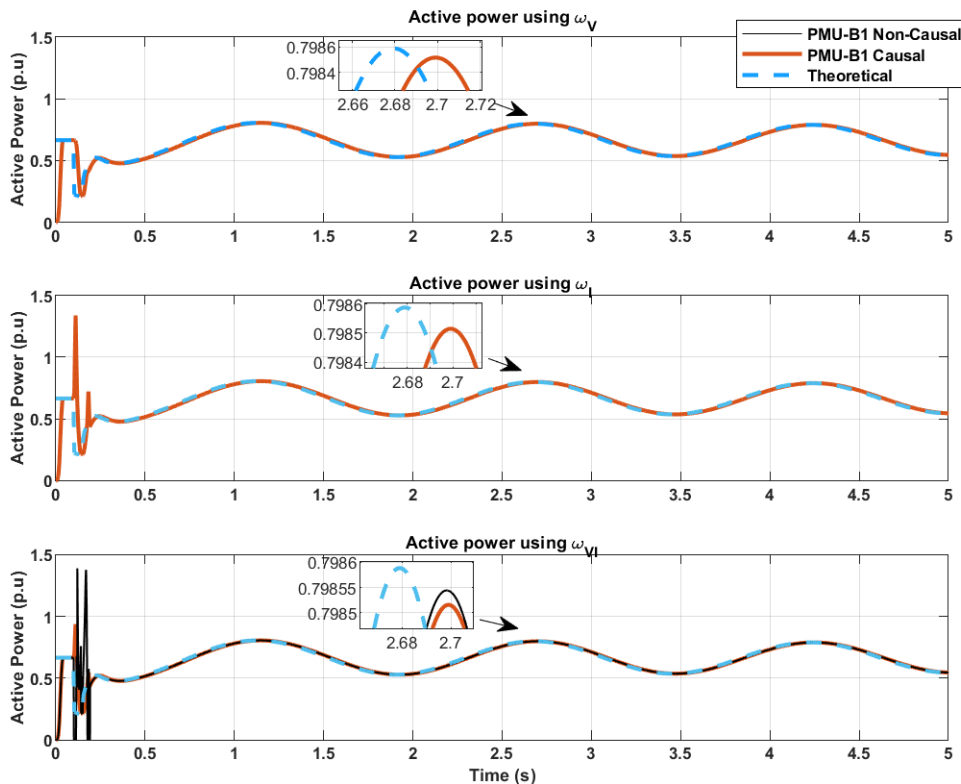


Figure 3.15: TVE for current and voltage at Bus-9 using Scheme-3 for case-1.

### 3.4.2.2 Power calculation: Small-signal stable case

Now, that both the voltage and the currents are being estimated by the PMU, the complex power can be calculated as an indirect measurement using (3.13). The active and reactive power plots obtained employing different schemes of compensation are given in Figs. 3.16 and 3.17 respectively. It can be seen in the active power plots that Schemes-1 and 2 lead to identical measurements as that of the non-causal estimates, with the computed active power lagging the theoretical by the group delay. Similarly, in case of the reactive powers as given in Fig. 3.17, Scheme-1 and Scheme-2 yield the same results as the non-causal values, since the value of  $\omega_V - \omega_I = 0$  in (3.13). However, for Scheme-3, since the value of  $\omega_V - \omega_I \neq 0$ , there is a difference in the causal and the non-causal based power estimates, with the reactive power plot showing a greater delay.



**Figure 3.16:** Active power flowing through line-1 using different schemes of compensation for case-1.

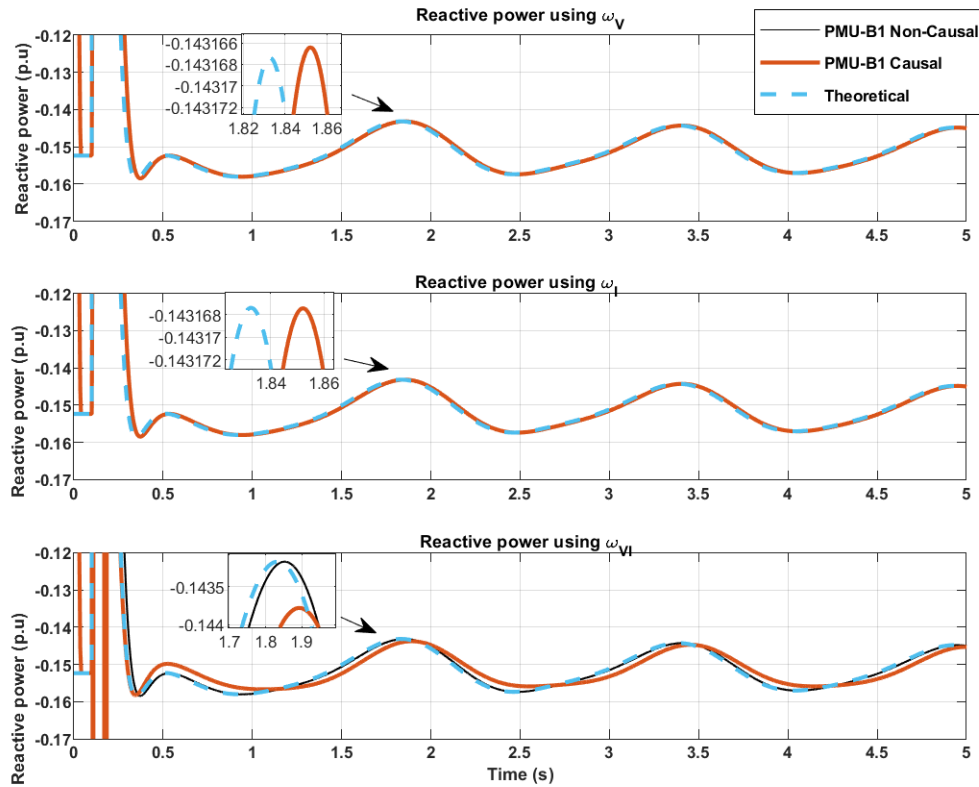


**Figure 3.17:** Reactive power flowing through line-1 using different schemes of compensation for case-1.

The per unit errors in the active and the reactive powers using scheme 1 and scheme 3 are given in Fig. 3.18. The errors using the three schemes are alike for the most part except for the causal PMU-B1 where scheme 3 is employed leading to a non-zero value of  $\omega_V - \omega_I$ . This leads to a variation in the active and the reactive power estimates which are seen to further drift from the theoretical values resulting in a higher value of error. The values of error for this case are summarized in Table. 3.16.

**Table 3.16:** Maximum error value comparison for stable Case 1

PMU type →	Causal PMU			Non-Causal PMU
Error ↓	Scheme-1	Scheme-2	Scheme-3	Scheme-1/2/3
Voltage TVE (%)	0.0263	0.31	0.0263	$1.1 \times 10^{-3}$
Current TVE (%)	1.92	1.88	1.88	0.0138
Active Power Error (p.u)	0.0123	0.0123	0.0117	0.0123
Reactive Power Error (p.u)	$7.3 \times 10^{-4}$	$7.3 \times 10^{-4}$	$2.85 \times 10^{-3}$	$7.3 \times 10^{-4}$

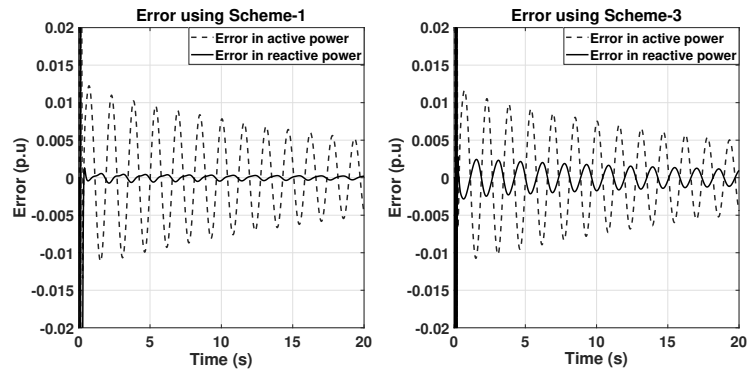


**Figure 3.18:** Error in active and reactive power flow through line-1 using Scheme-1 and Scheme-3 based compensations for case-1.

### 3.4.3 Case-2 : Small-Signal Unstable Condition

In this case study a modified 4-machine-10-bus power system is used. Two of the three lines connecting buses 9 and 10 are not functional, hence, line-1 alone serves as a connection between area 1 and area 2. With this system in place, a three-phase fault with a fault initiation time of 0.5 s and a duration of 0.05 s is applied to bus-9, (Shubhanga, 2018). The rotor angle plots for all the four generators are shown in Fig. 3.19. The rotor angle oscillations can be seen increasing with time and hence the system can be attributed as small-signal unstable.

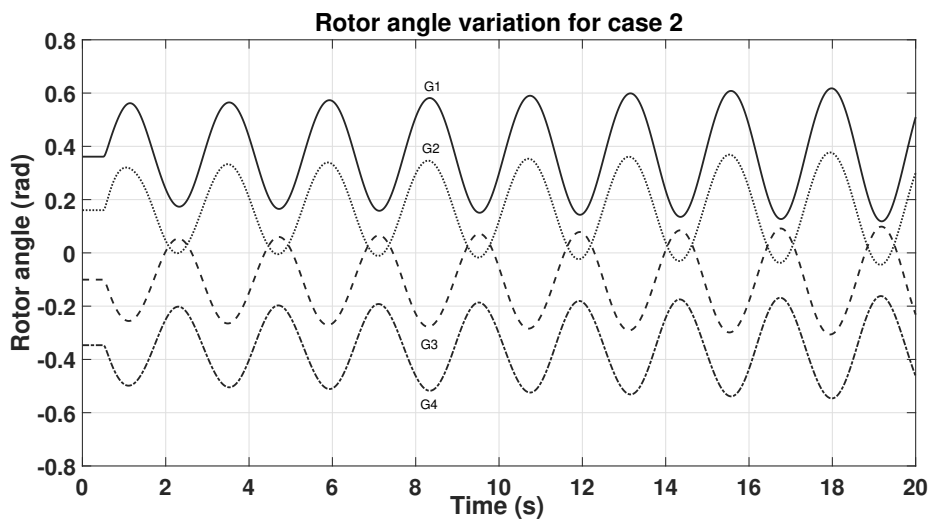


**Figure 3.19:** Rotor angle plots for case-2.

Now, for the six-input PMU as shown in Fig. 3.9 the instantaneous current and the voltage input signals for phase-a, when the system is small-signal unstable, are given in Fig. 3.20.

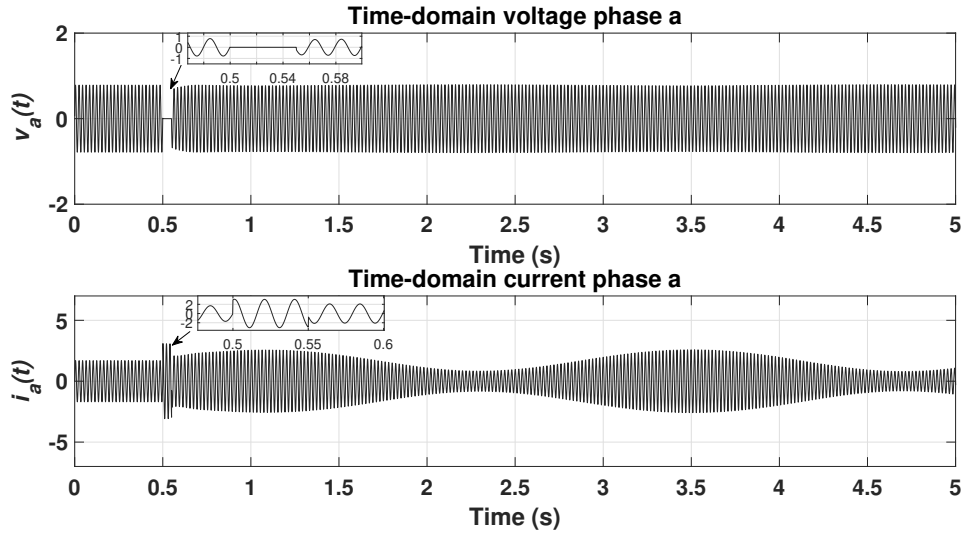


**Figure 3.20:** Instantaneous voltage for bus-9 and current through line-1 for case-2.

The bus-9 voltage frequency and the line-1 current frequency values for this case are shown in Fig. 3.21. Similar to the previous case, the voltage and the current based frequency estimates are different which effect the estimates obtained using causal PMUs.

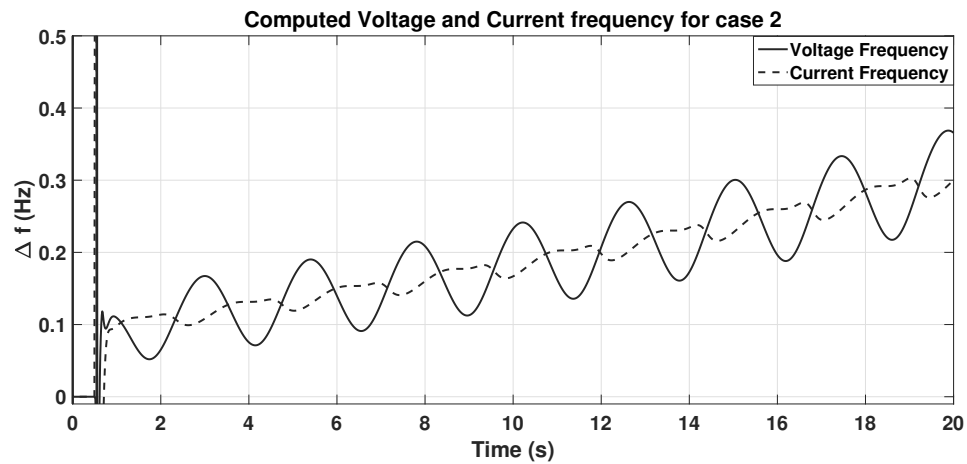


**Figure 3.21:** Current and Voltage based frequency for case-2.

### 3.4.3.1 TVE and Power Error calculations

The errors obtained using the proposed compensation schemes are summarized in Table. 3.17. The voltage TVE obtained employing Schemes-1 and 3 is similar, since the voltage based frequency and ROCOF are used for compensation in both the schemes. Whereas, while using Scheme-2 based compensation the voltage TVE is relatively higher (1.01% as compared to 0.116% ). In case of the current phasor compensation all the schemes result in similar TVE values. The current TVE values are less effected by Scheme-1 ( $\omega_V$ ) based compensation, whereas the voltage TVE values are effected to a much higher degree if Scheme-2 ( $\omega_I$ ) based compensation is used. Active power estimates obtained using all the schemes are similar, whereas reactive power obtained using Scheme-3 based compensation is slightly better than Schemes 1 and 2.

**Table 3.17:** Error value comparison for Unstable Case 2

PMU type →	Causal PMU			Non-Causal PMU
	Scheme-1	Scheme-2	Scheme-3	Scheme-1/2/3
Error↓				
Voltage TVE (%)	0.116	1.01	0.116	0.005
Current TVE (%)	4.9	4.87	4.87	0.048
Active Power Error (p.u)	0.068	0.068	0.066	0.068
Reactive Power Error (p.u)	0.033	0.033	0.011	0.033

### 3.4.3.2 A Large Disturbance Condition

This case study is performed using the same modified 4-machine 10-bus power system as used in the small-signal unstable case. A fault is applied on bus-9 with a fault initiation time of 0.5 s, but the fault duration is increased from 0.05 s to 0.1 s. The time-domain voltage for bus-9 and line-1 current for this disturbance are shown in Fig. 3.22. Due to a comparatively large fault duration, the angle separations in this case are large, hence fluctuations in the current signal are more compared to the voltage signal. The frequency estimated using the voltage and the current signal is shown in Fig. 3.23 which clearly shows high peaks in the current signal. Hence, angle as well as magnitude compensation with Scheme-2 and Scheme-3, i.e., using  $\omega_I$  and  $\omega_{VI}$  based compensation factors, fails in such scenarios. Therefore, during such large disturbance conditions only Scheme-1 i.e.,  $\omega_V$ , based compensation is feasible, due to bounded nature of the voltage frequency estimates.

The following are some of the findings from the case studies:

- The choice of schemes dominantly influences the causal PMU estimates than that of the non-causal PMUs. This is because frequency value is used only in the magnitude compensation of the non-causal phasor estimates. However, in the causal variant the magnitude as well as the angle compensations are done using the frequency and ROCOF values.

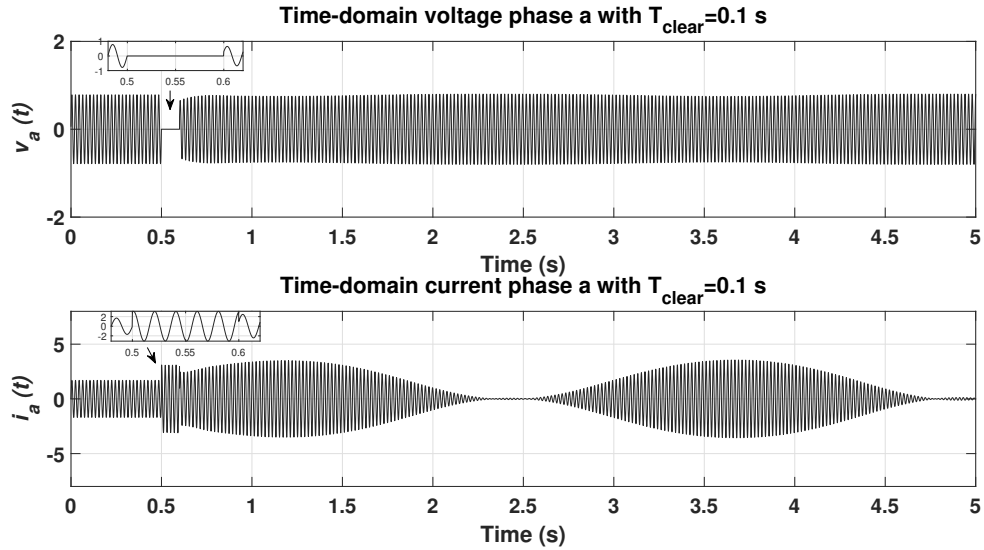


**Figure 3.22:** Instantaneous voltage for bus-9 and current through line-1 for a large disturbance.

- Accuracy of power estimates is less effected by different schemes.
- Though Scheme-3 accurately compensates the magnitude attenuation as well as the phase delays introduced by a PMU, due to erroneous estimates of current-based frequency (and ROCOF) under unstable system conditions (large disturbances), see Fig. 3.23, Scheme-1 is the only available option.
- From Tables. 3.16 and 3.17, it can also be seen that current phasors compensated using Scheme-1 ( $\omega_V$ ) suffer to a lesser extent in terms of TVE when compared to voltage phasors, if compensated using Scheme-2 ( $\omega_I$ ).
- Based on the above observations it can be stated that for system protection/control applications Scheme-1 is a reliable option. However for monitoring/measurement application, any scheme may be chosen depending on accuracy of estimates desired, taking care to see that the system is operating under normal conditions.



- For numerical relay application, where it is expected to operate in one or two cycles of the fundamental period under transient system condition, say to detect fault on a line, these compensation schemes are of little importance.
- Accurate estimation of frequency under unstable operating conditions of a power system is a real challenge. This also influences the choice of a scheme.

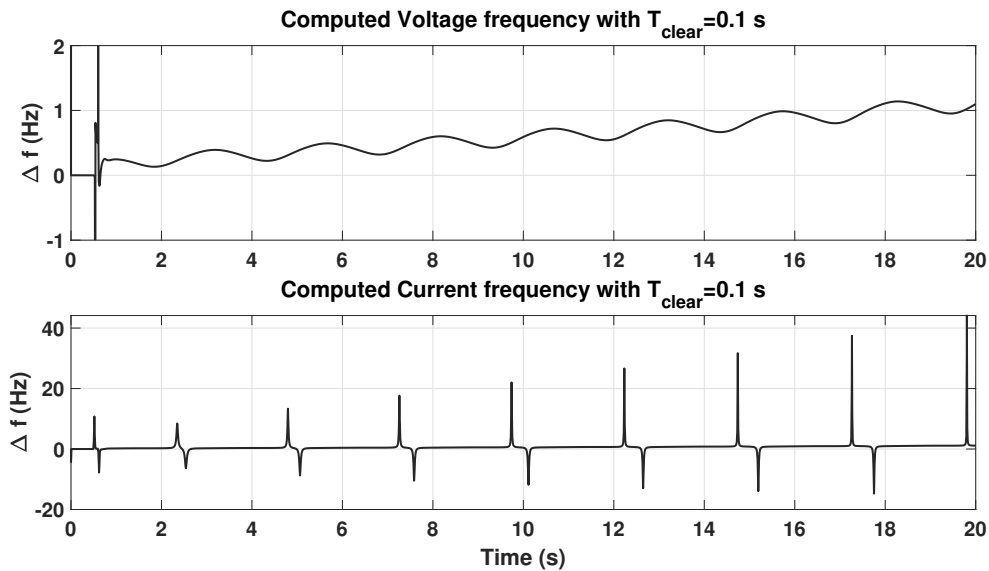


**Figure 3.23:** Frequency using voltage and current phasor for a large disturbance.

### 3.4.4 Impedance calculations

The apparent impedance ( $z_{app}$ ) as seen at a bus can be computed using the ratio of the voltage phasor at the bus and the current flowing out of the bus into the line. This can be shown as follows,

$$z_{app} = \frac{\vec{V}_c}{\vec{I}_c} = \frac{\vec{V}_{uc} \times e^{j\omega_V \Delta t N_L}}{\vec{I}_{uc} \times e^{j\omega_I \Delta t N_L}} \quad (3.17)$$

As can be seen from (3.17), if schemes 1 and 2 are employed the causal and the non-causal impedance estimates will be similar. Scheme-3 based impedance varies depending on the difference frequency component i.e.,  $(\omega_V - \omega_I)$ .

Due to the transient nature of the current frequency estimates especially during unstable scenarios only Scheme-1 based impedance plots are given here.

### 3.4.4.1 Small-signal stable case

The ratio of the bus-9 voltage phasor and the current leaving the bus-9 is computed. Both the voltage and the current phasors are obtained using the six-input PMU-B1 employing Scheme-1 based compensation. The apparent impedance plot is given in Fig. 3.24. The arrows in the plot originate from the pre-fault impedance value which is equal to  $1.3605 - 0.3115j$  and the trajectory can be clearly followed to visualize the during and the post fault impedance.

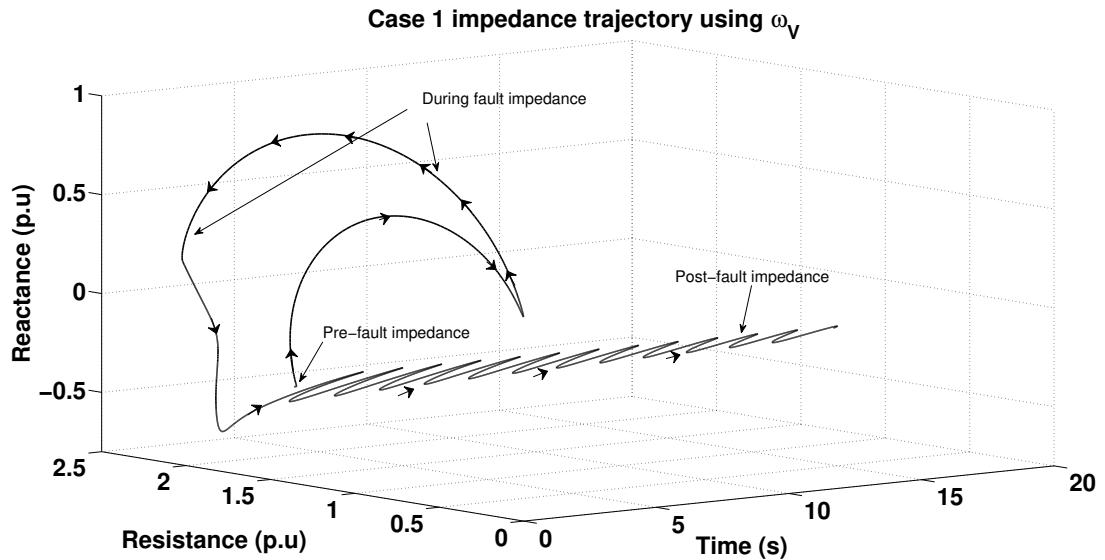


Figure 3.24: Impedance using Scheme-1 based compensation for case-1.

### 3.4.4.2 Small-signal unstable case

Impedance trajectory for this case is given in Fig. 3.25. The initial value of the impedance is  $0.4615 + 0.0392j$ , which is lower as compared to previous scenario due to the absence of line 2 and 3 from the original system given by Fig. 3.9. Since this case leads to instability the eccentricity of the impedance plot can be seen increasing with time which depicts the post fault scenario in this case. The trajectory followed by the impedance plot is again depicted using arrows originating from the pre-fault impedance values.

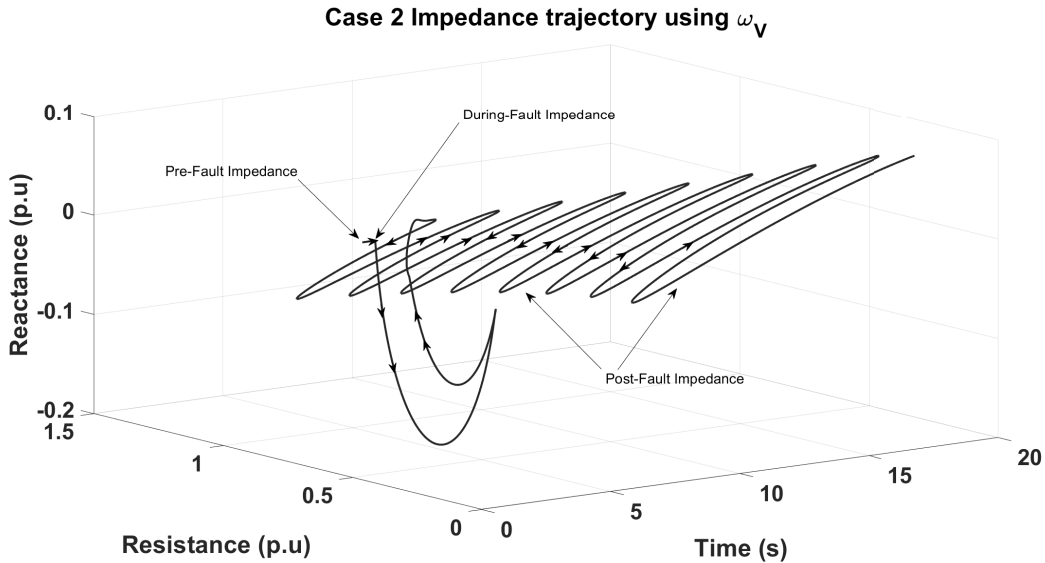


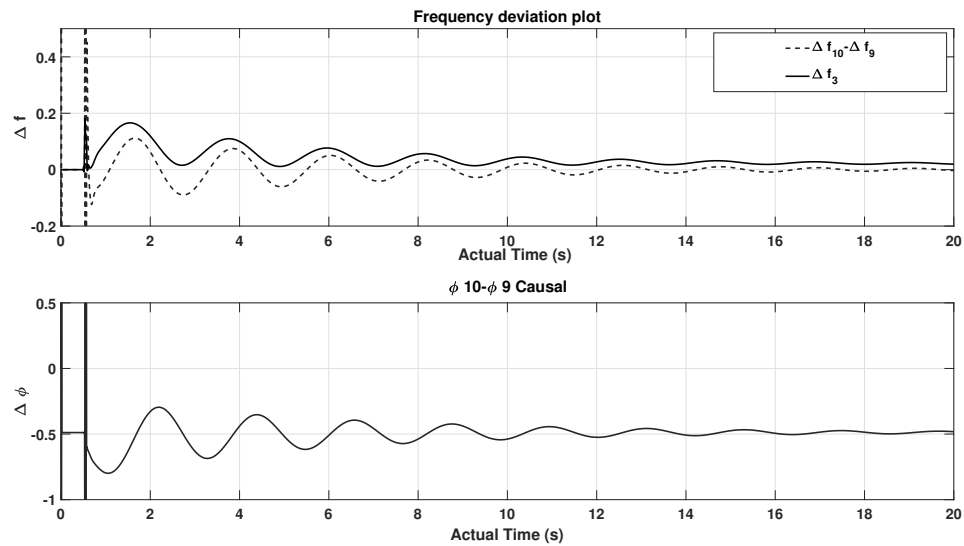
Figure 3.25: Impedance using Scheme-1 based compensation for case-2.

## 3.5 Role of Causality in Power System Stability

### 3.5.1 Local versus WAMS based frequency input to PSS

In this section the behaviour of slip with respect to center of Inertia (slip COI) of generator 3 is studied. Case-2, as given in Section 3.4.3 is used for demonstration purposes. For this study, PMU-B1 V2 (PMU-B1 Version 2) is used instead of PMU-B1. This PMU-B1 V2 is a hybrid PMU consisting of the phasor estimation module of PMU-B1 and the frequency estimation module of PMU-A, as the LS-based frequency estimation method is more accurate than the sample based method present in PMU-B1. The phasor estimation module of PMU-B1 V2 computes phasors using DFT in conjunction with a 2-cycle triangular window as in PMU-B1. The frequency and ROCOF are computed using the Least Squares based method as in PMU-A. This new PMU is placed at bus-3, feeding the computed voltage based frequency to a frequency input Power System Stabilizer (PSS) namely PMU-freq PSS installed at generator 3. Different quantities of the power system for this case are compared in Fig. 3.26.

In order to highlight the effectiveness of using WAMS based measurements rather than local measurements, frequency signals obtained via PMU-B1 V2 and PMU-D placed at buses 9 and 10, have been used as inputs to the PMU-freq PSS. It can be clearly seen from



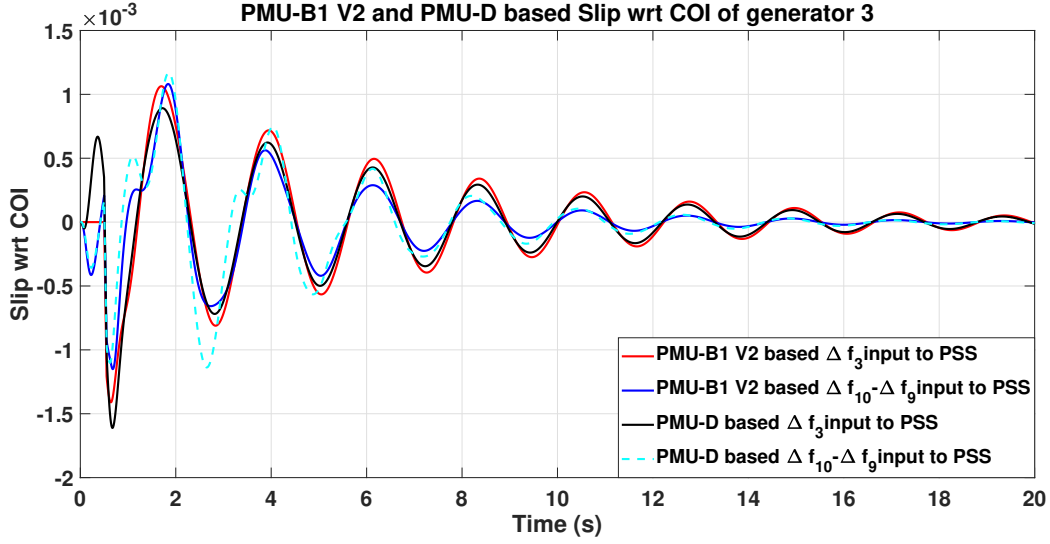
**Figure 3.26:** Frequency deviation (Hz), frequency difference and angular difference (radians) plot obtained using causal PMU-B1 V2.

Fig. 3.27, that the WAMS based signal provides excellent results in terms of oscillation damping.

The dominant modes of all the slip signals available using the Prony analysis, (Rao and Shubhanga, 2018), (Sarkar et al., 2018), (Rubeša et al., 2020) are compared in Table.3.18, along with that obtained using a slip signal PSS. Here again it can be seen that the WAMS based signal provides much better damping than local signals (0.0959 and 0.095 using WAMS input compared to 0.0596 and 0.0605 using local input for PMU-B1 V2 and PMU-D, respectively).

Comparing the damping provided by the  $\Delta f_{10} - \Delta f_9$  signal with the values obtained using slip signal based PSS, it can be inferred that the frequency based PSS if using WAMS based signals as an input outperforms the slip based PSS. It can also be observed that both the PMUs perform almost similarly.

When frequency is used as the PSS input signal it should be noted that both the causal and non-causal frequency estimates lead to identical results due to absence of compensation in the frequency computation process. However, when bus angles are used as PSS input signals the performance is quite different and it brings out the importance of the causal PMU over non-causal PMU variants more distinctly. Some aspects are shown in the following section.



**Figure 3.27:** Slip COI signal for generator 3 using local frequency ( $\Delta f_3$ ) and WAMS based frequency ( $\Delta f_{10} - \Delta f_9$ ) input to the PSS, obtained using causal PMU-B1 V2 and PMU-D.

**Table 3.18:** The Prony analysis of slip COI signals of generator 3 obtained employing different PSS input signals.

Parameters ↓	Using $\Delta f_3$		Using $\Delta f_{10} - \Delta f_9$		Using Slip signal
	PMU-B1 V2	PMU-D	PMU-B1 V2	PMU-D	
Amplitude	0.000974	0.000835	0.000917	0.0011	0.000923
Damping factor	0.0596	0.0605	0.0959	0.095	0.0646
Frequency (Hz)	0.4533	0.4561	0.4534	0.4573	0.4563
Dominant Mode	$-0.17 + 2.848j$	$-0.173 + 2.865j$	$-0.271 + 2.849j$	$-0.274 + 2.873j$	$-0.185 + 2.867j$

### 3.5.2 Angle input based PSS

The system becomes stable when the PMU-freq based PSS is employed as seen previously from the slip COI plots of generator 3, see Fig. 3.27. The stability of a system can also be visualized from the frequency as well as the bus angle difference across a line. This has been shown in Fig. 3.26, using the frequency deviations at bus 3, frequency difference between bus 9 and 10, and also using the phase angle difference between bus 9 and 10. All the plots have a decreasing oscillation trend depicting small signal stability.

From the phase angle and frequency plots in Fig. 3.26 it can be seen that the  $\Delta f_{10} - \Delta f_9$  values lead the  $\phi_{10} - \phi_9$  values, approximately by  $90^\circ$ . This inference is used in the modification of the frequency based PSS to switch to phasor angle inputs. This is predominantly

done here to monitor the behaviour of the system while using causal and non-causal inputs to the PSS, (Meng et al., 2017), since causality is not reflected in frequency signals. Since the angular difference between two buses is to be used as an input to the PSS instead of the frequency, the PMU-freq based PSS compensator needs to be redesigned to provide more lead angle which will enable the compensator to use  $\phi_{10} - \phi_9$  as an input signal.

The frequency based PSS is redesigned for angle inputs by adjusting the value of time constants  $T_1$ ,  $T_2$  and the center frequency  $f_{mpss}$  of the PSS. This is done according to the phase lead or lag to be provided by the PSS block. An overall lead angle of  $\phi_m = 70^\circ$  is chosen, and compensation is provided using two cascading blocks, with each providing a lead of  $35^\circ$ . A center frequency of 3 Hz is used. The transfer function of the angle input PSS is given in Fig. 3.28.

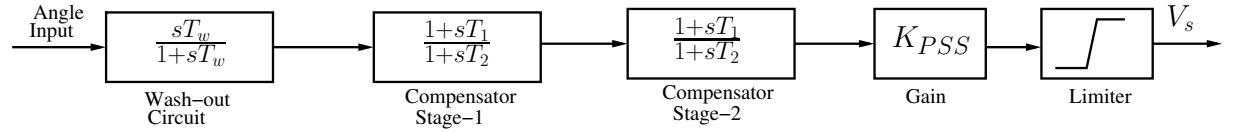


**Figure 3.28:** Transfer function representation of an angle input based PSS.

For the new lead angle,  $\phi_m = 35^\circ$ , and the chosen center frequency,  $f_{mpss} = 3$  Hz,  $T_1$  and  $T_2$  are calculated as follows,

Using

$$\sin(\phi_m) = \frac{1 - \alpha}{1 + \alpha} \quad (3.18)$$

compute  $\alpha$  as 0.2710. We also have,

$$\alpha = \frac{T_2}{T_1}$$

and

$$\omega_m = 2\pi f_{mpss} = \frac{1}{\sqrt{\alpha T_1}}$$

From the above expressions, we have  $T_1 = 0.1019$  s and  $T_2 = 0.0276$  s, and  $T_1/T_2=3.69$ .

In the PSS block, the washout time constant,  $T_w = 10$  s. The gain of the PSS,  $K_{PSS}$  is set to a preliminary value of 17 which gave adequate damping for the inter-area swing mode with the slip-signal PSS. The limiter is set to  $\pm 0.1$  pu.

Using the redesigned PSS with the new time constant values, angular difference be-

tween buses 9 and 10, in the form of  $\phi_{10} - \phi_9$  is used as input to the PSS at generator 3. The slip COI for generator 3 obtained using the causal and the non-causal angle as inputs is given in Fig. 3.29.

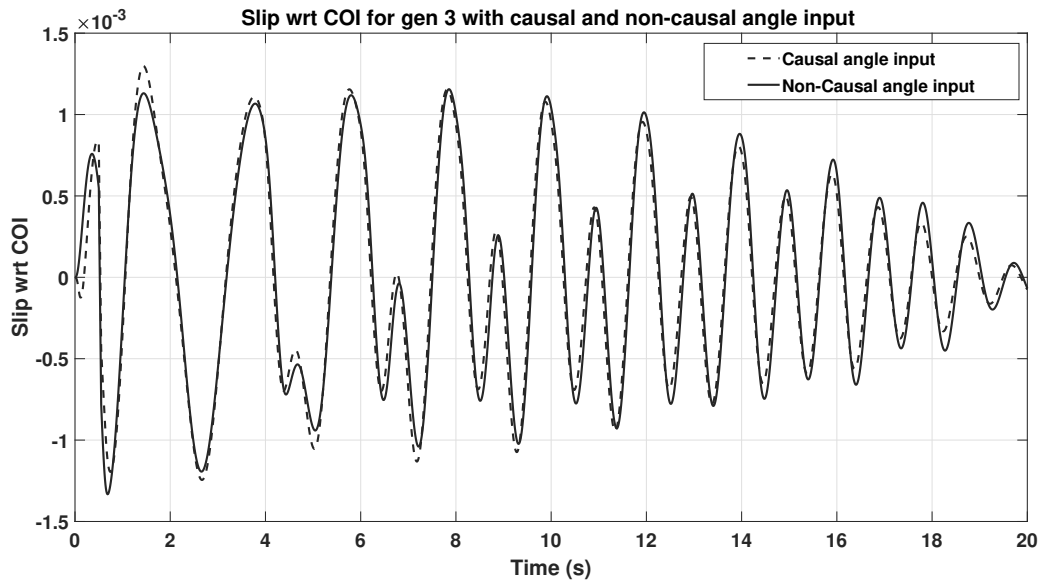


**Figure 3.29:** Slip COI for gen 3 using causal and non-causal angle input for PSS.

**Table 3.19:** List of dominant modes obtained using the Prony analysis with cascading compensators ( $\phi_m = 35^\circ$  each)

Dominant modes for slip COI signals for gen 3	
Causal angle input to PSS	Non-Causal angle input to PSS
$-0.2077 + 2.9328j$	$-0.2337 + 2.9159j$
$0.0947 + 6.3517j$	$0.0545 + 6.317j$
$-0.1197 + 3.2791j$	$-0.1434 + 3.2124j$
$-0.2976 + 8.9358j$	$-0.0425 + 5.9185j$
-	$-0.1862 + 9.2862j$
-	$-0.3772 + 8.8114j$

The dominant modes of both the slip signals obtained using the Prony analysis are listed in Table. 3.19, from which it can be seen that the damping of the local swing mode i.e., with a swing frequency of 6.3 rad/s is relatively low as compared to the inter-area mode with a swing frequency of 2.9 rad/s.

### 3.5.3 Performance evaluation using Causal and Non-Causal PSS inputs

In order to bring out the influence of group delay associated with different PMU algorithms and filters on the efficacy of control action, an artificial delay,  $t_d$ , is introduced in the signal path of the phasor estimation as shown in the Fig 3.30. In the causal variant of the PMU, this delay,  $t_d$ , is compensated through a phase angle compensation technique similar to group delay compensation. However, in case of the non-causal type, the signals are left uncompensated.

**Note :** If at all delay compensation is to be done in case of the non-causal PMU as well, it is purely an off-line process which involves time-tag shifting as stated earlier.

The delay of an actuating input signal to a PSS particularly in case of signals which are acquired using Wide Area Measurement Systems can lead to delayed control action, which can be the difference between a stable and an unstable system. To make sure that delays introduced at the phasor level of the signal do not effect the controller performance, causal phasors are preferred to non-causal estimates as PSS inputs Meng et al. (2017). Delay introduced during phasor computation stage if not taken care of can result in system instability, if the same delayed quantity is used as a PSS input. In the upcoming text this is shown as an example for an arbitrary value of  $t_d$ .

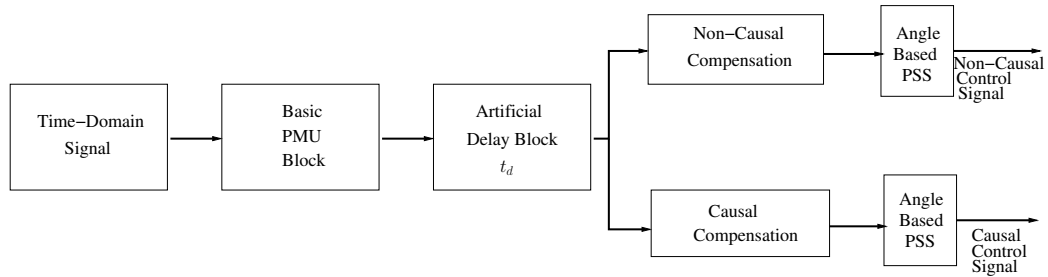


**Figure 3.30:** Methodology of introducing artificial delay at the phasor level

#### 3.5.3.1 Case Studies for Additional Delays of 0.1 s and 0.12 s.

An additional delay of 0.1 s is introduced during the phasor computation process as depicted using Fig. 3.30, and the causal and non-causal  $\phi_{10} - \phi_9$  is used as input to the angle based PSS. Since the causal based angle is compensated for the additional delay as well as



the group delay introduced by the PMU, it can be seen in Fig. 3.31 that the slip COI plot for generator 3 shows a decreasing trend with time hence leading to a stable system.

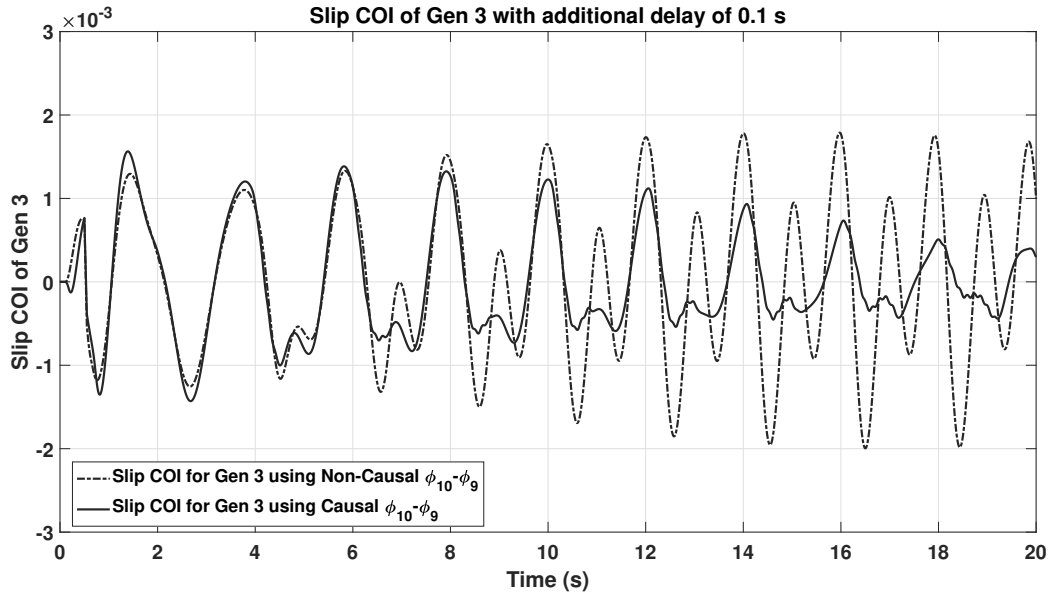


**Figure 3.31:** Comparing Slip COI of gen 3 obtained using causal compensated and non-causal inputs to PSS (additional delay  $t_d = 0.1s$ ).

**Table 3.20:** List of dominant modes for non-causal and causal based slip signals (additional delay of 0.1 s).

Dominant modes of Slip COI signal for gen 3 ( $t_d = 0.1s$ )	
Causal angle input to PSS	Non-Causal angle input to PSS
-0.1628+2.9415 $j$	0.0262+3.2832 $j$
-0.0112+3.172 $j$	-0.1775+3.05601 $j$
-0.1075+6.021 $j$	-0.2792+9.199 $j$
-0.7293+6.1042 $j$	0.1392+6.4975 $j$
-1.2201+7.8546 $j$	-0.0059+6.1843 $j$
-	-0.6524+8.9246 $j$

The same cannot be said about the non-causal input to the PSS, in which the delay is not compensated at any level, and the slip COI plot can be seen increasing with time leading to an unstable system. Slip COI shows an increasing amplitude from cycle to cycle denoting worsening of small-signal stability. The eigenvalues listed in Table. 3.20, clearly show that the usage of the angle estimates from the non-causal PMU has destabilized the 6.49 rad/s local swing mode, whereas the causal variant has stabilized the system.

Similar results are observed when  $t_d$  is increased to 0.12 s. This can be seen in Fig. 3.32 where again the causal input to the PSS is seen to stabilize the system whereas the non-causal input does not. List of all the dominant modes pertaining to the slip COI signals of generator 3, using delayed causal and non-causal inputs are given in Table. 3.21.

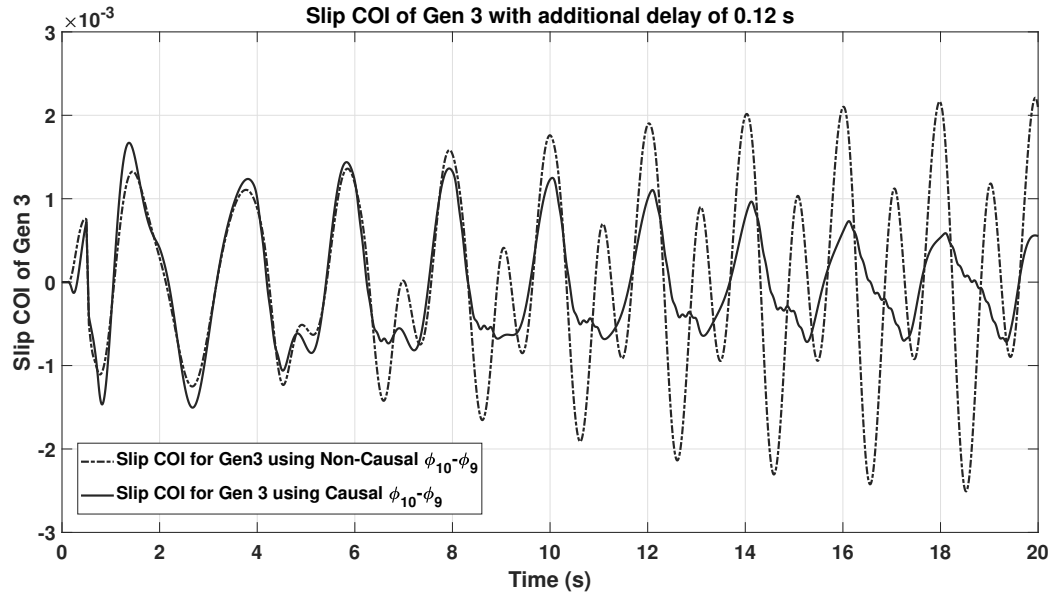


**Figure 3.32:** Comparing Slip COI of gen 3 obtained using causal compensated and non-causal inputs to PSS (additional delay  $t_d = 0.12s$ ).

**Table 3.21:** List of dominant modes for non-causal and causal based slip signals (additional delay of 0.12 s).

Dominant modes of Slip COI signal for gen 3 ( $t_d = 0.12s$ )	
Causal angle input to PSS	Non-Causal angle input to PSS
-0.0124+3.1228 $j$	0.0703+6.4272 $j$
-0.166+2.9516 $j$	-0.0818+6.1575 $j$
-0.0098+6.3585 $j$	0.0264+3.2144 $j$
-0.1584+5.8423 $j$	-0.4243+5.816 $j$
-	-0.2457+3.005 $j$

### 3.6 Summary of the Presented Work

In this chapter, an integrated PMU architecture is presented to provide both causal and non-causal phasors using a single module. Such a realization is not only useful to understand

causality in PMUs, but also suitable for implementing multiple applications. The causal phasor with the low latency could be used for on-line WAMPAC applications, whereas the non-causal phasor could be used for off-line applications.

Studies carried out and observations made in this chapter are enumerated below:

1. Several PMU algorithms are implemented based on the integrated PMU architecture, thus providing causal as well as non-causal estimates. This implementation is accomplished for each PMU in the MATLAB environment using both SIMULINK models (".mdl") as well as script files (".m").
2. Compliance with protection class or measurement class accuracy limits for causal and non-causal outputs provided by the integrated architecture is also verified as per the IEEE standard for synchrophasor measurements.
3. For all the PMUs, TVE values calculated using the non-causal phasor samples are lower compared to their causal counterparts. This is especially true for signals with amplitude modulations and varying ROCOF.
4. It is observed that an appropriate scheme of compensation provided in the integrated architecture results in better phasor estimates with lower TVE values. These accurate estimates can prove helpful if they are to be used for protection and control functions.
5. Case studies are carried out using a six-input PMU based on this integrated architecture. PMU-B1 is applied to a 4-machine 10-bus power system with three-phase bus voltages and three-phase line currents as inputs.
6. Problems arising during dynamic conditions, especially when there is a difference between the voltage phasor-based frequency and the current phasor-based frequency, are discussed. Different schemes of compensation are introduced in case of causal PMUs. Effect of these compensation schemes on power and impedance calculations during dynamic conditions is investigated.
7. From the case studies it is shown that Scheme-1, (which uses voltage phasor based frequency signal) provides a reliable compensation for causal PMUs.
8. To demonstrate the utility of PMUs for feedback control applications, a causal PMU along with its non-causal version built on the same module, has been designed to provide angle input to a PSS on a generator. The results demonstrated that only

causal PMU has the ability to stabilize the small-signal unstable power system due to its real-time delay compensation features.

9. From the analysis, it is clear that using the PMU-time vector, by a mere time-tag shifting, the non-causal estimates can be obtained easily along with the causal estimates from a given PMU algorithm. Hence, realization of measurement/monitoring functions using non-causal estimates and protection/control functions employing causal estimates, can be carried out on the same platform. This is the advantage of the proposed integrated approach, compared to the existing approach, where causal and non-causal PMUs are treated as two separate units.

Accurate frequency and ROCOF estimation in case of the integrated PMU architecture is important due to their use in causal compensation. It is also clearly evident that even for positive sequence signals, the static model based PMU algorithms provide poor frequency as well as phasor estimates when inter-harmonics are present in the input signal. The quality of the estimates degrades even further, in case single-phase signals are employed. Therefore, in the next chapter, a reconstruction-based technique is proposed which provides compliant frequency estimates during dynamic as well as inter-harmonic signal conditions. Further, the application of frequency and ROCOF estimates obtained via the reconstruction-based method for mode estimation is also demonstrated.



---

## Chapter 4

# FREQUENCY ESTIMATION USING SIGNAL RECONSTRUCTION APPROACH

### 4.1 INTRODUCTION

Frequency is one of the most critical health indicators of a highly interconnected grid, (Kirkham et al., 2018). The regulation and monitoring of frequency is therefore necessary to achieve generation-load balance while maintaining synchronous operation. Several power system protection and control applications require precise and quick frequency estimates computed using PMUs. For M-class compliance, a PMU must provide frequency values (among others) which are very accurate as dictated by the latest synchrophasor standard, especially while dealing with signals consisting of inter-harmonic frequencies. Such a compliance is hard to achieve, as inter-harmonic frequencies, unlike integral harmonic frequencies cannot be easily filtered out using DFT or its variants. Several PMU algorithms such as PMU-D, E and F, satisfy the M-class standard requirements when 3-phase-based positive-sequence estimates are used, but fail when tested on a single-phase basis. Compliance for such a test is usually achieved by the use of additional filters in the phasor computing module or by using long windows, such as in Castello et al. (2014). In case of positive-sequence estimates, the task is simplified by a natural elimination of the second harmonic component which is not the case with single-phase signals (Phadke and Thorp, 2010), (Xia and Liu, 2009).

Therefore, in this chapter, a signal-reconstruction-based approach has been described to estimate the frequency and ROCOF for a single-phase system. This approach retains the simplicity and the computationally light nature of the conventional algorithms such as the DFT and yet provides estimates which are compatible with the latest standards even for single-phase signals. This method reduces the frequency errors during the presence of frequency excursions, inter-harmonics and modulation conditions, without the need for complicated estimation techniques. It is mathematically shown that even during off-nominal conditions the frequency information in case of reconstructed signals is preserved. From the reconstructed time-domain signals, the frequency is estimated using the Convolution Average Filter (CAF) based method (Li et al., 2019) and a single-phase demodulation technique employing Hilbert filter (HFD). Accuracy of the reconstruction-based approach is verified through test signals recommended by IEEE Std (2018), as well as by using signals obtained from practical power systems and simulation based studies. The frequency estimates obtained using the reconstruction-based methods are compared with PMU-based frequency estimates obtained for single-phase signals. The output frequency and ROCOF signals are also used for mode identification using the Prony method. Effect of window length, window starting point and data frame rate on the mode estimation capabilities of the Prony algorithm is also demonstrated.

## **4.2 Signal Reconstruction Using DFT-Based Phasors**

Reconstructed signals provide valuable information to operators at control centers for diagnosing, flagging and clearing network disturbances (Salunkhe and Kulkarni , 2015), (Das and Sidhu, 2013). Signals can be accurately retrieved back from their phasor estimates if the original input-signal frequency matches with the nominal frequency of the system. Although, due to the dynamic nature of the power system, nominal and signal frequencies always differ leading to inaccurate phasor estimates. The reconstruction of the time-domain signals during such off-nominal conditions is explored in the following section.

### **4.2.1 Off-nominal frequency performance**

Consider a sinusoidally varying signal,  $x_a(t)$  with nominal frequency  $\omega_0 = 2\pi f_0$  and phase angle  $\phi$  as

$$x_a(t) = X \cos(\omega_0 t + \phi) \quad (4.1)$$

where  $X$  denotes the maximum amplitude of the signal.

If the above continuous time signal is sampled at a sampling frequency pertaining to the nominal value given by  $(f_0N)$  Hz, we get, (Proakis and Manolakis, 2007)

$$x_a(n\Delta t) = X \cos(\omega_0 n\Delta t + \phi) \quad (4.2)$$

where  $n = 0, 1, 2, 3, \dots$  and  $\Delta t = 1/(f_0N)$  where  $N$  denotes the number of samples per cycle of the fundamental frequency in Hz.

Now considering an off-nominal frequency signal,

$$x_a(n\Delta t) = X \cos(\omega n\Delta t + \phi) \quad (4.3)$$

where  $\omega = 2\pi f$  with  $f = f_0 + \Delta f$ , and  $\Delta f$  is the frequency deviation in Hz.

Phasors calculated for (4.3) using the DFT method are accurate, whenever the signal frequency is exactly equal to the nominal frequency ( $f = f_0$ ). This scenario is seldom seen in practical power systems, where frequency is always around the nominal value but never exactly equal to it. Therefore, the quality of the phasor estimates severely degrades as the frequency deviation ( $\Delta f$ ), increases. It is known that the spectral leakage is primarily the reason for erroneous behaviour of the DFT algorithm (Belega and Petri, 2013). It is caused due to the presence of non-integer periods in an observation window and results in a leakage of energy into the adjacent frequency bins of the DFT spectrum. Another reason for the poor performance of the conventional DFT algorithm is its static nature, which assumes that the amplitude and the phase of the time-domain signal are time-invariant in an observation window. This assumption results in the unreliable performance of the DFT algorithm especially during dynamic conditions, when the properties of the signal are fast changing.

The effect of frequency excursions on the performance of the DFT algorithm are explored in Phadke and Thorp (2010). For the time-domain signal given in (4.3), the theoretical value of the off-nominal phasor obtained using the DFT algorithm is given as follows,

$$\bar{X}_{est} = [P\bar{X}e^{jr(\omega-\omega_0)\Delta t} + Q\bar{X}^*e^{-jr(\omega+\omega_0)\Delta t}] \quad (4.4)$$

where

$$P = \frac{\sin(\Delta t \frac{(\omega-\omega_0)}{2} N) e^{j(\frac{\omega-\omega_0}{2})\Delta t(N-1)}}{N \sin(\Delta t (\frac{\omega-\omega_0}{2}))} \quad (4.5)$$



$$Q = \frac{\sin(\Delta t \frac{(\omega + \omega_0)}{2} N) e^{-j(\frac{(\omega + \omega_0)}{2} \Delta t (N-1))}}{N \sin(\Delta t \frac{(\omega + \omega_0)}{2})} \quad (4.6)$$

Note that  $P$  and  $Q$  are complex numbers, and their values for different frequencies, and a given  $N$  can be obtained as in Phadke and Thorp (2010). For example, for a 52 Hz signal, the value of  $\bar{P}$  is  $0.9973704 \angle 7.128^\circ$  and the value of  $\bar{Q}$  is  $0.01957 \angle -3.528^\circ$  for  $N = 100$  and for  $f_0 = 50$  Hz.

From (4.4), by separating real and imaginary parts we have,

$$\begin{aligned} Re(\bar{X}_{est}) = a_1(t) &= |P||X| \cos(\angle P + \phi + \omega t - \omega_0 t) \\ &+ |Q||X| \cos(\angle Q - \phi - \omega t - \omega_0 t) \end{aligned} \quad (4.7)$$

$$\begin{aligned} Im(\bar{X}_{est}) = b_1(t) &= |P||X| \sin(\angle P + \phi + \omega t - \omega_0 t) \\ &+ |Q||X| \sin(\angle Q - \phi - \omega t - \omega_0 t) \end{aligned} \quad (4.8)$$

The above expressions reveal that the real and imaginary parts of the off-nominal phasor contain sum  $(\omega + \omega_0)$  and difference  $(\omega - \omega_0)$  frequency components. Now, we can find the magnitude of  $\bar{X}_{est}$  as

$$|X_{est}| = \sqrt{(a_1(t))^2 + (b_1(t))^2} \quad (4.9)$$

$$\begin{aligned} |X_{est}| &= \left( |P|^2 |X|^2 + |Q|^2 |X|^2 \right. \\ &\left. + 2|P||Q||X|^2 (\cos(\angle P - \angle Q + 2(\phi + \omega t))) \right)^{1/2} \end{aligned} \quad (4.10)$$

and the phase angle can be given as,

$$\phi_{est} = \tan^{-1} \left( \frac{Im(\bar{X}_{est})}{Re(\bar{X}_{est})} \right) = \tan^{-1} \left( \frac{b_1(t)}{a_1(t)} \right) \quad (4.11)$$

It should be clear that the magnitude of the off-nominal phasor estimate contains only one frequency component given by  $2\omega$  which is present neither in the real part nor in the imaginary part. The same double frequency component is present in the phase angle signals.

### 4.2.2 Time- Domain Signal Reconstruction Procedure

After obtaining the phasor estimates using DFT we can easily reconstruct the time-domain signal using the real and the imaginary parts of the phasor, as given in IEEE Std (2018),

$$x_{aR}(t) = x_r(t) - x_i(t) \quad (4.12)$$

where  $x_{aR}(t)$  is the reconstructed signal and

$$x_r(t) = a_1(t) \times \cos(\omega_0 t), \quad x_i(t) = b_1(t) \times \sin(\omega_0 t) \quad (4.13)$$

Using (4.7) and (4.8) in (4.13), we get,

$$x_r(t) =$$

$$\begin{aligned} &= \frac{|P||X|}{2} (\cos(\angle P + \phi + \omega t - 2\omega_0 t) + \cos(\angle P + \phi + \omega t)) \\ &+ \frac{|Q||X|}{2} (\cos(\angle Q - \phi - \omega t - 2\omega_0 t) + \cos(\angle Q - \phi - \omega t)) \end{aligned} \quad (4.14)$$

and  $x_i(t) =$

$$\begin{aligned} &= \frac{|P||X|}{2} (\cos(\angle P + \phi + \omega t - 2\omega_0 t) - \cos(\angle P + \phi + \omega t)) \\ &+ \frac{|Q||X|}{2} (\cos(\angle Q - \phi - \omega t - 2\omega_0 t) - \cos(\angle Q - \phi - \omega t)) \end{aligned} \quad (4.15)$$

From (4.14) and (4.15) we can write,

$$x_{aR}(t) = |P||X| (\cos(\angle P + \phi + \omega t)) + |Q||X| (\cos(\angle Q - \phi - \omega t)) \quad (4.16)$$

Using sum of cosines relationships, (4.16) can be further simplified as,

$$x_{aR}(t) = X_{Rm} \times \cos(\omega t + \beta) \quad (4.17)$$

where

$$X_{Rm} = \sqrt{|P|^2|X|^2 + |Q|^2|X|^2 + 2|P||Q||X|^2 \cos(\angle P + \angle Q)} \quad (4.18)$$

and

$$\beta = \tan^{-1} \left( \frac{|P||X| \sin(\angle P + \phi) + |Q||X| \sin(-\angle Q + \phi)}{|P||X| \cos(\angle P + \phi) + |Q||X| \cos(-\angle Q + \phi)} \right)$$

Note that the reconstructed signal contains a single frequency component given by  $\omega$ , which is the frequency of the original signal. The value of  $\cos(\angle P + \angle Q)$  in (4.18) tends to 1 and -1 for positive and negative frequency deviations, respectively. This observation helps us to rewrite (4.18) approximately as,

$$X_{Rm} = |P||X| \pm |Q||X| \quad (4.19)$$

Note that the maximum amplitude of the time-domain signal is  $|P||X| + |Q||X|$  for a positive frequency deviation and for a negative frequency deviation, it is  $|P||X| - |Q||X|$ . Assuming  $\bar{X} = 1\angle 0^\circ$  and using (4.12), the reconstructed time-domain signals for 52 and 48 Hz off-nominal frequencies are given by

$$x_{aR}(t)_{52} = 1.01689 \sin(2\pi 52t + 7.0588^\circ) \quad (4.20)$$

and

$$x_{aR}(t)_{48} = 0.9771109 \sin(2\pi 48t - 7.0531^\circ) \quad (4.21)$$

The above expressions clearly show that only the magnitude and phase errors are introduced in the reconstructed signals when the phasor samples obtained using DFT at off-nominal frequencies are employed for the reconstruction. Based on this observation, it is felt that these time-domain signals can provide better frequency estimates in comparison to phase angle-based frequency measurements.

## 4.3 Frequency Measurement

### 4.3.1 Reconstruction based frequency estimation

Most Phasor Measurement Units advocate the use of three phases for phasor, frequency and ROCOF computation since the use of positive-sequence quantities drastically reduces the magnitude of the second harmonic component and hence leads to low TVE, frequency and ROCOF error values. Several PMU algorithms despite working with positive-sequence phasors, fail to provide estimates (especially frequency) which are M-class compatible, while using rudimentary algorithms. In case of single-phase measurements, where the error due to the double harmonic components is not naturally eliminated, PMU compliance is very hard to achieve. This is even more true for frequency and ROCOF estimates where

the phase angle error obtained via single-phase PMUs is accentuated due to derivative calculations. Therefore, instead of evaluating the time-derivative of the phase angles of the phasors to obtain frequency, it is better to estimate the frequency directly using the time-domain signals which can be reconstructed from their phasor samples as given by (4.12). Here, our focus will be on frequency estimation by two methods namely, the Convolution Averaging Filter (CAF) method, (Li et al., 2019) and the Hilbert Filter-Demodulation (HFD) method (Hao et al., 2007), (Ansari, 1985). An overview of the frequency estimation based on reconstruction methods are given in Fig. 4.1. In case the PMU block is malfunctioning or out of service, the input time domain signal  $x_a(t)$  can be directly fed to the CAF or HFD modules for frequency estimation using switches provided in Fig. 4.1.

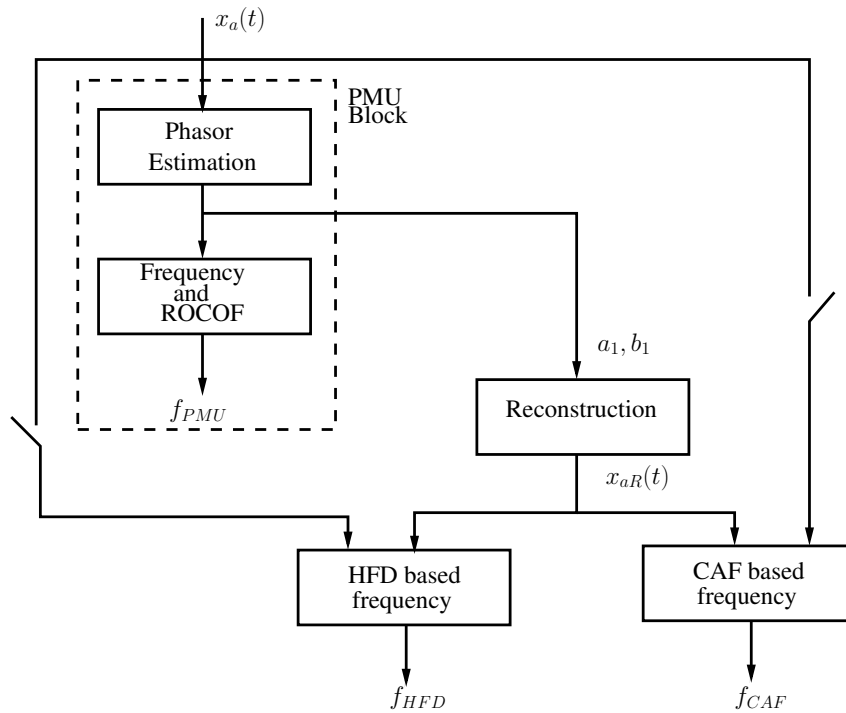


**Figure 4.1:** A functional block diagram for frequency measurement using reconstructed signals.

An important advantage of this approach is that the signal reconstruction module can be integrated with any existing PMU block as an additional module. This avoids the requirement of extra hardware setup. In the PMU block any PMU algorithm can be used for phasor calculations. It also enables the reconstruction-based methods to utilize the filtering

abilities of the PMU algorithms chosen. In the following lines, CAF and HFD methods are discussed.

#### 4.3.1.1 Convolution Averaging Filter (CAF)-based Method

The cosine wave given in (4.3) can be rewritten as follows,

$$x_a(n\Delta t) = \frac{1}{2}(\bar{X}e^{j\omega n\Delta t} + \bar{X}^*e^{-j\omega n\Delta t}) \quad (4.22)$$

Now, defining a reference signal to be used for shifting the above original signal

$$r(n) = e^{j\omega_0 n\Delta t} \quad (4.23)$$

The shifted version of the originally sampled signal can be obtained by multiplying (4.22) by (4.23)

$$x_s(n\Delta t) = \frac{1}{2}(\bar{X}e^{j(\omega+\omega_0)n\Delta t} + \bar{X}^*e^{-j(\omega-\omega_0)n\Delta t}) \quad (4.24)$$

The frequency components of the original signal have been shifted from  $\omega$  to  $\omega - \omega_0$  and  $\omega + \omega_0$ .

Using a simple moving average filter of length  $M_L$  given as

$$h_{av}(m) = \begin{cases} 1/M_L, & m = 0, 1, 2, \dots, M_L - 1. \\ 0, & \text{otherwise.} \end{cases} \quad (4.25)$$

suppression of the high frequency component in (4.24) can be achieved. The frequency response of the filter is given as (Li et al., 2019),

$$H(e^{j\omega}) = \frac{\sin(\omega M_L/2)}{M_L \sin(\omega/2)} e^{-j\omega(M_L-1)/2} \quad (4.26)$$

The magnitude response of the above given moving average filter is  $\approx 1$  for frequencies,  $\omega_0 - \omega$ , and 0 for  $\omega_0 + \omega$ . This results in preservation of only the  $\omega_0 - \omega$  component. Since  $\omega_0 - \omega$  for practical cases, is close to zero, enhanced suppression of  $\omega_0 + \omega$  component can be achieved by using a convolution average filter (CAF), which is given as, (Li et al., 2019)

$$h_p(n) = \underbrace{h_{av}(m) * \dots * h_{av}(m)}_p \quad (4.27)$$

where  $*$  denotes the convolution operator and  $p$  is the number of the convolution filters. The final filtered signal can be given by

$$x_f(n\Delta t) = x_s(n\Delta t) * h_p(n) \quad (4.28)$$

The frequency deviation is computed as (Li et al., 2019),

$$\Delta f = \frac{(\arg(x_f(n_2)) - \arg(x_f(n_1)))M_L f_0}{2\pi(n_2 - n_1)} \quad (4.29)$$

where  $x_f(n_1)$  and  $x_f(n_2)$  are two samples of  $x_f(n\Delta t)$ .

The steps involved in frequency computation using the CAF-method are listed as follows:

1. Signal  $x_{aR}(t)$  is reconstructed using its phasor samples, as given in (4.12).
2. The reconstructed signal is multiplied by a reference signal  $r(n)$ , depicted by (4.23).
3. The resultant signal given by  $x_s(n\Delta t)$  in (4.24) is complex in nature. The real and imaginary parts of this signal are filtered using  $p$  averaging filters implemented in convolution as shown in (4.27).
4. Frequency deviation is finally estimated using the arguments of the filtered signal  $x_f(n\Delta t)$  separated by  $n_2 - n_1$  samples, as given in (4.29).

#### **4.3.1.2 Hilbert Filter-Demodulation (HFD) method**

Complex demodulation of a waveform is an effective technique used for frequency estimation in three-phase balanced systems (Akke, 1997). A balanced set of time-domain voltages or currents is first transformed using the Clarke's transformation matrix to  $0\alpha\beta$ -frame.

At the  $n^{th}$  sampling interval, the output of the Clarke's transformation matrix is represented in a complex form given by

$$V(n\Delta t) = V_\alpha + jV_\beta \quad (4.30)$$

This can also be represented as

$$V(n\Delta t) = |V_1|e^{j(\omega n\Delta t + \phi)} \quad (4.31)$$

where  $|V_1|$  represents the magnitude of the signal,  $\omega$  denotes the frequency and  $\phi$  represents the phase of the complex voltage  $V(n\Delta t)$ . Now, (4.31) is multiplied by  $e^{-j\omega_0 n\Delta t}$  to yield a signal with no double frequency components which has the form

$$V_2(n\Delta t) = |V_1| \left[ \cos((\omega - \omega_0)n\Delta t + \phi) + j \sin((\omega - \omega_0)n\Delta t + \phi) \right] \quad (4.32)$$

Using  $V_2(n\Delta t)$ , an intermediate variable is obtained as

$$V_3(n\Delta t) = V_2(n\Delta t)V_2((n-1)\Delta t)^* = |V_1|^2 e^{j(\omega - \omega_0)n\Delta t} \quad (4.33)$$

where  $*$  denotes the complex conjugate operator.

Now, the frequency of the system is obtained as

$$f = f_0 + \frac{f_s}{2\pi} \times \tan^{-1} \left[ \frac{\text{Im}[V_3(n\Delta t)]}{\text{Re}[V_3(n\Delta t)]} \right] \quad (4.34)$$

where,  $f_s = 1/\Delta t$  denotes the sampling frequency.

Here, unlike in the three-phase demodulation technique only one phase which is reconstructed using PMU phasor samples is used. The steps involved are given as follows:

1. Reconstructed signal  $x_{aR}(t)$  is computed using phasor samples of the original input signal  $x_a(t)$ .
2. The reconstructed signal is passed through a pair of IIR based Hilbert filters. Such a pair is used to obtain an in-phase,  $V_\alpha$  and a phase-quadrature,  $V_\beta$  component for the signal  $x_{aR}(t)$ .
3. The in-phase and phase quadrature components are used to represent the signal in a complex form as given in (4.30).
4. The complex signal is multiplied by  $e^{-j\omega_0 n\Delta t}$  to obtain  $V_2(n\Delta t)$ , shown in (4.32).
5. Frequency is finally obtained using (4.34) employing an intermediate variable  $V_3(n\Delta t)$ , constructed using (4.33).
6. The frequency output obtained using (4.34) is filtered using a Hamming window based Finite Impulse Response (FIR) filter before the rate-of-change of frequency

(ROCOF) is computed.

The  $z$  domain transfer functions for the two Hilbert filters are given by (4.35) and (4.36). Coefficients of the filters as computed following the procedure given in (Hao et al., 2007) and (Ansari, 1985), are given as  $a_1 = 0.144, a_3 = -0.9776, a_5 = 1.8158, a_7 = -1, b_2 = -1.8158, b_4 = 0.9776, b_6 = -0.144$  and  $p_0 = 0.024482, p_2 = -0.44410, p_4 = 1.31688, p_6 = -1, q_2 = -1.31688, q_4 = 0.44410, q_6 = -0.0244800$ . These coefficients are calculated for a 50-Hz nominal system with a sampling frequency of 2000 Hz. The frequency range of the Hilbert IIR filter is from 40 to 960 Hz with passband and stopband ripple attenuation ( $\delta_p$  and  $\delta_s$ ) equal to 0.0001.

$$HF_1(z) = \frac{a_1 z^{-1} + a_3 z^{-3} + a_5 z^{-5} + a_7 z^{-7}}{1 + b_2 z^{-2} + b_4 z^{-4} + b_6 z^{-6}} \quad (4.35)$$

$$HF_2(z) = \frac{p_0 + p_2 z^{-2} + p_4 z^{-4} + p_6 z^{-6}}{1 + q_2 z^{-2} + q_4 z^{-4} + q_6 z^{-6}} \quad (4.36)$$

The IIR based Hilbert filter pair can be designed for any sampling frequency. The order of the filter increases with the increase in the sampling rate (for example, for a 5000 Hz sampling frequency,  $HF_1(z)$  and  $HF_2(z)$  have an order of 10 and 9, respectively), hence, increasing the computational burden.

### 4.3.2 ROCOF Computation

The rate-of-change of frequency for the reconstructed signals is computed using the least squares approach given in (Zhan et al., 2016), (Zhan and Liu, 2014). The frequency,  $f$  obtained using the previously given methods (HFD and CAF) is approximated using a second order polynomial, given as follows,

$$f(i) = F_{R1} + F_{R2} \left( i - \frac{(L_{RF} + 1)}{2} \right) (f_{step} \Delta t) + F_{R3} \left( i - \frac{(L_{RF} + 1)}{2} \right)^2 (f_{step} \Delta t)^2 \quad (4.37)$$

or

$$[f] = M_{rf} [F_{RF}] \quad (4.38)$$



where  $[F_{RF}] = [F_{R1}, F_{R2}, F_{R3}]$  and  $M_{rf}$  can be calculated as,

$$M_{rf}(i, j) = \left(i - \frac{(L_{RF} + 1)}{2}\right) \times f_{step} \times \Delta t)^{(j-1)} \quad (4.39)$$

where  $i = 1, 2, \dots, L_{RF}$  and  $j = 1, 2, 3$ .

$L_{RF}$  is the number of samples used for ROCOF computation and  $f_{step}$  is the step size used in the frequency window. The coefficients of the frequency polynomial given in (4.37) can be calculated as,

$$[F_{RF}] = (M'_{rf}M_{rf})^{-1}M'_{rf}[f] \quad (4.40)$$

Finally, the rate-of-change of frequency is given by

$$ROCOF = |R \times [f]| \quad (4.41)$$

where,  $R$  is the second row of the matrix  $(M'_{rf}M_{rf})^{-1}M'_{rf}$  and  $[f] = [f(1), f(2 \times f_{step}) \dots f(L_{RF} \times f_{step})]'$ .

## 4.4 Latency Computation

The frequency output from the Hilbert filter is subjected to FIR filtering for smoothing. The order of the FIR filter ( $N_{od}$ ) is chosen according to the level of accuracy desired keeping in mind the latency requirements. The latency associated with the filtered estimates can be calculated as (Meng et al., 2017),

$$\tau_f = (N_{od}/2) \times \Delta t \quad (4.42)$$

The IIR-based Hilbert Filtering process itself imparts a delay of 0.007 s (which is around 14 samples for the chosen sampling rate of 2 kHz) around the frequency range which is of interest in power system studies. Hence, the total latency involved in the frequency computation due to the HFD method is given by,

$$\tau_h = \tau_f + 0.007s \quad (4.43)$$

In this chapter,  $N_{od}$  is fixed at 52, which results in a total latency,  $\tau_h$  of 0.02 s for a 2 kHz sampling frequency.

The delay involved with the CAF method is greater than the HFD method due to the

convolution of multiple moving average filters. The latency associated with frequency estimates obtained using CAF method is given as

$$\tau_c = \frac{(p(M_L - 1) + 1)}{2} \Delta t + \frac{(n_2 - n_1)}{2} \Delta t \quad (4.44)$$

where,  $p$  is the number of averaging filters used and  $n_2 - n_1$  represents the window length used for frequency estimation. In this report  $p$  is chosen to be 8, and  $M_L = 40$ . The window length,  $n_2 - n_1$  is chosen to be 40 samples. This results in a total latency of 0.089 s for a sampling rate of 2 kHz.

For rate-of-change of frequency, the latency  $\tau_{rf}$  is calculated as follows,

$$\tau_{rf} = \frac{(L_{RF} \times f_{step})}{2} \Delta t \quad (4.45)$$

$L_{RF}$  is chosen to be 15 and  $f_{step}$  is set to 6. It results in a latency of 0.0225 s for 2 kHz sampling rate. It should be noted that the total latency associated with the frequency and ROCOF estimates consists of latency involved in the phasor computing process as well. All the involved latency's are compensated in error calculations so as to align the computed and the theoretical measurements.

## **4.5 Testing of the Reconstruction Method Using IEEE Standard Signals**

In this section some IEEE standard based tests have been carried out to verify the accuracy of the developed methods. It should be noted that all tests have been carried out using single-phase signals only. The output phasor is used to reconstruct back the time-domain signal which is then used for frequency estimation as shown in Fig. 4.1. Three frequencies are obtained and compared. The one using the PMU inherent frequency estimation method is labelled as  $f_{PMU}$ . The frequencies obtained using the reconstruction methods namely, the CAF method and the HFD method are labelled as  $f_{CAF}$  and  $f_{HFD}$ , respectively. The results obtained using the reconstruction based methods are compared against some popular PMU algorithms available in the current literature, given in Table. 2.5, these are listed as follows:

1. PMU-1 (P-class) (Phadke and Thorp, 2010): Using One-cycle Discrete Fourier Transform with LS-based method for frequency and ROCOF computation.

2. PMU-2 (P-class) (IEEE Std, 2018): It is suggested by the IEEE standard with time-derivative based frequency and ROCOF computation.
3. PMU-3 (M-class) (Zhan and Liu, 2014): Using Improved Weighted Least Squares based Taylor Fourier transform for phasor estimation and a polynomial approximation based Least Squares approach for frequency and ROCOF estimation.
4. PMU-4 (M-class) (IEEE Std, 2018): Based on the IEEE-M Class filter. Correction term for magnitude attenuation for this PMU is provided in Gurusinghe et al. (2014). Frequency and ROCOF for this PMU are computed using methods given in Zhan and Liu (2014).
5. PMU-5 (P-class) (Belega and Petri, 2013): This PMU employs a Hanning window based interpolated DFT algorithm. Frequency and ROCOF is computed using the method given in Zhan and Liu (2014).

For each of the above listed PMU algorithms, only the phasor estimates are used to reconstruct the signal. Once the signal is reconstructed in time-domain, the frequency is obtained using the HFD and CAF-based methods and the ROCOF is evaluated using (4.41). The nominal frequency for these tests is 50 Hz and a sampling rate of 2 kHz is chosen.

#### **4.5.1 Off-Nominal Frequency Test**

The time-domain signal used as an input to the PMU for this test is given as follows,

$$x(t) = X_m \cos(2\pi(f_0 + \Delta f)t + \phi) \quad (4.46)$$

This test is performed for both P and M class PMUs. The static frequency deviation i.e.,  $\Delta f$  for P-class testing is capped at  $\pm 2$  Hz, whereas for M-class PMUs the limit is extended to  $\pm 5$  Hz, (IEEE Std, 2018). The errors in frequency estimation obtained using the reconstruction based method are compared against those obtained using different PMUs. The results are given in Table. 4.1 where compliant estimates are shown using grey colour.

1. It is seen that PMU-1, PMU-2 and PMU-5 frequency estimation algorithms perform poorly in terms of single phase frequency estimation. The error values surpass the 5 mHz limit set by IEEE Std (2018). On the other hand reconstruction-based frequency

estimates obtained from the same PMUs vastly outperform the inherent PMU algorithms. This is especially true in case of algorithms which utilize static model based methods for phasor and frequency computation (such as PMU-1, 2, 4, 5).

2. The errors obtained via reconstruction methods are seen to comply with both P as well as M class PMU limits.
3. In case of PMU-3, the inherent frequency estimation algorithm provides frequency estimates which are comparable to those obtained using both the reconstruction based methods.

**Table 4.1:** Frequency error for static off-nominal signals

Error	FE (Hz) (0.005 Hz)					
	±2 Hz			±5 Hz		
$\Delta f_{sig}$	PMU	HFD	CAF	PMU	HFD	CAF
PMU-1	0.23	1.44e-4	8.2e-5	0.99	1.32e-4	7.7e-4
PMU-2	0.04	8.2e-5	7e-7	0.25	6e-4	7e-5
PMU-3	2.5e-6	7.8e-5	7e-7	7.8e-7	1.5e-4	7.3e-5
PMU-4	7.7e-4	7.8e-5	7e-7	4.2e-5	1.5 e-4	7.3e-5
PMU-5	0.003	6.2e-5	7e-7	9.1e-4	0.0012	7.6e-5

The rate-of-change of frequency error (RFE) estimates obtained using all the methods are provided in Table. 4.2.

**Table 4.2:** ROCOF Error for static off-nominal signals

Error	RFE (Hz/s) (0.1 Hz/s)					
	±2 Hz			±5 Hz		
$\Delta f_{sig}$	PMU	HFD	CAF	PMU	HFD	CAF
PMU-1	53.4	0.0016	9.3e-4	24.1	0.0016	0.0092
PMU-2	26.5	4.57 e-4	3.9e-6	173	0.007	8.1e-4
PMU-3	1.42e-5	4.4e-4	3.9e-6	8e-6	0.0017	8.5 e-4
PMU-4	0.0048	4.4e-4	3.9e-6	4.3e-4	0.0017	8.5e-4
PMU-5	0.035	5.6e-4	7.5e-6	0.083	0.016	9.6e-4

1. Due to the presence of the second harmonic component in the single-phase frequency estimates, RFE obtained using the inherent PMU algorithms for the static model based approaches (PMU-1, 2, 4, 5) is amplified due to the differential relation between the frequency and ROCOF.

2. Reconstruction-based frequency paves way for relatively better ROCOF estimation in case of static models especially for PMU-1 and PMU-2, due to the absence of the second harmonic frequency component in the frequency estimates.
3. While using reconstruction-based approaches the CAF-based method offers better accuracy than the HFD-based methods.

### **4.5.2 Inter-harmonic test**

This test is recommended only for M-class PMU compliance verification, as per the updated IEEE standard (IEEE Std, 2018). The time-domain test signal consisting of an out-of-band frequency is depicted as follows,

$$x(t) = X_m \cos(2\pi f_b t) + X_{ih} \cos(2\pi f_{ih} t) \quad (4.47)$$

where  $X_{ih} = 10\% \times X_m$ ,  $f_b$  is known as the base frequency which is the frequency of the fundamental component and  $f_{ih}$  is the frequency of the inter-harmonic component. For a certain reporting rate of  $F_{rr}$  frames per second (fps), the base frequency is varied between

$$f_b = f_0 \pm (0.1 \times F_{rr}/2) \quad (4.48)$$

Further, the range and the frequency of the inter-harmonics added to the base signal depend on the reporting rate chosen by the PMU operator as given in (4.49).

$$f_{ih} = f_0 \pm F_{rr}/2 \quad (4.49)$$

In this paper a reporting rate of 50 fps is chosen, hence the base frequency is set to 47.5 Hz, 50 Hz and 52.5 Hz (as can be calculated using (4.48)) whereas the inter-harmonic frequencies are set to 10 Hz, 25 Hz, 75 Hz and 100 Hz, for example  $x(t) = \cos(2\pi 47.5t) + 0.1 \cos(2\pi 10t)$  is one such signal.

The frequency error estimates for the inter-harmonic test obtained using different PMUs as well as the reconstruction-based methods are provided in Table. 4.3.

1. It can be seen that even though PMU-1, PMU-2 and PMU-5 are not intended for M-class application the reconstruction-based frequency estimates obtained especially using the CAF method are very accurate.

2. The FE values for all the PMUs are well within the 0.01 Hz limit (IEEE Std, 2018) when obtained using the reconstruction method employing CAF. Thus an addition of a reconstruction-based frequency calculation block to an existing P-class PMU, extends its utility even for M-class range.
3. PMU-3 and PMU-4 which are intended for M-class compliance as per, (Zhan and Liu, 2014), (IEEE Std, 2018), fail to provide accurate frequency estimates when employed on a *single-phase* basis whereas if reconstruction-based methods are used accurate frequency estimates can be obtained.
4. HFD-based method also reduces the FE values for PMU-1 and PMU-2. By designing the FIR filter appropriately, desired accuracy can be achieved in the frequency estimates.

As per the standard, the ROCOF error limits have been suspended for this test.

**Table 4.3:** Frequency Error for inter-harmonic test ( $F_{rr} = 50$  fps)

Frequency Error (Hz) (0.01 Hz)					
$f_m \rightarrow$		10	25	75	100
$f_{base} \rightarrow$		47.5/50/52.5	47.5/50/52.5	47.5/50/52.5	47.5/50/52.5
PMU-1	PMU	2.7/2.7/3.2	3.1/3.2/3.9	2.6/2.2/2	0.3/7.1e-12/0.09
	HFD	0.55/0.52/0.49	1.2/1.3/1.3	1.2/1.1/1.1	1.5e-4/9.3e-5/3.4e-5
	CAF	2.9e-4/1.7e-4/1.9e-4	0.0026/2.2e-13/0.0025	0.0024/2.1e-13/0.0023	1.3e-4/2.6e-13/1.7e-6
PMU-2	PMU	0.41/0.37/0.45	1.26/1.42/1.48	1.33/1.08/1.13	0.063/1.1e-10/0.062
	HFD	0.17/0.14/0.12	0.82/0.82/0.82	0.8/0.77/0.75	1.1e-4/3.2e-5/1.7e-5
	CAF	1.3e-4/5.3e-5/1.2e-4	0.0034/0.0057/0.0055	0.0053/0.0054/0.0028	2.1e-6/7.4e-13/1.8e-6
PMU-3	PMU	0.011/0.013/0.013	0.32/0.24/0.15	0.15/0.24/0.32	8.2e-5/2.8e-12/7.7e-5
	HFD	0.062/0.058/0.054	0.82/0.85/0.87	0.88/0.86/0.83	9.2e-5/3.2e-5/6.6e-6
	CAF	2.8e-5/2.2e-5/2.1e-5	0.0063/0.006/0.0063	0.0063/0.0061/0.0063	2.2e-6/7.4e-13/1.8e-6
PMU-4	PMU	6.5e-4/0.0011/0.0011	0.09/0.053/0.017	0.016/0.053/0.09	2.3e-4/7.5e-4/7.1e-4
	HFD	0.0017/0.0015/0.0014	0.35/0.36/0.37	0.37/0.36/0.35	3e-4/2.6e-4/2.7e-4
	CAF	2.9e-6/5.7e-7/2.3e-6	0.0028/0.0026/0.0027	0.0027/0.0026/0.0028	2.3e-6/6.4e-13/1.9e-6
PMU-5	PMU	0.048/0.043/0.041	1.47/1.63/1.8	1.79/1.63/1.48	0.001/6.7e-4/0.0038
	HFD	0.076/0.075/0.07	1.8/2/2.32	2.41/2.1/1.72	0.0023/0.0016/0.002
	CAF	5.1e-4/1.4e-4/1.3e-4	0.009/0.0012/8e-4	9.7e-4/0.0012/0.009	2.3e-6/2.7e-13/1.9e-6

### 4.5.3 Bandwidth Compliance Test

Here to demonstrate the frequency estimation capabilities of the reconstruction based methods during dynamic conditions, only the phase modulation test is performed. The time-domain signal is phase modulated using a modulation factor  $k_a = 0.1$  p.u, and a modulation frequency  $f_m = 2$  Hz for P-class compliance and  $f_m = 5$  Hz for M-class compliance, (IEEE

Std, 2018). The test signal is given by,

$$x_a(t) = \cos(\omega_0 t + k_a \times \cos(2\pi f_m t - \pi)) \quad (4.50)$$

The frequency errors for both P and M-class compliance are given in Table. 4.4.

**Table 4.4:** Frequency error for phase modulation test ( $k_a = 0.1$ ).

Error	FE (Hz) (0.3 Hz)					
	2 Hz			5 Hz		
$f_m$						
Freq Method	PMU	HFD	CAF	PMU	HFD	CAF
PMU-1	0.016	1.2e-3	5.5e-3	0.06	0.015	0.08
PMU-2	4.1e-3	1.45e-3	6.3e-3	0.03	0.022	0.09
PMU-3	1.6e-3	4.8e-4	5.4e-3	0.026	7.7e-3	0.078
PMU-4	4.6e-3	2.55e-3	7.1e-3	0.058	0.036	0.1
PMU-5	0.023	0.021	0.019	0.24	0.24	0.19

1. It can be seen that the reconstruction based methods, especially the HFD method, outperforms the inherent PMU algorithm for both P and M class measurements.
2. This observation is true even when compared to the recent state-of-the-art frequency estimation techniques given in PMU-3.
3. The RFE values for this test are presented in Table. 4.5. In case of ROCOF signals, the errors obtained using the phasor based methods increase especially in case of PMUs employing static model based algorithms such as PMU-1, PMU-2.
4. However, the HFD-based method offers good accuracy even compared to the CAF-method in most of the cases.

**Table 4.5:** ROCOF error for phase modulation test ( $k_a = 0.1$ ).

Error	RFE (Hz/s) (14 Hz/s)					
	2 Hz			5 Hz		
$f_m$						
Freq Method	PMU	HFD	CAF	PMU	HFD	CAF
PMU-1	3.7	0.034	0.09	12	1.17	3.1
PMU-2	2.5	0.042	0.1	15.4	1.44	3.5
PMU-3	0.044	0.03	0.09	1.54	1.03	3.09
PMU-4	0.068	0.05	0.11	2.44	1.8	3.8
PMU-5	0.26	0.25	0.23	6.6	6.82	5.2

#### 4.5.4 Step in Phase test

This particular test is performed to monitor the phase jump performance of various PMU algorithms. The time-domain signal used for this test is given as follows,

$$x(t) = X_m \times \cos(2\pi f_0 t + k_a u(t)) \quad (4.51)$$

where  $k_a = \pi/18$  rad is the phase step value and  $u(t)$  denotes the step function.

The concerned parameters for this test are the response times for the various error parameters such as the Total Vector Error (TVE), FE and RFE. Response time is defined as the time required by an error parameter to return to values within the set limits and stay within those limits whenever a step is induced, (IEEE Std, 2018). The response time values for frequency and ROCOF obtained using the PMU and the reconstruction-based methods are given in Table. 4.6.

**Table 4.6:** Response time for FE and RFE

PMU↓	Response time for FE (s)			Response time for RFE (s)		
	PMU	HFD	CAF	PMU	HFD	CAF
PMU-1	0.046	0.065	0.124	0.046	0.093	0.162
PMU-2	0.041	0.057	0.12	0.041	0.096	0.16
PMU-3	0.11	0.091	0.105	0.141	0.129	0.142
PMU-4	0.09	0.07	0.125	0.128	0.107	0.164
PMU-5	0.087	0.087	0.15	0.119	0.11	0.18

1. It is seen that the response time values obtained using all the methods are well within the 0.28 s ( $14/f_0$  or  $14/F_{rr}$  whichever is greater) limit required for M-class compliance. Although, the response times for the reconstruction-based methods (CAF and HFD) are greater than the PMU based methods, all the values are well within the required standard limits.
2. In comparison to the CAF-method the HFD-based method offers response time values very close to the PMU-based methods.

**Note:** In this chapter the lengths for the filters used in the frequency computation process are selected such that they comply with the response time requirements for M-class PMUs for the step test and simultaneously meet the frequency error requirements of the inter-harmonic test.



## 4.6 Case Studies Using a 4-Machine Power System

The described frequency estimation methods are applied on a typical 4-machine 10-bus power system as shown in Fig. 4.2. Different faults which excite power system rotor oscillations or power swing, are simulated. A description of the 4-machine 10-bus system and the method employed for obtaining the required signals is given below:

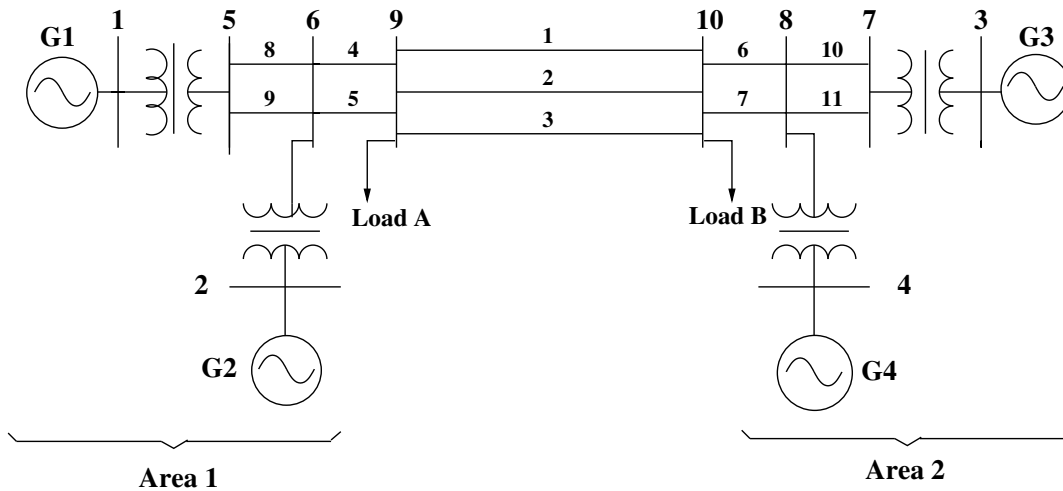


Figure 4.2: A 4-machine 10-bus power system

1. Generators are modeled pertaining to the 2.2 model.
2. The network is assumed to be in quasi-sinusoidal steady-state. The calculated bus voltages/line currents are transformed from the synchronous-frame to  $abc$ -frame (i.e., from  $DQ$  to  $abc$ ) using the inverse KRON's transformation.
3. From the three-phase signals obtained using the transformation, only *phase-a* signal is used in Fig. 4.1. The phasor samples are computed using PMU-1, 2 and then reconstruction is performed. The reconstructed signal is used for frequency and RO-COF estimation.

### 4.6.1 Case-1: Small-Signal Oscillatory Performance

For this case study, all generators are enabled with a single-time constant static exciter and the load is modelled as constant impedance type. A three-phase fault is applied at bus 9 and no line is tripped. The time of fault is 0.5 s and the fault is cleared after 0.05 s (Shubhanga,

2018). Here, phase-a voltage at bus-1 is fed to the PMU block. The frequency deviations obtained using PMU-1 and the reconstruction-based methods are shown in Fig. 4.3 for a duration of 5 s.

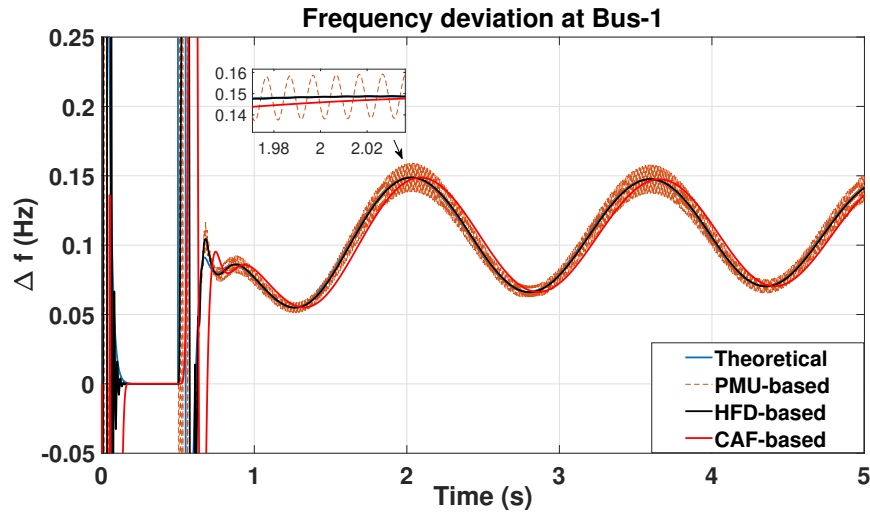


**Figure 4.3:** Frequency measurements for Case-1 using PMU-1.

An oscillation frequency of 0.65 Hz can be verified from the frequency plots which represents the inter-area swing mode. It is clearly visible from the figure that the PMU-1 based frequency estimate consists of a second harmonic component due to the dynamic nature of the voltage signal used for frequency estimation. On the other hand, HFD and the CAF methods provide estimates which are relatively free from such harmonics, hence result in low frequency error values as can be seen from Fig. 4.4. Similarly, the ROCOF estimates for bus-1 provided by PMU-1 and the reconstruction-based methods are given in Fig. 4.5. The ROCOF errors are given in Fig. 4.6. For PMU-1, the errors in the ROCOF estimates are amplified compared to the frequency error values due to the differential relation between the frequency and ROCOF estimates.

It should be noted that in conventional power systems electromechanical oscillation (swing) frequencies lie in the range of 0.2 and 2 Hz, (Kundur, 1994), (Padiyar, 2008), which are relatively small when compared to the 5 Hz modulation frequencies employed for M-class testing. Hence, the reconstruction-based methods effectively measure the frequency and ROCOF values as is demonstrated for this case. The errors for frequency and ROCOF obtained using PMU-2 are also shown in Figs. 4.7 and 4.8 respectively. The error values for both the parameters are again low when employing the reconstruction-based methods,

compared to the PMU-based method.

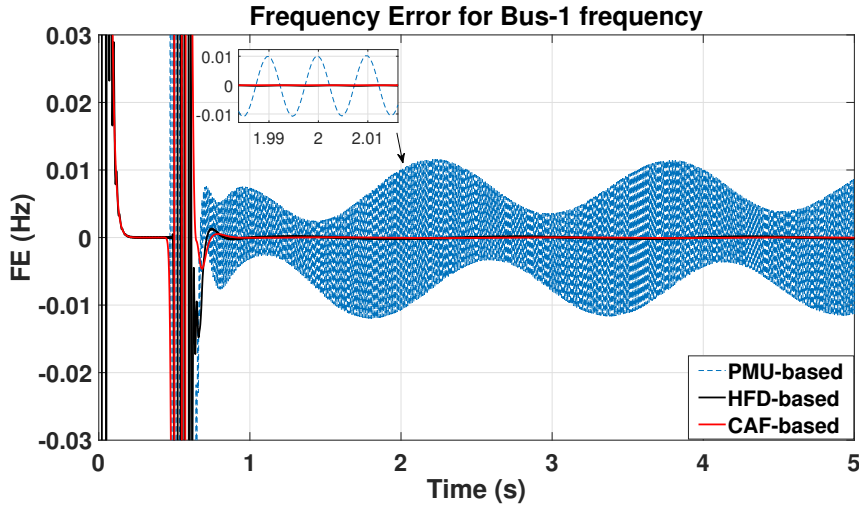


Figure 4.4: Frequency errors for Case-1 using PMU-1.

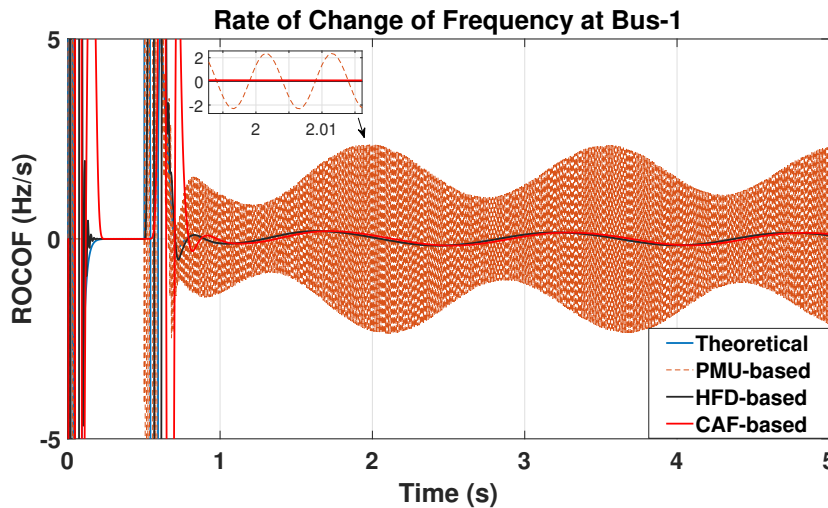


Figure 4.5: ROCOF measurements for Case-1 using PMU-1.

In order to verify the accuracy of the swing mode frequency for case-1 which is reflected roughly in the frequency estimates (see Fig. 4.3), Prony analysis has been performed on the frequency signals obtained using the reconstruction-based method. Results for the Prony analysis are given in Table. 4.7. The frequency of the dominant mode estimated using the Prony method matches the swing frequency which is visible in the frequency plots.

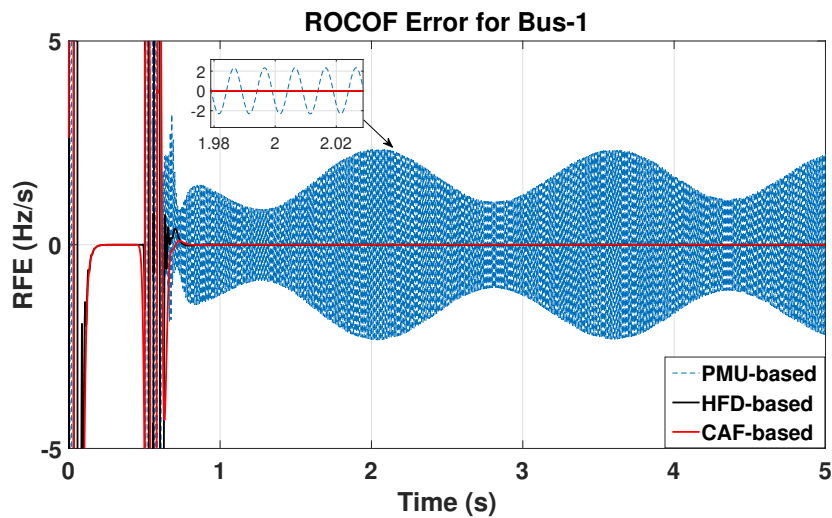


Figure 4.6: Rate-of-change of frequency errors for Case-1 using PMU-1.

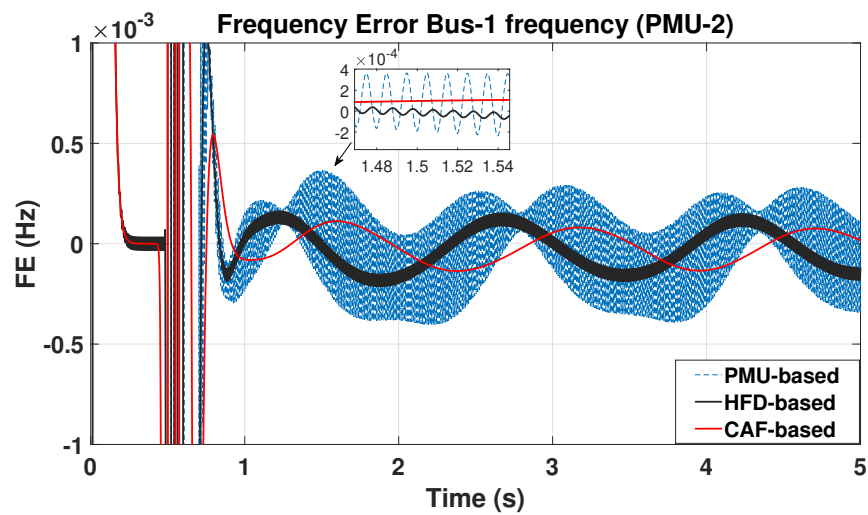


Figure 4.7: Frequency errors for Case-1 using PMU-2.

Table 4.7: Prony analysis for case-1 frequency and ROCOF signals obtained using PMU-2

Signal Type	Dominant Mode	$f$ (Hz)	Damping ratio	Time (s)	$n$
$f_{CAF}$	$-0.0436 + 4.056j$	0.645	0.0107	1.3	72
$ROCOF_{CAF}$	$-0.0453 + 4.056j$	0.645	0.0112	0.55	24

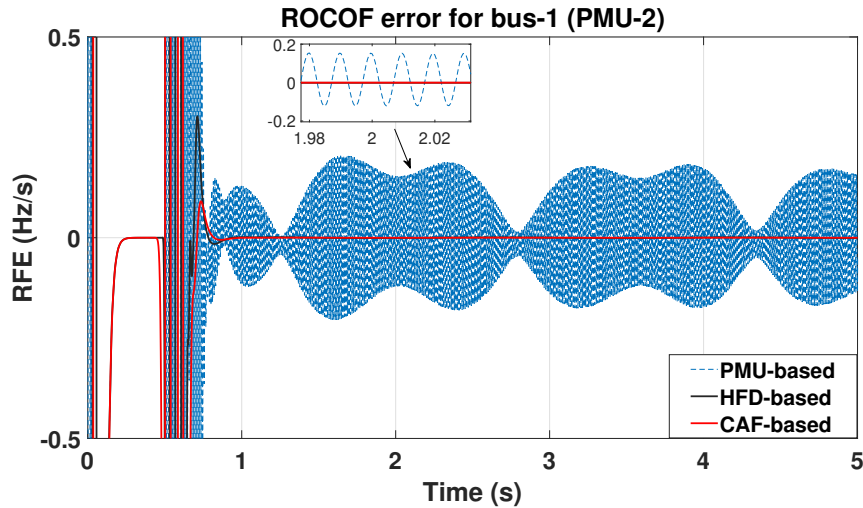


Figure 4.8: Rate-of-change of frequency errors for Case-1 using PMU-2.

#### 4.6.2 Case-2: A Large-Disturbance Unstable Performance

For this case the following controllers and load models are employed, (Shubhanga, 2018)

1. Generators 1 and 2 are equipped with ST-1A type exciters.
2. Generators 3 and 4 are equipped with static single-time constant type exciters.
3. Generator 2 is provided with a slip-signal based Power System Stabilizer (PSS).
4. Hydro-type turbines are enabled on generators 1 and 2.
5. Steam turbine of reheat type is enabled on generator 4.
6. Loads are assumed to be frequency dependent.
7. Real power component of load is modelled as 30% constant power, 30% constant current and 40% constant impedance type.
8. Reactive power component of load is modelled as 100% constant impedance type.

Considering the above system details, a three-phase fault is initiated at 0.6 s at bus-9 of the 4-machine, 10-bus power system and line 1 is tripped. The fault duration is set to 0.291 s which leads to an unstable power system. This can be clearly seen using the frequency deviation values plotted in Fig. 4.9 for bus-1, where the deviation from the nominal values

is seen to be increasing with time. The frequency error estimates shown in Fig. 4.10 again depict the superiority of the reconstruction-based methods over the single-phase phasor based method.

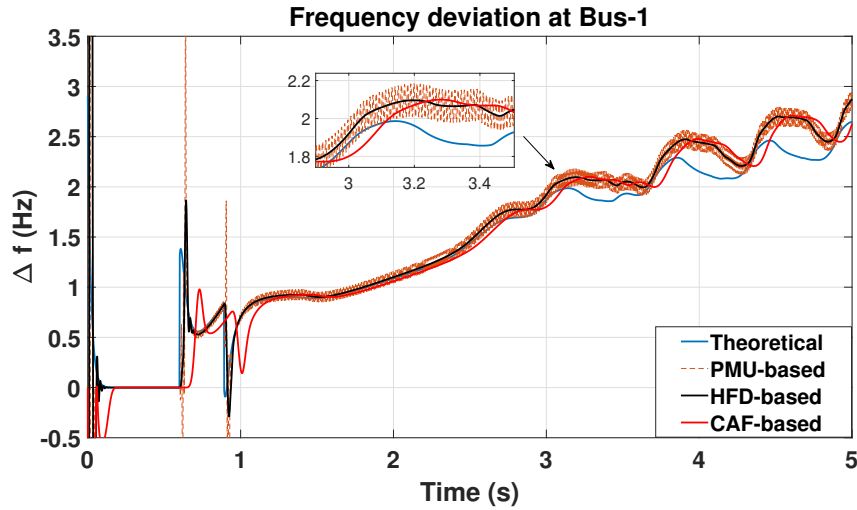


Figure 4.9: Frequency measurements for Case-2 using PMU-1.

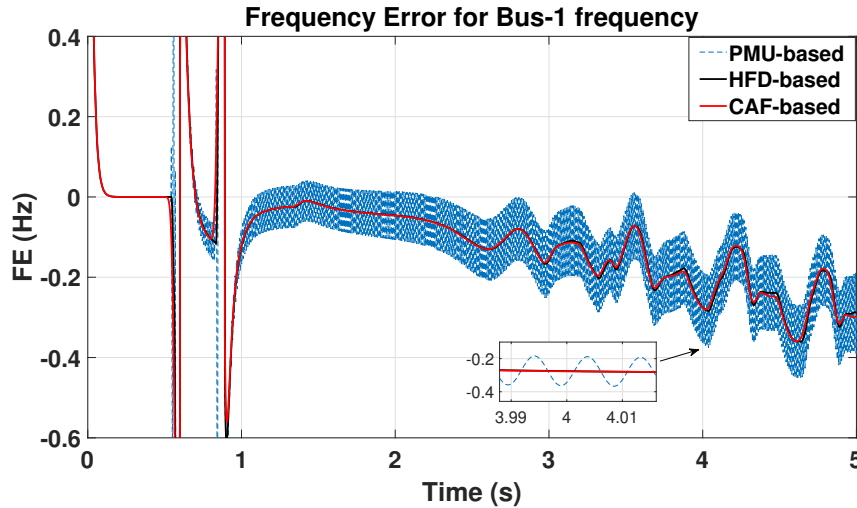


Figure 4.10: Frequency errors for Case-2 using PMU-1.

The ROCOF values and the errors obtained for this case are plotted in Fig. 4.11 and Fig. 4.12, respectively. Estimates for ROCOF obtained using the reconstruction-based

methods are found to be accurate in comparison to the estimates which are obtained via the single-phase PMU.

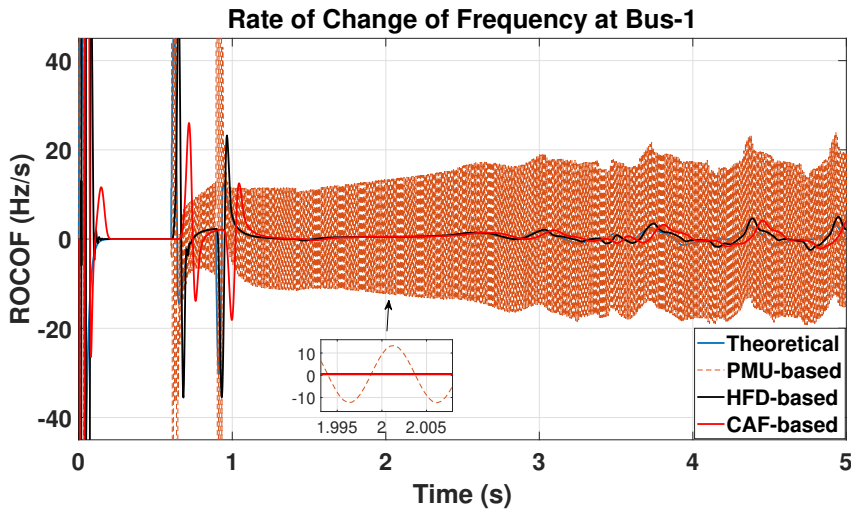


Figure 4.11: ROCOF measurements for Case-2 using PMU-1.

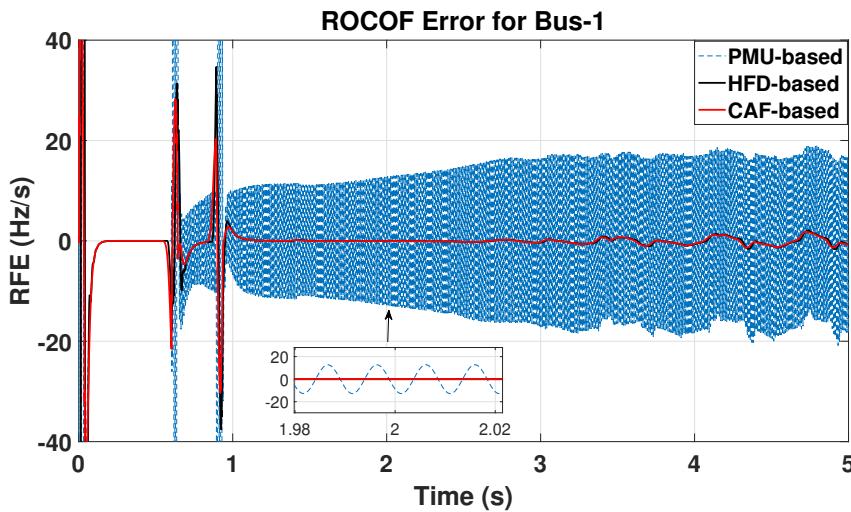


Figure 4.12: Rate-of-change of frequency errors for Case-2 using PMU-1.

The error values for both the cases are summarized in Table. 4.8. As previously mentioned the error values obtained using the reconstruction based methods are lower than the inherent single-phase PMU based methods for all the cases. For case-1, all the values are well within the required standard limits (considering M-class dynamic compliance)

for both the PMUs. However, for unstable case-2, even though the reconstruction-based methods again outperform the PMU, the error values for frequency are not compliant with the latest standard (0.3 Hz). Though, in case of ROCOF, compliant estimates are provided using the reconstruction based methods. The ROCOF error in case-2 for the PMU method is 20.9 Hz/s which is far greater than recommended by the IEEE standard for synchrophasor measurements (14 Hz/s) whereas that obtained using either HFD or CAF (2.07 and 1.8 respectively) is well within the limits.

In case-2 the frequency pertaining to the line-2 current is computed using both the described reconstruction-based methods. The computed frequency estimates are similar to those given in Aalam and Shubhanga (2021), where the current-frequency plots consist of spikes and are unusable for measurement, control or protection applications.

**Table 4.8:** Maximum frequency and ROCOF errors for case-1, case-2.

Cases↓	Max FE (Hz)			Max RFE (Hz/s)		
	PMU	HFD	CAF	PMU	HFD	CAF
Case-1 (PMU-1)	0.012	2.61e-4	7.6e-5	2.34	2.84e-3	2.51e-4
Case-1 (PMU-2)	4.1e-4	2.2e-4	1.37e-4	0.21	1.2e-3	1.8e-4
Case-2 (PMU-1)	0.45	0.361	0.36	20.9	2.07	1.8

### 4.6.3 Mode estimation using frequency and ROCOF signals

The reference voltage,  $V_{ref}$ , setting of machine-1 is perturbed in order to excite a local swing mode associated with generators 1 and 2 of the 4-machine 10-bus power system, (Shubhanga, 2018). This is shown in Fig. 4.13, where slip variables are plotted with respect to COI. The figure shows a local mode in the initial part and an inter-area mode in the later part. For this case, the frequency at bus-1 of the 4-machine 10-bus power system is computed using PMU-2 for a duration of 20 s, -see Fig. 4.14. Similarly, the ROCOF for bus-1 is plotted in Fig. 4.15.

The frequency signal plot given in Fig. 4.14, shows a decreasing trend throughout the simulation time period and this trend has to be removed before subjecting the signal for mode estimation using the Prony method (Aalam and Shubhanga, 2021), (Rao and Shubhanga, 2017). However, such a problem is not faced while dealing with the ROCOF signal which is inherently detrended, as can be seen in Fig. 4.15. The results of the prony



analysis are tabulated in Table. 4.9. From the results, it can be noted that the execution time as well as the order of the linear predictor ( $n$ ) required for the achievement of a good fitment for the input signal is also substantially less for the ROCOF signal when compared to its frequency counterpart. Hence, the ROCOF signal can be considered as a candidate signal for mode estimation in power systems.

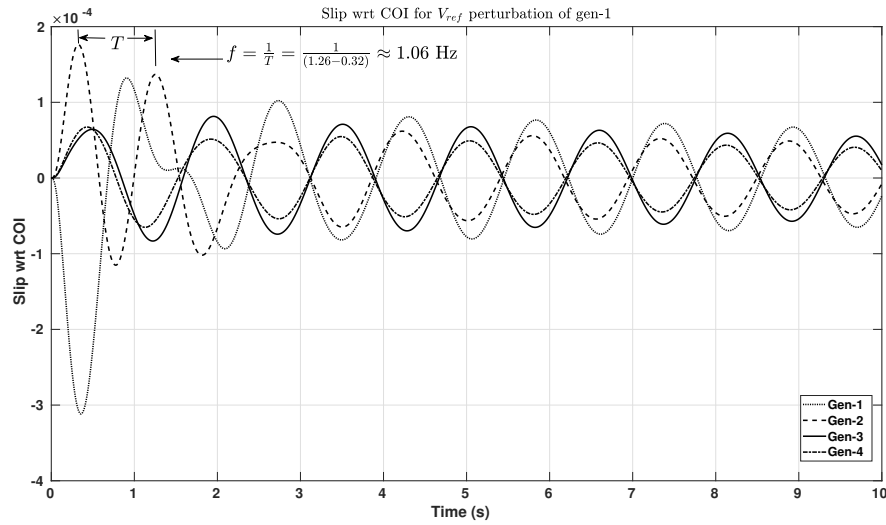


Figure 4.13: Slip excursions during  $V_{ref}$  perturbation of gen-1.

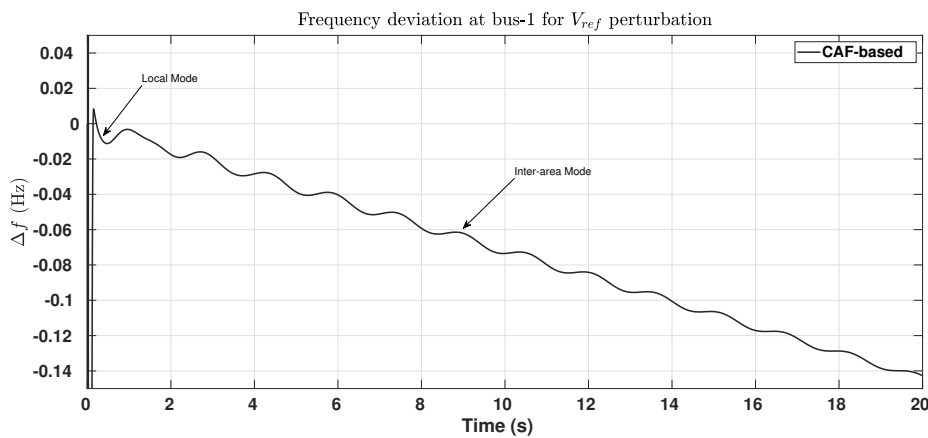


Figure 4.14: Frequency deviation at bus-1 for  $V_{ref}$  perturbation of gen-1.

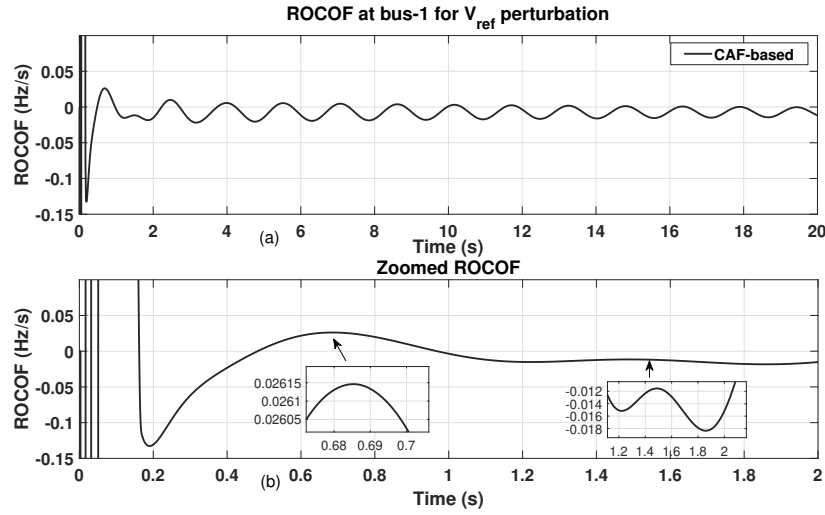


Figure 4.15: ROCOF at bus-1 for  $V_{ref}$  perturbation of gen-1.

Table 4.9: Prony analysis of case-3 signals obtained using PMU-2

Signal Type	Dominant Mode	$f$ (Hz)	Damping ratio	Time (s)	$n$
$f_{CAF}$	$-0.079 + 4.07j$	0.648	0.0194	5.28	168
	$-1.103 + 6.72j$	1.07	0.1618		
$ROCOF_{CAF}$	$-0.0447 + 4.07j$	0.648	0.011	0.54	22
	$-1.118 + 6.673j$	1.06	0.165		

## 4.7 Case Studies Using ISO New-England Power System Signals

In this section, the reconstruction-based frequency estimation technique has been applied to practical signals acquired from PMUs installed throughout the ISO New-England (ISO-NE) power system.

### 4.7.1 Construction of time-domain sinusoidal signals from phasor samples

PMU data provided for the ISO-NE power system, (EECS, 2022), (Maslennikov et al., 2016) consists of positive sequence voltage, current and frequency values acquired from

many locations over the entire grid. According to the data sheets provided by EECS (2022), Maslennikov et al. (2016), a total of 35 PMUs are installed all over the ISO-NE power system. The PMUs installed at the ISO-NE power system transmit data at a rate of 30 fps. Using PMU data which is available at such a low frame rate, i.e., one phasor sample per two cycles (for a 60 Hz fundamental), it is not feasible to construct the time-domain sinusoidal signal. Therefore, the PMU phasor data provided for the ISO-NE system is interpolated to a higher sampling rate (choosing 20 samples per cycle of the fundamental) so that the sinusoidal signals in the  $abc$ -frame are fed to the chosen PMU algorithm, -see Fig. 4.16. This approach is justified in the later part of the paper by comparing the modal features of the frequency signal provided by the ISO-NE system data and the computed frequency signals obtained via the reconstruction-based approach.

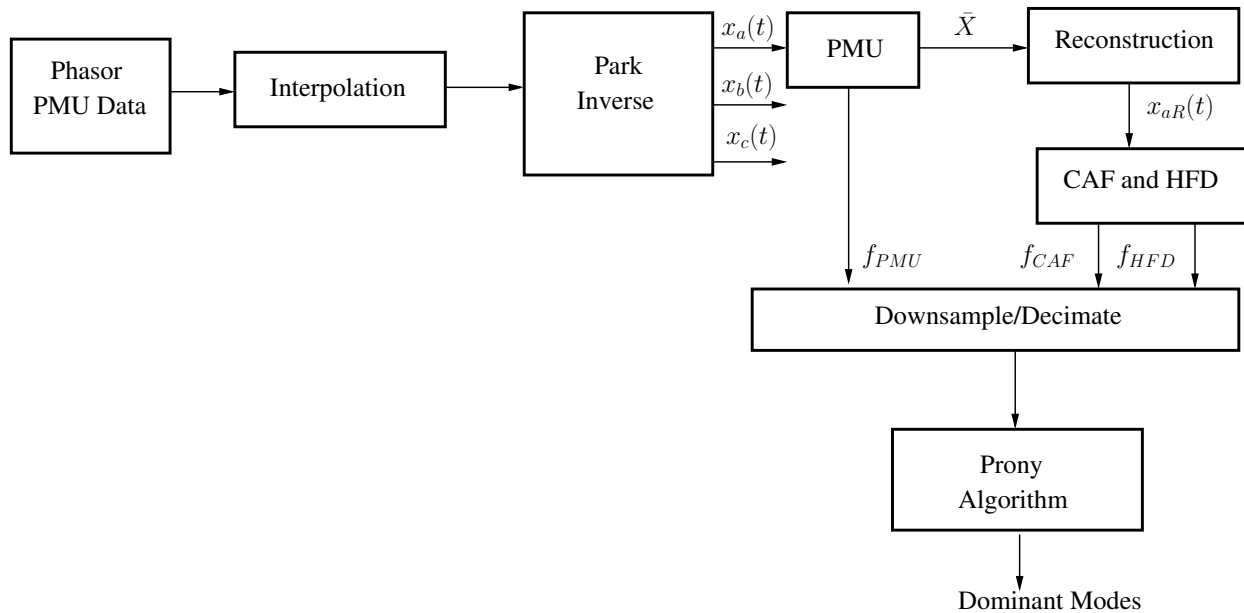


**Figure 4.16:** Schematic approach for construction of sinusoidal signals from phasor data.

In EECS (2022), Maslennikov et al. (2016), data is provided for different power system events caused by different faults in the ISO-NE power system or its surrounding areas as depicted in Fig. 4.17. To show the efficacy of the reconstruction-based methods, two case studies are chosen. The description of the cases is provided in Table. 4.10 and are detailed below:

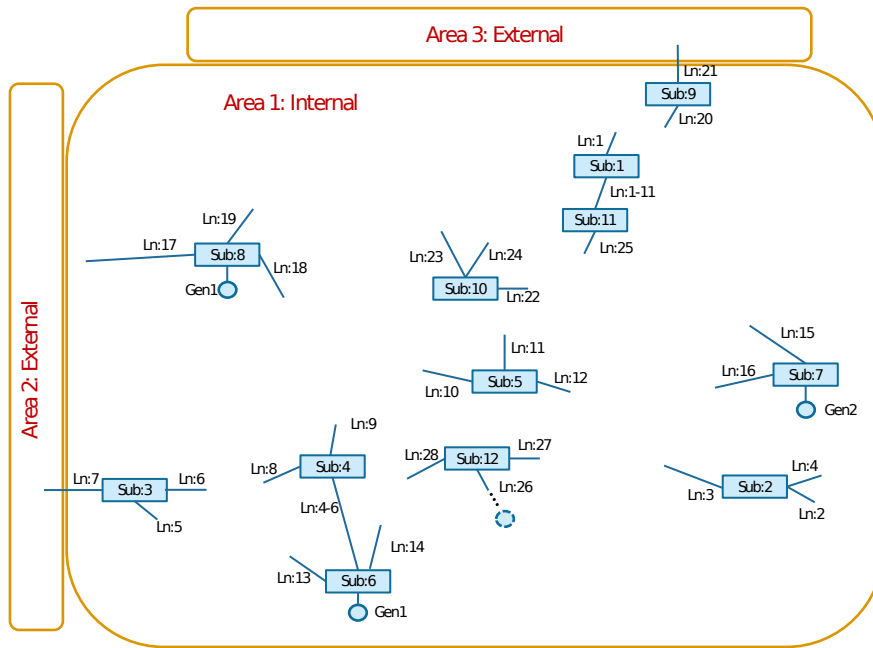


**Figure 4.17:** Area map of the ISO-NE power system with Area-1 denoting the internal area of the ISO-NE power system, whereas Area-2 and Area-3 denoting the surrounding areas, (EECS, 2022), (Maslennikov et al., 2016).

**Table 4.10:** List of Events in ISO-NE power system (EECS, 2022), (Maslennikov et al., 2016).

Case No	Event date	Oscillation type	Frequency (Hz)	Data duration (s)	Source and location
Case-1	June 16, 2017	System wide mode	0.27	180	<ul style="list-style-type: none"> <li>• Large generator fault</li> <li>• Located outside ISO-NE in area-2</li> </ul>
					<ul style="list-style-type: none"> <li>• Large generator fault</li> <li>• Located in ISO-NE in area-1</li> <li>• Source is located East from Sub-2 connected by Line-2 and Line-4</li> </ul>
Case-3	July 20, 2017	Regional mode	1.13	180	<ul style="list-style-type: none"> <li>• Large generator fault</li> <li>• Located in ISO-NE in area-1</li> <li>• Source is located East from Sub-2 connected by Line-2 and Line-4</li> </ul>

1. **Case-1:** In this case, system-wide oscillations are caused due to a large generator fault in the Southern part of the Eastern interconnection located outside the ISO-New-England Power System in area-2 as depicted in Fig. 4.17. The oscillation frequency for this case is around 0.27 Hz and is observed at several locations throughout the New-England power grid. For this case, the original frequency data provided by the PMUs at Sub-3, Line-7 and Sub-2, Line-2 are plotted in Fig. 4.18.

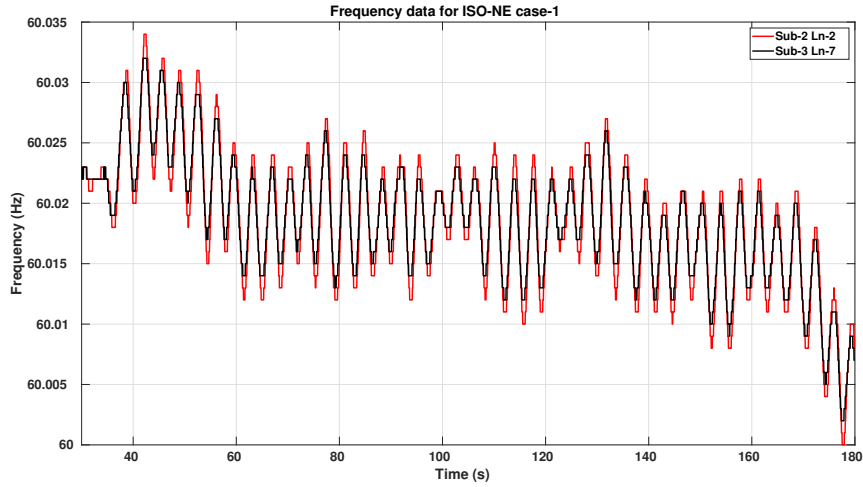


**Figure 4.18:** Frequency estimates for case-1 from ISO-NE PMU data.

The positive-sequence voltage phasor samples provided by a PMU on Line-7 connecting Substation-3 is used for frequency estimation since it is electrically close to the fault origin. The constructed sinusoidal signal at the output of the park-inverse block (see Fig. 4.16) is fed to PMU-2 and in-turn to reconstruction-based approaches to compute  $f_{PMU}$ ,  $f_{CAF}$  and  $f_{HFD}$  as given in Fig. 4.19.

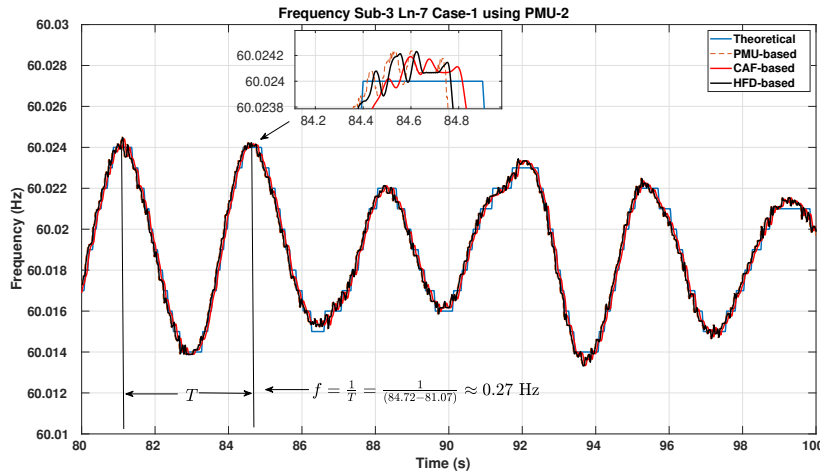


**Figure 4.19:** Frequency estimates for case-1 using PMU-2.

A similar plot is obtained for PMU-3 in Fig. 4.20. The frequency errors correspond-

ing to these two PMUs are given in Fig. 4.21.

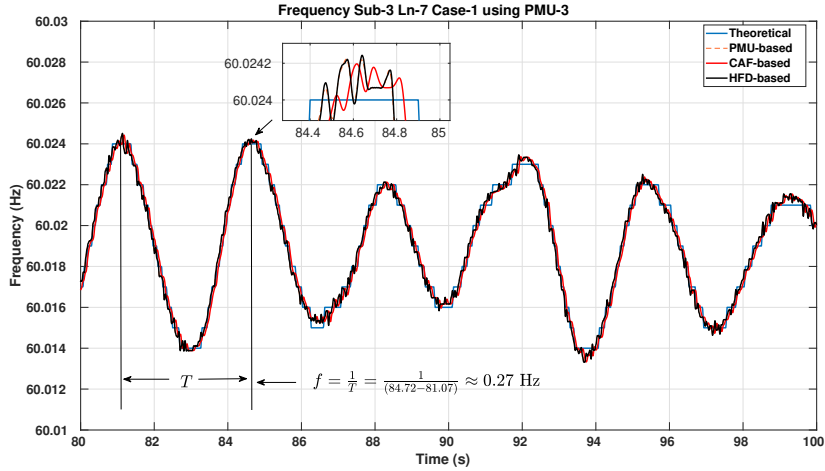


Figure 4.20: Frequency estimates for case-1 using PMU-3.

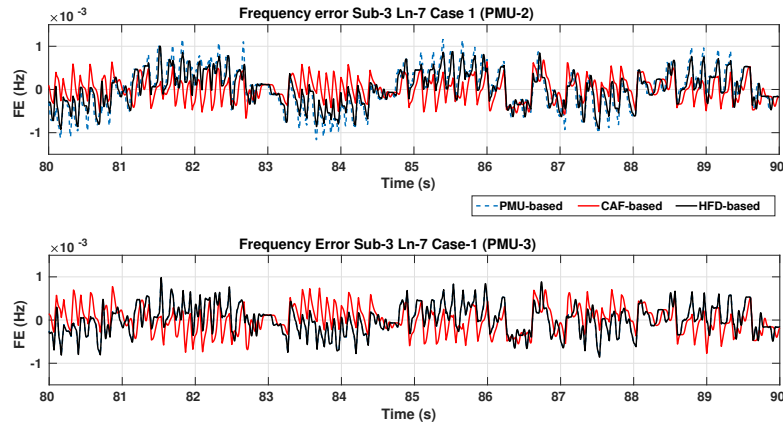


Figure 4.21: Frequency error for case-1 using PMU-2 and PMU-3.

It is observed that the frequency estimates obtained using PMU-2 are less accurate compared to the reconstruction-based estimates. This is due to lack of elimination of the second harmonic component for the single-phase signals as well as the poor performance of the time-derivative based frequency estimation, especially for noisy

signals. Even for PMU-3, the frequency estimates provided by the reconstruction-based methods are better than the inherent PMU-algorithm for a single-phase basis. The maximum frequency error obtained using the  $f_{CAF}$  estimates in the 80 to 90 s window is  $7.74 \times 10^{-4}$  Hz, whereas the error computed for the  $f_{PMU}$  (for PMU-3) estimates is  $9.41 \times 10^{-4}$  Hz. The oscillation frequency of 0.27 Hz can be roughly calculated from the frequency plots in Figs. 4.19 and 4.20. The rate-of-change of frequencies for case-1 signals computed using PMU-3 and the reconstruction-based methods are shown in Fig. 4.22, where the superiority of the reconstruction-based estimates over the single-phase PMU based estimates can be verified.

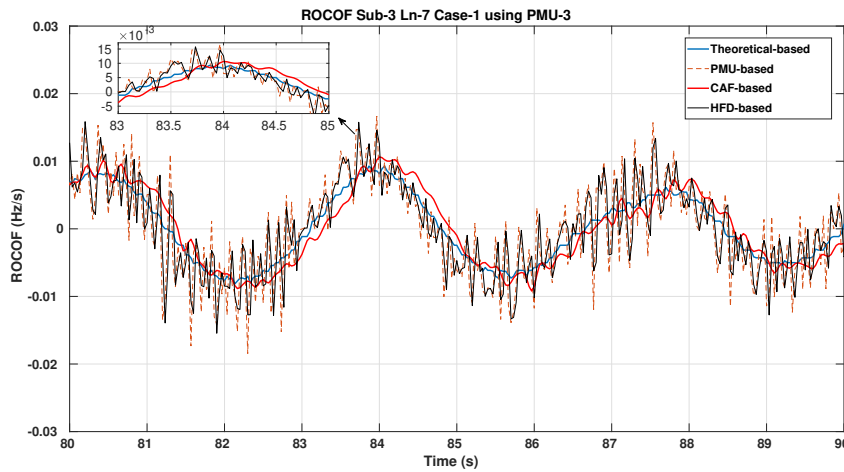
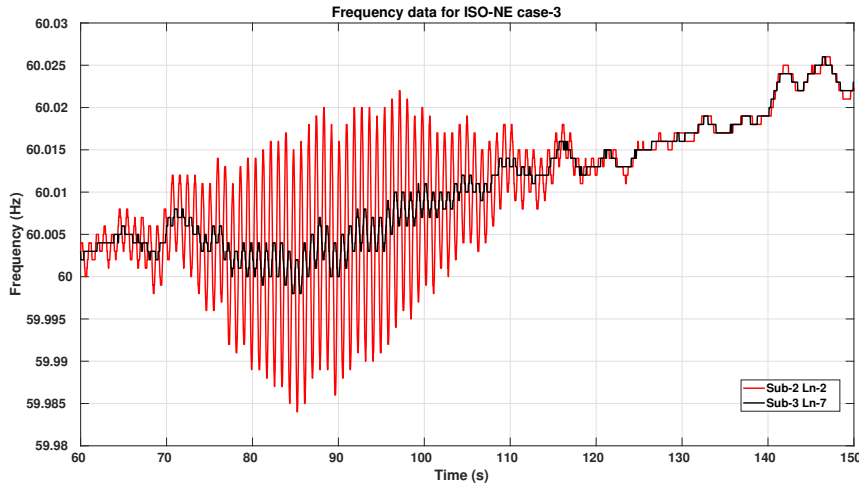


Figure 4.22: ROCOF for Case-1 using PMU-3.

2. **Case-3:** In this case regional oscillations are caused due to a large generator fault located inside the ISO-NE power system in area-1. The source of the fault is located east from Substation-2 connected by line 2 and line 4. Oscillation frequency of 1.13 Hz is observed at some locations in the ISO-NE power system with growing magnitude for 40 s. For this case, the original frequency data provided by PMUs at Sub-3, Line-7 and Sub-2, Line-2 are plotted in Fig. 4.23.

The PMU data at Substation-2, Line-2 is fed to the interpolation block in Fig. 4.16. The frequencies computed using PMU-2 and PMU-3 are plotted in Figs. 4.24 and 4.25, respectively. The frequency errors for both PMU-2 and PMU-3 are shown in Figs. 4.26. The PMU-based frequency error using PMU-2 is slightly greater than that

obtained using the reconstruction-based methods, whereas for PMU-3, the inherent frequency estimation results closely match with the reconstruction-based results. The oscillation frequency of 1.13 Hz can be clearly visualized using the frequency plots given in Figs. 4.24 and 4.25.



**Figure 4.23:** Frequency estimates for case-3 from ISO-NE PMU data.

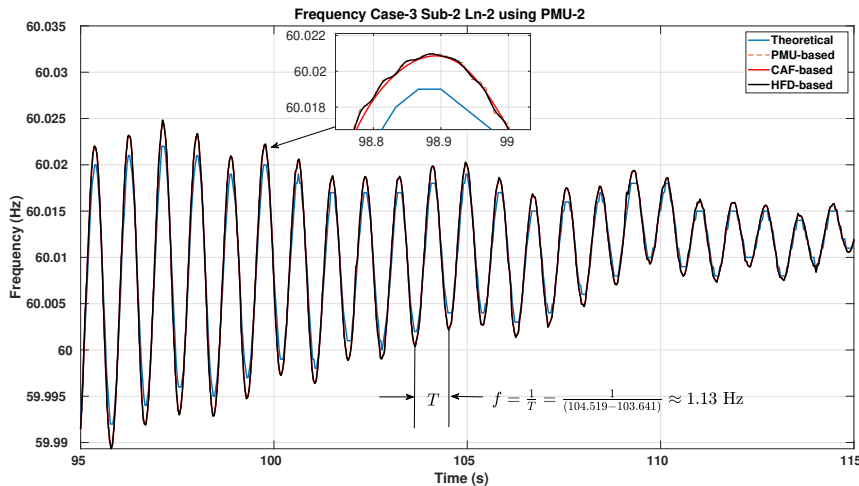


**Figure 4.24:** Frequency estimates for Case-3 using PMU-2.

The ROCOF for case-3 computed using PMU-3 is shown in Fig. 4.27. The zoomed



version of the estimates clearly shows the superiority of the ROCOF computed using the reconstruction-based approach (especially CAF), over those computed using the single-phase PMU based frequency. The error due to the second harmonic component is accentuated in the ROCOF estimates due to its derivative nature, which is clearly seen in the PMU-based estimates.

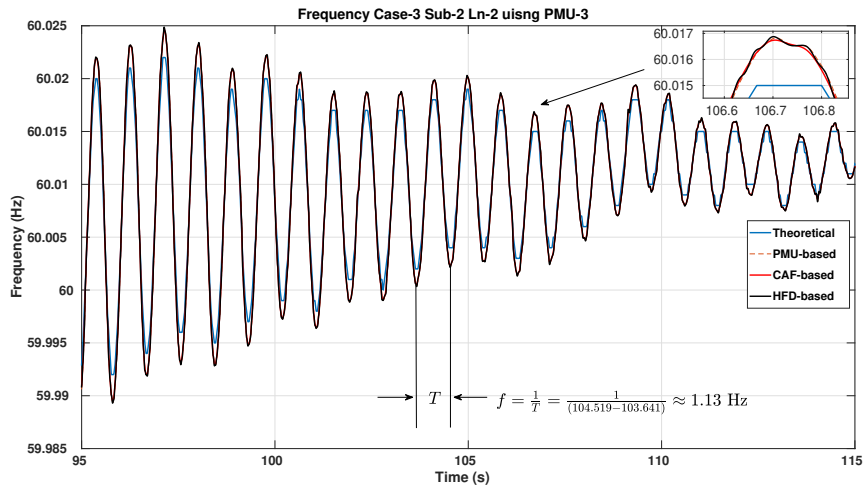


Figure 4.25: Frequency estimates for Case-3 using PMU-3.

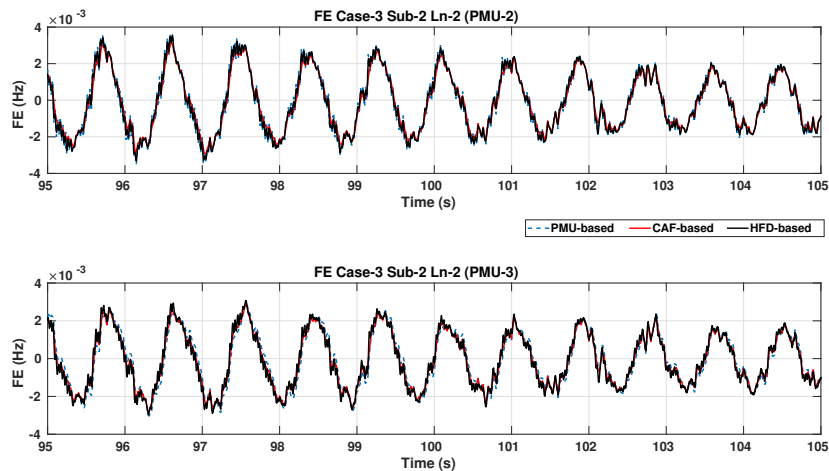


Figure 4.26: Frequency error for Case-3 using PMU-2 and PMU-3.

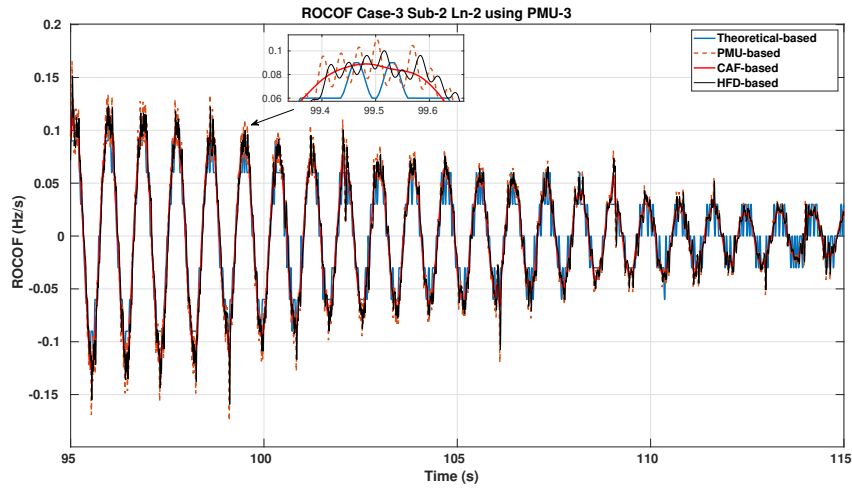


Figure 4.27: ROCOF for Case-3 using PMU-3.

#### 4.7.2 Mode estimation using frequency signals

Frequencies computed using the ISO-NE PMU data for various oscillation scenarios are subjected to mode estimation using the Prony algorithm to analyse the prevalent dominant modes and their damping performance. For the case studies presented, the PMU-based as well as the reconstruction-based (CAF) frequency signals are employed. Frequency estimates obtained from both the static PMU model (PMU-2) as well as the dynamic PMU model (PMU-3) are used for mode estimation. Table. 4.11, lists the dominant modes obtained through different frequency signals at 30 fps, for case-1 and case-3. For demonstration purposes, two sample windows of 10 s duration are chosen for the Prony analysis as listed in the table. For example in case-1, the frequency estimates during the time interval of 80 to 90 s show a gradual decrease in amplitude as can be seen from Figs. 4.19 and 4.20. This is further verified by a positive damping ratio associated with the observed mode. The same approach is applied for case-3 signals, where a time interval of 95 to 105 s is chosen -see Figs. 4.24 and 4.25.

It can be observed that for both the cases the frequency of oscillation obtained using the Prony method is very close to that mentioned in EECS (2022), Maslennikov et al. (2016). The column “ $n$ ” denotes the order of the Linear predictor required by the Prony algorithm to find a best fit for the input frequency signal. It is seen that the execution time for the Prony algorithm for the PMU-based frequency signal is slightly greater than the reconstruction-based (CAF) signals for both the PMU-2 and PMU-3. For case-3,  $F_{R1}$  and its truncated

mean version, (Dai and Tate, 2021) are subjected to Prony analysis for mode estimation. The results are provided in Table. 4.12. The frequency of the dominant modes are accurate and match with those provided in Table. 4.11, but no major improvements are observed with respect to the execution time while using  $F_{R1}$  or its truncated mean version.

**Table 4.11:** Prony analysis of different frequency signals

Case	PMU	Freq Method	Dominant Mode	$f$ (Hz)	Damping Ratio	Time (s)	$n$
1 (80 to 90 s)	2	CAF-based	-0.1695+1.801 $j$	0.286	0.0937	1.315	138
1 (80 to 90 s)	2	PMU-based	-0.0689+1.74 $j$	0.276	0.0396	1.376	140
1 (80 to 90 s)	3	CAF-based	-0.1526+1.8073 $j$	0.287	0.084	1.29	138
1 (80 to 90 s)	3	PMU-based	-0.2031+1.75 $j$	0.278	0.115	1.29	138
3 (95 to 105)	2	CAF-based	-0.0523+7.221 $j$	1.149	0.0072	1.1	122
3 (95 to 105)	2	PMU-based	-0.0529+7.225 $j$	1.149	0.0073	1.15	124
3 (95 to 105)	3	CAF-based	-0.0517+7.221 $j$	1.149	0.0072	1	118
3 (95 to 105)	3	PMU-based	-0.0468+7.22 $j$	1.149	0.0065	1.1	122

**Table 4.12:** List of dominant modes obtained using Prony analysis for  $F_{R1}$  frequency.

Case-3		
Parameters ↓	$F_{R1}$	$F_{R1}$ with truncated mean
Dominant Mode	-0.0558 + 7.22 $j$	-0.0529 + 7.22 $j$
Frequency (Hz)	1.149	1.149
Time elapsed	1.11	1.08
$n$	120	120

### 4.7.3 Time-Window/Piece-Wise Prony analysis of ISO-NE signals

Extracting dominant modes from power system signals for oscillation monitoring is not a straightforward task, especially during fault conditions when the nature of the signals is highly non-stationary and when the signal consists of a non-linear trend. Such signatures can be clearly seen in case-1 and case-3 frequency signals as shown in Figs. 4.18 and 4.23, respectively. While handling such a non-stationary signal using conventional mode estimation algorithms such as the Prony method, the following observations are made:

1. It is not easy to simply choose a single window of a given time interval a priori to compute the dominant modes present in a signal, effectively.
2. The placement of the window relative to the start of the disturbance influences the reliable estimation of the damping performance of the modes.

3. Choice of a suitable window length depends on the frequency of oscillation.

These issues are addressed for case-1 and case-3 signals as follows:

#### 4.7.3.1 Case-1

Here, observations based on the Prony analysis are noted for time-windows ranging from 60 s to 100 s for case-1. The reporting rate for frequency signals is also varied in order to compare the modal behavior across different reporting rates. The results are given in Tables. 4.13-4.14, including the theoretical. Four 10 s time-windows are examined using the Prony method and the following observations are made:

1. The time-window ranging from 60 s to 70 s is shown in Fig. 4.28 (a). A frequency of oscillation of 0.28 Hz along with a very slight decreasing trend can be seen during this time interval. These observations are correctly identified by the Prony analysis across all frame rates as given in Tables. 4.13-4.14.

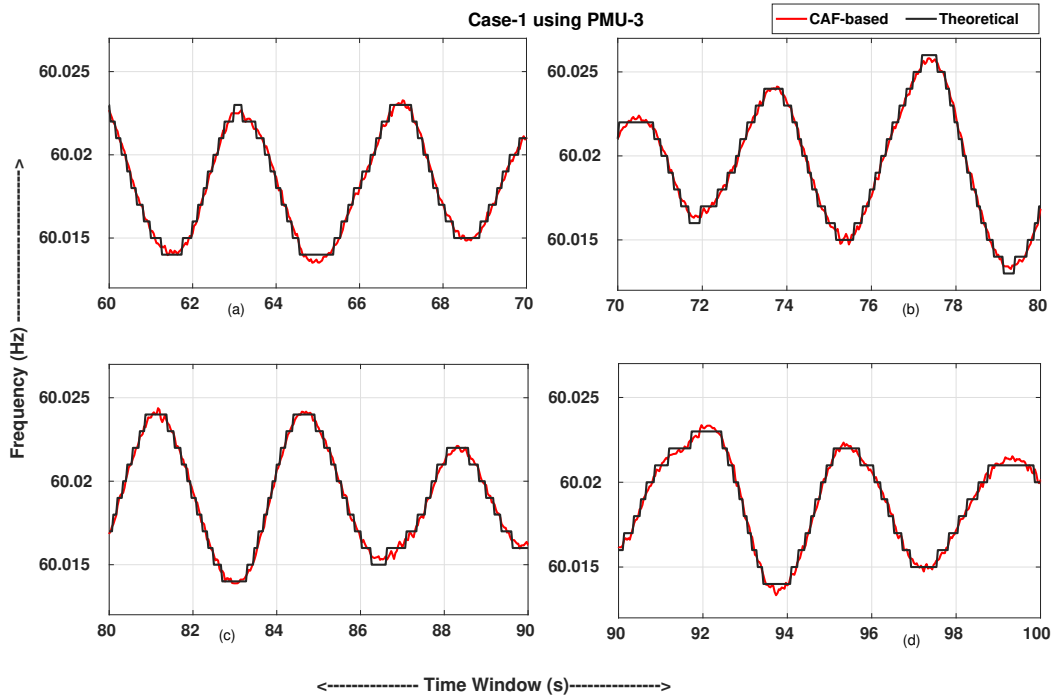


**Figure 4.28:** Four 10 s data windows for case-1 for Prony Analysis.

**Table 4.13:** Prony analysis of different 10 s windows for case-1 using theoretical and PMU-3 CAF signal at 30 fps.

Signal →	Theoretical signal					PMU-3 CAF at 30 fps				
Time Window Chosen (s)	Dominant Modes	Freq (Hz)	Damping ratio	Time (s)	$n$	Dominant Modes	Freq (Hz)	Damping ratio	Time (s)	$n$
60 to 70	$-0.0006 + 1.76j$	0.28	$3.4 \times 10^{-4}$	1.36	140	$-0.012 + 1.75j$	0.27	0.0073	1.4	142
70 to 80	$0.2 + 1.618j$	0.25	-0.125	1.39	142	$0.1856 + 1.589j$	0.25	-0.116	1.27	132
	$-0.136 + 2.054j$	0.32	0.066			$-0.17 + 2.054j$	0.32	0.0825		
80 to 90	$-0.09 + 1.71j$	0.27	0.0526	1.35	138	$-0.1512 + 1.8j$	0.28	0.083	1.3	138
	-	-	-			$0.281 + 1.46j$	0.23	0.19		
90 to 100	$-0.082 + 1.77j$	0.28	0.0463	1.43	140	$-0.122 + 1.75j$	0.27	0.0695	1.42	144
	$-1.35 + 0j$	0	-			$-2.53 + 0j$	0	-		

**Table 4.14:** Prony analysis of different 10 s windows for case-1 using PMU-3 CAF signals at 60 fps and 120 fps.

Signal →	PMU-3 CAF at 60 fps					PMU-3 CAF at 120 fps				
Time Window Chosen (s)	Dominant Modes	Freq (Hz)	Damping ratio	Time (s)	$n$	Dominant Modes	Freq (Hz)	Damping ratio	Time (s)	$n$
60 to 70	$-0.0103 + 1.76j$	0.27	0.0059	9.94	282	$-0.0142 + 1.75j$	0.27	0.008	36.7	386
70 to 80	$0.1839 + 1.6j$	0.25	-0.114	7.78	252	$0.186 + 1.58j$	0.25	-0.117	33	372
	$-0.1726 + 2.073j$	0.32	0.083			$-0.168 + 2.04j$	0.32	0.0821		
80 to 90	$-0.124 + 1.81j$	0.28	0.068	9.33	274	$-0.139 + 1.8j$	0.28	0.077	37.4	394
	$-0.24 + 1.38j$	0.22	-0.171			$-0.28 + 1.42j$	0.22	0.193		
90 to 100	$-0.121 + 1.752j$	0.28	0.069	10.3	286	$-0.128 + 1.75j$	0.27	0.073	49	408
	$-2.4 + 0j$	0	-			$-0.69 + 2.83j$	0.45	0.237		
	-	-	-			$-3.72 + 0j$	0	-		

- As can be clearly seen from the second time-window ranging from 70 to 80 s in Fig. 4.28 (b), the amplitude of the frequency signal is increasing with time through the window. This increase in the amplitude is reflected by the negative damping ratio associated with the dominant modes computed for the time-window, as is verified in Tables. 4.13-4.14. The value of the frequency and the damping ratio for all frame rates is very close to each other and in turn close to the theoretical values.
- For the time interval of 80 to 90 s, the amplitude of the frequency signal is clearly decreasing as shown in Fig. 4.28 (c). For this window, the frequency of oscillation as calculated using the Prony method for the dominant mode is approximately 0.28 Hz for all the frame rates. A positive damping ratio is also a feature of this time-window, which varies between 0.07 and 0.09 for different reporting rates, for CAF-based frequency signals -see Tables. 4.13-4.14.
- In the time interval ranging from 90 to 100 s the frequency signal amplitude is again seen to decrease with time, shown by Fig. 4.28 (d). The dominant mode frequency of

the signal is 0.28 Hz approximately across all the frame rates whereas the damping ratio lies around 0.07 for CAF-based frequency signals.

**Note :** In the 80-90 s time-interval an additional low amplitude mode is observed across all the frame rates for the CAF-based frequency signals, as depicted by the Prony results.

### 4.7.3.2 Case-3

The time-window based Prony analysis results for case-3 frequency signals for a duration of 40 seconds starting from 75 s and ending at 115 s are given in Tables. 4.15-4.16, for different frame rates, ranging from 30 fps to 120 fps, including the theoretical. The following observations are made :

1. The frequency plot for the 75 s to 85 s time interval is shown in Fig. 4.29 (a). The dominant mode for this time-window as computed using the Prony algorithm for all frame rates correctly reflects the frequency component of 1.13 Hz present in the signal. A negative damping ratio is also noted, clearly indicating growing oscillations in this time interval.

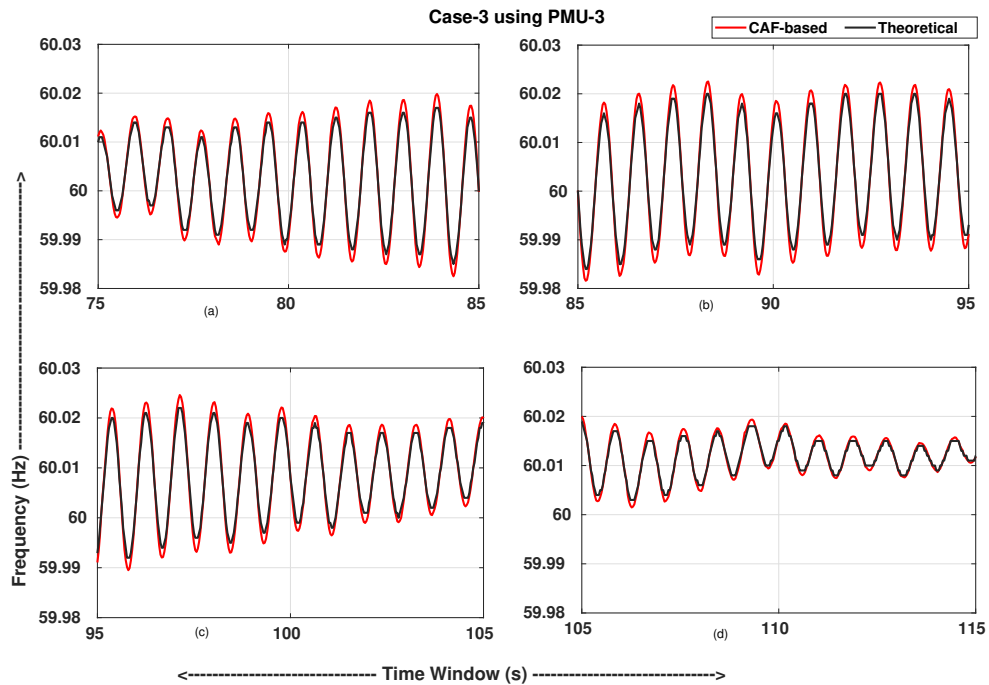


**Figure 4.29:** Four 10 s data windows for case-3 for Prony Analysis.

**Table 4.15:** Prony analysis of different 10 s windows for case-3 using theoretical and PMU-3 CAF signal at 30 fps.

Signal →	Theoretical					PMU-3 CAF at 30 fps				
Time Window Chosen (s)	Dominant Modes	Freq (Hz)	Damping ratio	Time (s)	$n$	Dominant Modes	Freq (Hz)	Damping ratio	Time (s)	$n$
75 to 85	$0.06 + 7.12j$	1.13	-0.008	1	110	$0.048 + 7.13j$	1.13	-0.0067	1.01	112
85 to 95	$-0.007 + 7.11j$	1.13	0.001	1.22	128	$-0.009 + 7.11j$	1.13	0.0013	1.02	112
95 to 105	$-0.05 + 7.22j$	1.14	0.0069	1.1	122	$-0.051 + 7.22j$	1.14	0.0072	1.1	122
105 to 115	$-0.178 + 7.24j$	1.15	0.0246	1.34	140	$-0.272 + 1.1j$	0.17	0.24	1.14	124
	$-0.32 + 1.145j$	0.18	0.269			$-0.118 + 7.3j$	1.16	0.016		

**Table 4.16:** Prony analysis of different 10 s windows for case-3 using PMU-3 CAF signals at 60 fps and 120 fps.

Signal →	PMU-3 CAF at 60 fps					PMU-3 CAF at 120 fps				
Time Window Chosen (s)	Dominant Modes	Freq (Hz)	Damping ratio	Time (s)	$n$	Dominant Modes	Freq (Hz)	Damping ratio	Time (s)	$n$
75 to 85	$0.049 + 7.12j$	1.13	-0.007	5.62	218	$0.05 + 7.13j$	1.13	-0.007	19	318
85 to 95	$-0.009 + 7.11j$	1.13	0.0013	5.82	222	$-0.009 + 7.12j$	1.13	0.0013	19.8	320
95 to 105	$-0.0565 + 7.2j$	1.14	0.0078	6.7	238	$-0.057 + 7.22j$	1.14	0.0079	25	334
105 to 115	$-0.27 + 1.097j$	0.17	0.241	7.3	246	$-0.263 + 1.09j$	0.17	0.234	26	340
	$-0.1192 + 7.3j$	1.16	0.016			$-0.1192 + 7.3j$	1.16	0.0163		

2. From 95 s to 105 s, the amplitude of the frequency signal is seen to decrease as indicated in Fig. 4.29 (c). A dominant frequency component of 1.13 Hz can also be verified using Fig. 4.29 (c). The damping ratio for this particular time window is positive and it ranges from 0.0072 to 0.0079 for different reporting rates as can be verified from Tables. 4.15 and 4.16, for CAF-based frequency signals.

For case-3, even the HFD based frequency estimates at 30 fps are subjected to time-window based Prony analysis. The results are given in Table. 4.17. The values for the dominant modes, execution time and order of the linear predictor are found to be similar to those obtained using the CAF as well as the theoretical based frequency signals.

**NOTE:**

1. Across different frame rates the value of frequency and damping ratio for identical time-windows is approximately the same.
2. The value of “ $n$ ” as well as the execution time is seen to increase as higher frame rate signals are used. Estimates obtained at high fps values cannot be used directly for online analysis and must be decimated to lower rates to enable fast processing.

3. The mode estimates for different frame rates for a given time-window with CAF/HFD-based frequency signals closely match those obtained for theoretical signals. This justifies the idea of interpolating the phasor samples available from the ISO-NE power system in order to accurately construct the time-domain sinusoidal 3-phase signals for frequency estimation.

**Table 4.17:** Prony results of different 10 s windows for case-3 using PMU-3 HFD signals (30 fps)

Time Window Chosen (s)	Dominant Modes	Frequency (Hz)	Damping Ratio	Time (s)	$n$
65 to 75	$0.0322 + 0.8493j$ $0.1134 + 7.17j$	0.1352 1.14	-0.038 -0.0158	1.29	130
75 to 85	$0.0525 + 7.134j$	1.13	-0.0074	1.07	116
85 to 95	$-0.0092 + 7.12j$	1.13	0.0013	1.05	114
95 to 105	$-0.0475 + 7.213j$	1.15	0.0066	1.15	122
105 to 115	$-0.2747 + 1.05j$ $-0.1187 + 7.297j$	0.176 1.161	0.2413 0.0163	1.21	124

#### 4.7.4 Effect of initial value of the order of linear predictor (OLP) on execution time

The number of component modes present in a power system signal is denoted by the order of the linear predictor “ $n$ ”. This value is not known a priori and hence it is obtained through an iterative process in the Prony algorithm until the estimated signal matches the input original signal as determined by a fitness metric, referred to as SNR, (Sarkar et al., 2018). The initial value of, “ $n$ ”, used for the Prony analysis in this chapter is two, which is increased in steps of two till the desired fitment is achieved. This iterative approach is the primary reason that signals with high frame rates lead to higher values of execution time. This can be avoided by carefully choosing an initial value of “ $n$ ”. For example, in case-1 across different frame rates the initial value of  $n = n_i$  is set to 120, 240 and 350 for 30, 60 and 120 fps, respectively, instead of 2. These values are chosen based on the previously computed estimates of “ $n$ ” for case-1. Such a technique drastically reduces the execution time for the Prony analysis as can be seen in Table. 4.18. Such an approach can enable quick and precise mode estimation even for higher frame rate signals if an appropriate value of  $n_i$  is chosen.



**Table 4.18:** Effect of base initial value of  $n$  on execution time

Time Window (s)	Case-1 execution time (s)		
	$30fps/n_i = 120$	$60fps/n_i = 240$	$120fps/n_i = 350$
<b>60 to 70</b>	0.75	3.37	12.5
<b>70 to 80</b>	0.59	1.28	8.91
<b>80 to 90</b>	0.68	2.81	13.6
<b>90 to 100</b>	0.76	3.64	18.6

#### 4.7.4.1 An approach to avoid iteration in the Prony algorithm

Choosing a value of  $n_i$  which is slightly on the higher side of the maximum value of “ $n$ ” obtained in the previous studies (across all time windows for a particular case) leads to an instant convergence of the Prony method for a particular input signal. For example, in Table. 4.13, the maximum value of “ $n$ ” obtained across all time windows is 144 (for 30 fps), and hence choosing the value of  $n_i$  as 146 for that particular frame rate, completely eliminates iterative procedure and drastically reduces the execution time. This is shown in Table. 4.19, where the value of  $n_i$  for different fps values is altered, leading to an instant convergence of the Prony method. This technique is seen to reduce the execution time to less than one second across all frame rates.

**Table 4.19:** Effect of high initial value of  $n$  on execution time

Time Window (s)	Case-1 execution time (s)		
	$30fps/n_i = 146$	$60fps/n_i = 290$	$120fps/n_i = 420$
<b>60 to 70</b>	0.419	0.546	0.965
<b>70 to 80</b>	0.417	0.57	0.975
<b>80 to 90</b>	0.417	0.576	0.979
<b>90 to 100</b>	0.431	0.565	0.979

Such an approach enables the Prony analysis, an iterative algorithm, to be used as a real-time mode estimation tool. However, this requires a careful offline study about system signal characteristics under different disturbance scenarios, to understand the convergence behaviour of the Prony method.

### **4.7.5 Effect of window length on mode estimation**

During fault conditions power system signals exhibit non-stationary behaviour. Power system oscillations during such conditions can last for a few cycles to several minutes. It would have been ideal to have a signal with uniform characteristics during the entire interval to enable easy mode identification. But this is not the case with power system signals which constantly change due to the non-linear nature of the system. Therefore, processing such signals over the entire interval for mode identification can lead to erroneous results. Hence, the previous analysis included piece-wise windows where the entire interval is broken down into consecutive 10 s windows and then analyzing them taking one window at a time. This technique is based on the observation that within a time window, the signal has a uniform characteristic, therefore eliminating ambiguity in the Prony based results. The mode estimation task is repeated for case-1 and case-3 for several 20 s windows as given in Fig. 4.30 and Fig. 4.31, respectively in the following lines.

#### **4.7.5.1 Case-1**

The Prony results for a 20 s window for case-1 are given in Table. 4.20.

1. The corresponding frequency plot for 50 to 70 second time interval is given in Fig. 4.30 (a). The amplitude of the oscillations during this time interval is seen to be sustained. Such a behaviour is not properly captured by the Prony method where the dominant mode is seen to have a negative damping indicating a growth in oscillations.
2. The amplitude of the oscillations in 70 to 90 s interval is showing an increasing as well as decreasing trend as shown in Fig. 4.30 (b). Prony analysis for this time span indicates a single dominant mode with positive damping, which does not adequately represent the whole signal in the window -see Table. 4.20.

From Table. 4.13, it can be seen that the said interval is divided into two consecutive windows of each 10 s duration. When mode estimations are carried in these two windows the respective damping factors correctly predict the oscillation trends.

3. Similarly, for the time interval ranging from 90 to 110 s -see Fig. 4.30 (c) the Prony method throws up modes which are having both negative and positive damping.
4. For 110 to 130 s window -see Fig. 4.30 (d), the Prony estimates indicate a single

dominant mode with positive damping, which fails to validate the signal characteristics in the said interval.

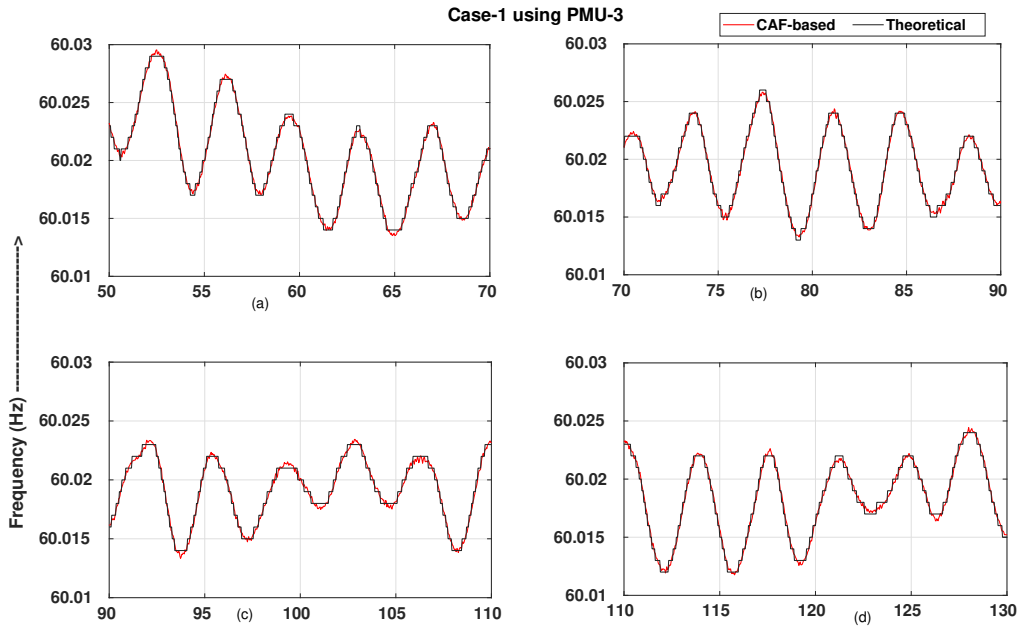


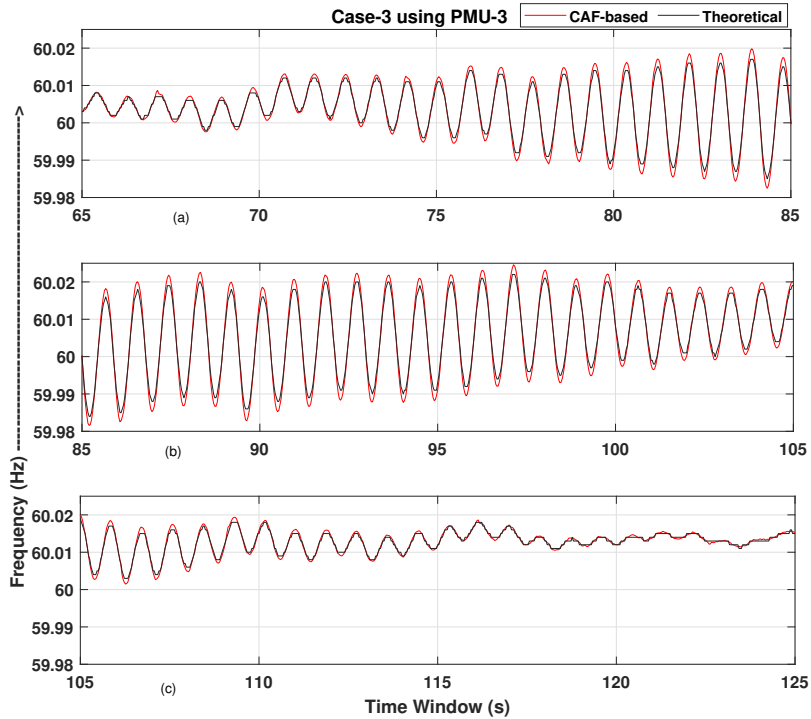
Figure 4.30: Prony based mode estimation for case-1 using 20 s data windows

Table 4.20: Prony analysis of different 20 s windows for case-1 using PMU-3 CAF signals (30 fps)

Time Window Chosen (s)	Dominant Modes	Frequency (Hz)	Damping Ratio	Time (s)	$n$
50 s to 70 s	$0.044 + 1.67j$	0.26	-0.0263	11.4	276
70 s to 90 s	$-0.0458 + 1.66j$	0.26	0.0276	9.17	282
90 s to 110 s	$0.137 + 1.902j$	0.3	-0.0718	9.08	282
	$-0.115 + 1.841j$	0.29	0.0623		
110 s to 130 s	$-0.058 + 1.74j$	0.27	0.033	7.5	258

#### 4.7.5.2 Case-3

For 20 s window, the results of mode estimation are given in Table. 4.21.



**Figure 4.31:** Prony based mode estimation for case-3 using 20 s data windows

1. For the first, window ranging from 65 to 85 seconds, the signal shows a conspicuous increasing trend throughout, as indicated in Fig. 4.31 (a). Here the Prony algorithm is able to accurately estimate the frequency of oscillation as well as its damping ratio, as given in Table. 4.21.
2. The frequency plot from 85 s to 105 s range shows an oscillation trend which gradually decreases, as shown in Fig. 4.31 (b). The Prony method fails to identify the decreasing oscillation trend of the dominant mode, indicating only a slight negative damping present in the initial part of the signal. This is indicated in Table. 4.21. However from Table. 4.15, it can be verified that when the said interval is divided into two consecutive windows of a shorter duration of 10 s, the estimated damping factors in these windows, accurately depict the decreasing oscillation trend.
3. The last window shown here ranges from 105 to 125 s, with a single dominant trend present in the signal as shown in Fig. 4.31 (c). Here, the Prony method successfully estimates the dominant mode, -see Table. 4.21.

**Table 4.21:** Prony analysis of different 20 s windows for case-3 using PMU-3 CAF signals (30 fps)

Time Window Chosen	Dominant Modes	Frequency (Hz)	Damping Ratio	Time (s)	$n$
65 s to 85 s	$0.0813 + 7.18j$	1.14	-0.0116	8.9	278
85 s to 105 s	$0.0142 + 7.125j$	1.13	-0.002	8.6	274
105 s to 125 s	$-0.15 + 7.31j$	1.16	0.0205	8.4	272

### 4.7.5.3 Case-1 and Case-3 with 40 s window

Prony estimates for a window length of 40 s, for case-1 and case-3, PMU-3 CAF signals, ranging from 90 to 130 s and 65 to 105 s, respectively are given in Tables. 4.22 and 4.23. As seen previously, for longer window lengths with multiple signatures the Prony method fails to segregate the dominant modes. For example, in case-1 an increasing oscillation trend can be observed during the 105 to 115 s interval, -see Fig. 4.32. This increase in the amplitude is not reflected in the Prony analysis results of the signal, as given in Table. 4.22. On the other hand the frequency values for both the cases are accurately identified, even for the longer window length. The execution time as well as the value of the order of the linear predictor ( $n$ ) are high due to the increased window length for both the cases. Due to such a high value of “ $n$ ”, the reconstructed signal based on the Prony estimates closely matches with the original input signal, as shown in Fig. 4.32.

**Table 4.22:** Prony analysis of a 40 s window for case-1 using PMU-3 CAF signal (30 fps)

Time Window Chosen	Dominant Modes	Frequency (Hz)	Damping Ratio	Time (s)	$n$
90 s to 130 s	$-0.0124 + 1.7013j$ $-0.0152 + 1.43j$	0.27 0.226	0.0073 0.0106	113.78	554

**Table 4.23:** Prony analysis of a 40 s window for case-3 using PMU-3 CAF signal (30 fps)

Time Window Chosen	Dominant Modes	Frequency (Hz)	Damping Ratio	Time (s)	$n$
65 s to 105 s	$0.0075 + 7.1582j$ $-0.0046 + 6.99j$	1.139 1.11	-0.001 0.0007	87.7	518

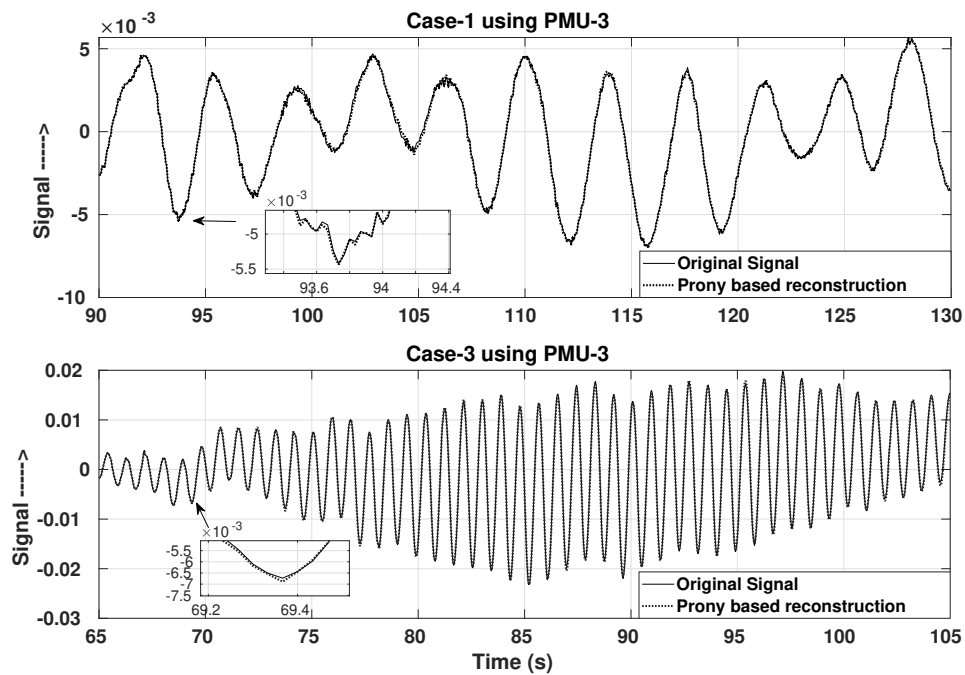


**Figure 4.32:** Fitment for 40 s data windows for case-1 and case-3.

The above analysis clearly demonstrate that one should be very careful while choosing the window length for a proper mode estimation. Some guidelines for choosing an appropriate window length for mode estimation are given as follows :

1. Since electromechanical oscillation frequencies range from 0.05 to 4 Hz, a window span of 40 s can be initially chosen. On the other hand, one can use FFT/power spectrum analysis to get a rough estimate of the dominant frequency present in the signal. Based on this a window length may be chosen which pertains to 5 times the time-period for inter-area frequencies and 20 times the time-period for local mode frequencies (in the range of 1 to 3 Hz).
2. Using the chosen window of data, a preliminary mode estimation can be made based on the Prony algorithm. A visual comparison of the signal oscillation trend and the estimated modal values may be made. If this validation is not adequate, the length of the data window is halved.

3. After halving the data window length, the mode estimation is again performed and checked for consistency based on visual inspection.
4. This process may be repeated until the Prony results match with the features of the signal in the chosen data window.
5. The frequency in the data window can be roughly estimated by approximately choosing a cycle of data and can be compared with the Prony based results as in Fig. 4.19. Visual inspection can also provide a rough idea of the nature of the damping existent in the chosen window which can be compared with the Prony based results.
6. Increasing the window length to 40 s for case-1 and case-3 Prony analysis, leads to further ambiguity in the dominant mode estimates. Such long duration windows result in an increased execution time as well as the order of “ $n$ ”, even while using low frame rate signals.

#### 4.7.6 Effect of starting point of the data window on mode estimation

Another point to be noted while performing mode estimation using the Prony method is choosing the starting point of the data window. Usually, an event detection algorithm locates the start of an oscillatory event and initiates a data window for mode estimation. This initial placement of the data window is found to effect the dominant mode calculation for signals with multiple characteristics in a short time-span, such as seen in case-1 and case-3. This is shown by delaying the starting point by 5 s for case-1 as depicted in Fig. 4.33, and similarly advancing by 5 s for case-3, as shown in Fig. 4.34. The shifting of the starting time for the window resulted in some inconsistency in the damping factor estimation for the 85 s to 95 s window, -see Table. 4.24 for case-1. However, for case-3, the change in the starting point has shown no major effect on the mode estimates, -see Table. 4.25.

**Table 4.24:** Prony analysis for Case-1 CAF-based (30 fps) frequency signals using 10 s windows with a delay of 5 s

Time Window Chosen	Dominant Modes	Frequency (Hz)	Damping Ratio	Time (s)	$n$
75 s to 85 s	$-0.0075 + 1.678j$	0.26	0.0045	1.23	134
85 s to 95 s	$-0.08 + 1.764j$	0.28	0.0453	1.27	136
95 s to 105 s	$-0.0375 + 1.715j$	0.27	0.0219	1.23	134
105 s to 115 s	$0.05 + 1.64j$	0.26	-0.0305	1.27	132

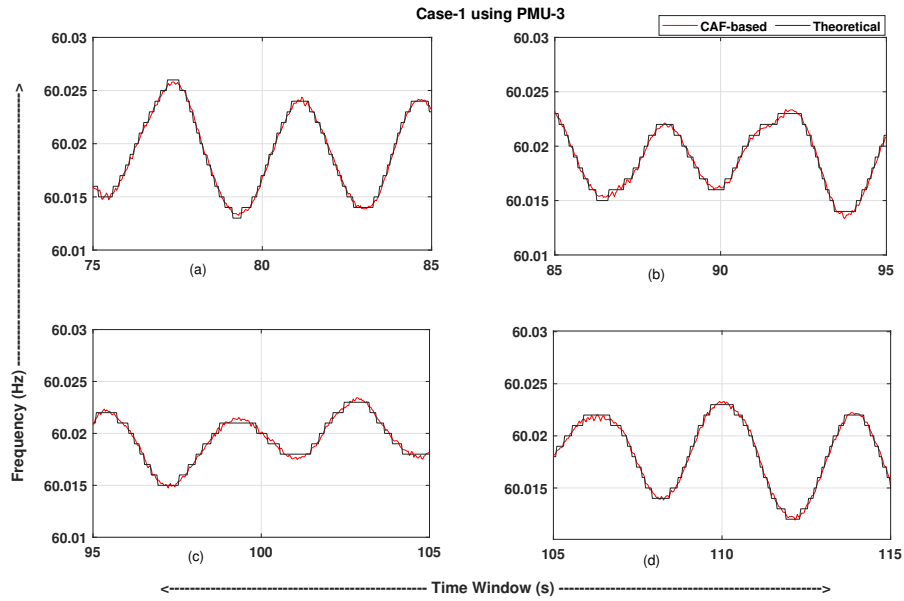


Figure 4.33: Change of starting point of 10 s frequency window for case-1

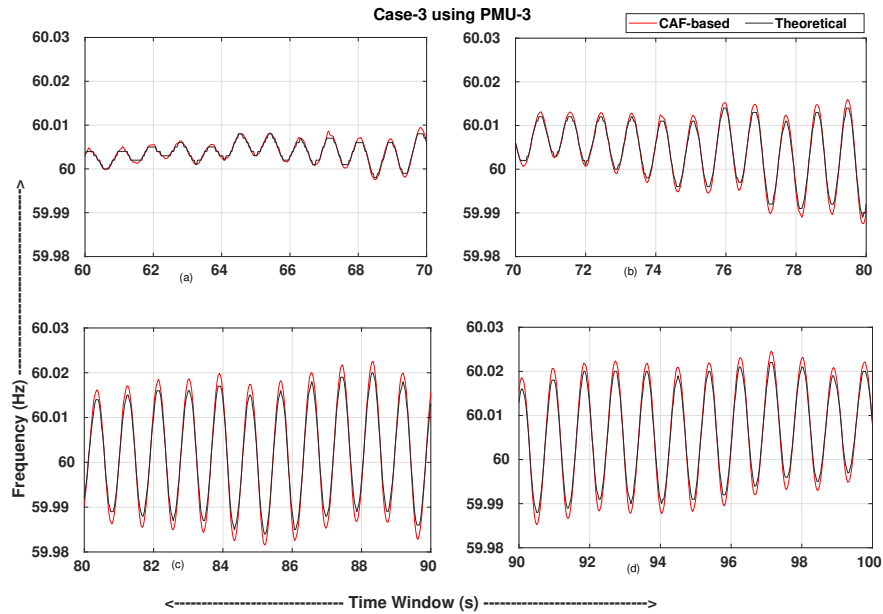


Figure 4.34: Change of starting point of 10 s frequency window for case-3



**Table 4.25:** Prony analysis for Case-3 CAF-based (30 fps) frequency signals using 10 s windows with an advancement of 5 s

Time Window Chosen	Dominant Modes	Frequency (Hz)	Damping Ratio	Time (s)	$n$
60 s to 70 s	$0.129 + 7.18j$	1.14	-0.018	1.3	138
70 s to 80 s	$0.0724 + 7.16j$	1.14	-0.0101	1.1	130
80 s to 90 s	$0.0047 + 7.13j$	1.13	$-6.6 \times 10^{-4}$	1.03	116
90 s to 100 s	$-0.0035 + 7.124j$	1.13	$4.9 \times 10^{-4}$	1.25	134

#### 4.7.6.1 Inclusion of Pre-Event Signal for Prony Analysis

For case-3 data points pertaining to the pre-event time are included in the Prony analysis time-window. The window ranging from 57 to 67 s is subjected to Prony analysis and the results are given in Table. 4.26. Compared to the results obtained in Tables.4.15 and 4.16, where the time-window consisting of the event is subjected to Prony analysis, Table. 4.26, indicates multiple dominant modes. This includes the regional mode with a frequency of 1.14 Hz, along with a low frequency mode of frequency 0.321 Hz with a negative damping ratio. This shows that the use of pre-event signal results in erroneous modal estimation results.

**Table 4.26:** Inclusion of pre-event signal in Prony time window for case-3

Time Window chosen (s)	Dominant Modes	Frequency (Hz)	Damping Ratio	Time (s)	$n$
57 to 67	$0.0177 + 2.017j$	0.321	-0.008	1.24	142
	$-0.1185 + 0.8063j$	0.128	0.1454		
	$0.0883 + 7.1919j$	1.144	-0.123		

#### 4.7.7 Mode estimation using ROCOF signals

ROCOFs evaluated for case-1 and case-3 are used for mode estimation and the results are compared with the Prony estimates obtained from their frequency counterparts. Both the frequency deviation and the ROCOF obtained using the CAF-based method, for the same time-windows are compared in Figs. 4.35 and 4.36, for case-1 and case-3, respectively. This is shown in order to visualize the time-lead nature of the ROCOF estimates compared to the frequency estimates. The dominant modes evaluated using the Prony method for the ROCOF signals are given in Tables. 4.27 and 4.28 for case-1 and case-3, respectively,

where the modal characteristics of the ROCOF signals can be compared with their frequency counterparts for the same time-window. The frequencies of oscillations obtained for either frequency or ROCOF signals via the Prony method for the same time-window are approximately the same. The damping nature of the ROCOF signals in the time-windows is also well reflected using the Prony method.

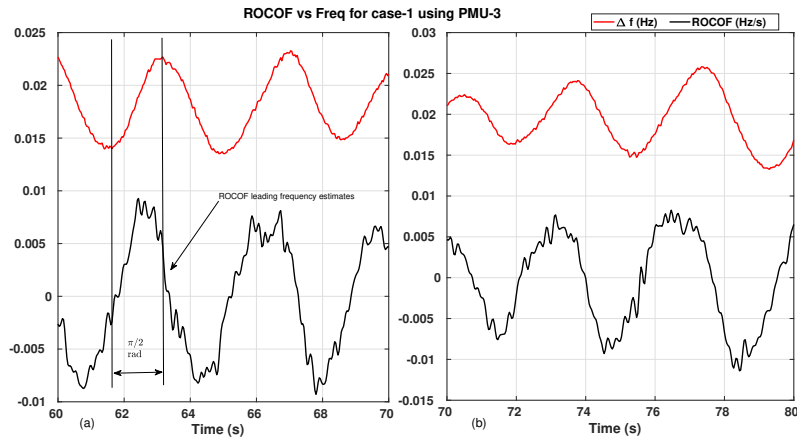


**Figure 4.35:** CAF-based ROCOF vs frequency for case-1

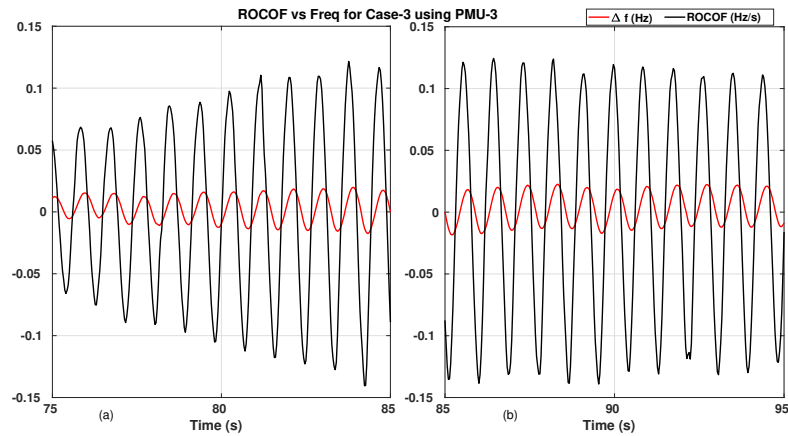


**Figure 4.36:** CAF-based ROCOF vs frequency for case 3

Based on the results obtained from the analysis of the 4-machine 10-bus power system

---

and using the ISO-NE signals, the following inferences can be made:

1. Power system frequency signals tend to have highly non-stationary characteristics along with linear or non-linear trends during fault conditions. Removing such trends prior to mode estimation is a challenging task in itself. In case of ROCOF, since the signals are inherently detrended to some extent, because of the derivative nature of the estimates, the order of the fitness is lower and may reduce the computation time.

**Table 4.27:** Modal performance comparison of ROCOF and frequency signals for case-1 (30 fps)

Parameters ↓	ROCOF Time-window (s)		Frequency Time-Window (s)	
	60-70	70-80	60-70	70-80
Dominant mode	$-0.024 + 1.7315j$	$0.2042 + 1.557j$	$-0.0127 + 1.75j$	$0.1856 + 1.589j$
	-	$-0.109 + 1.9836j$	-	$-0.17 + 2.054j$
$f$ (Hz)	0.27	0.248, 0.31	0.279	0.25, 0.32
Damping ratio	0.014	-0.13, 0.0552	0.0073	-0.116, 0.0825
Exec Time (s)	1.27	1.01	1.4	1.27
$n$	132	114	142	132

**Table 4.28:** Modal performance comparison of ROCOF and frequency signals for case-3 (30 fps)

Parameters ↓	ROCOF Time-window (s)		Frequency Time-Window (s)	
	75-85	85-95	75-85	85-95
Dominant mode	$0.0407 + 7.1287j$	$-0.0088 + 7.12j$	$0.048 + 7.13j$	$-0.009 + 7.11j$
$f$ (Hz)	1.13	1.13	1.13	1.13
Damping ratio	-0.0057	0.0012	-0.0067	0.0013
Exec Time (s)	1	0.8	1.01	1.02
$n$	96	86	112	112

2. It is shown using Tables. 4.27 and 4.28, that the execution time as well as the order of the linear predictor ( $n$ ) is lower while using ROCOF signals as compared to frequency signal, for the same time-window. This enables rapid mode estimation and therefore makes ROCOF signals viable candidates for Prony based analysis.
3. The execution time can be further reduced by appropriately choosing a base value of “ $n$ ”, for ROCOF based mode estimation. The base value of “ $n$ ” varies depending on the type of the system, nature of the fault and the frame rate chosen, etc. Hence, baseline analysis could be done for a particular system choosing an appropriate frame

rate, in order to allot a sensible value of “ $n$ ” which reduces the execution time for modal analysis.

## 4.8 Frequency Estimation During Loss-of-Synchronism of a Lab Machine

In this section frequency estimation using voltage signals during loss-of-synchronism condition of a laboratory generator is attempted. The terminal voltage  $v_a(t)$  of the generator during such an event is shown in Fig. 4.37 (a). Once the machine losses synchronism, it exhibits a slipping of pole and it continues until the machine is finally tripped. During this period the peak voltage value is seen to dip to as low as zero. Therefore, an accurate frequency computation during such conditions is very hard to achieve. Fig. 4.37 (b), shows the frequency estimates obtained employing PMU-3 as well as the reconstruction-based approaches. Clearly, all the frequency estimation methods fail to properly track the fast frequency changes in the signal during the loss-of-synchronism. This is also verified in Denys et al. (1992), where the author uses different methods to compute frequency during loss-of-synchronism but fails due to the extremely non-stationary nature of the voltage waveform. The “refined frequency” i.e.  $F_{R1}$ , obtained from (4.40) using PMU-3 also fails to track the fast frequency changes of the signal during such a condition.

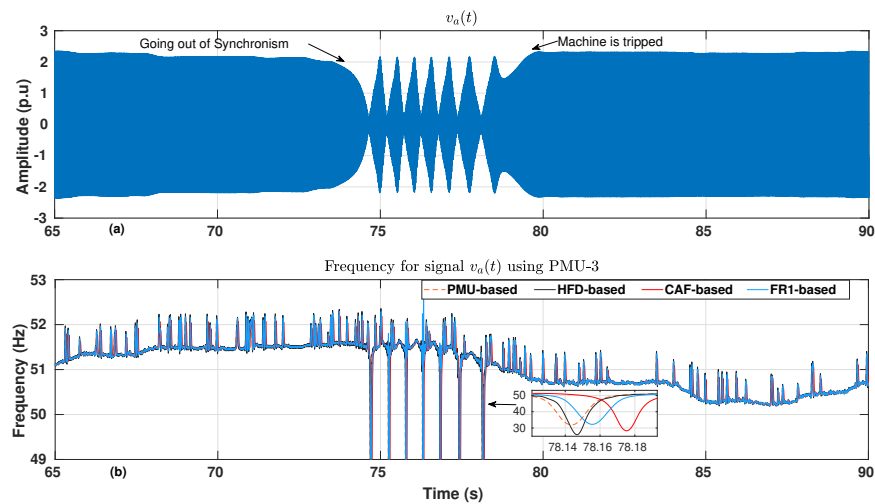


**Figure 4.37:** (a) Voltage signal during loss of synchronism. (b) Frequency computed during loss of synchronism.

## **4.9 Summary of the Presented Work**

In this chapter, a reconstruction-based frequency estimation technique is proposed. This method is shown to provide standard compliant frequency values during adverse signal conditions, even when employing computationally light phasor estimation techniques.

The work reported in this chapter can be summarized as follows :

1. It is shown that the time-domain signals obtained via reconstruction using off-nominal phasor samples accurately reflect the original signal frequency. These reconstructed signals are used as inputs to the CAF and the HFD method, for frequency estimation.
2. For different IEEE synchrophasor standard based test signals, the frequency estimates obtained employing the reconstruction-based method are shown to be far more accurate than those obtained using the PMU-based approach (especially in case of PMUs employing static model based algorithms). These frequency estimates are compliant with the latest synchrophasor standard, even for test signals containing inter-harmonic frequencies.
3. It is shown that the reconstruction block can be used as an extra module in the existing PMU architecture without disrupting the PMU overall structure. Therefore, even basic P-type PMU algorithms can be augmented with the reconstruction module in order to enhance their frequency estimation capabilities and make them M-class compliant.
4. The reconstruction-based approach is shown to successfully estimate the frequency and subsequently ROCOF for a simulated 4-machine, 10-bus power system. These signals are compared with the PMU-based frequency estimates and the FE, RFE values are noted. Mode identification is also performed using the reconstruction-based frequency and ROCOF estimates.
5. Disturbance related signals obtained from the ISO-NE power system are also subjected to the reconstruction-based approach and the computed frequency estimates are compared against values provided by the practical PMUs.
6. The reconstruction-based frequency and ROCOF estimates computed for different cases of the ISO-NE power system are subjected to Prony analysis for mode identification. The effect of window length, starting time instant, frame rate and the order of the linear predictor, on mode estimation is also studied.

7. Advantages of using ROCOF signals over frequency signals as inputs to the Prony algorithm for mode estimation are also demonstrated in this chapter.
8. It is also noted through a lab experimentation that an accurate frequency estimation during loss-of-synchronism condition is not straightforward.

The occurrence of events in a power system must be identified as accurately as possible in order to initiate appropriate action for protecting the power system. As shown in this chapter, for a power swing event, variation of the start time of windows employed for mode estimation results in ambiguity, especially in the damping ratio values. Such a discrepancy among others can be successfully avoided if the event start time is estimated with precision. Such a task is not easy due to the growing number of PMUs in WAMS. Identifying the occurrence of events and their location identification are therefore a challenge for power system operators. Hence, in the next chapter various event detection algorithms are discussed. These algorithms process data from multiple PMUs simultaneously in order to identify the occurrence of an event as well as provide information related to the localization. These algorithms employ signal processing based techniques to point out anomalies in PMU data, such as phasor magnitude, frequency and ROCOF. The capability of event detection algorithms to identify disturbances such as fault, load loss or loss-of-synchronism etc, is also verified in the next chapter.



---

## **Chapter 5**

# **POWER SYSTEM EVENT DETECTION AND LOCALIZATION-A NEW APPROACH**

### **5.1 INTRODUCTION**

Phasor measurement units connected to a wide area network send enormous amount of data to control centers, where the PDC streamlines the data to enable ease of analysis. This data encapsulates steady-state as well as dynamic behavior and therefore must be thoroughly analysed in order to understand the overall functioning of the power system. Data points exhibiting abnormal variation are identified using event detection algorithms, which help the power system operator to initiate appropriate protection or control actions. Event detection in power systems is the process of analyzing PMU data streams in order to discover sets of data points which do not match with the ambient or normal values. Event detection algorithms primarily include training and non-training based techniques. Any irregular patterns or signatures left on a power system signal define the type of an event. Whenever an event detection algorithm flags the occurrence of a disturbance the localization and classification processes are initiated. The portion of the power system where an event is originated or which is affected the most by a disturbance, is identified using the localization logic. This helps the power system operator to take necessary actions in order to curtail the spread of the disturbance.



In this chapter an event identification, localization and classification tool is designed in order to illustrate an application of WAMS signals. Data obtained from multiple PMUs is analysed using non-training based event detection techniques, notably the wavelet transform and the standard deviation method. Signals obtained from multiple PMUs installed throughout the power system are examined using these methods in order to accurately identify the occurrence of an event. The effectiveness of these methods is demonstrated using practical signals from the ISO-NE power system as well as signals obtained from a simulation based 4-machine 10-bus power system. These signals include, the voltage phasor magnitude, frequency and the ROCOF. Occurrence of an event is flagged by comparing the wavelet energy and standard deviation values of a certain PMU signal against a set threshold. Two methods such as the Percentile and  $3 - SD$  approaches are illustrated and compared to determine an appropriate threshold. An event localization algorithm based on the number of PMUs involved in the event detection stage is also presented. Based on the presented algorithm, disturbances are classified as local or wide-spread events. Finally, a method to identify a loss-of-synchronism condition using phase angle difference signals obtained across transmission lines is also proposed.

## **5.2 Stages Involved in Event Detection and Localization**

The overall process of analysing PMU/PDC data for power system disturbance related studies is called as event analysis. It must be noted that event detection is an integral part of the wider event analysis process. The event analysis process includes aspects such as root cause analysis, disturbance categorization, duration of disturbances, actions to be taken, lessons to be learned, etc. Our focus in this chapter will be the event detection and localization aspect of event analysis. Detection and localization of an event can be undertaken either on-line or off-line and generally includes the following stages :

1. Detection of an event.
2. Localization of an event.
3. Classification of an event.

These steps are summarized in Fig. 5.1. In the first stage, data is gathered from multiple PMUs and processed using event detection algorithms. In case the PMU data consists of samples which can be categorized as outliers based on a chosen threshold, an event is

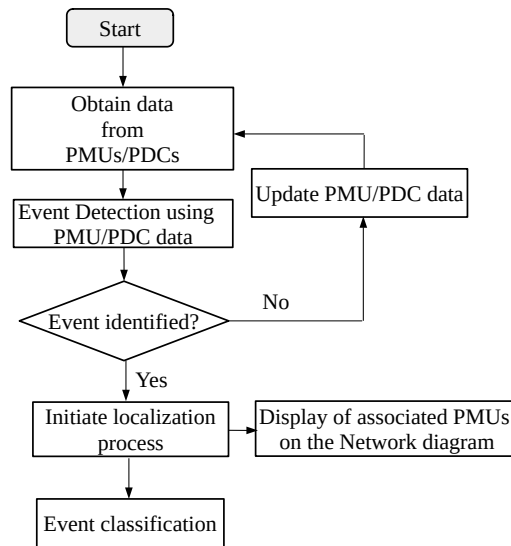


**Figure 5.1:** A generalized representation of PMU data based event detection, localization and classification.

flagged, otherwise the PMU data set is updated to incorporate new samples. Once an event is detected, the localization process is initiated. This step involves identification of the portion of the grid where the disturbance has originated or which is affected the most. Localization enables highlighting of the affected substations or areas in order to help the operator to take decisions for ensuring normal operation of the overall power system. The procedure for event localization is followed by event classification. In Kim et al. (2015), events are classified as voltage and/or frequency-related, whereas in Ge et al. (2015), events are categorized as real power type or reactive power type. Authors in Pandey et al. (2020), group disturbances as, active power related events, reactive power related events or fault events. Similarly, authors in Shaw and Jena (2020), have classified events as, a) generation loss, b) load loss, c) impulse type, d) oscillatory type, e) islanding type.

In case of oscillation mode identification, event detection plays a crucial role. The correct instant at which the oscillations begin in a given signal (for example, frequency, voltage magnitude or ROCOF) must be identified using the event detection algorithms. If the onset of oscillations is detected preemptively then the pre-event signal will be used as an input to the mode identification algorithms resulting in a failure to estimate the modal parameters, as depicted in the previous chapter. Same is true if an event is detected later than its actual incipient time (Gajjar and Soman, 2014). Such estimates can severely influence the modal inferences and possible control actions.

### **5.3 Wavelet Transform**

Time-domain analysis reveals time-information of a signal, whereas frequency domain analysis provides us with information related to the frequency content present in a signal. The trade off being lack of frequency and time information respectively. This problem is overcome by the “Gabor” transform, (Misiti et al., 1996), (Proakis and Manolakis, 2007), where a fixed length window of  $t_w$  s, is slid across the whole signal duration to extract useful frequency information at any time,  $t$  of the time-domain signal. Such a method proves helpful while extracting frequency and time information from a signal. The lowest frequency fitting in the window, i.e.,  $1/t_w$  Hz is the frequency resolution provided by the “Gabor” filter. This resolution is constant due to the fixed window size and hence if a small window size is used, one loses low frequency content (which is not localized) present in the signal, while as if a relatively long duration window is used high frequency contents which are localized in the signal are not appreciated. Therefore, it can be said that frequency fitting the Gabor window length are retained whereas others are lost.

Such a problem is addressed using the Wavelet Transform. Wavelet literally means a little wave. Wavelet is a waveform of short time-duration with zero mean. Signals with sharp changes can be better analyzed using irregular wavelets, than smooth sinusoids. Popular methods for extracting time-related and/or frequency-related features from signals are shown in Fig. 5.2. The x-axis represents time, whereas the y-axis represents the frequency. The vertical lines indicate time resolution whereas the horizontal lines indicate the frequency resolution offered by the method. Time-series representation of a signal provides excellent resolution in time but the frequency resolution or information is almost non-existent, as shown in Fig. 5.2 (a). The Fourier method on the other hand provides excellent frequency resolution, but absolutely no time information about the occurrence of a given frequency in the signal, as seen in Fig. 5.2 (b). Uniform time and frequency resolution is obtained while using the “Gabor” transform as indicated in Fig. 5.2 (c). The window length is constant and is moved across the whole signal to extract frequency information at various time instances. The constant window length results in a uniform frequency resolution, while as movement of the window across the signal leads to a uniform time resolution. The wavelet transform on the other hand provides the best of the both worlds (Mallat, 2008), (Kutz, 2013). A good time resolution is obtained via the translation parameter, and an excellent frequency resolution is obtained via the scaling parameter to extract high and low

frequency contents from a signal, this is demonstrated in Fig. 5.2 (d).

The salient differences between the wavelet and the Fourier transform are listed as follows:

- Basis functions for the Fourier transform are smooth sinusoids of infinite duration ranging from  $-\infty$  to  $+\infty$ , whereas the basis functions for the wavelet transforms are irregular and predictable signals of a very short duration (Kutz, 2013).
- Fourier analysis involves breaking up of signals into sine waves of different frequencies whereas the Wavelet analysis involves breaking up of a signal into shifted and scaled versions of the mother wavelet.

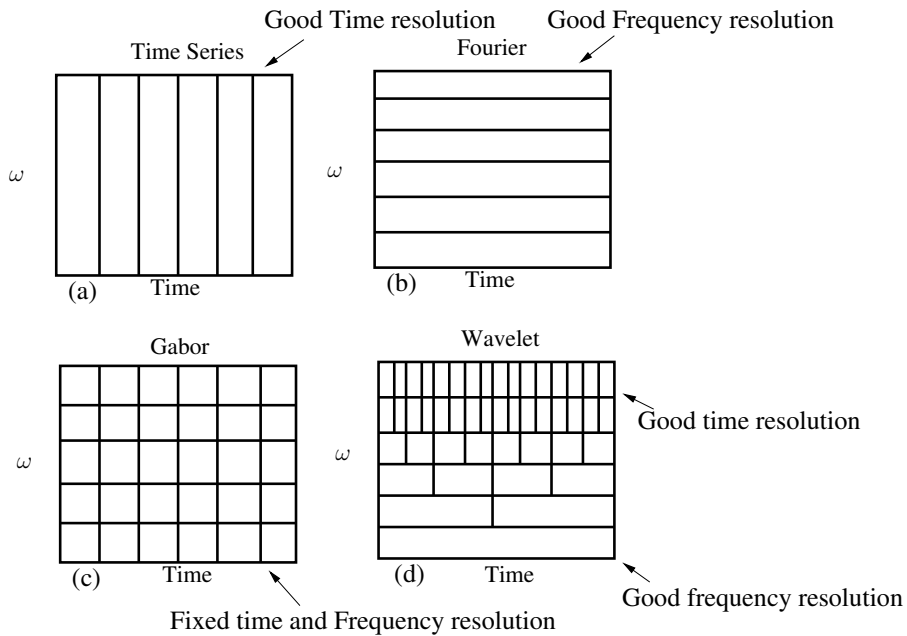


**Figure 5.2:** Different transformations comparison

A mother wavelet basis function is represented as,

$$\psi_{a,b}(t) = \frac{1}{\sqrt{a}} \psi\left(\frac{t-b}{a}\right) \quad a, b \in R \quad (5.1)$$

$$a \neq 0$$

$a$ , is known as the scaling parameter and  $b$  is the translation parameter. Scaling a wavelet simply means, stretching or compressing it, whereas translating a wavelet means moving it back and forth in time. Also note that, low scale  $a$ , indicates a compressed wavelet which captures rapidly changing details from high frequency signals, whereas, a high value of  $a$ , indicates a stretched wavelet which captures the low frequency details from a signal. Hence, the wavelet transform is also synonymous with Multi Resolution Analysis (MRA), due to the scaling factor feature which enables the compression and expansion of the wavelet function. Such a flexibility is a feature of the wavelet transform and therefore enables it to analyse irregular and distorted signals better than conventional frequency or time-domain methods. The continuous wavelet transform (CWT) of a signal  $x(t)$  is obtained by using the scaled and shifted versions of the wavelet function  $\psi$ , as,

$$C(\text{scale}, \text{position}) = \int_{-\infty}^{+\infty} x(t) \psi(\text{scale}, \text{position}, t) dt \quad (5.2)$$

or

$$C(a, b) = \int_{-\infty}^{+\infty} x(t) \psi_{a,b}(t) dt \quad (5.3)$$

$C$ , represents the wavelet coefficients which are scale and position dependent.

### 5.3.1 Discrete Wavelet Transform

The discrete wavelet transform (DWT) is implemented using a two-channel sub-band coder algorithm given by (Mallat, 1989), (Mallat, 2008), (Kutz, 2013). This algorithm involves two types of filters which help in computing the detail and the approximation coefficients of the signal. The detail coefficients represent the high frequency part of the signal whereas the approximation coefficients represent the low frequency part of the signal. The filters are related to the scaling ( $\phi$ ) and the wavelet function ( $\psi$ ) as follows,

$$\phi(t) = \sqrt{2} \sum_{-\infty}^{\infty} h_0(n) \phi(2t - n) \quad (5.4)$$

$$\psi(t) = \sqrt{2} \sum_{-\infty}^{\infty} h_1(n) \phi(2t - n) \quad (5.5)$$

where  $h_0$  and  $h_1$  represent the discrete FIR based low-pass and high-pass filter coefficients, respectively.

The scaling function ( $\phi$ ) and the wavelet function ( $\psi$ ) should form an orthogonal basis so that the approximation and detail coefficients can be easily calculated using inner products such as,

$$c_{j,k} = \langle x(t), \phi_{j,k}(t) \rangle \quad (5.6)$$

$$d_{j,k} = \langle x(t), \psi_{j,k}(t) \rangle \quad (5.7)$$

where  $c_{j,k}$  and  $d_{j,k}$  represent the approximation and the detail coefficients, respectively. It should be noted that  $(a, b)$  in the continuous domain are replaced by  $(j, k)$  in the discrete domain.

Single stage of filtering is shown in Fig. 5.3. Two output signals are obtained by passing the input signal  $x(t)$  through two complementary filters. “A” represents the first stage approximation coefficients ( $c_{j,k}$ ) whereas “D” represents the detail coefficients ( $d_{j,k}$ ) of the input time-domain signal  $x(t)$ . Such an operation leads to doubling of the amount of data, for example if  $x(t)$  consists of 1000 samples, “A” and “D” will each have 1000 samples. A better way to perform such a decomposition is by keeping one point out of two in each of the two 1000-length samples, without loss of information. Such an exercise enables the use of the wavelet transform as an effective data compression tool. This is the idea of downsampling involved in discrete wavelet transform as shown in Fig. 5.4. The “cA” and “cD” represent the approximation and detail coefficients available at the output end of a single stage of a DWT.

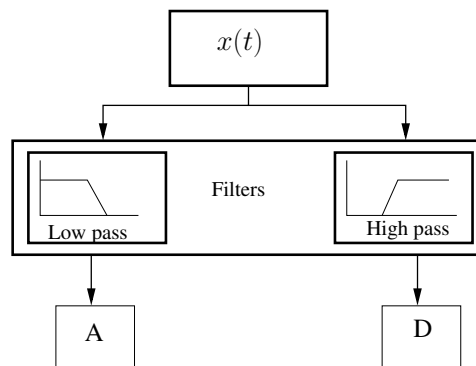


**Figure 5.3:** Complementary filters used in discrete wavelet transform

The process of decomposition of the original input signal can be iterated, with contin-

uous approximations (cA's) being decomposed as and when they are obtained, in order to break down a signal into many lower resolution components. This is popularly known as the wavelet decomposition tree, as shown in Fig. 5.5.

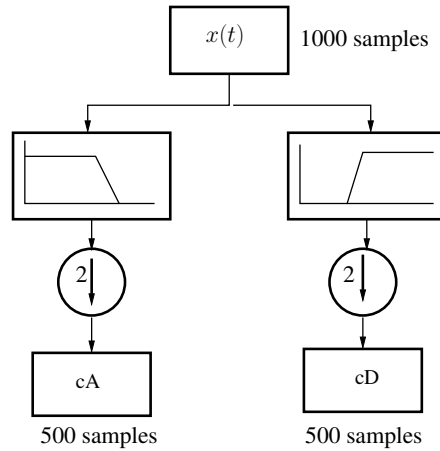


**Figure 5.4:** Downsampling in discrete wavelet transform

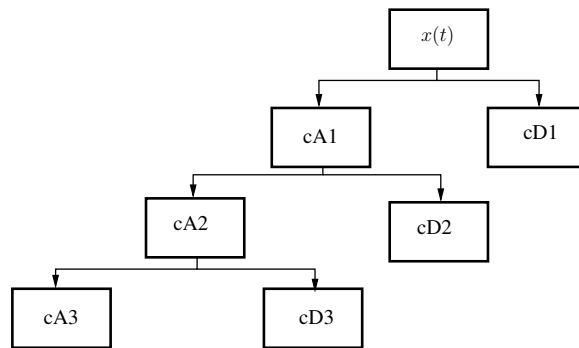


**Figure 5.5:** Wavelet decomposition tree

### 5.3.2 Event Detection Using Wavelet Transform

The detail coefficients computed using (5.7), represent the high frequency content present in the signal. These coefficients are capable of depicting the abrupt changes occurring throughout the signal duration. The number of detail coefficients depends on the level of decomposition one chooses to perform as is shown in Fig. 5.5. The detail coefficients used for event detection in Gao and Ning (2011), are computed for “db2” wavelet with level 5

decomposition. The level of decomposition and the type of wavelet to be chosen for event detection applications depends on the signal used as an input, the system behaviour, nature of the noise, etc. Generally, the level of decomposition is chosen by calculating the detail coefficients energy (WE) and the level with the highest energy values are considered as best fit for the application. The wavelet energy,  $WE_n$ , for the  $n^{th}$  window can be computed using the detail coefficients of a signal as follows,

$$WE_n = \sqrt{\frac{1}{N} \sum_{j=1}^J \sum_{k=1}^{N_j} |d_{j,k}|^2} \quad (5.8)$$

where  $J$  is wavelet decomposition level and  $N_j$  is the number of coefficients in each decomposition level,  $N$  is the window length chosen to compute the wavelet energy. The wavelet energy parameter therefore reflects the features of the detail coefficients and can be used as an indicator for detecting events.

$WE_n$  can be normalized to reduce the impact of non-event disruption on detection reliability. High  $WE_n$  values can be obtained for PMU data with a lot of fluctuations but no event occurrences. As a result, when compared to a signal with slow variations, a highly varying signal is shown as an incorrect event. Hence, the normalized wavelet energy (NWE) parameter has been introduced by Kim et al. (2015), in order to reduce the number of false alarms caused due to the  $WE_n$  based event detection algorithms. A base window length pertaining to a 1 h duration is chosen in Kim et al. (2015), which represents both tendency and stationary properties of signals for the purpose of normalization of the highly varying  $WE_n$  values. The  $NWE_n$  can be computed as,

$$NWE_n = \frac{WE_n}{WE_{nBase}} \quad (5.9)$$

where  $WE_{nBase}$  denotes the  $WE_n$  calculated for 1 hr window length. The value of  $NWE_n$  is around unity for ambient conditions for all signals (voltage magnitude, frequency, ROCOF etc). The value of threshold is set to 3.38 and 3.16 for frequency and voltage signals, respectively by Kim et al. (2015).

As an example,  $NWE_n$  values are computed for the ISO-NE case-3 voltage magnitude and frequency signal for Sub-2 Ln-2. The length of the data window used for  $WE_n$  calculation is chosen to be 1 s, i.e., 30 samples (since frame rate of data provided by ISO-NE system is 30), whereas the length of the data window used for  $WE_{nBase}$  is chosen as 30 s, i.e., 900 samples ( $N_h$ ), because of non availability of data for an hour. The resulting plots



are given in Figs. 5.6 and 5.7, respectively.

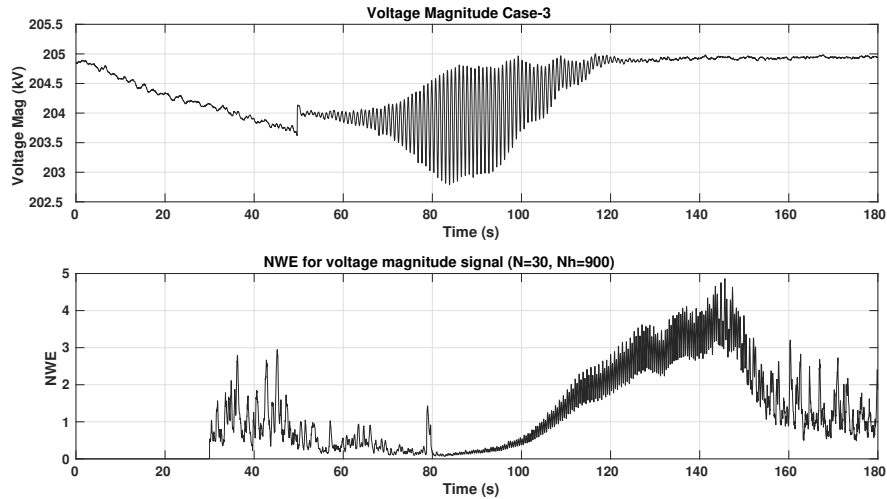


**Figure 5.6:** Normalized wavelet energy for voltage magnitude signal case-3.

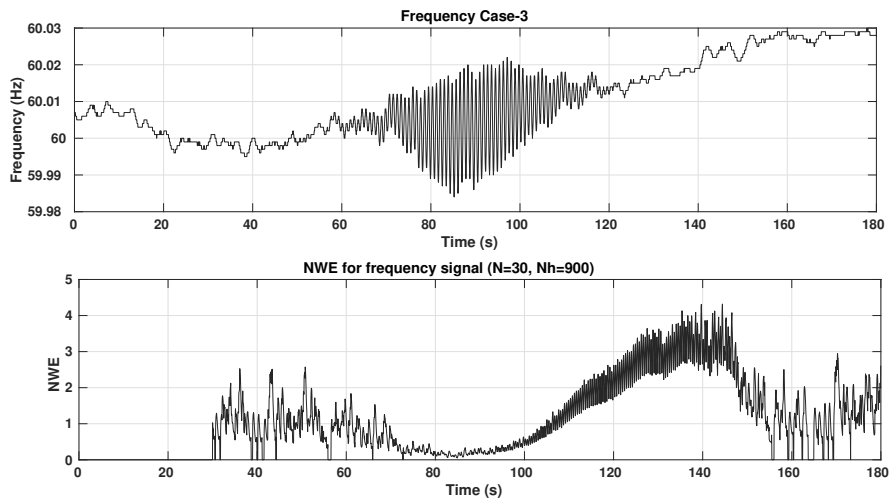


**Figure 5.7:** Normalized wavelet energy for frequency signal case-3

Clearly the events are not properly detected at the exact incipient time and choosing the thresholds for such a case also emerges as a challenge. No sudden spikes in the  $NWE_n$  values are seen over the duration of the data which might help one to pin point the time at which the fault occurred. A gradual increase in the  $NWE_n$  values is seen after the fault

incipient time and hence it is not easy to choose a suitable threshold value for voltage or frequency signals. Therefore, it is concluded that the lack of availability of historical data for normalization results in poor event detection in case the  $NWE_n$  is used. Hence, hereafter for the purpose of analysis, only the wavelet energy,  $WE_n$ , is computed and used for event detection.

## 5.4 Standard Deviation

Standard deviation is a useful tool for finding anomalies in normally distributed data (Shaw and Jena, 2020). Outliers in a large data set can be identified using standard deviation calculation. The standard deviation is a measure of how spread out the data is in comparison to the mean. A low value of standard deviation indicates that data is grouped around the mean, whereas a high value of standard deviation indicates that the data is more dispersed. The extent of variability of data points in a large data set is indicated by the value of the standard deviation. The standard deviation (SD) of a data set “x” with  $N$  elements can be calculated as follows,

$$SD = \sqrt{\frac{\sum_{i=1}^N (x_i - \mu)^2}{N}} \quad (5.10)$$

where  $x_i$  represents the  $i^{th}$  element of the data set and  $\mu$  is the mean of the data set.

Some of the key features of Standard deviation of a data set are:

1. The value of  $SD = 0$  only when there is no spread among the data points, i.e., when all the sets of observations have the same value. The data is tightly packed around the mean.
2.  $SD > 0$  shows the spread of the data points far away from the mean denoting variability of data values. The data in this case is loosely packed around the mean.
3. Extreme observations or outliers in the data set drastically affect the SD, even more than they affect the mean ( $\mu$ ).
4. Addition of a constant value to a data set, affects the mean values, but not the spread of the data. Therefore the SD of the data set does not change due to the addition of a constant value.

Based on the above observations, to identify events occurring in a power system, standard deviation of PMU data is computed using a sliding window approach for the ISO-NE case-3, Sub-2 Ln-2 signals. The resultant SD plots are shown in Figs. 5.8 and 5.9, for voltage magnitude and frequency signals, respectively.

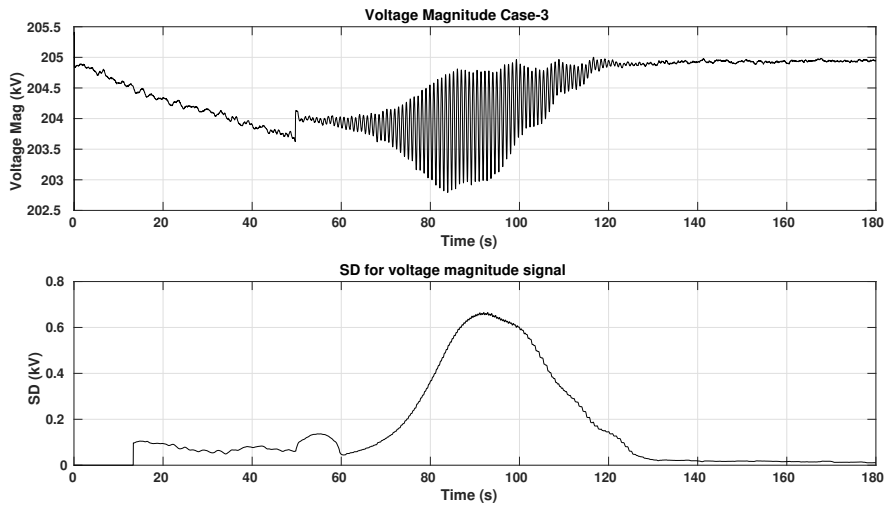


**Figure 5.8:** SD for voltage magnitude signal case-3.

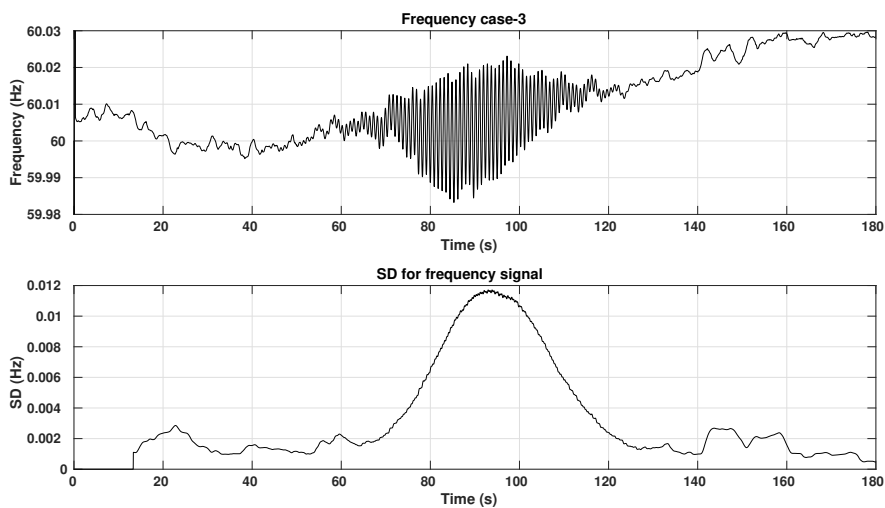


**Figure 5.9:** SD for frequency signal case-3

A 10 second long data window is used for standard deviation calculations and is moved

across the whole data set. Outliers in each data window exhibit high values of standard deviation, as can be observed around 49 s and 70 s, for the voltage magnitude signal, -see Fig. 5.8. For the frequency signal high values of SD can be observed starting from 70 s as shown in Fig. 5.9. The standard deviation of a window of data is compared against a set threshold to identify the occurrence of an event. The steps involved in event detection using the wavelet energy and the standard deviation based approaches are generalized and listed as follows.

## **5.5 Steps Involved in Event Detection and Localization Using WE and SD Methods**

Steps involved in event detection and localization are as follows :

1. Gather PMU data from, say  $N$  number of PMUs, installed in a power system. This includes, time-stamped voltage phasor, frequency and ROCOF signals.
2. De-noise the signals, using the wavelet transform. Here, the “db4” wavelet with level 2 decomposition is used.
3. A moving window of 10 s duration is chosen for all events except for generation or load loss, where a 20 s window is used.
4. Wavelet energy (WE) and Standard deviation (SD) of three signals, i.e., voltage magnitude, frequency and ROCOF are calculated, over a window.
5. The WE and SD values associated with a certain window are time-tagged pertaining to the end of the window.
6. If the values of WE or SD for a signal show an excursion above a chosen threshold ( $WE_{th}$  or  $SD_{th}$ ), an event is flagged depending on the following conditions:
  - (a) If  $N_1$  number of PMUs, such that  $N_1 \leq 10\%$  of  $N$  show excursions in WE or SD at the same time interval, then it is verified whether these  $N_1$  PMUs belong to a given sub-station.
    - If YES, a local event close to that sub-station/area is declared.
    - If NO,  $N_1$  PMUs are further checked for any malfunctioning.

- (b) In case  $N_1$  number of PMUs, such that  $N_1 > 10\%$  of  $N$ , show excursions in WE/SD at the same time interval, an event is flagged. Excursions in WE/SD can be seen in voltage or frequency or ROCOF signal or in all of the three signals of a PMU, depending on the nature of the disturbance.
7. The  $N_1$  PMUs ( $> 10\%$  of  $N$ ) exhibiting WE/SD excursions are sorted in the decreasing order of their highest WE/SD values. From this sorted list, the PMUs exhibiting excursions greater than 40% of the maximum value of WE/SD among the  $N_1$  PMUs are selected. This value of WE/SD is labelled as  $WE_{ce} = 40\%$  of  $WE_{max}$  and  $SD_{ce} = 40\%$  of  $SD_{max}$ , where  $WE_{max}$  and  $SD_{max}$ , represent the maximum value of WE and SD exhibited by the topmost PMU in the sorted list. The number of PMUs which demonstrate excursions greater than  $WE_{ce}$  and  $SD_{ce}$  are designated as  $N_2$ , and categorized as having “considerable excursions”.
  8. If  $N_2 \leq 20\%$  of  $N_1$ , then the disturbance is classified as a local event in the neighborhood of those substation(s)/area(s) to which  $N_2$  PMUs are connected.
  9. If  $N_2 > 20\%$  of  $N_1$ , then the disturbance is flagged as a wide-spread event. Here the disturbance might have occurred within the area or in an interconnected neighbouring area.
  10. Immediately after an event is flagged, the PMUs showing excursions are listed. In addition to that, the sub-stations and areas to which the PMUs are associated with, are also noted. By declaration of substation number or the area and highlighting in the layout diagram, the event localization procedure can be accurately verified. A flowchart depicting the steps involved in the event detection and event localization process is presented in Fig. 5.10.

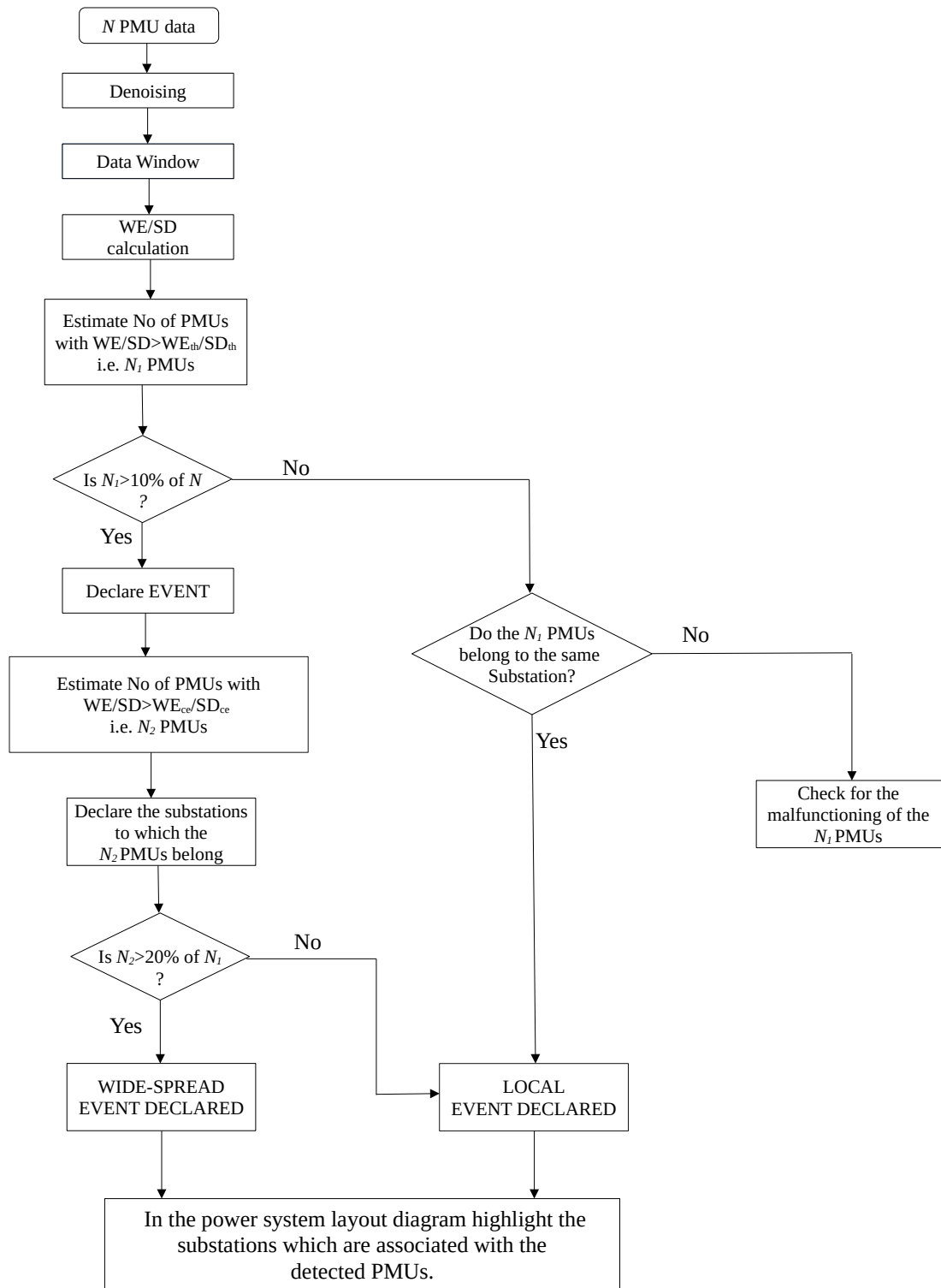


Figure 5.10: Event detection and localization flow chart

## 5.6 WE-based Detection Using ISO-NE Power System Signals

Data from the ISO-NE power system is used to demonstrate the detection of events using the Wavelet energy based approach. Data for the ISO-NE power system is available only for a limited duration of time which thereby hampers the Normalized WE calculations. Hence, a trail and error based threshold is chosen to demonstrate the event detection and localization procedure using only  $WE_n$  values. Note that a formal procedure to estimate a suitable threshold has been discussed in Section.5.9. Case-1 and Case-3 as labelled in (EECS, 2022) are chosen since they represent a wide-area as well as a local disturbance scenario, respectively. Data from all the 35 PMUs is used for event detection. The numbering of the PMUs is given in Appendix. A, which is done on the basis of the order in which they appear in the data file as provided by (EECS, 2022). It should be noted that among these 35 PMUs, PMUs-1, 29, 30, 31 for case-1 and only PMU-1 for case-3 are not utilized in the analysis as they are found to have errors in the PMU data while executing the algorithm. These PMUs are designated as malfunctioning PMUs.

The voltage magnitude, frequency and ROCOF signals for case-1 and case-3 for all the PMUs are shown in Figs. 5.11-5.16.

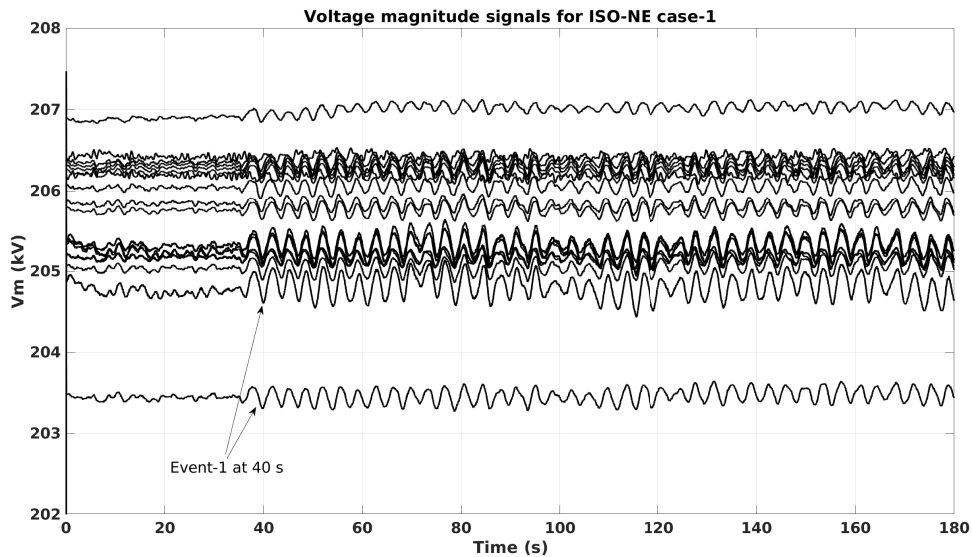
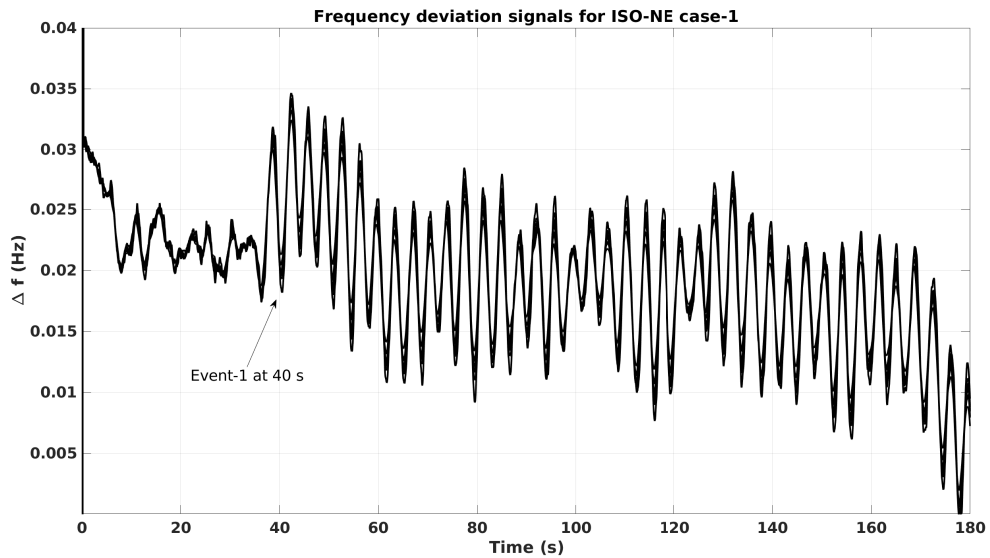
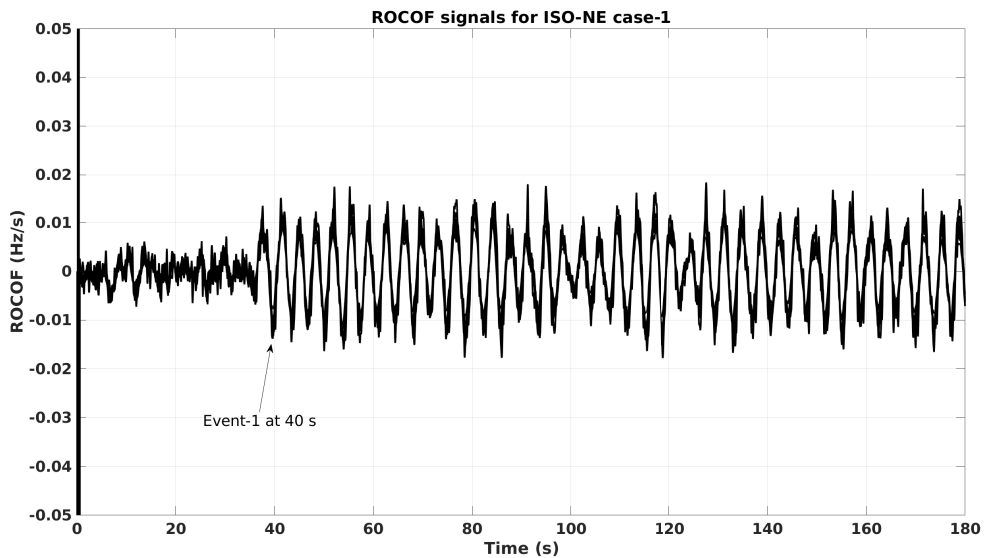


Figure 5.11: ISO-NE case-1 all voltage magnitude signals.



**Figure 5.12:** ISO-NE case-1 all frequency signals.



**Figure 5.13:** ISO-NE case-1 all ROCOF signals.

The low frame rate data available from the ISO-NE system is interpolated to a higher sampling rate (20 samples per cycle), in order to successfully construct the time-domain signals from phasor samples. These time-domain signals are fed to PMU-D for phasor,



frequency and ROCOF estimation as indicated in Fig. 4.16. The following cases are considered:

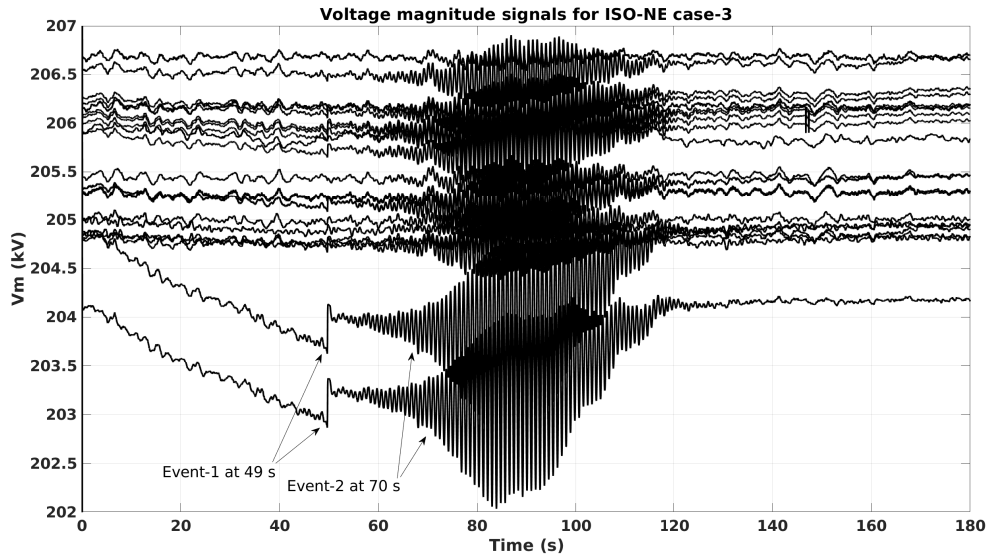


Figure 5.14: ISO-NE case 3 all voltage magnitude signals.

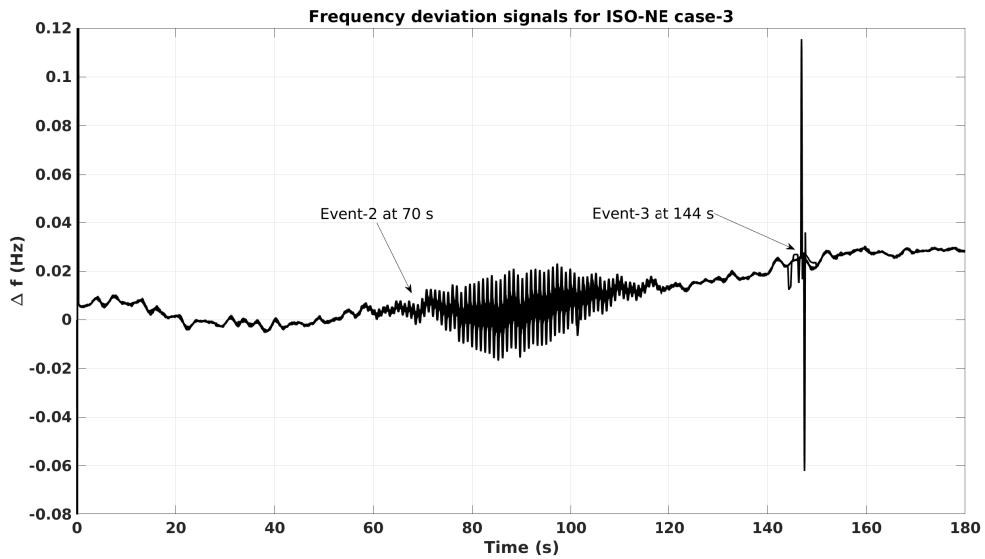
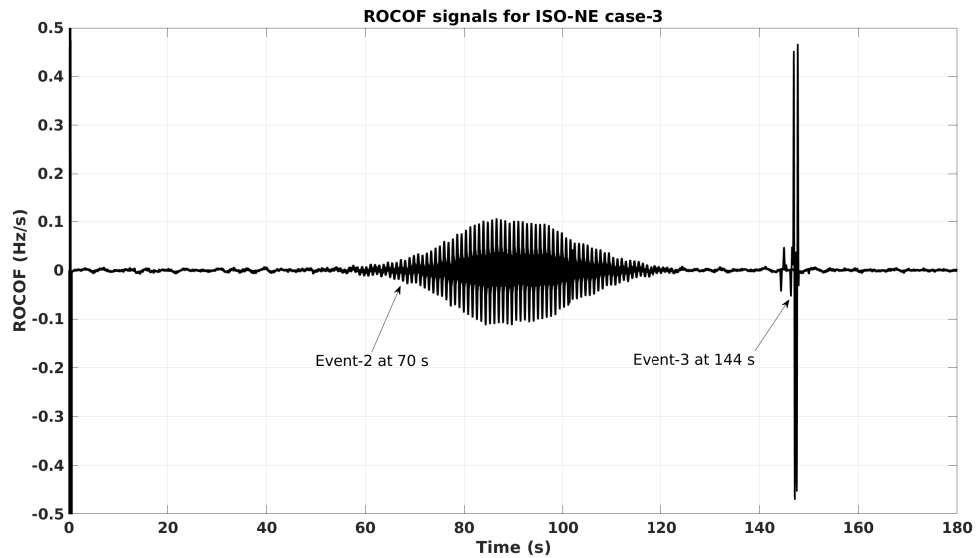


Figure 5.15: ISO-NE case 3 all frequency signals.



**Figure 5.16:** ISO-NE case-3 all ROCOF signals.

1. All case-1 signals indicate the occurrence of an oscillatory disturbance at around 40 s as marked in Figs. 5.11-5.13. This event is caused due to a large generator fault located outside ISO-NE in area-2 (EECS, 2022). Due to the system-wide nature of the oscillations all the functioning PMUs in the ISO-NE power system reflect a 0.27 Hz oscillation frequency.
2. For case-3, the following events are noted:
  - (a) A sharp spike in the voltage magnitude estimates can be visualized at around 49 s, -see Fig. 5.14. The magnitude of the spike varies in different PMUs, with some PMUs not reflecting the event at all. This event in the voltage signal is labelled as **Event-1**.
  - (b) Following the switching event, a sustained oscillatory event is seen in all the three signals, i.e., voltage magnitude, frequency, ROCOF as shown in Figs. 5.14-5.16. This event starts around 70 s and an oscillation frequency of 1.13 Hz is observed. This oscillatory event is labelled as **Event-2**.
  - (c) An irregular abrupt event is reflected only in frequency and ROCOF signals for this case at around 144 s. This event is labelled as **Event-3**.

Clear distinction cannot be made looking at these plots as to when and where the event takes place, hence these signals are processed using event detection algorithms to enable ease of analysis and visualization, so that power system operators can take better decisions.

### 5.6.1 Event Detection Using Case-1 Signals

Power system signals for case-1 obtained using PMU-D are subjected to wavelet energy calculations using (5.8). dB1 wavelet with level 3 decomposition is employed to obtain the detail coefficients which in-turn are used for energy computation. Data window of 10 s duration is slid across the entire signal duration and the obtained energy values are compared against thresholds for event detection. Event localization is achieved based on the logic provided in Fig. 5.10, where excursions in  $WE_n$  are compared across PMUs spread over a power system.

#### 5.6.1.1 Event detection in voltage signals

Using (5.8) and the algorithm given in Fig. 5.10, the following observations are made:

1.  $WE_{th}$  for the voltage magnitude signal is set to 0.012.
2. Based on the chosen threshold the event is identified at 40 s, as can be seen in Fig. 5.17.

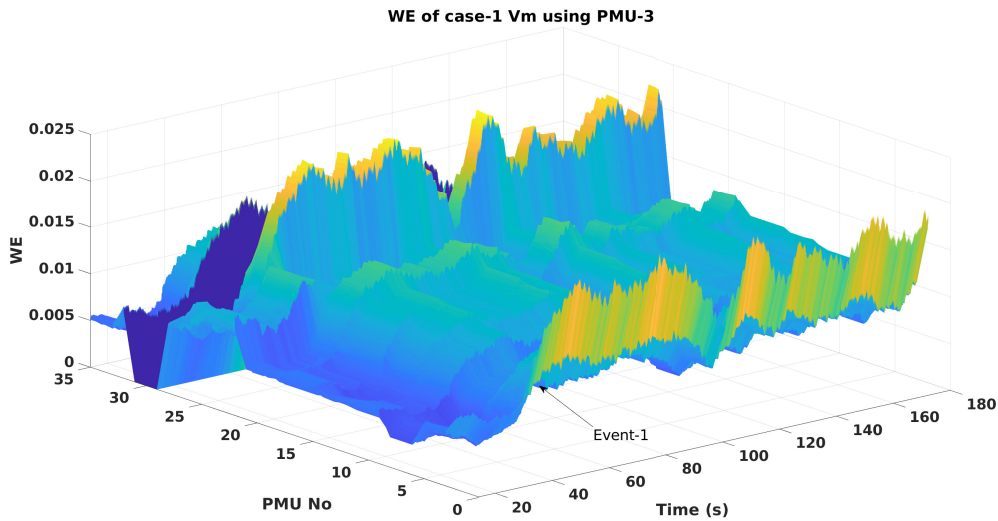


**Figure 5.17:** WE for voltage magnitude across all PMUs for ISO-NE case-1.

3. The number of PMUs crossing the  $WE_{th}$  limit is given by  $N_1 = 22 (> 10\% \text{ of } N)$ . Therefore, an EVENT is declared. The maximum values of wavelet energy exhibited by all the functional PMUs are shown in Fig. 5.18.
4. All the PMUs showing WE excursions satisfy the  $WE_{ce}$  criteria, and hence  $N_2 = N_1$ .
5. Therefore, the disturbance is classified as a WIDE-SPREAD event.

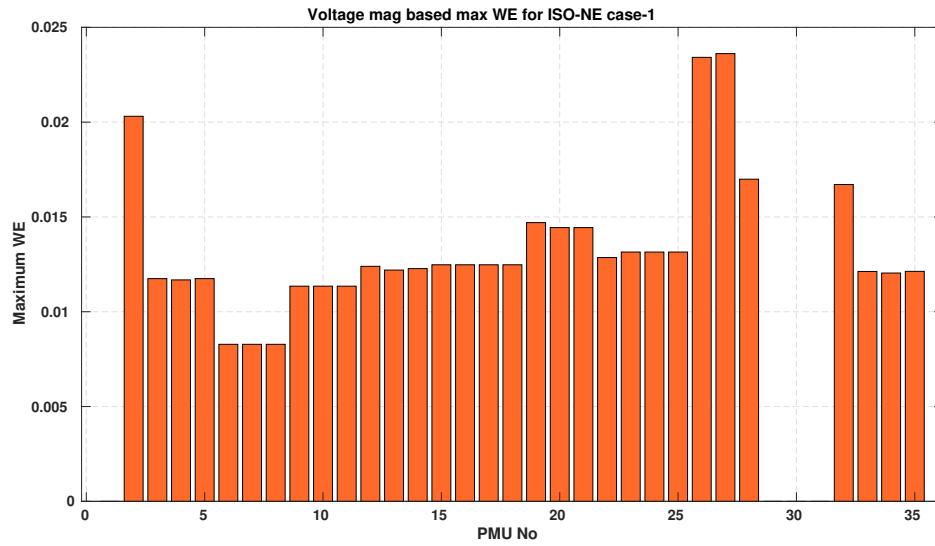


**Figure 5.18:** Maximum values for voltage magnitude WE across all PMUs for ISO-NE case-1.

### 5.6.1.2 Event detection in frequency signals

The following observations are made:

1. For this signal, a threshold equal to  $5.5 \times 10^{-4}$  is chosen for wavelet energy based event detection.
2.  $N_1 = 28 (> 10\% \text{ of } N)$ , PMUs cross the threshold value, therefore an EVENT is flagged at around 40 s. The wavelet energy excursions for the frequency signals are shown in Fig. 5.19.
3. The maximum values of wavelet energy exhibited by all the PMUs are shown in Fig. 5.20, with all the 28 PMUs showing excursions greater than  $WE_{ce}$ .

4. Therefore, since  $N_2 = N_1 = 28$ , the disturbance is labelled as a WIDE-SPREAD event.

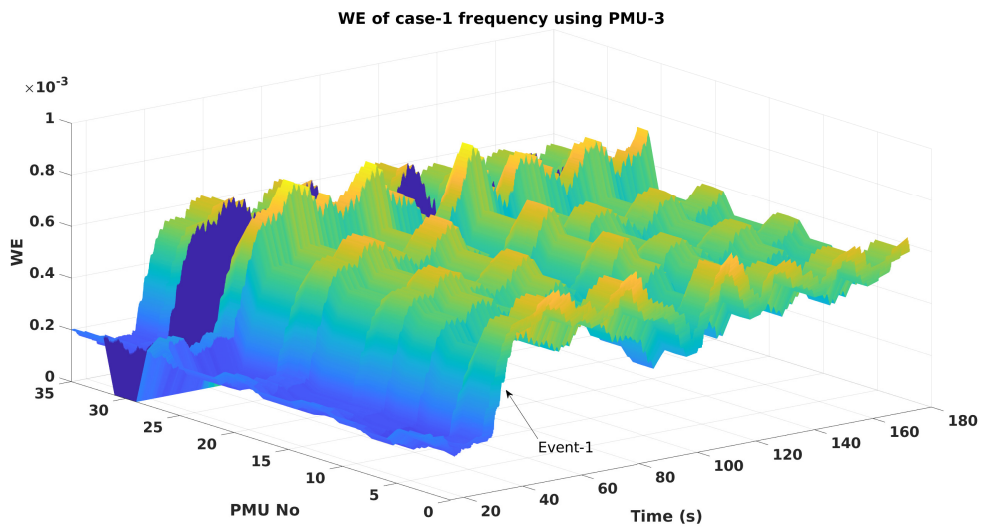


**Figure 5.19:** WE for frequency signal across all PMUs for ISO-NE case-1.

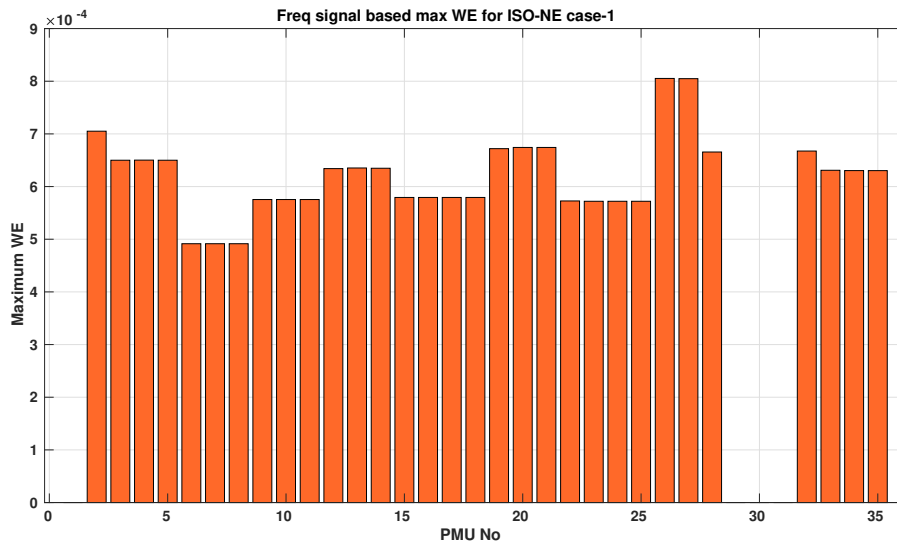


**Figure 5.20:** Maximum values for frequency signal WE across all PMUs for ISO-NE case-1.

### 5.6.1.3 Event detection in ROCOF signals

The following observations are made:

1. Threshold for event detection, i.e.,  $WE_{th}$ , for the case-1 ROCOF signal is set to  $1 \times 10^{-3}$ .
2.  $N_1 = 28 (> 10\% \text{ of } N)$  PMUs, show WE values greater than the above set threshold. Therefore an EVENT is declared. The wavelet energy excursions and the maximum values of wavelet energy shown by all the PMUs are given in Figs. 5.21 and 5.22, respectively.
3. For this case  $N_2 = N_1 = 28$ , therefore, the disturbance is flagged as a WIDE-SPREAD event.

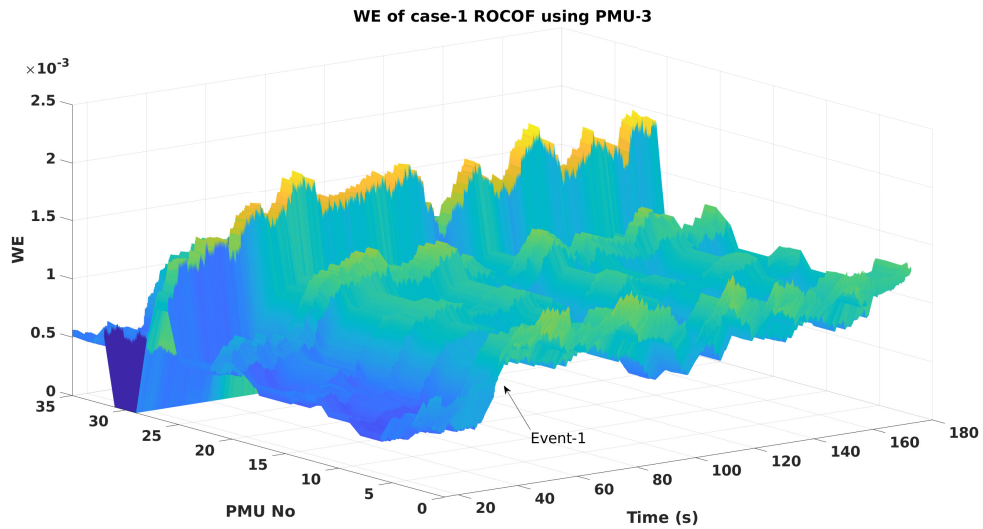


**Figure 5.21:** WE for ROCOF signal across all PMUs for ISO-NE-case-1.

Decision on the event localization for ISO-NE case-1 is summarized in Table. 5.1. The disturbance is overall classified as a WIDE-SPREAD event and  $N_2$  number of PMUs are highlighted on the layout diagram to visualize the spread of the event.

**Table 5.1:** Localization decision based on wavelet energy computation of ISO-NE data for case-1 for event at 40 s.

ISO-NE Case-1	Vm-based	Freq-based	ROCOF-based	Decision
	Wide-Spread	Wide-Spread	Wide-Spread	Wide-Spread

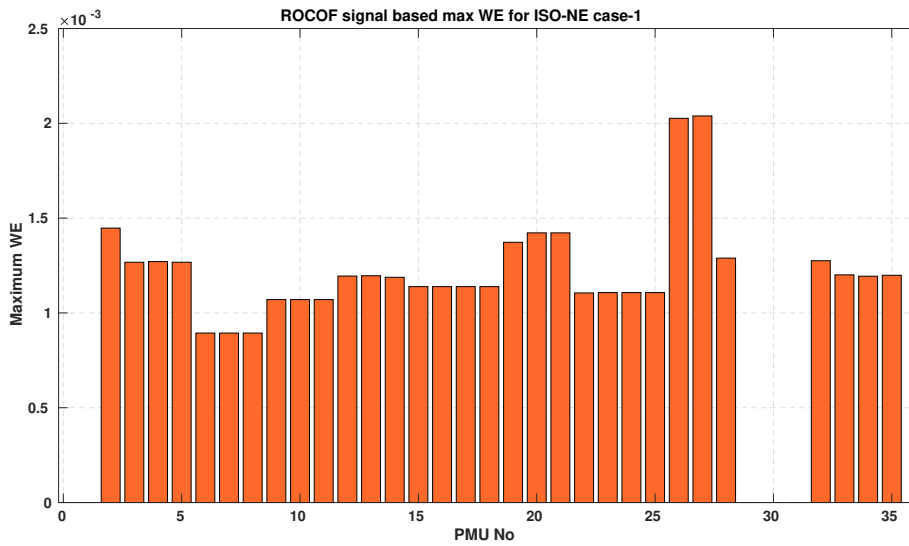


**Figure 5.22:** Maximum values for ROCOF signal WE across all PMUs for ISO-NE-case-1.

## 5.6.2 Event Detection Using Case-3 Signals

As mentioned earlier, Event-1 and Event-2 are dominant in voltage signal whereas Event-2 and 3 are observed in the frequency and ROCOF signals as well.

### 5.6.2.1 Event-1 in voltage signal

The following observations are made:

1. The chosen  $WE_{th}$  for the voltage magnitude signal is 0.03.
2. Based on the threshold, only PMUs-3, 4 and 5 show excursions in wavelet energy at around 49 s. The excursions exhibited by the wavelet energy of the voltage magnitude signals are shown in Fig. 5.23.

- Since  $N_1 = 3 (< 10\% \text{ of } N)$  and these PMUs belong to the same substation, i.e., Sub-2 (see Appendix . A). The disturbance is labelled as a LOCAL event to Substation-2.

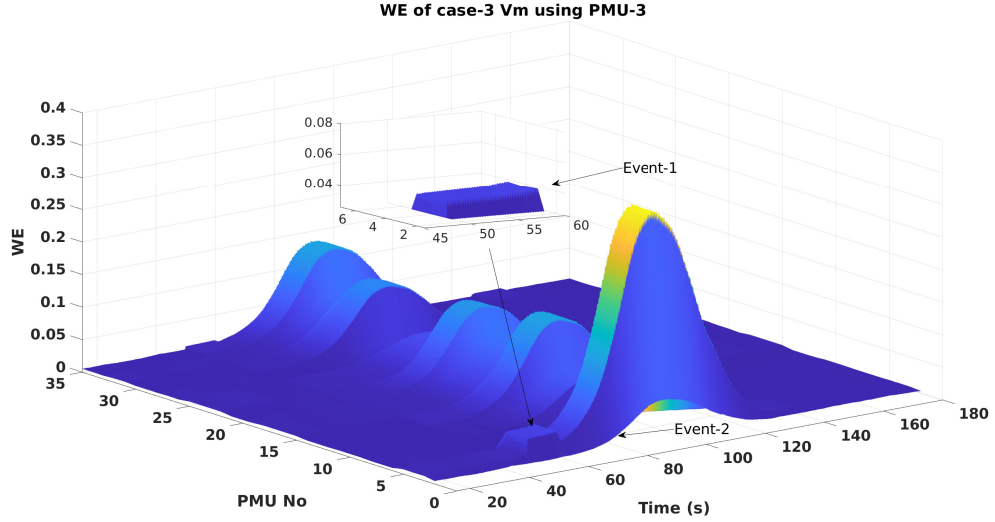


**Figure 5.23:** WE for voltage magnitude data across all PMUs for ISO-NE case-3.

### 5.6.2.2 Event-2 in voltage signal

The following observations are made:

- $WE_{th} = 0.03$ , as fixed previously. Using this threshold an additional oscillatory event is detected at 70 s using the voltage magnitude signal as can be seen in Fig. 5.23 and the maximum values of wavelet energy excursion exhibited by all the functional PMUs are shown in Fig. 5.24.
- $N_1 = 29 (> 10\% \text{ of } N)$ , PMUs show excursions in wavelet energy during this time interval. Therefore an EVENT is flagged.
- Among the  $N_1$  PMUs, only PMU-3, 4 and 5 show excursions above  $WE_{ce}$ . Hence  $N_2 = 3 (< 20\% \text{ of } N_1)$  and thus the disturbance is labelled as a LOCAL event.

### 5.6.2.3 Event-2 in frequency signal

The following observations are made:



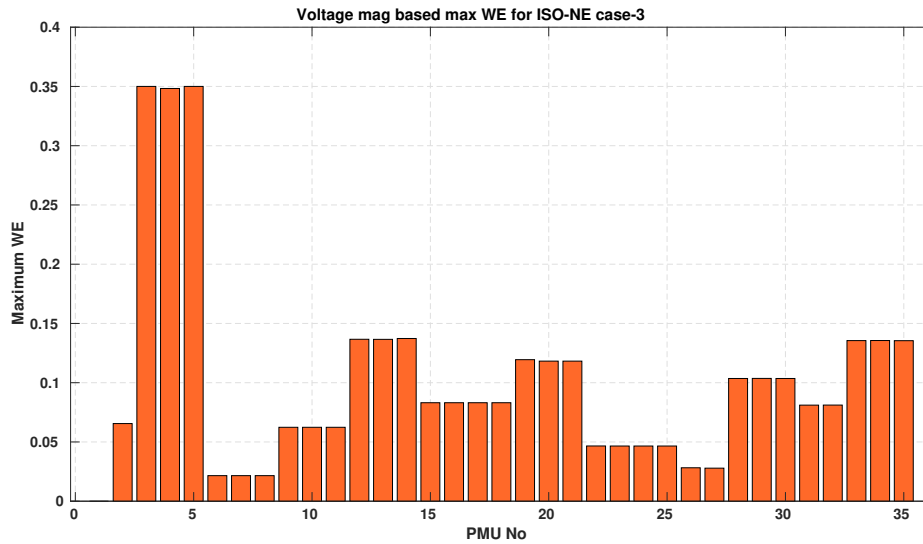


**Figure 5.24:** Maximum values for voltage magnitude WE across all PMUs for ISO-NE case-3.

1. The WE threshold for the frequency signal for case-3 is set to  $1 \times 10^{-3}$ .
2. According to the threshold, the first event in the frequency signal is detected around 70 s, as can be seen in Fig. 5.25. From Fig. 5.15, it is clear that Event-1 is not observable in frequency signals, which is further confirmed by the wavelet energy plot.
3. Excursions in wavelet energy greater than the set threshold are depicted by  $N_1 = 29 (> 10\% \text{ of } N)$  PMUs. Therefore, an EVENT is flagged. The maximum values of the wavelet energy excursions shown by all the functional PMUs are plotted in Fig. 5.26.
4. For Event-2 in the frequency signal, only PMUs 3, 4 and 5 show wavelet energy excursions greater than  $WE_{ce}$ . Hence,  $N_2 = 3 (< 20\% \text{ of } N_1)$  and the disturbance is declared as a LOCAL event.

#### 5.6.2.4 Event-3 in frequency signal

The following observations are made:

1. For the same WE threshold value, Event-3 in the frequency signal is identified at 144 s, as can be seen using Fig. 5.25.

2. Excursions in wavelet energy crossing  $WE_{th}$  are seen only in PMUs 32, 33 and 34. Therefore,  $N_1 = 3 (< 10\% \text{ of } N)$ .

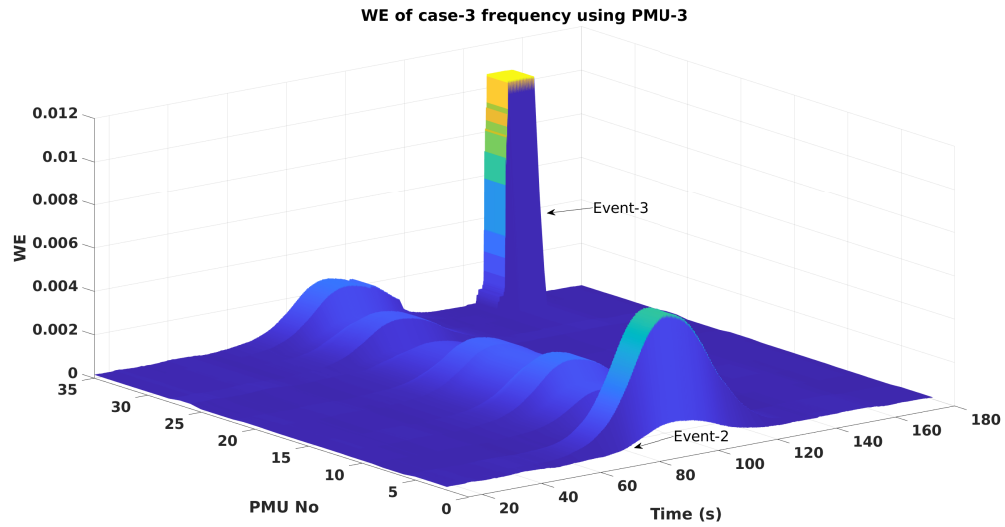


**Figure 5.25:** WE for frequency data across all PMUs for ISO-NE case-3.

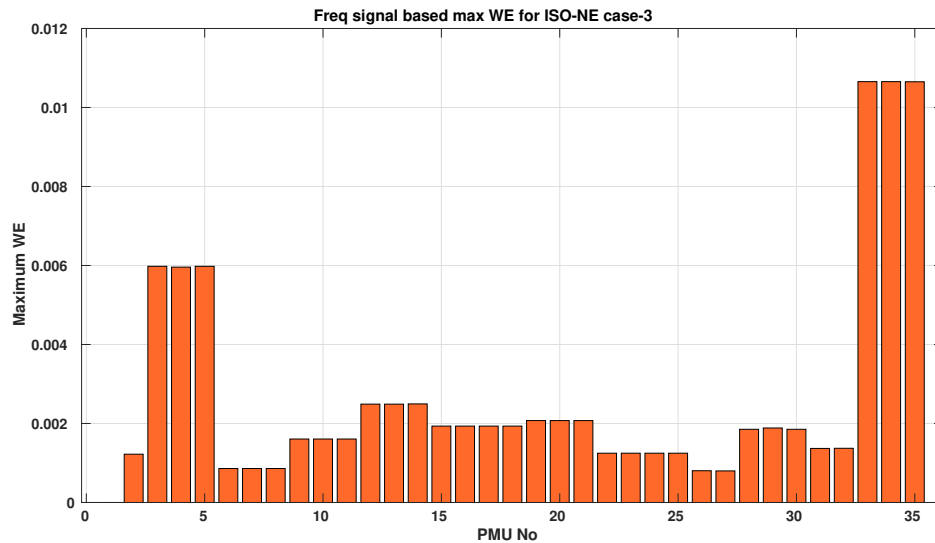


**Figure 5.26:** Maximum values for frequency WE across all PMUs for ISO-NE case-3.

3. It is confirmed that all the three PMUs belong to a single substation, i.e., Sub-12.

Therefore, the disturbance is declared as LOCAL to Substation-12.

### 5.6.2.5 Event-2 in ROCOF signal

The following inferences are made:

1. The  $WE_{th}$  for the ROCOF signal for case-3 is set to 0.01.
2. The WE excursions exhibited by all the PMUs are shown in Fig. 5.27. Excursions greater than  $WE_{th}$  are visualized in  $N_1 = 22 (> 10\%$  of  $N$ ) PMUs at around 70 s. Hence an EVENT is flagged.

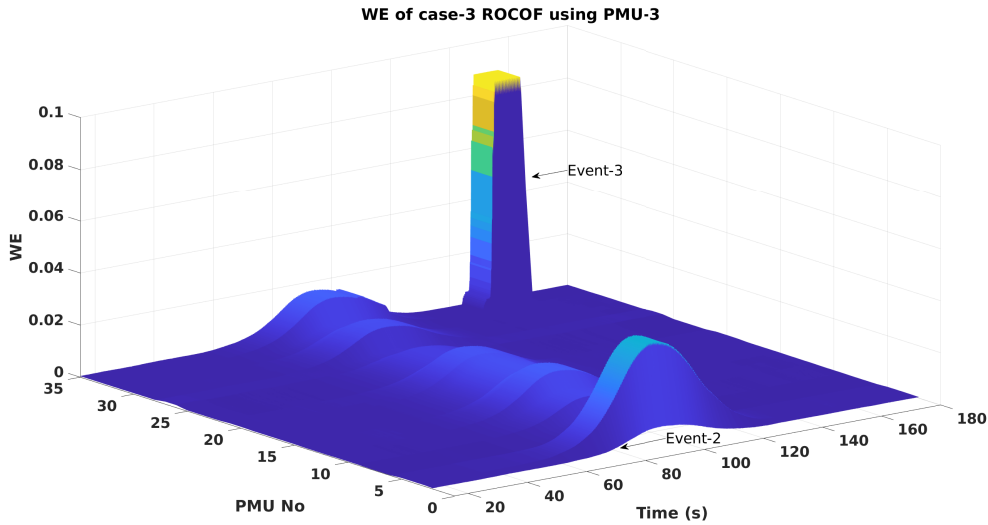


**Figure 5.27:** WE for ROCOF data across all PMUs for ISO-NE case-3.

3. Among  $N_1$  PMUs, only three show excursions greater than the  $WE_{ce}$  limit. These include PMUs-3, 4 and 5. The maximum values of wavelet energy exhibited by all the PMUs are shown in Fig. 5.28.
4. Since the value of  $N_2 = 3 (< 20\%$  of  $N_1$ ), the disturbance is labelled as a LOCAL event.

### 5.6.2.6 Event-3 in ROCOF signal

The following observations are made:

1. For the same WE threshold, i.e., 0.01, excursions are seen in the ROCOF signal wavelet energy at around 144 s, as can be seen in Fig. 5.27.
2. PMUs-32, 33, 34 cross the set  $WE_{th}$  threshold for ROCOF wavelet energy. Therefore,  $N_1 = 3 (< 10\% \text{ of } N)$ , and it is verified that the  $N_1$  PMUs belong to a single substation, i.e., Sub-12.
3. Hence, an event LOCAL to Substation-12 is declared.

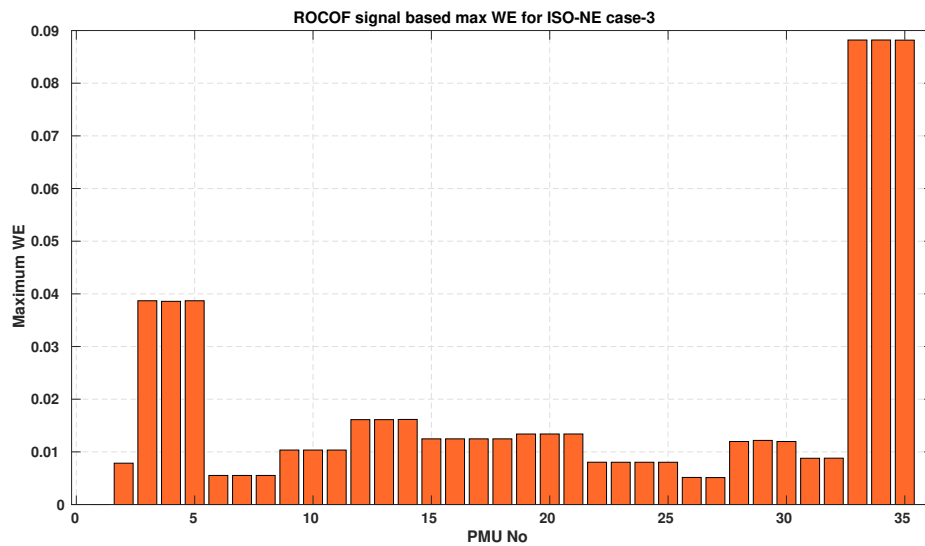


**Figure 5.28:** Maximum values for ROCOF WE across all PMUs for ISO-NE case-3.

Localization decisions for events occurring at different time instances in ISO-NE Case-1 and ISO-NE Case-3 signals are summarized in Table. 5.2.

**Table 5.2:** Event localization decision based on Wavelet energy estimates for ISO-NE power system

Case No	Vm-based	Freq-based	ROCOF-based	Localization Decision
Event-1 ISO-NE Case-1 (40 s)	Wide-Spread	Wide-Spread	Wide-Spread	Wide-Spread
Event-1 ISO-NE Case-3 (49 s)	Local	Not reflected	Not reflected	Local to Sub-2
Event-2 ISO-NE Case-3 (70 s)	Local	Local	Local	Local to Sub-2
Event-3 ISO-NE Case-3 (144 s)	Not reflected	Local	Local	Local to Sub-12

Based on the type of disturbances, localization decisions may be taken based on the voltage magnitude or frequency/ROCOF signals. Using this logic, events occurring in

ISO-NE case-1 are categorized as wide-spread whereas the events occurring in ISO-NE case-3 are categorized as local, restricted to substation-2 and substation-12 only.

## **5.7 SD-based Detection Using ISO-NE Power System Signals**

Voltage, frequency and ROCOF signals are subjected to standard deviation computation using (5.10) for anomaly detection. High value of standard deviation of a certain data point represents deviant behavior, which is indicative of a disturbance scenario. Standard deviation values of PMU data from the ISO-NE system are computed and compared against a set threshold to identify events. After the detection of events, segregation of PMUs based on the amplitude of SD excursions is carried out using the logic provided in Fig. 5.10 in order to enable the localization process.

### **5.7.1 Event Detection Using Case-1 Signals**

#### **5.7.1.1 Event-1 in voltage signal**

1. For SD based event detection, a threshold of 0.07 p.u is chosen for case-1 voltage magnitude signal.
2. Based on this  $SD_{th}$ , excursions in SD start around 40 s, as can be seen in Fig. 5.29.
3. Excursions in SD are reflected around this time by,  $N_1 = 24 (> 10\% \text{ of } N)$ , PMUs. Therefore, an event is flagged. The maximum value of SD computed for all functional PMUs is shown in Fig. 5.30.
4. As per the considerable amplitude criteria, all  $N_1$  PMUs show SD excursions greater than  $SD_{ce}$ , hence,  $N_2 = 24$ . This leads to the conclusion that the event is WIDE-SPREAD in nature.

#### **5.7.1.2 Event-1 in frequency and ROCOF signals**

Here, frequency and ROCOF signals are employed for event detection. The results obtained following the steps as per the flow chart in Fig. 5.10, are tabulated in Table. 5.3. From the

SD-based analysis for case-1, it can be concluded that the Event-1 is detected reliably and the results are almost identical to those obtained with the WE-based method.

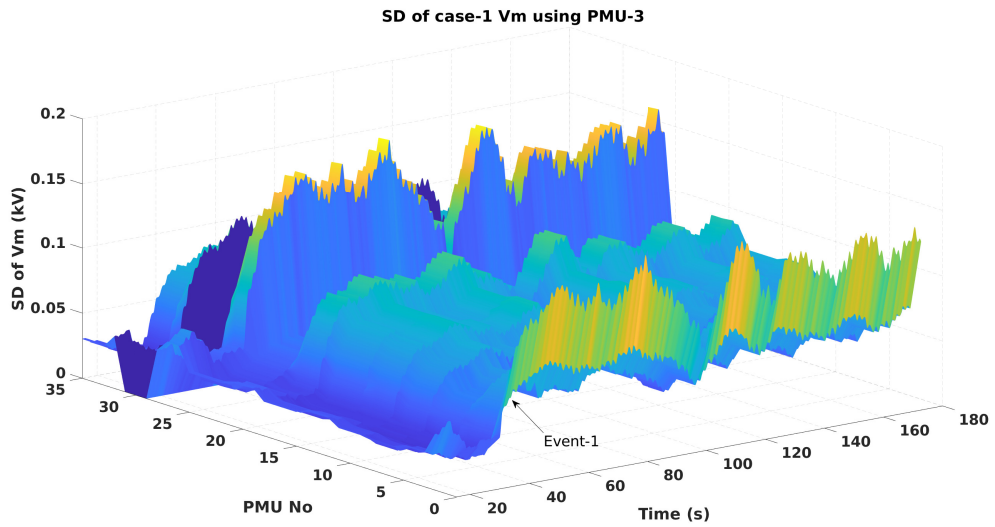


Figure 5.29: SD for voltage magnitude across all PMUs for ISO-NE case-1.

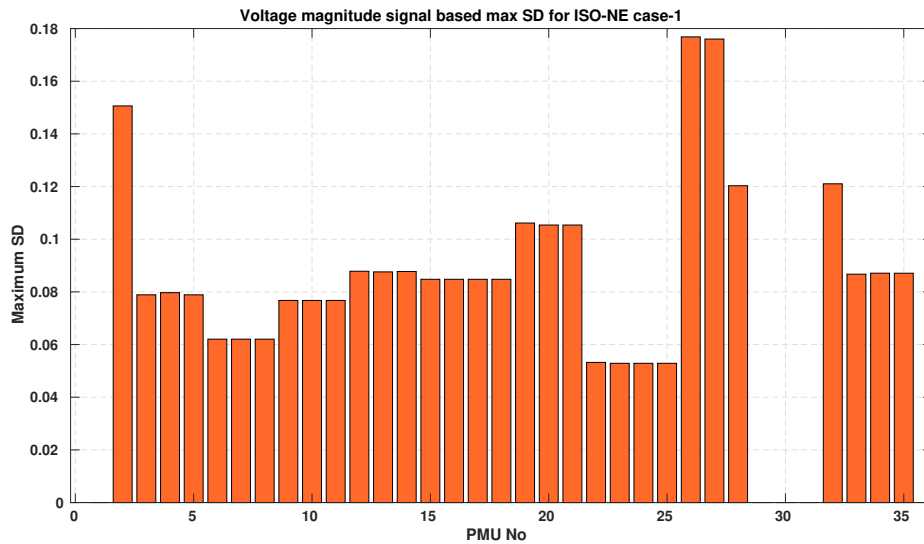


Figure 5.30: Maximum values of voltage magnitude SD across all PMUs for ISO-NE case-1.

**Table 5.3:** Event localization decision based on SD estimates for case-1 ISO-NE power system

Signal	$SD_{th}$	$N_1$	$N_2$	Time of occurrence	Localization decision
Frequency	$5 \times 10^{-3}$ Hz	28	28	40 s	Wide-Spread
ROCOF	0.007 Hz/s	28	28	40 s	Wide-Spread

### 5.7.2 Event Detection Using Case-3 Signals

- Here, instead of WE-based method, SD-based technique is employed to detect events using case-3 signals. A sample plot of SD of voltage magnitude, frequency and ROCOF signals for PMUs-3, 4, 5 and 8 is shown in Fig. 5.31

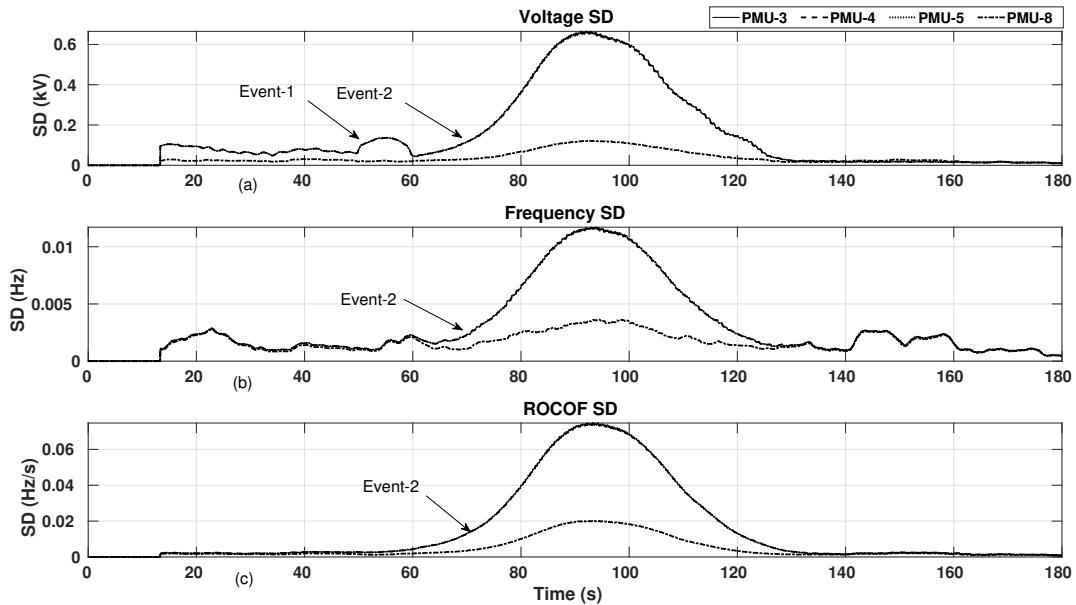


**Figure 5.31:** SD for PMU-3, 4, 5 and 8 for case-3, a) voltage magnitude b) frequency c) ROCOF.

- Event-1 occurrence is detected only using the voltage magnitude signal, as shown in Fig. 5.31 (a), where relatively high values of SD can be observed around the 49 s time interval. On the other hand occurrence of event-2 is observed in all the three signals, i.e., voltage magnitude, frequency and ROCOF, around 70 s. Due to the relatively

local nature of disturbances in case-3, SD estimates for PMU-8 signals do not show any major excursions for any of the three signals, as can be seen in Fig. 5.31.

3. The event localization results for case-3, based on the SD estimates are summarized in Table. 5.4 for all the three signals. The SD excursion plot for the frequency signal is shown in Fig. 5.32, depicting the occurrence of event-2 at 70 s and event-3 at around 144 s. Maximum value of SD exhibited for frequency estimates by all PMUs is shown in Fig. 5.33. SD excursions in frequency for event-3 are absent in Fig. 5.31, since the disturbance is local to Sub-12. Event-2 on the other hand is visible in all the three signals as can be confirmed from Figs. 5.31 and 5.32.

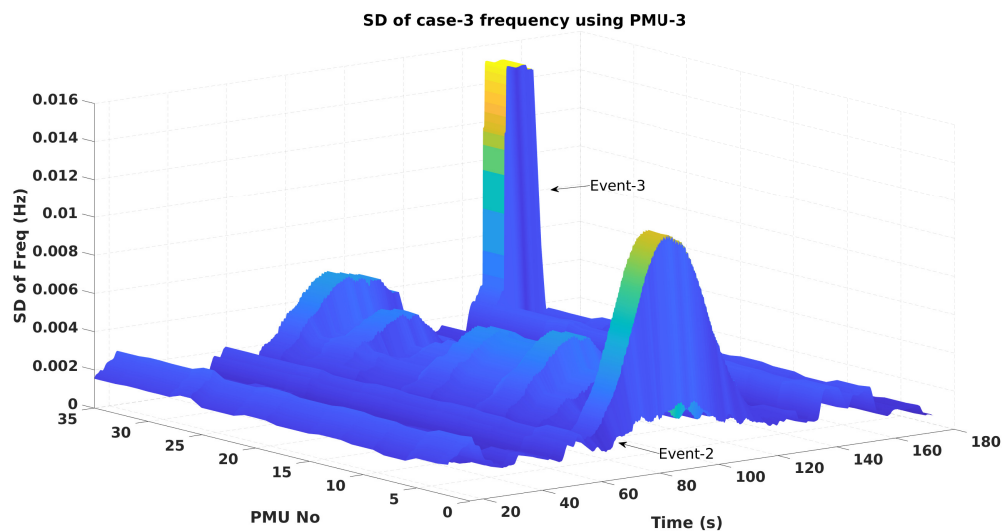


**Figure 5.32:** SD for frequency across all PMUs for ISO-NE case-3.

4. Both the WE as well as the SD based methods provide identical results for ISO-NE case-3 signals. Based on the hit and trial thresholds chosen for each method, events in voltage, frequency and ROCOF signals are properly detected around their actual incipient time. Localization decisions taken based on the WE and SD estimates are also similar and accurately depict the region where the disturbance has occurred in the power system.



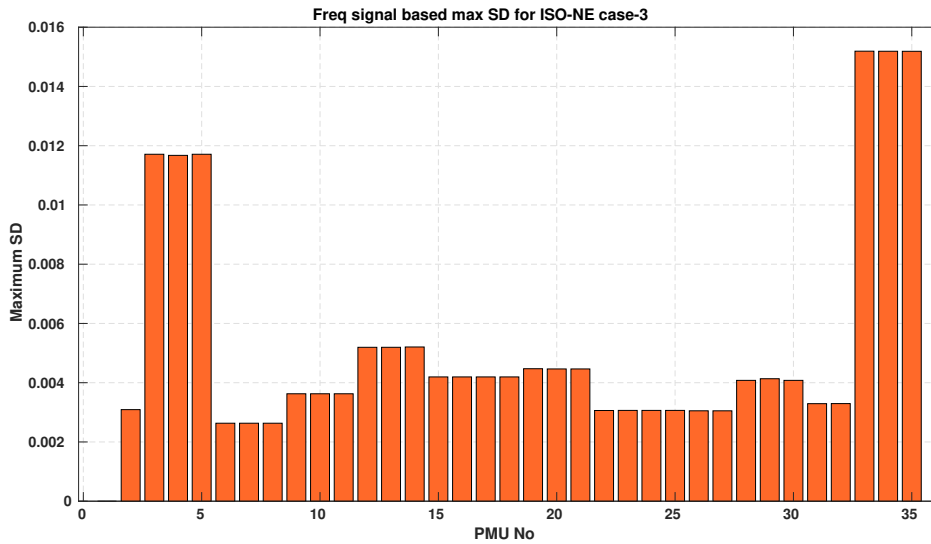


Figure 5.33: Maximum value of frequency SD across all PMUs for ISO-NE case-3.

Table 5.4: Event detection and localization procedure for case-3 based on SD estimates.

Signal	Event No	$SD_{th}$	$N_1$	$N_2$	Time of occurrence	Localization decision
Voltage	Event-1	0.135 kV	3	-	49 s	Local to Sub-2
	Event-2	0.135 kV	21	3	70 s	Local to Sub-2
	Event-3	Not detected	-	-	-	-
Frequency	Event-1	Not detected	-	-	-	-
	Event-2	0.004 Hz	19	3	70 s	Local to Sub-2
	Event-3	0.004 Hz	3	-	144 s	Local to Sub-12
ROCOF	Event-1	Not detected	-	-	-	-
	Event-2	0.02 Hz/s	22	3	70 s	Local to Sub-2
	Event-3	0.02 Hz/s	3	-	144 s	Local to Sub-12

## 5.8 Event Detection in a 4-Machine 10-Bus Power System

Here, case studies are performed using a 4-machine 10-bus power system. A typical 4-machine 10-bus power system is slightly modified by introducing an additional bus at bus-11, connected to bus-7 by a transmission line of reactance  $j0.05$  p.u, as shown in Fig. 5.34, (Shubhanga, 2018). An additional load-C in the form of  $P + jQ$ , is connected to bus-11.

PMU-D is installed on each bus to provide wide area visualization. In the figure only two PMUs are shown for illustration purpose.

To identify and localize events only the standard deviation (SD) based method is used (since both the wavelet energy and standard deviation are seen to provide exactly the same results). Trial and error based thresholds are chosen for different signals to help detect and localize the events. Simulations are run for a 50 s duration and data is collected at a rate of 100 fps. The following disturbances are considered,

1. Case-1: A three-phase fault at bus-7.
2. Case-2: Line-12 is tripped to disconnect load-C (purely Q-type).

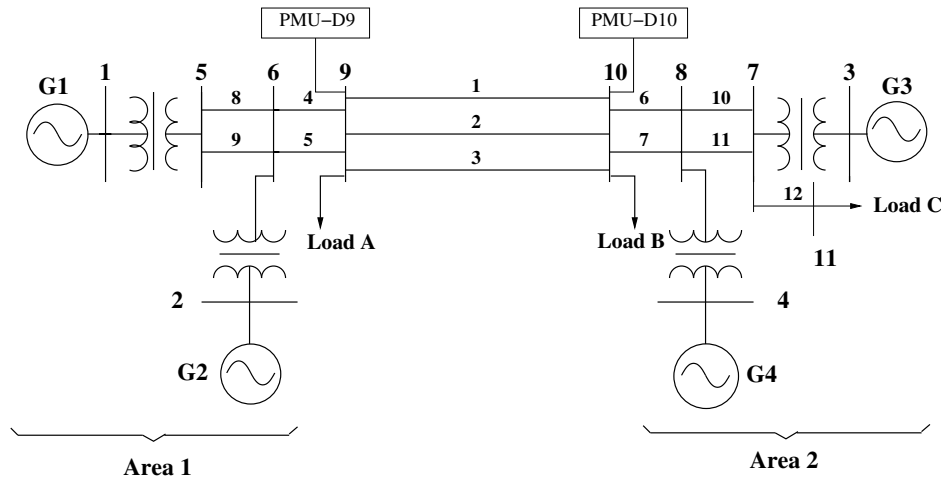
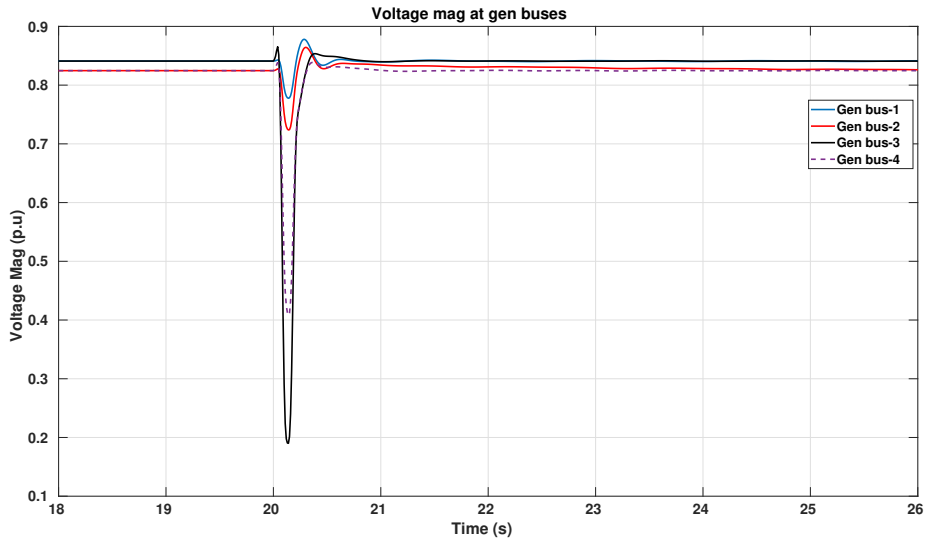


Figure 5.34: Modified 4-machine 10-bus system with an additional  $P + jQ$  load at bus-11.

### 5.8.1 Case-1 : Fault at bus-7

A three-phase fault is introduced at bus-7 at time,  $T_{fault} = 20$  s with  $T_{clear} = 0.1$  s, without any line tripping. Since PMUs are installed at all buses of the power system,  $N = 11$ . The voltage magnitudes as computed by PMUs at each generator bus are plotted in Fig. 5.35. The generator at bus-3 and bus-4 show considerable dips in the voltage magnitude since they are closer to the fault location compared to generators 1 and 2. Using the standard deviation based approach for the voltage magnitude, frequency and the ROCOF signals, event detection and localization is undertaken in the upcoming sections.



**Figure 5.35:** Voltage magnitude at all generator buses for a fault case.

### 5.8.1.1 Event detection using voltage magnitude signals

The following inferences are made:

1. For the above mentioned case, the voltage magnitude standard deviation threshold is chosen to be  $SD_{th} = 0.02$  p.u.
2. Six PMUs are seen to cross the  $SD_{th}$  limit. These include PMUs placed at buses 3, 4, 7, 8, 10, 11. Excursions in SD with time can be seen in Fig. 5.36, while the maximum values of SD obtained across different PMUs are shown in Fig. 5.37. The event start time,  $t_{es}$ , for the voltage magnitude signal is 20.108 s associated with PMU-7.
3. Since  $N_1 = 6 (> 10\% \text{ of } N)$ , an EVENT is declared.
4. All the  $N_1$  PMUs exhibit excursions greater than  $SD_{ce}$ . Therefore,  $N_2 = N_1$ .
5. Hence, the disturbance is labelled as a WIDE-SPREAD EVENT.

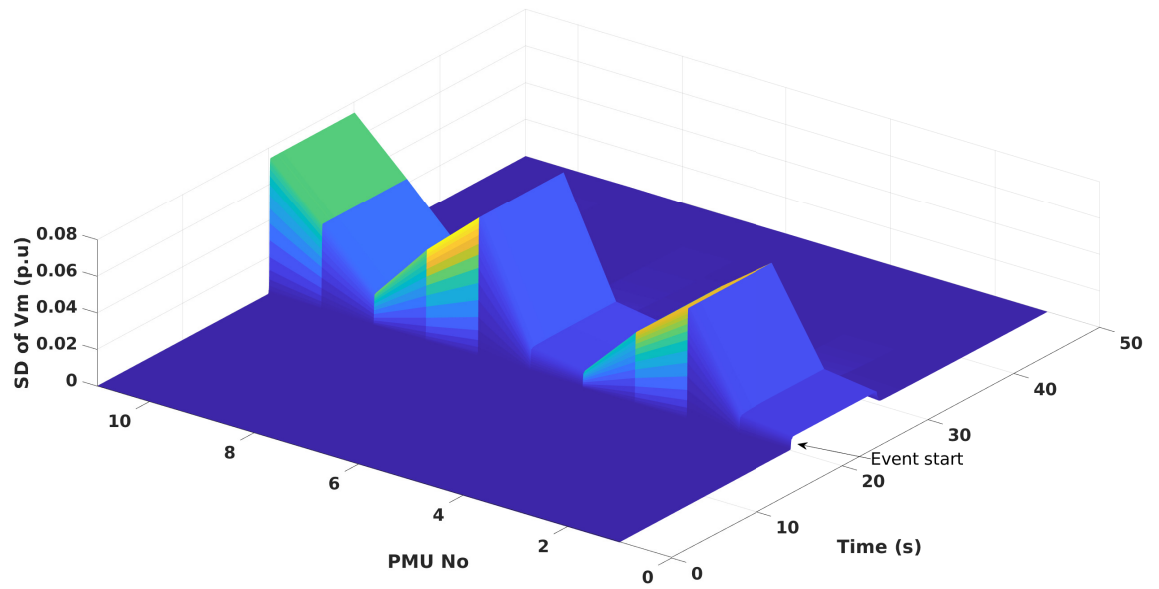


Figure 5.36: SD for voltage magnitude data across all PMUs for a fault case.

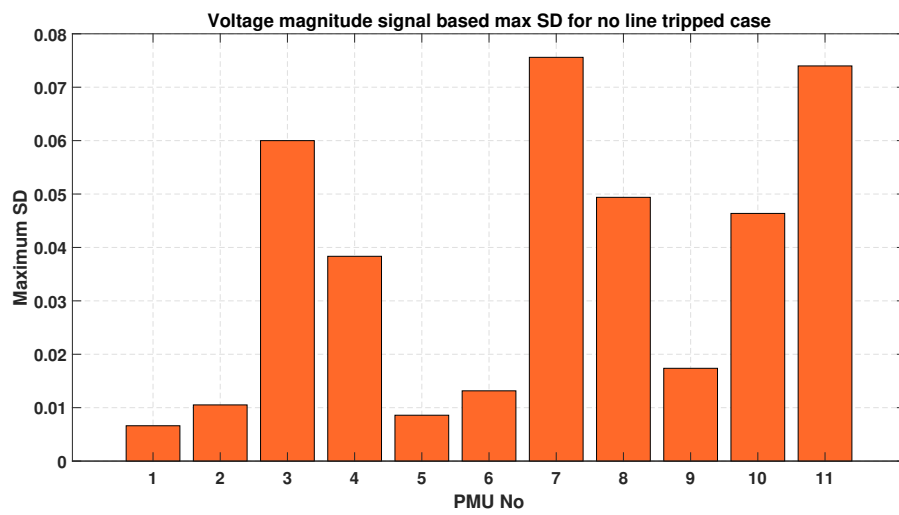
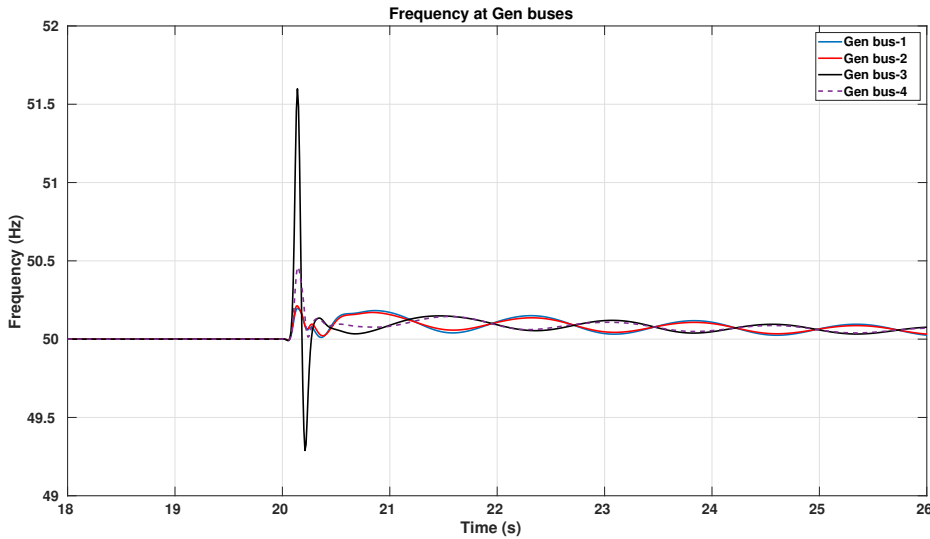


Figure 5.37: Maximum values for voltage magnitude SD across all PMUs for a fault case.

### 5.8.1.2 Event detection employing frequency and ROCOF signals

Frequencies estimated at generator buses are plotted in Fig. 5.38. Generator-3 which is connected to bus-3 shows the highest frequency excursion followed by bus-4. Generators at bus-1 and bus-2 do not show such high values of excursions on account of them being located far away from the fault location. When frequency signals are used, the following observations are made :



**Figure 5.38:** Frequency at all generator buses for a fault case.

1. The frequency standard deviation threshold is set to 0.1 Hz.
2. Three PMUs cross the  $SD_{th}$  limit. These include, PMUs-3, 7, 11 and therefore  $N_1 = 3$ .
3. Excursions in frequency SD with time and across all the installed PMUs can be visualized using Fig. 5.39.
3. The maximum values of standard deviation exhibited by all the PMUs are shown in Fig. 5.40.
4. The event start time,  $t_{es}$ , for the frequency signal is 20.134 s associated with PMU-11.
5. Since  $N_1 = 3 (> 10\% \text{ of } N)$ , an EVENT is declared.
6. Only PMUs-7 and 11 exhibit excursions greater than  $SD_{ce}$ . Therefore  $N_2 = 2 > 20\% \text{ of } N_1$  and the disturbance is labeled as a WIDE-SPREAD event.

Similar inferences are made when ROCOF signals are employed.

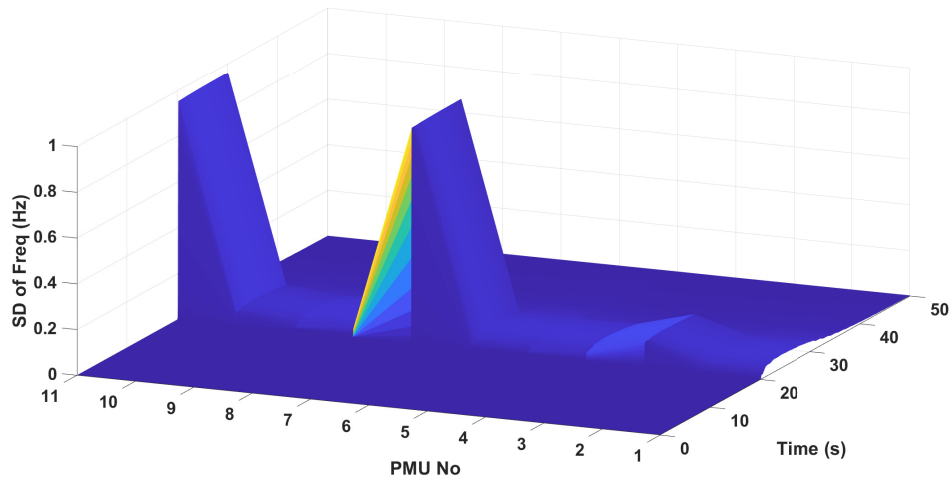


**Figure 5.39:** SD for frequency data across all PMUs for a fault case.

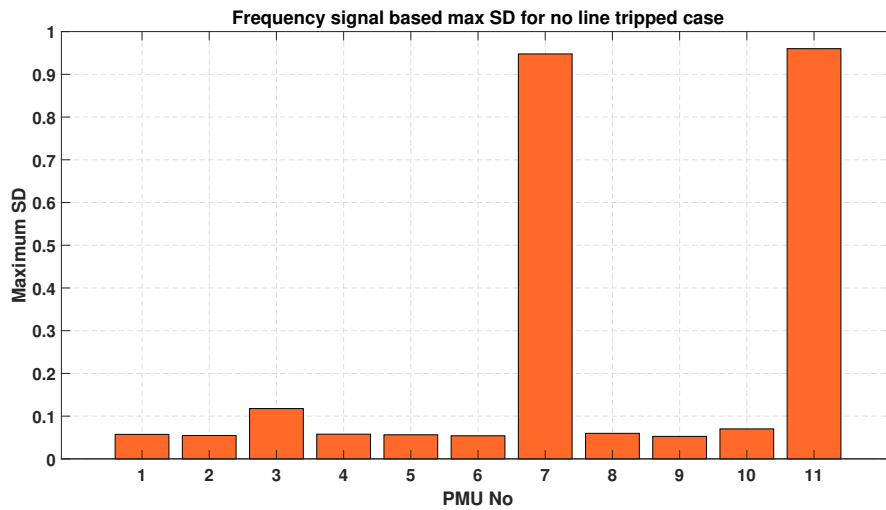


**Figure 5.40:** Maximum values for frequency SD across all PMUs for a fault case.

Detection and localization results for case-1 are summarized in Table. 5.5. The disturbance is overall categorized as a WIDE-SPREAD event.

**Table 5.5:** Event detection results for case-1, 4-machine, 10-bus power system

Case-1 using trial and error thresholds				
Signal Used ( $SD_{th}$ )	$N_1$	$N_2$	$t_{es}$ (s)	Decision
Voltage (0.02 p.u)	6, (PMUs-3,4,7,8,10,11)	6, (PMUs-3,4,7,8,10,11)	20.108 (PMU-7)	Wide-Spread
Frequency (0.1 Hz)	3, (PMUs-3,7,11)	2, (PMUs-7,11)	20.134 (PMU-11)	Wide-Spread
ROCOF (1.5 Hz/s)	3, (PMUs-3,7,11)	2, (PMUs-7,11)	20.13 (PMU-11)	Wide-Spread

### 5.8.2 Case-2 : Disconnection of Load-C (Purely Q-type)

For this case, the load-C is considered as only reactive type. At 20 s line-12 is tripped to disconnect load-C. Such a case simulates a loss-of-load scenario involving a pure reactive load. The magnitudes of voltage at generator buses are shown in Fig. 5.41. The highest deviation can be seen in generators 3 and 4 which are nearer to the fault location. It is to be noted that due to the line-trip the voltage magnitude obtained from PMU-11 is close to zero and hence its estimates are not considered for event detection. The following observations are made,

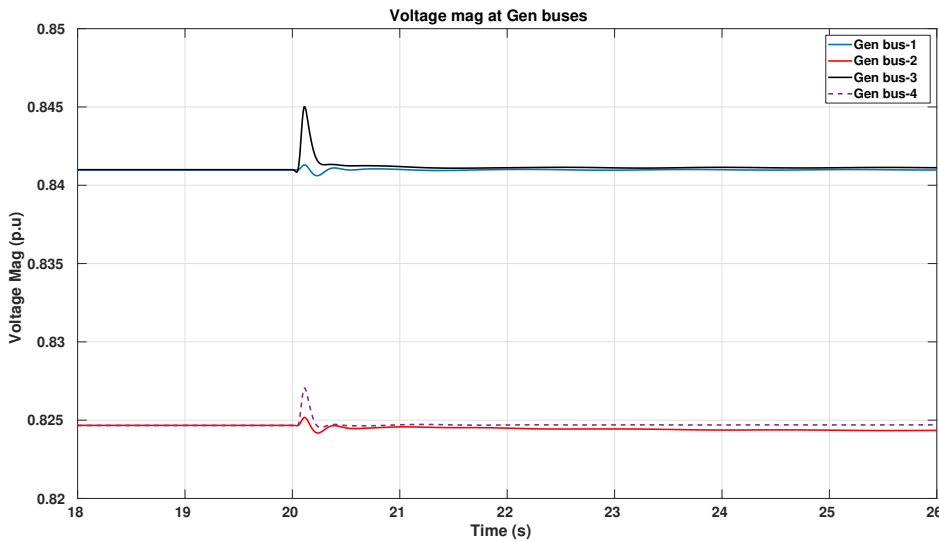


**Figure 5.41:** Voltage magnitude at all generator buses for line trip case-2.

1. Threshold for the voltage magnitude,  $SD_{th}$  is chosen as  $2 \times 10^{-4}$  p.u.
2. Based on the above mentioned threshold, PMUs-3, 7, 8, 10 are listed and hence

$N_1 = 4 > 10\%$  of  $N$ . The event start time,  $t_{es}$ , for the voltage magnitude signal is 20.11 s associated with PMU-7.

3. The maximum values of SD exhibited by PMUs are shown in Fig. 5.42.
4. Further,  $N_2 = 1 (> 20\%$  of  $N_1)$ , as only PMU-7 shows excursions greater than  $SD_{ce}$ .
5. Therefore, a WIDE-SPREAD Event is declared.

The frequency excursions at generator buses for this case are shown in Fig. 5.43 and the results have been summarized in Table. 5.6.

**Table 5.6:** Case-2 using trail and error thresholds

Case-2 using trial and error thresholds				
Signal Used ( $SD_{th}$ )	$N_1$	$N_2$	$t_{es}$ (s)	Decision
Voltage (0.0002 p.u)	4, (PMUs-3,7,8,10)	1, (PMU-7)	20.11 (PMU-7)	Wide-Spread
Frequency (0.0005 Hz)	10, (All PMUs)	10, (All PMUs)	20.15 (PMU-3)	Wide-Spread
ROCOF (0.004 Hz/s)	10, (All PMUs)	5, (PMUs-3,4,7,8,10)	20.13 (PMU-3)	Wide-Spread

1. Based on the percentage levels, (i.e., 10% and 20%), set in the flowchart in Fig. 5.10, the case-2 event, as seen from the voltage magnitude signal is incorrectly declared as WIDE-SPREAD event. However, one can adjust these percentage levels depending on the number of PMUs,  $N$  and  $SD_{th}$  values.

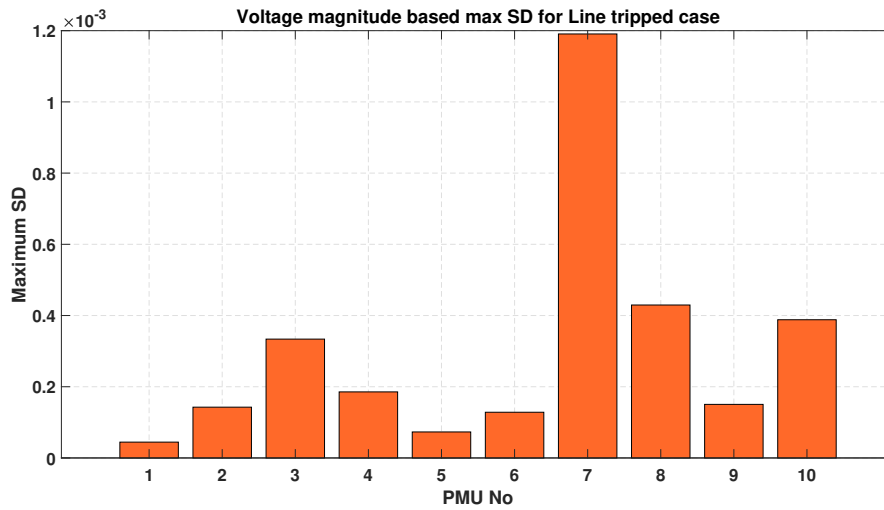


**Figure 5.42:** Maximum values for voltage magnitude SD across all PMUs for load trip case ( $0 + jQ$  load only).



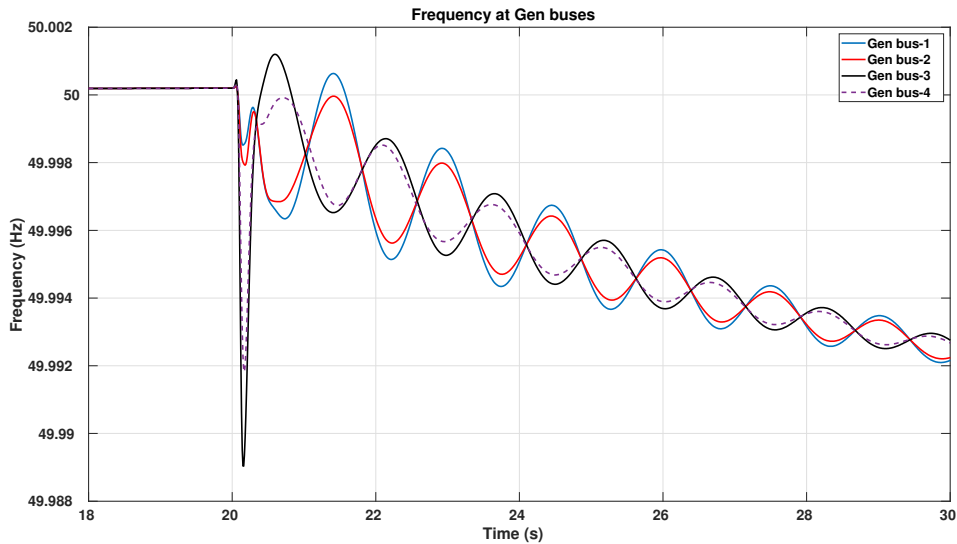


**Figure 5.43:** Frequency at all generator buses for line trip case-2.

2. A comparison of Fig. 5.43 and Fig. 5.38, shows that the magnitude of frequency deviation in case-2 is relatively small than those values in case-1. This implies that if  $SD_{th}$ - frequency signal = 0.1 Hz (chosen for case-1) is adopted as threshold for case-2, then the algorithm might not detect any event from frequency signals. This correctly signifies the local nature of case-2 event. A similar argument applies for ROCOF signals.
3. A display of candidate PMUs ( $=N_2$ ) based on voltage magnitude, frequency and ROCOF signals on the layout diagram will further validate the local nature of the event.
4. Based on the dominance of events in different signals, say, voltage or frequency or both voltage and frequency, one can classify the events as disturbances which involve active or reactive changes (Kim et al., 2015).

## 5.9 Methods for Estimating Threshold Values

In the previous sections, the threshold values,  $WE_{th}$  and  $SD_{th}$  are determined by a trial and error process in order to illustrate the event detection procedure shown in Fig. 5.10. However, selection of a suitable threshold level for a given signal is very essential primarily,

1. To reliably detect any critical events in a large data stream.
2. To accurately estimate the time of occurrence of an event.
3. To enable identification of region of spread of a disturbance.
4. To classify the nature of disturbance.

In this section, the following two approaches have been discussed to get an estimate for the threshold value :

1. Percentile-approach (Shaw and Jena, 2020)
2. 3-SD-approach (Allen et al., 2013)

### **5.9.1 Percentile-Based Threshold Calculation**

Here, threshold values are calculated using Percentile-approach (Shaw and Jena, 2020), where historical data is processed to determine 99% limit of the data-set. If 99% limit of a data-set is say, “x”, this indicates that 99% of the values of the data-set lie below “x”. The threshold values are computed for the standard deviation of the voltage magnitude, frequency and ROCOF signals obtained for different cases. Care should be taken to see that a large historical data-set is used. Otherwise, thresholds computed using limited data points and high limits can result in a deficient event detection system caused by improper thresholds. In this work, Percentile-based thresholds are calculated in MATLAB using the “*prctile*” command which uses a sorting based algorithm. The inputs to the command are either SD or WE of the PMU signal and the limit (between 0-100).

Performance of event detection algorithm using the percentile-based threshold is demonstrated for the 4-machine 10-bus power system using SD-method. Simulations are run for 1000 seconds to have enough data points. It should be noted that the percentage values associated with the algorithm given in Fig. 5.10 (i.e., 10% for detection and 20% for localization) are changed to 40%.

The following steps are employed for calculating percentile-based thresholds,

1. Compute the moving window-based SD for all  $N$  PMUs.
2. Using the percentile-approach determine the threshold SD for each of the PMUs.
3. The mean of  $N$  thresholds is then computed to arrive at the final value of the threshold  $SD_{th}$ , to be used for a particular signal.

### **5.9.1.1 Event detection based on voltage magnitude signal using percentile threshold (Case-1)**

1. The voltage magnitude standard deviation threshold is obtained as 0.0257 p.u. This is calculated based on the 99% limit of the data.
2. Six PMUs are seen to cross the  $SD_{th}$  limit. These include PMUs placed at buses 3, 4, 7, 8, 10, 11. The event start time,  $t_{es}$ , for the voltage magnitude is 20.11 s, associated with PMU-7.
3. Hence the value of  $N_1$  for the voltage magnitude signal is 6.
4. Since  $N_1 > 40\%$  of  $N$ , an EVENT is declared.
5. All the  $N_1$  PMUs exhibit excursions greater than  $SD_{ce}$  and hence  $N_2 = N_1$  and the disturbance is labelled as a WIDE-SPREAD EVENT.

### **5.9.1.2 Event detection based on frequency signal using percentile threshold (Case-1)**

1. The frequency standard deviation threshold calculated using the percentile method is 0.154 Hz.
2. Two PMUs cross the  $SD_{th}$  limit. These include, PMUs- 7 and 11, therefore  $N_1 = 2$ . The event start time,  $t_{es}$ , for the frequency signal is 20.14 s, associated with PMU-11.
3. Since  $N_1 < 40\%$  of  $N$ , a check is performed to see if both the PMUs belong to the same area/substation.
4. It is seen that both the PMUs-7 and 11 are located in Area-2 of the power system in question.
5. Thus the disturbance can be classified as a LOCAL EVENT restricted to Area-2 only.

### **5.9.1.3 Event detection based on ROCOF signal using percentile threshold (Case-1)**

1. The computed ROCOF standard deviation threshold is 2.97 Hz/s.
2. PMUs-3, 7 and 11 cross the set threshold limit. The event start time,  $t_{es}$ , for the ROCOF signal is 20.14 s, associated with PMU-11.

3. Therefore  $N_1 = 3 < 40\%$  of  $N$ .
4. All the  $N_1$  PMUs belong to the same area (i.e., Area-2).
5. Therefore the disturbance is classified as a LOCAL EVENT, restricted to Area-2 only.

The results for case-1 as well as case-2 using percentile-based threshold calculations are summarized in Tables. 5.7 and 5.8.

**Table 5.7:** Case-1 using percentile based threshold

Case-1 using percentile thresholds				
Signal Used ( $SD_{th}$ )	$N_1$	$N_2$	$t_{es}$ (s)	Decision
Voltage (0.0257 p.u)	6, (PMUs-3,4,7,8,10,11)	6, (PMU-3,4,7,8,10,11)	20.11 (PMU-7)	Wide-Spread
Frequency (0.154 Hz)	2, (PMUs-7,11)	-	20.14 (PMU-11)	Local
ROCOF (2.97 Hz/s)	3, (PMUs-3,7,11)	-	20.14 (PMU-11)	Local

**Table 5.8:** Case-2 using percentile based threshold

Case-2 using percentile thresholds				
Signal Used ( $SD_{th}$ )	$N_1$	$N_2$	$t_{es}$ (s)	Decision
Voltage (0.000125 p.u)	8, (PMUs-2,3,4,6,7,8,9,10)	7, (PMU-2,3,4,7,8,9,10)	20.105 (PMU-7)	Wide-Spread
Frequency (0.0014 Hz)	10, (All PMUs)	10, (All PMUs)	22.123 (PMU-3)	Wide-Spread
ROCOF (0.006 Hz/s)	5, (PMUs-3,4,7,8,10)	5, (PMUs-3,4,7,8,10)	20.149 (PMU-3)	Wide-Spread

1. Since, the disturbance in case-1 involves a 3-phase fault, frequency excursions are localized in nature, as can be seen in Fig. 5.40. Using this signal the same disturbance was wrongly categorized as a wide-spread event as given in Table. 5.5. Using the percentile-based thresholds and the increased percentage limits for event localization (40%) the same event was rightly categorized as a local event as shown in Table. 5.7. Due to the thresholds being on the higher side when calculated using the percentile-based approach, the event start time for case-1 given in Table. 5.7 is slightly greater than those given in Table. 5.5 for all the signals.
2. For the voltage signal in case-2, since the percentile-based threshold (0.000125 p.u) is slightly lower compared to the trial and error based threshold (0.0002 p.u), the number of PMUs deemed to be exhibiting excursions are more, as shown in Table. 5.8 as compared to Table. 5.6. The overall localization decisions for all the signals for case-2 provided by the two methods are the same.

### 5.9.2 3-SD-Based Threshold Calculations

In this method (Allen et al., 2013), the given signal is first transformed to get spectral information. Any transformation technique such as FFT or mode decomposition methods or wavelet transformation may be used for this purpose employing moving window approach. For the transformed data set, standard deviation is computed. Now, the threshold is obtained by taking 3 *times* the standard deviation. Data points above the threshold are classified as outliers and tagged as possible events. For the base case unmodified 4-machine 10-bus system -see Fig. 4.2, (Shubhanga, 2018), the following procedure is employed to illustrate the 3-*SD* method,

1. Obtain the WE of signals for each PMU.
2. Compute the standard deviation of the transformed data set. Note that  $N$  standard deviation values will be obtained.
3. The mean of the  $N$  standard deviations is calculated.
4. The final mean value of the standard deviation is multiplied by three to obtain a threshold,  $WE_{th}$ .

In order to compare the 3-*SD* approach with the Percentile-approach to estimate the threshold, a large disturbance unstable case (Case-3) is considered in the base power system where a 3-phase fault is applied at bus-9 with clearing of line-1.  $T_{fault}$  is set to 20 s and the fault duration is 0.291 s. Frequency excursions at generator buses for this case is shown in Fig. 5.44. The simulation run is carried out for 1000 s and WE of PMU signals are used to estimate the  $WE_{th}$  employing both the approaches. While analyzing the case in hand, a plot of the maximum value of the WE attained by individual frequency signal is obtained as in Fig. 5.45. From the figure, it can be observed that the frequency signal of PMU-9 shows the highest excursion in WE as it is connected to a fault bus, whose voltage reaches near about zero during the fault. Hence, while applying the average of  $N$ -PMUs in the threshold evaluation two variations are considered where in one case PMU-9 is accounted and in the another PMU-9 is excluded in the average computation. The results of these variants are given in Tables. 5.9 and 5.10.

From Table. 5.9 it can be seen that the disturbance has been incorrectly categorized as a local event based on the frequency and ROCOF signals by both approaches, while the disturbance has wide-spread effects. Such a false localization is as a result of using PMU-9

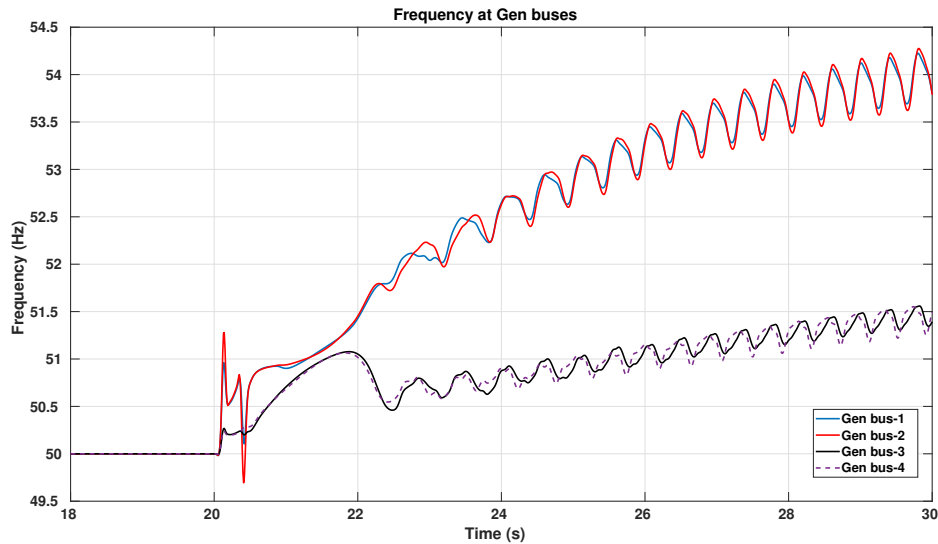


**Figure 5.44:** Frequency at all generator buses for case-3.

based estimates which show extremely high excursions and disrupt the event detection and localization process. For the same case, if PMU-9 based estimates are excluded then a correct localization information can be obtained with the Percentile-based threshold calculation method, -see Table. 5.10. However, the 3-SD based approach fails to properly detect and localize the events even if PMU-9 estimates are excluded from the event detection process. It is also observed that the event start time ( $t_{es}$ ) for the voltage signal (especially calculated using the 3-SD threshold) is much later than its actual incipient time. Such poor detection can be associated with the improper thresholds computed for the large-signal unstable case due to limited number of data points. Such a latency in the event detection procedure can have adverse effects on the system protection and control functions.

**Table 5.9:** Event detection and localization for the unstable case with PMU-9 estimates.

Percentile thresholds (With PMU-9)				
Signal Used ( $WE_{th}$ )	$N_1$	$N_2$	$t_{es}$ (s)	Decision
Voltage (0.032)	5, (PMUs-4,6,8,9,10)	5, (PMU-4,6,8,9,10)	24.288 (PMU-9)	Wide-Spread
Frequency (0.1)	3, (PMUs-6,9,10)	-	20.136 (PMU-9)	Local
ROCOF (2.6579)	3, (PMUs-6,9,10)	-	20.1413 (PMU-9)	Local
3-SD thresholds (With PMU-9)				
	$N_1$	$N_2$	$t_{es}$ (s)	Decision
Voltage (0.0453)	3, (PMUs-8,9,10)	-	28.69 (PMU-9)	Local
Frequency (0.0977)	3, (PMUs-6,9,10)	-	20.13 (PMU-9)	Local
ROCOF (2.116)	3, (PMUs-6,9,10)	-	20.13 (PMU-9)	Local

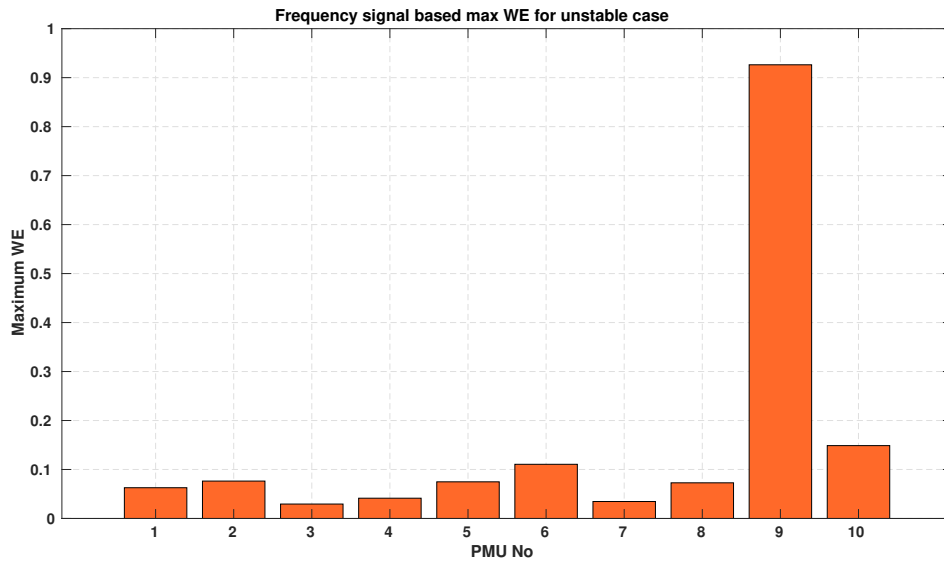


Figure 5.45: Maximum value of Frequency WE with PMU-9 (case-3).

Table 5.10: Event detection and localization for the unstable case without PMU-9 estimates.

Percentile thresholds (Without PMU-9)				
Signal Used ( $WE_{th}$ )	$N_1$	$N_2$	$t_{es}$ (s)	Decision
Voltage (0.0305)	6, (PMUs-2,4,6,7,8,10)	6, (PMU-2,4,6,7,8,10)	26.44 (PMU-10)	Wide-Spread
Frequency (0.0582)	6, (PMUs-1,2,5,6,8,10)	6, (PMUs-1,2,5,6,8,10)	20.215 (PMU-6)	Wide-Spread
ROCOF (1.2737)	6, (PMUs-1,2,5,6,8,10)	6, (PMUs-1,2,5,6,8,10)	20.196 (PMU-6)	Wide-Spread
3-SD thresholds (Without PMU-9)				
	$N_1$	$N_2$	$t_{es}$ (s)	Decision
Voltage (0.0431)	2 (PMUs-8,10)	-	29.4 (PMU-10)	Local
Frequency (0.0775)	2, (PMUs-6,10)	-	20.47 (PMU-6)	Local
ROCOF (1.519)	5, (PMUs-2,5,6,8,10)	5, (PMUs-2,5,6,8,10)	20.2 (PMU-6)	Wide-Spread

**Note:**

1. The threshold estimates are more reliable when
  - A large historian data set is used for threshold calculations.
  - This historian data-set consists of records of multiple events occurring in the power system.
  
2. The threshold values can be used to detect events in signal streams either for off-line analysis or for online event identification. For offline analysis, an hourly data-set may be adequate whereas for reliable online detection, 24 hourly data set (Kim et al., 2015) may be reliable.

## **5.10 Utilization of PAD-Signals for Out-Of-Step Condition Detection**

Based on the observations made in Lavand and Soman (2016), here only the bus angles across different transmission lines are employed to detect OOS condition of a power system. In the literature the bus voltage angle across a transmission line is usually referred to as a Phase Angle Difference (PAD) signal, (Shaw and Jena, 2020), and is determined using the positive sequence voltages obtained from PMUs installed at both the ends of the line. Following steps are used to obtain PAD signals for a power system network :

1. Using PMUs, the bus voltages across a transmission line are noted. Then compute,

$$\bar{V}_R = \frac{\bar{V}_{to}}{\bar{V}_{from}} \quad (5.11)$$

where  $\bar{V}_{to}$ ,  $\bar{V}_{from}$  are the voltage phasors of the two buses across which the transmission line is connected.

2. The phase of the evaluated voltage ratio, i.e.,  $\bar{V}_R$ , is computed to obtain the PAD signal for a transmission line.
3. PAD signals for the post fault system are used for further analysis.

After computing the unwrapped post fault PAD signals the following steps are employed to identify an out-of-step condition on a power system,

1. PAD signals are plotted for important transmission lines in a power system to track whether any PAD signal crosses  $180^\circ$ .
2. In case the PAD across a line crosses  $180^\circ$ , the system can be declared as unstable and an out-of-step condition can be flagged. During such a condition one or several PAD signals might exhibit excursions greater than  $180^\circ$

If a power system remains stable after a fault the PAD across transmission lines shows excursions which are well within the  $180^\circ$  limits. To demonstrate this, PAD signals for case-1 (see Section. 5.8.1) are shown in Fig. 5.46. From the figure it is clear that the PAD signals show small oscillations with positive damping indicating a stable post fault



system. To demonstrate the occurrence of an out-of-step condition and its detection using PAD signals the following two cases are considered:

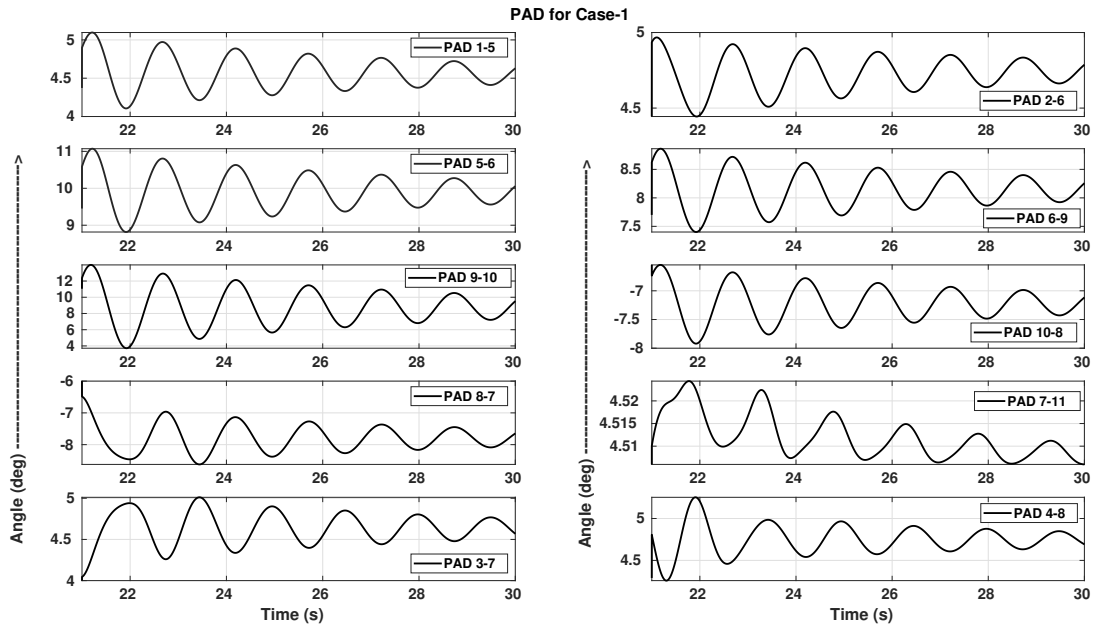


**Figure 5.46:** Phase angles across transmission lines for Case-1.

1. A large-signal unstable case in the base power system -see Section. 5.9.2.
2. A small-signal unstable case.

### 5.10.1 Large-signal unstable system (Case-3)

For this case, the rotor angle excursions are as shown in Fig. 5.47. The corresponding phase angle differences across all the transmission lines are plotted in Fig. 5.48. It is observed that line-2, (see-Fig. 4.2) connected across buses 9 and 10, for which PAD 9-10 is computed, shows an angle excursion greater than  $180^\circ$  at  $t=21.73$  s. This indicates an OOS condition for the power system.

In order to demonstrate the occurrence of an electrical center (Kundur, 1994) on this line, the apparent impedance,  $Z_{app}$ , is computed (as  $\bar{V}_9/\bar{I}_{cl9}$ , where  $\bar{I}_{cl9}$  is the current through the line-2) and its trajectory is plotted as shown in Fig. 5.49, for the pre-fault, fault as well as the post-fault scenario. A Mho impedance characteristics for a relay located at

bus-9 along with the post-fault impedance trajectory is also shown in Fig. 5.50. In this figure, the post fault impedance trajectory which is shown using a circular marker, enters the Mho characteristic at point “A”, at  $t = 20.53$  s, with the impedance value being equal to  $0.178\angle 15.9^\circ$ . The line impedance setting for the Mho characteristic circle denoted by the vector “OB”, is intersected at point “E” by the post fault impedance trajectory at time,  $t = 21.73$  s. At this point  $Z_{app} = 0.12\angle 85.04^\circ$  p.u. The value of PAD (9-10) at point “E” is  $180^\circ$ , -see Fig. 5.48, indicating an OOS condition, (Lavand and Soman, 2016). This particular point is called as the electrical center and lies approximately at the center of the line impedance vector “OB”. The voltage at the electrical center is zero and hence it appears as a three-phase fault at that point on the line (Kundur, 1994).

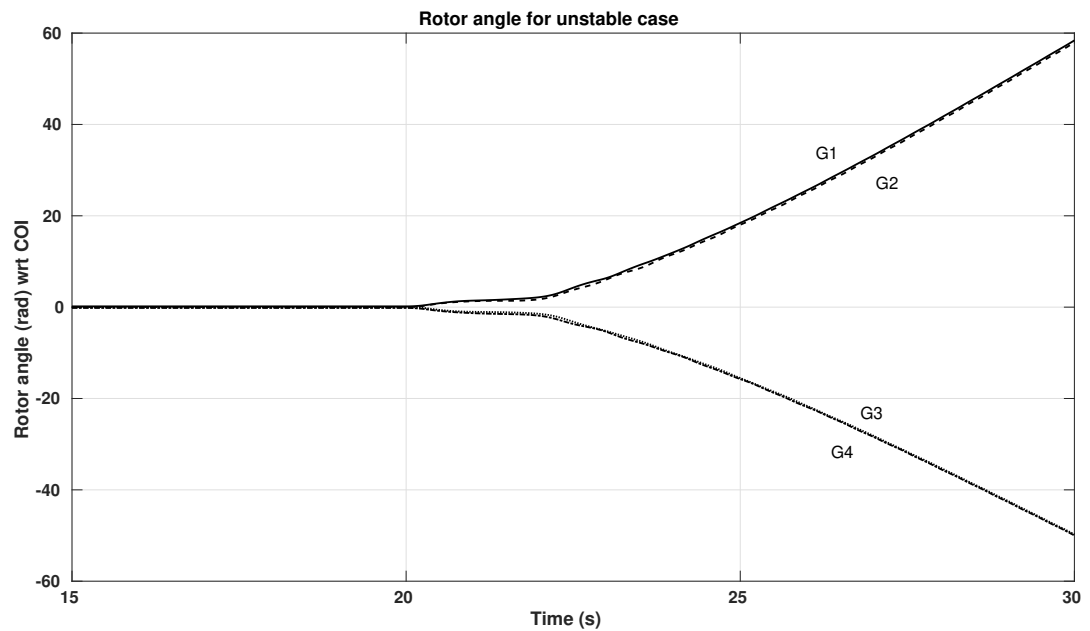


**Figure 5.47:** Rotor angle excursions for large-signal unstable case (Case-3).

The values of the pre and post fault impedance (at point E) are summarized in Table 5.11. The ratio of the magnitude of the post fault impedance at the electrical center “E” to the impedance of the line “OB”, i.e.,  $|Z_{app2}|/|Z_L|$  shows that the electrical center formation has occurred at 54.45% of the transmission line length starting from bus-9.

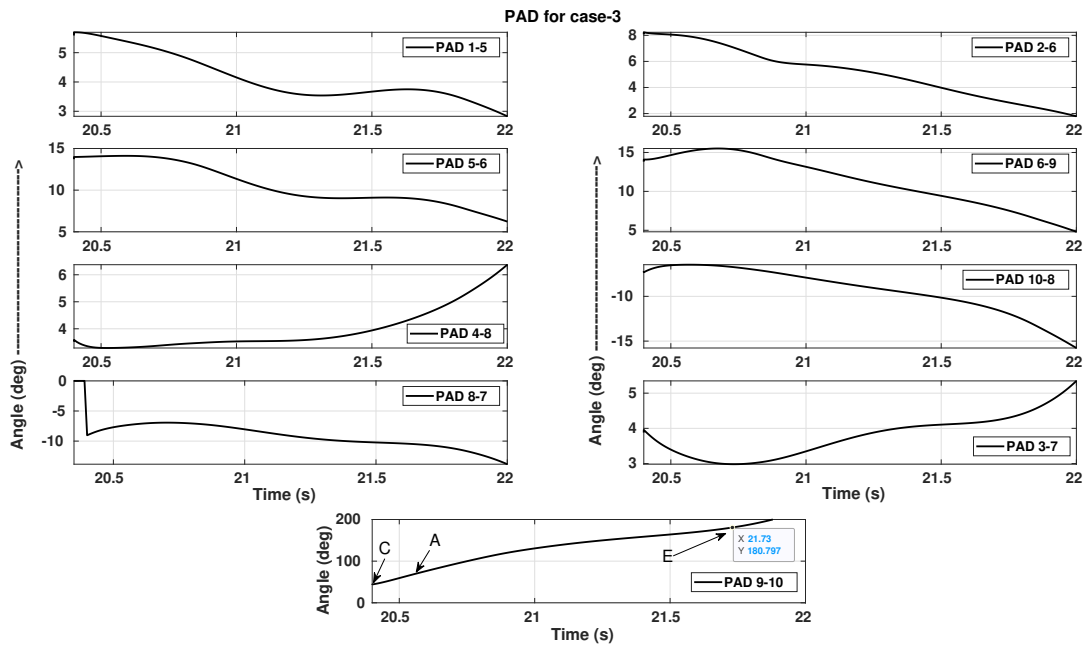


Figure 5.48: Phase angles across transmission lines for Case-3.

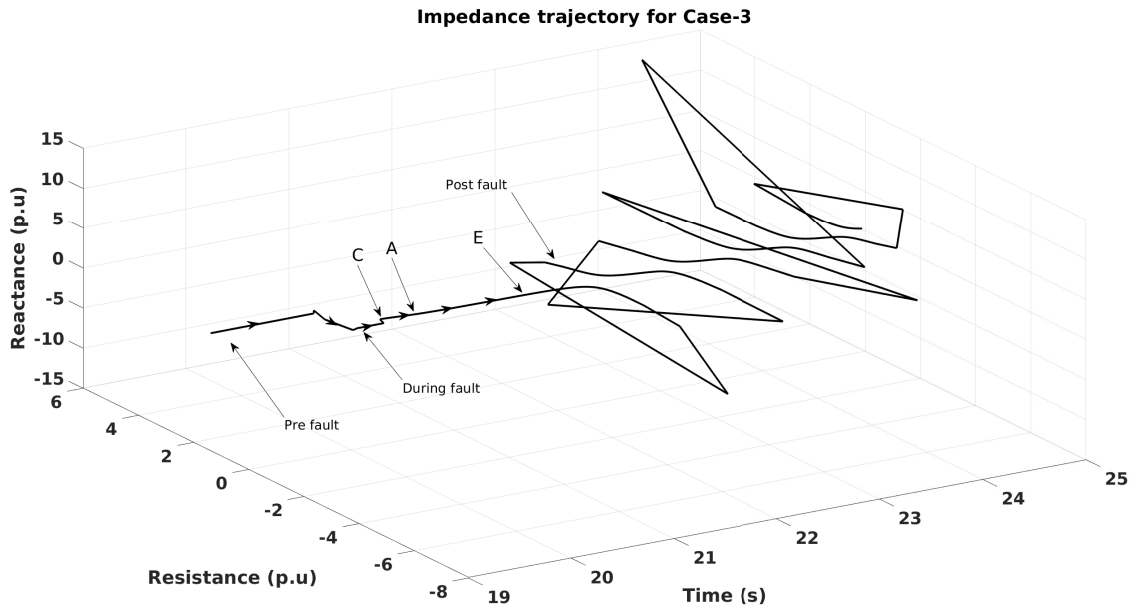
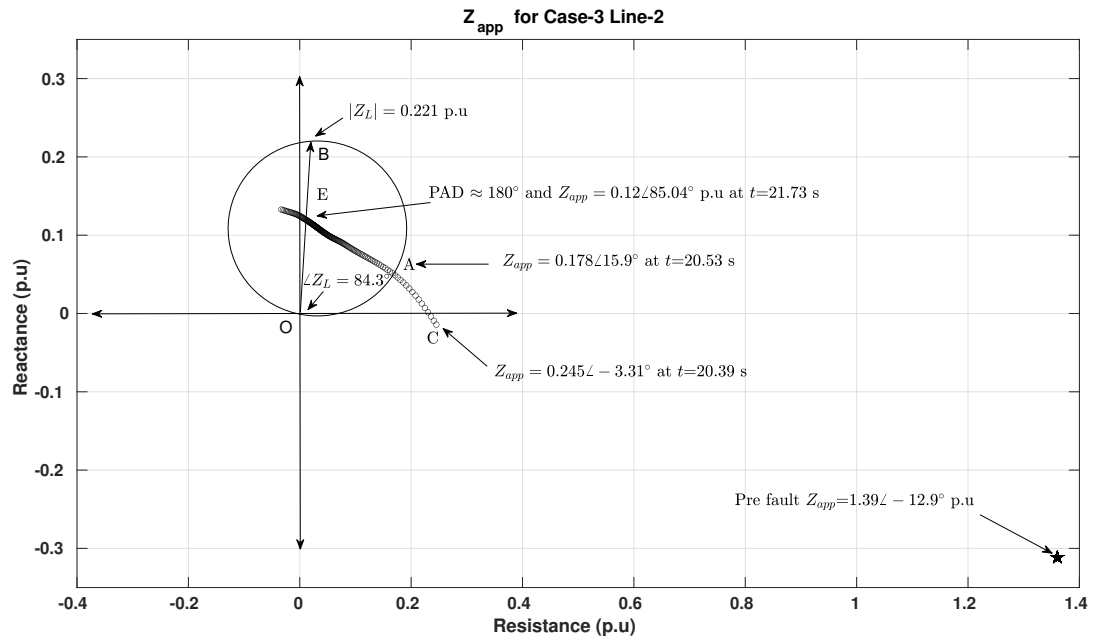


Figure 5.49: Apparent impedance trajectory of line 9-10 (Case-3).

**Table 5.11:** Pre and post fault  $Z_{app}$  for Case-3.

$Z_L = 0.221 \angle 84.3^\circ$ p.u		
Pre fault $Z_{app1}$ p.u	Post fault $Z_{app2}$ p.u (at E)	$ Z_{app2} / Z_L $
$1.396 \angle -12.9^\circ$ ( $1.36 - j0.3115$ )	$0.12 \angle 85.04^\circ$ ( $0.0104 + j0.12$ )	0.5445

To show, the non-existence of an electric center on a transmission line across which PAD excursions are less than  $180^\circ$  the pre and post fault impedance trajectories for line-10 which connects buses 8 and 7 are plotted in Fig. 5.51. Since the angle across line-10, i.e., PAD 8-7 does not cross the  $180^\circ$  limit, no electric center is formed on the transmission line. Both the pre and the post fault impedance values lie far away from the Mho characteristic circle and do not intersect it at any point.



**Figure 5.50:** R-X plot of apparent impedance of line 9-10 (Case-3).

### 5.10.2 Small-signal unstable case (Case-4)

For this case, a modified 4-machine 10-bus power system with only line-1 connecting buses 9 and 10 (lines 2 and 3 are considered to be out of service for this case) is employed (Shubhanga, 2018). At time,  $T_{fault} = 20$  s, a small duration fault of 0.05 s is applied at

bus-7 without any line clearing. This triggers a growing electromechanical oscillation of rotors since the operating point is small-signal unstable. For this case, the PAD across various transmission lines are plotted as shown in Fig. 5.52. From the figure it is clear that PAD 9-10 signal, corresponding to line-1, only exhibits angle excursions greater than  $180^\circ$ . However, the PAD signal crosses the  $180^\circ$  threshold at a much later time, at  $t=153.5$  s which is very large in comparison to the previous case (which involves a large disturbance). The apparent impedance trajectory,  $Z_{app}$ , for this case is shown in Fig. 5.53, for the pre-fault, fault and the post-fault scenario.

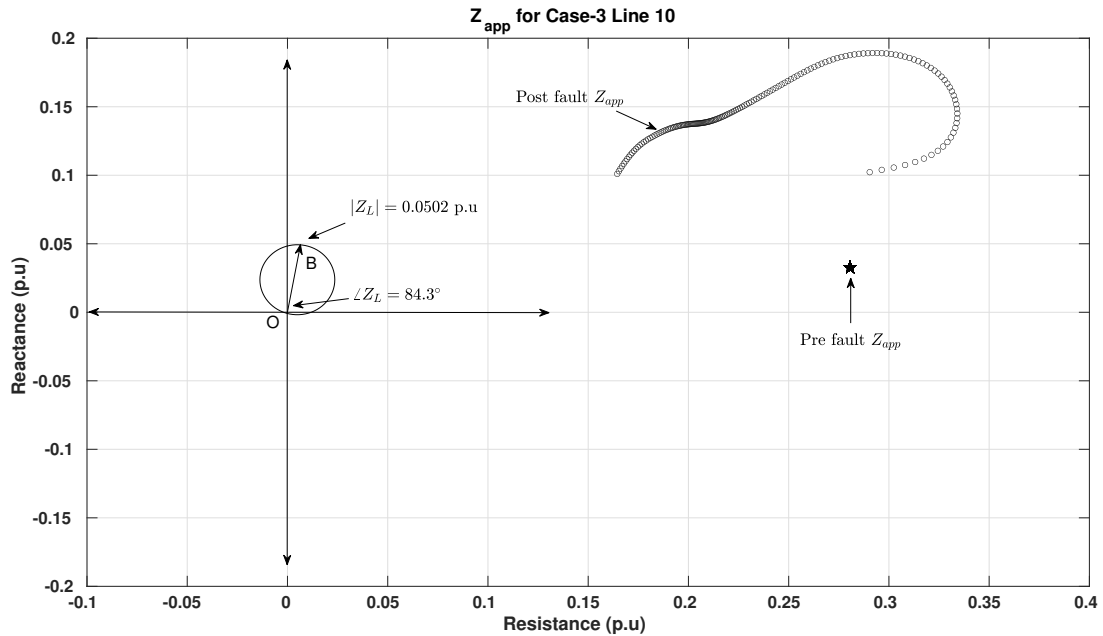


**Figure 5.51:** R-X plot of apparent impedance of line 8-7 (Case-3).

The Mho characteristics for a relay located at bus-9 along with the pre and post fault impedance are shown in Fig. 5.54. From this figure it can be noted that the post fault impedance values enter the Mho characteristic curve at point “A”, at  $t = 151.66$  s where the value of apparent impedance is  $0.1678 \angle 34^\circ$  p.u. The trajectory finally intersects the line impedance vector “OB” at point “E”, at  $t = 153.5$  s. At this point the phase angle difference across the transmission line-1 is equal to  $180^\circ$  and hence “E” represents the electric center of the transmission line. The value of the apparent impedance  $Z_{app}$  at PAD equal to  $180^\circ$  is  $0.1145 \angle 84.8^\circ$  p.u.

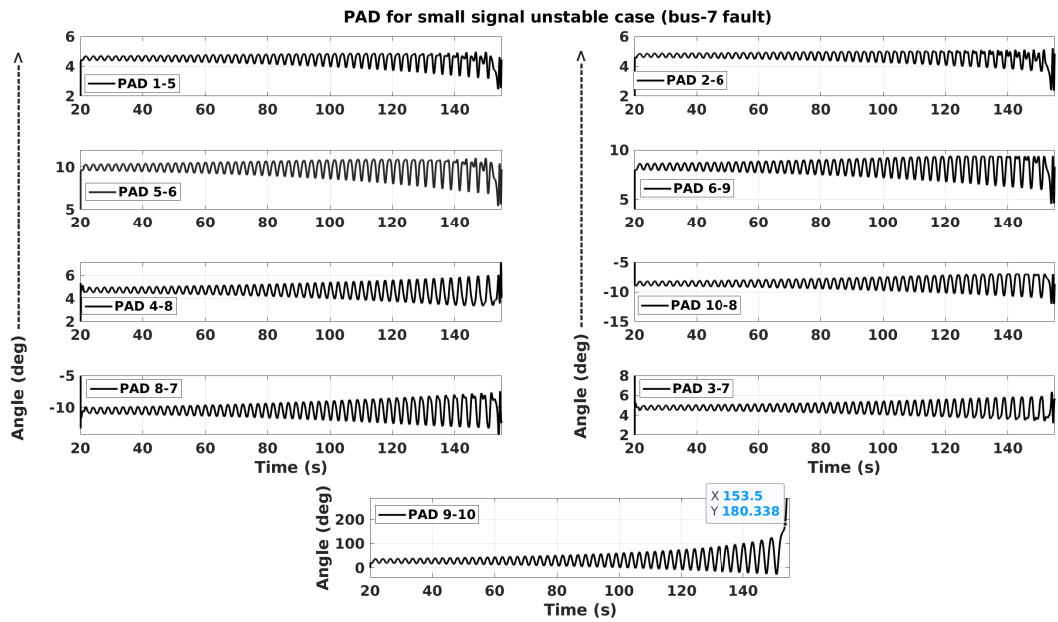


Figure 5.52: Phase angle across transmission lines for small signal unstable case (Case-4).

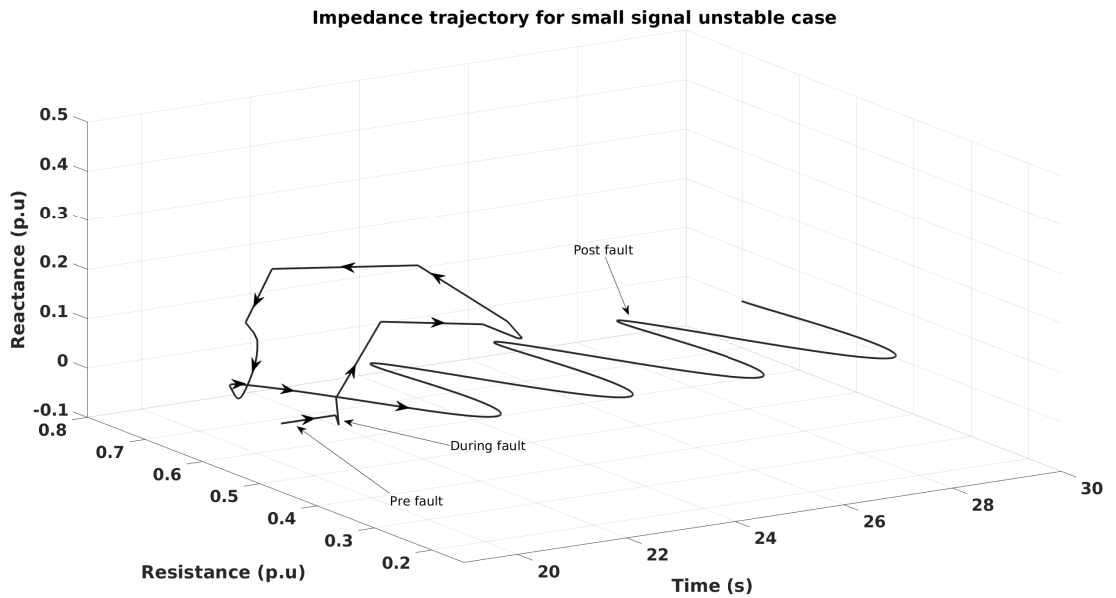
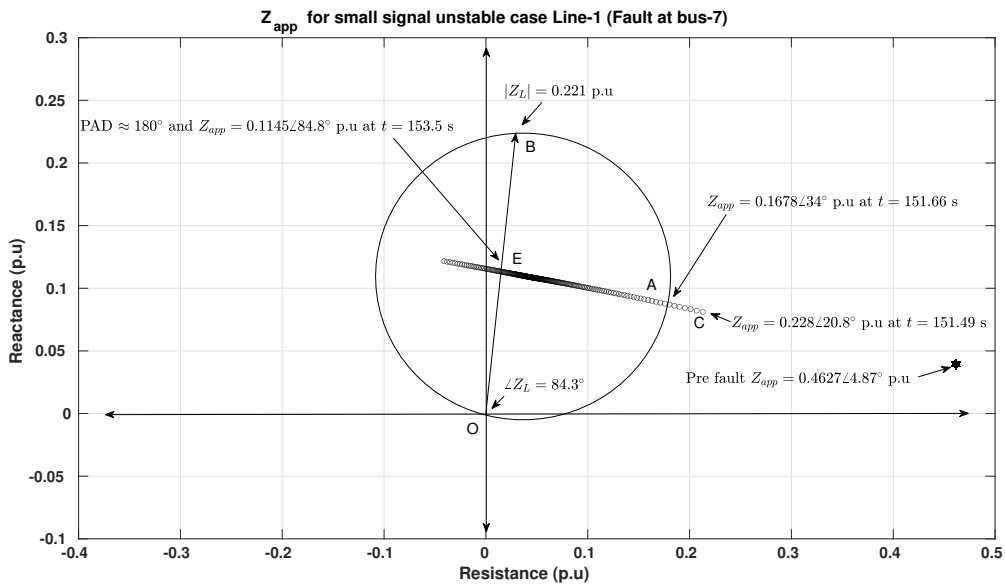


Figure 5.53: Apparent impedance trajectory of line 9-10 for small-signal unstable case (Case-4).

**Note :**

1. The value of PAD 9-10 signal for case-3 at point “C” in Fig. 5.48 is  $44^\circ$  which advances to  $64.5^\circ$  at point “A”. Similarly for case-4, the value of PAD 9-10 signal at point “C” is  $56.9^\circ$  increasing to  $81.82^\circ$  at point “A”.
2. A threshold value for PAD excursions can be set, for example say  $100^\circ$ , crossing which would initiate an algorithm to extrapolate the PAD signal and predict the trend of the future samples. Such a technique can be useful to determine in advance whether the PAD signals will cross the  $180^\circ$  threshold and result in an electric center somewhere on the transmission line. A power swing block (PSB) command can be initiated in advance in order to prevent undesired lines from tripping across the network whenever such a condition is anticipated (Lavand and Soman, 2016).



**Figure 5.54:** R-X plot of apparent impedance of line 9-10 for small signal unstable case (Case-4).

## 5.11 Summary of the Presented Work

Event analysis is a major application of WAMS and can be undertaken either in an online or an offline fashion. An insight into the detection and localization aspect of event analysis

is provided in this chapter, with the main points listed as follows :

1. Non-training based techniques, including the wavelet transform and standard deviation are used for demonstrating the event detection procedure.
2. Methods for threshold computation such as the percentile-based and the  $3 - SD$  based approach are described. It is noted that the value of threshold influences the overall event detection process.
3. The impact of lack of availability of historian data on the event detection procedure is demonstrated, especially with respect to threshold calculations. Due to the lack of availability of historian data, several event detection algorithms such as the MWE method fail to properly recognize the incipient time of disturbances.
4. An event localization algorithm is proposed which categorizes disturbances as local or wide-spread. The localization of a disturbance is determined using the number of PMUs that exhibit WE or SD excursions greater than the threshold.
5. The event localization logic is applied to disturbance cases from the ISO-NE power system and a simulation based 4-machine 10-bus power system. It is demonstrated that the method of choosing a threshold value also influences the overall localization decision of a power system event. The localization algorithm must be adjusted depending on factors such as the overall structure and the number of PMUs in the power system, in order to ensure correct decisions.
6. PAD signals obtained across transmission lines are used to detect a loss-of-synchronism condition in a power system. Careful extrapolation of PAD signals can be carried out in order to detect an OOS condition beforehand. PSB logic can be initiated ahead of time in order to prevent uncontrolled tripping of relays at vulnerable points in a transmission network. This in-turn can aid a power system operator to initiate controlled separation at pre-determined locations to prevent a blackout.





---

# Chapter 6

## CONCLUSIONS

### 6.1 Work Carried Out and Inferences

The topics discussed in this thesis deal with phasor measurement units and their applications in wide area measurement systems. The work carried out in this thesis includes :

1. Test procedures with regards to the IEEE standard for synchrophasor measurements in power systems are demonstrated. Updates of the standards over the years are compared with emphasis on the changes to the test cases and their respective error limit requirements. Compliance verification procedure based on the latest IEEE synchrophasor standard is demonstrated using the one-cycle DFT algorithm. Three methods employed for time-tagging phasor estimates are indicated with focus particularly on the RE and the RC approach.
2. Several PMU algorithms, based on the static and the dynamic models are described. These algorithms are implemented in the integrated PMU architecture environment to provide causal as well as non-causal phasor estimates. The application of both the estimates for power system studies is also demonstrated. It is observed that for most of the standard based test cases, the non-causal estimates result in low TVE values, due to the off-line time-tag adjustments. Contrary to this, the causal phasor estimates exhibit high values of TVE, especially during amplitude modulation conditions as the phasor estimates are provided with only angle compensation. Effect of different angle compensation schemes on direct measurements such as voltage and current phasors, as well as on pseudo measurements such as complex power and impedance is also investigated. TVE values obtained for causal phasors compensated using

voltage based frequency are shown to be lower as compared to phasors compensated using current signal frequency. Influence of the integrated PMU architecture outputs on power system stability is demonstrated by using both the causal and non-causal estimates as inputs to a power system stabilizer for oscillation damping.

3. A frequency estimation technique involving the reconstruction of time-domain signals using phasor samples is proposed. It is shown that if time-domain signals are reconstructed using phasor samples, frequency information is preserved even if off-nominal frequencies are involved. Hilbert filter demodulation (HFD) and Convolution averaging filter (CAF) methods are used for estimating frequency using the reconstructed signals. It is demonstrated that the reconstruction-based approach outperforms the conventional frequency-domain based frequency estimating techniques, especially when single-phase signals are involved. Several IEEE synchrophasor standard based tests are carried out and the results are compared with state-of the art single-phase PMUs. A simulation based 4-machine 10-bus power system is used as a test-bed in addition to realistic phasor data samples obtained from the ISO-NE power system to demonstrate the effectiveness of the reconstruction-based approach. Frequency and ROCOF obtained using the signal reconstruction-based approach for different fault cases are compared with the theoretical, and these signals are also subjected for mode-identification via the Prony method. Effect of window length, start time, frame rate and order of the linear predictor on the behaviour of the Prony method is also explored. It is also noted through a lab experimentation that an accurate frequency estimation during a loss-of-synchronism condition is not straight forward.
4. An event detection and localization tool is developed to illustrate an application of WAMS signals obtained from simulation studies as well as a practical ISO-NE power system. Effectiveness of highly sampled WAMS data for identification of different events is demonstrated using signal processing based approaches such as the wavelet transform and the standard deviation methods. Both the techniques lead to similar results when used for event detection. Disturbances are detected against thresholds which are obtained using different methods such as, a hit and trail technique, percentile-based approach and the  $3 - SD$ -approach. It is shown that the threshold values have a significant bearing on the overall event detection process. An event localization logic is also proposed which is based on the excursions exhibited by

individual PMUs once an event is successfully detected. Based on the localization results, events are classified as local or wide-spread, depending on their area of influence. This aids power system operators in understanding the severity of a disturbance and, in turn to take necessary action to avoid cascading outages. As a part of the event analysis a scheme to detect loss-of-synchronism condition, is developed using PAD signals obtained from across transmission lines. The relationship between the electrical center and the occurring of LOS event is demonstrated using simulations carried out on a 4-machine 10-bus power system.

## **6.2 Major Contributions**

The major contributions based on the work carried out in this thesis are as follows :

1. A comparison of the available IEEE standards for synchrophasor measurements in power systems is presented. This includes an exhaustive description of all the tests required for compliance verification. The standard based testing procedures are demonstrated using a one-cycle DFT algorithm, in a tutorial manner.
2. An integrated PMU architecture is proposed and several PMU algorithms, based on the static-model as well as the dynamic model are implemented using this architecture. The causal and non-causal PMUs implemented based on the integrated architecture are tested using the standard based signals. Applications of the outputs obtained using the integrated PMU architecture for power system monitoring and control are also demonstrated.
3. A single-phase time-domain signal reconstruction-based approach for frequency estimation is proposed. This approach provides an additional M-class compliant frequency estimator when augmented with a conventional DFT based P-class algorithm. Frequency and ROCOF signals obtained via the reconstruction-based approach are subjected to mode identification using the Prony method and the influence of frame rate, window length, order of the linear predictor etc on the dominant modal value is studied.
4. An event detection and localization tool is developed to demonstrate an application of WAMS signals. Effectiveness of the wavelet transform and standard deviation as event detection tools is demonstrated. Influence of the threshold values on the event

detection logic is also shown. A new event localization logic based on the number of PMUs involved in the event detection process is proposed. A method to identify an OOS condition based on PAD signals, is presented.

### 6.3 Future Work

1. *Improvements to phasor estimation techniques:* The use of synchrophasor estimates for model validation, inertia estimation or as control signals demands precise measurement. Therefore, computationally light and accurate algorithms which are both P and M class compliant can be designed in order to provide multiple functionalities. Hybrid model based algorithms which combine different techniques such as in (Khodaparast et al., 2022), to obtain phasor estimates can be explored.
2. *Denoising techniques:* PMU output data can be denoised before it is used for downstream applications involving measurement, protection or control. Methods such as the wavelet transform and the Fast Fourier Transform have been successfully used to denoise signals. Exploration of different methods such as the empirical mode decomposition (EMD) technique as a denoising tool can be explored in the future.
3. *Improvements to single-phase phasor estimation:* Since most of the present PMUs are installed in transmission networks, three-phase signals are available and hence accurate positive sequence phasors can be estimated. Recently, due to the emergence of  $\mu$ -PMUs, accurate single-phase algorithms must be designed for distribution system applications.
4. *Performance improvement of causal PMUs during amplitude modulation conditions:* Due to the absence of an amplitude compensation factor in causal PMUs, the TVE values during amplitude modulation conditions are very high and do not meet the requirements of the IEEE standards. The errors increase as the value of the group delay of a PMU algorithm increases. Therefore, the formulation of an amplitude compensation factor for causal PMUs needs to be devised.
5. *Frequency estimation during loss-of-synchronism condition:* Due to severe fluctuations of voltage as well as current signals during LOS conditions, traditional PMUs fail to accurately track the amplitude, phase and frequency of the signal. An accurate estimation of frequency during such conditions is a major requirement.

6. *Improvements to mode estimation algorithms:* Observations made with regards to mode estimation results obtained using the Prony method emphasized the need for improvement in the decrement factor estimation while dealing with signals with multiple signatures within a given data window. Online application of Prony method can be explored by carefully assigning an initial value for the order of the linear prediction ( $n$ ). This can lead to quick convergence of the Prony algorithm, thus enabling its application as an online tool for mode estimation.
7. *OOS detection using PAD signals:* An extrapolation method can be designed in order to predict in advance, whether a certain PAD signal crosses  $180^\circ$  for any transmission line. Such a logic can be used to initiate PSB on relays which are vulnerable to undesirable tripping, thus ensuring the integrity of the power system.
8. *Integrated simulation package:* In a multi-machine transient stability environment, several PMUs based on the integrated architecture can be developed, including mode identification algorithms. The complete integrated simulation package incorporating such features would be a great research potential.

---

# Appendix A

## PMU numbering for ISO-NE data

**Table A.1:** PMU No and the associated substation and line for the ISO-NE system.

PMU	Sub and Ln No
PMU-1	Sub-1 Ln 1
PMU-2	Sub-1 Ln 1-11
PMU-3	Sub-2 Ln 2
PMU-4	Sub-2 Ln 3
PMU-5	Sub-2 Ln 4
PMU-6	Sub-3 Ln 5
PMU-7	Sub-3 Ln 6
PMU-8	Sub-3 Ln 7
PMU-9	Sub-4 Ln 8
PMU-10	Sub-4 Ln 4-6
PMU-11	Sub 4 Ln 9
PMU-12	Sub-5 Ln 10
PMU-13	Sub-5 Ln 11
PMU-14	Sub-5 Ln 12
PMU-15	Sub-6 Ln 4-6
PMU-16	Sub-6 Ln 13
PMU-17	Sub-6 Ln 14
PMU-18	Sub-6 Gen 1
PMU-19	Sub-7 Ln 15
PMU-20	Sub-7 Ln 16
PMU-21	Sub-7 Gen 2
PMU-22	Sub-8 Ln 17
PMU-23	Sub-8 Ln 18
PMU-24	Sub-8 Ln 19
PMU-25	Sub-8 Gen 1
PMU-26	Sub-9 Ln 20
PMU-27	Sub-9 Ln 21
PMU-28	Sub-10 Ln 22
PMU-29	Sub-10 Ln 23
PMU-30	Sub-10 Ln 24
PMU-31	Sub-11 Ln-25
PMU-32	Sub-11 Ln 1-11
PMU-33	Sub-12 Ln 26
PMU-34	Sub-12 Ln 27
PMU-35	Sub-12 Ln 28





---

# Bibliography

- Aalam, M.K. and Shubhanga, K.N., (2021). "An integrated PMU architecture for power system applications." *International Journal of Emerging Electric Power Systems*.
- Aalam, M.K. and Shubhanga, K.N., (2021). "EMD based Detrending of Non-linear and Non-stationary Power System Signals." In *2021 IEEE 18th India Council International Conference (INDICON)* (pp. 1-6). IEEE.
- Adhikari, P.M., Hooshyar, H. and Vanfretti, L., (2019). "Experimental quantification of hardware requirements for fpga-based reconfigurable pmus." *IEEE Access*, 7, pp.57527-57538.
- Agarwal, P.K., Agarwal, V.K. and Rathour, H., (2013). "Application of PMU-based information in the Indian power system." *International Journal of Emerging Electric Power Systems*, 14(1), pp.79-86.
- Ahmed, H., Amamra, S.A. and Salgado, I., (2018). "Fast estimation of phase and frequency for single-phase grid signal." *IEEE Transactions on Industrial Electronics*, 66(8), pp.6408-6411.
- Ahmed, A., Sajan, K.S., Srivastava, A. and Wu, Y., (2021). "Anomaly detection, localization and classification using drifting synchrophasor data streams." *IEEE Transactions on Smart Grid*, 12(4), pp.3570-3580.
- Ahmed, M.M., Amjad, M., Qureshi, M.A., Imran, K., Haider, Z.M. and Khan, M.O., (2022). "A Critical Review of State-of-the-Art Optimal PMU Placement Techniques." *Energies*, 15(6), p.2125.
- Ahmed, H., Ushirobira, R. and Efimov, D., (2021). "A Simple Frequency Estimator For Power Systems." *IEEE Transactions on Instrumentation and Measurement*, 70, pp.1-2.

- Akke, M. and Thorp, J.S., (2010). "Sample value adjustment improves phasor estimation at off-nominal frequencies." *IEEE Transactions on Power Delivery*, 25(4), pp.2255-2263.
- Akke, M., (1997). "Frequency estimation by demodulation of two complex signals." *IEEE Transactions on Power Delivery*, 12(1), pp.157-163.
- Allen, A., Santoso, S. and Muljadi, E., (2013). "Algorithm for screening phasor measurement unit data for power system events and categories and common characteristics for events seen in phasor measurement unit relative phase-angle differences and frequency signals (No. NREL/TP-5500-58611)." *National Renewable Energy Lab.(NREL), Golden, CO (United States)*.
- Annakage, U., Rajapakse, A., Bhargava, B., Chaudhuri, N., Mehrizi-sani, A., Hauser, C., Wadduwage, D., Ribeiro Campos Andrade, S., Pathirana, V., Katsaros, K. and Chalraborty, A., (2017). "Application of phasor measurement units for monitoring power system dynamic performance (No. STANDARD). Cigré."
- Ansari, R., (1985). "Elliptic filter design for a class of generalized halfband filters." *IEEE transactions on acoustics, speech, and signal processing*, 33(5), pp.1146-1150.
- Ashton, P.M., Taylor, G.A., Irving, M.R., Pisica, I., Carter, A.M. and Bradley, M.E., (2013). "Novel application of detrended fluctuation analysis for state estimation using synchrophasor measurements." *IEEE Transactions on Power Systems*, 28(2), pp.1930-1938
- Ashton, P.M., Saunders, C.S., Taylor, G.A., Carter, A.M. and Bradley, M.E., (2014). "Inertia estimation of the GB power system using synchrophasor measurements." *IEEE Transactions on Power Systems*, 30(2), pp.701-709.
- Bansal, Y. and Sodhi, R., (2019), December. "An adaptive iir notch filter based half-cycle p-class phasor measurement estimation scheme." In *2019 8th international conference on power systems (ICPS)* (pp. 1-6). IEEE.
- Barchi, G., Belega, D. and Petri, D.(2013). "Performance of synchrophasor estimators in transient conditions: a comparative analysis." *IEEE Trans. Instrum. Meas.*, 62(9), 2410–2418.

- Barchi, G., Macii, D., Petri, D. (2012). “Accuracy of One-Cycle DFT based Synchronphasor Estimators in Steady-state and Dynamic Conditions,” *IEEE International Instrumentation and Measurement Technology Conference (I2MTC)*, Graz, Austria
- Barchi, G., Macii, D. and Petri, D., (2013). “Synchronphasor estimators accuracy: A comparative analysis.” *IEEE Transactions on Instrumentation and Measurement*, 62(5), pp.963-973.
- Barocio, E., Pal, B.C., Fabozzi, D. and Thornhill, N.F., (2013), August. “Detection and visualization of power system disturbances using principal component analysis.” In *2013 IREP Symposium Bulk Power System Dynamics and Control-IX Optimization, Security and Control of the Emerging Power Grid (pp. 1-10)*. IEEE.
- Belega, D. and Petri, D., (2013). “Accuracy analysis of the multicycle synchronphasor estimator provided by the interpolated DFT algorithm.” *IEEE Transactions on Instrumentation and Measurement*, 62(5), pp.942-953.
- Blumschein, J., Yelgin, Y. and Kereit, M., (2014). “Blackout prevention by power swing detection and out-of-step protection.” *Journal of Power and Energy Engineering (JPEE)*, Irvine CA, pp.694-703.
- Brahma, S., Kavasseri, R., Cao, H., Chaudhuri, N.R., Alexopoulos, T. and Cui, Y.,(2016). “Real-time identification of dynamic events in power systems using PMU data, and potential applications—models, promises, and challenges.”, *IEEE transactions on Power Delivery*, 32(1), pp.294-301.
- Canteli, M.M., Fernandez, A.O., Eguiluz, L.I. and Estebanez, C.R., (2006 ). “Three-phase adaptive frequency measurement based on Clarke’s transformation.” *IEEE transactions on power delivery*, 21(3), pp.1101-1105.
- Castello, P., Liu, J., Muscas, C., Pegoraro, P.A., Ponci, F. and Monti, A., (2014). “A fast and accurate PMU algorithm for P+ M class measurement of synchronphasor and frequency.” *IEEE Transactions on Instrumentation and Measurement*, 63(12), pp.2837-2845.
- Castello, P., Lixia, M., Muscas, C. and Pegoraro, P.A., (2012). “Impact of the model on the accuracy of synchronphasor measurement.” *IEEE Transactions on Instrumentation and Measurement*, 61(8), pp.2179-2188.

- Carcelen-Flores, A., Fuentes, J.A., Molina-Garcia, A., Gomez-Lazaro, E. and Viguera-Rodriguez, A., (2012). "Comparison of instantaneous frequency estimation algorithms under power system disturbances." In *2012 IEEE Power and Energy Society General Meeting* (pp. 1-8). IEEE.
- Cai, L., Thornhill, N.F., Kuenzel, S. and Pal, B.C., (2018). "Wide-area monitoring of power systems using principal component analysis and  $k$ -nearest neighbor analysis." *IEEE Transactions on Power Systems*, 33(5), pp.4913-4923.
- Chaudhuri, N.R., Chaudhuri, B., Ray, S. and Majumder, R., (2010). "Wide-area phasor power oscillation damping controller: A new approach to handling time-varying signal latency." *IET generation, transmission and distribution*, 4(5), pp.620-630.
- Chauhan, K., Reddy, M.V. and Sodhi, R., (2018). "A novel distribution-level phasor estimation algorithm using empirical wavelet transform." *IEEE Transactions on Industrial Electronics*, 65(10), pp.7984-7995.
- Cui, M., Wang, J., Tan, J., Florita, A.R. and Zhang, Y., (2018). "A novel event detection method using PMU data with high precision." *IEEE Transactions on Power Systems*, 34(1), pp.454-466.
- Dai, Z. and Tate, J.E., (2021). "Emulating synchrophasor frequency measurements with transient stability simulation." *IEEE Transactions on Power Systems*, 36(5), pp.4066-4074.
- Dagle, J. (2018 ). "An Electric Power Application of Precise Timming: Synchrophasors", *GNSS Timing Receiver Resilience Workshop*, McLean, Virginia.
- Das, S. and Sidhu, T.S., (2013). "Application of compressive sampling in synchrophasor data communication in WAMS." *IEEE Transactions on Industrial Informatics*, 10(1), pp.450-460.
- De La Ree, J., Centeno, V., Thorp, J.S. and Phadke, A.G., (2010). "Synchronized phasor measurement applications in power systems." *IEEE Transactions on smart grid*, 1(1), pp.20-27.
- Denys, P., Counan, C., Hossenlopp, L. and Holweck, C., (1992). "Measurement of voltage phase for the French future defence plan against losses of synchronism." *IEEE Transactions on Power Delivery*, 7(1), pp.62-69.

- De la O Serna, J.A. and Martínez, E.V., (2015). “Smart grids Part 2: Synchrophasor measurement challenges.” *IEEE Instrumentation and Measurement Magazine*, 18(1), pp.13-16.
- De la O Serna, J.A. (2007). “Dynamic phasor estimates for power system oscillations.”, *IEEE Trans. Instrum. Meas.*, 56(5), 1648–1659.
- De la O Serna, J.A. (2010). “Dynamic phasor and frequency estimates through maximally flat differentiators.”, *IEEE Trans. Instrum. Meas.*, 59(7), 1803–1811.
- De la O Serna, J.A., Ramirez, J.M., Mendez, A.Z. and Paternina, M.R.A. (2016). “Identification of electromechanical modes based on digital Taylor-Fourier transform.”, *IEEE Trans. Power Syst.*, 31(1), 206–215.
- De la O Serna, J.A., (2013). “Synchrophasor estimation using Prony’s method.” *IEEE Transactions on Instrumentation and Measurement*, 62(8), pp.2119-2128.
- De la O Serna, J.A and Rodriguez-Maldonado, J (2011). “Instantaneous Oscillating Phasor Estimates With Taylor -Kalman Filters,” *IEEE Transactions On Power Systems* Vol. 26, No. 4
- Derviškić, A., Romano, P. and Paolone, M., (2017). “Iterative-interpolated DFT for synchrophasor estimation: A single algorithm for P-and M-class compliant PMUs.” *IEEE Transactions on Instrumentation and Measurement*, 67(3), pp.547-558.
- Dotta, D., Chow, J.H., Vanfretti, L., Almas, M.S. and Agostini, M.N., (2013), July. “A matlab-based pmu simulator.” In *2013 IEEE Power and Energy Society General Meeting (pp. 1-5)*. IEEE.
- Dotta, D. and Chow, J.H., (2013). “Second harmonic filtering in phasor measurement estimation. *IEEE transactions on power delivery*, 28(2), pp.1240-1241.
- Dusabimana, E. and Yoon, S.G., (2020). “A survey on the micro-phasor measurement unit in distribution networks.” *Electronics*, 9(2), p.305.
- EECS (2022) Accessed on: March. 27, 2022. [Online]. Available at: <http://web.eecs.utk.edu/kaisun/Oscillation/>
- Elmore, W.A., (2003). “Protective relaying: theory and applications” (Vol. 1). CRC press.

- Frigo, G., Derviškadić, A. and Paolone, M., (2018). “Reduced leakage synchrophasor estimation: Hilbert transform plus interpolated DFT.” *IEEE Transactions on Instrumentation and Measurement*, 68(10), pp.3468-3483.
- Fu, L., Yu, L., Xiong, S., He, Z., Mai, R. and Li, X., (2021). “A dynamic synchrophasor estimation algorithm considering out-of-band interference.” *IEEE Transactions on Power Delivery*, 37(2), pp.1193-1202.
- Gajjar, G. and Soman, S.A., (2014), December. “Auto detection of power system events using wide area frequency measurements.” In *2014 Eighteenth National Power Systems Conference (NPSC)* (pp. 1-6). IEEE.
- Gajjar, K.K., Kulkarni, A.M., Gajjar, G., Soman, S.A. and Gajbhiye, R., (2021), December. “Testing of WAMS-based Supervised Zone-3 Distance Relay Protection Scheme using a Real-Time Digital Simulator.” In *2021 9th IEEE International Conference on Power Systems (ICPS)* (pp. 1-6). IEEE.
- Gao, W. and Ning, J., (2011). “Wavelet-based disturbance analysis for power system wide-area monitoring.” *IEEE Transactions on Smart Grid*, 2(1), pp.121-130.
- Ge, Y., Flueck, A.J., Kim, D.K., Ahn, J.B., Lee, J.D. and Kwon, D.Y., (2015). Power system real-time event detection and associated data archival reduction based on synchrophasors. *IEEE Transactions on Smart Grid*, 6(4), pp.2088-2097.
- Ghafari, C., Almasalma, H., Raison, B., Hadjsaid, N., Caire, R. and Martin, E., (2016). “Phasors estimation at offnominal frequencies through an enhanced-SVA method with a fixed sampling clock.” *IEEE Transactions on Power Delivery*, 32(4), pp.1766-1775.
- Ghafari, C., (2016). “Innovative numerical protection relay design on the basis of sampled measured values for smartgrids” (*Doctoral dissertation, Université Grenoble Alpes (ComUE)*).
- Ghiocel, S.G., Dotta, D., Chow, J.H (2013). “Applications of Synchrophasor Data to Power System State Estimation and Control”, *2013 IREP Symposium-Bulk Power System Dynamics and Control*, Rethymnon, Greec.
- Goklani, H., Gajjar, G. and Soman, S.A., (2020). “Instrument transformer calibration and robust estimation of transmission line parameters using PMU measurements.” *IEEE Transactions on Power Systems*, 36(3), pp.1761-1770.

- Gomez-Exposito, A. and Abur, A., (2013). “Foreword for the special section on synchrophasor applications in power systems.” *IEEE Transactions on Power systems*, 28(2), pp.1907-1909.
- Grebla, M., Yellajosula, J.R. and Høidalen, H.K., (2019). “Adaptive frequency estimation method for ROCOF islanding detection relay.” *IEEE Transactions on Power Delivery*, 35(4), pp.1867-1875.
- Guardado, R.A. and Guardado, J.L., (2015). “A PMU model for wide-area protection in ATP/EMTP.” *IEEE Transactions on Power Delivery*, 31(4), pp.1953-1960.
- Guo, Y., Li, K., Lavery, D.M. and Xue, Y., (2015). “Synchrophasor-based islanding detection for distributed generation systems using systematic principal component analysis approaches.” *IEEE Transactions on Power Delivery*, 30(6), pp.2544-2552.
- Gurusinghe, D.R., Rajapakse, A.D. and Narendra, K., (2014 ). “Testing and enhancement of the dynamic performance of a phasor measurement unit.” *IEEE transactions on power delivery*, 29(4), pp.1551-1560.
- Hadley, M.D., McBride, J.B., Edgar, T.W., O’Neil, L.R.O., Johnson, J.D (2007 ). “Securing Wide Area Measurement Systems.” *Manual prepared for U.S Department of Energy by Office of Electricity Delivery and Energy Reliability*.
- Hao, P., Zanzi, W. and Jianye, C., (2007). “A measuring method of the single-phase AC frequency, phase, and reactive power based on the Hilbert filtering.” *IEEE Transactions on Instrumentation and Measurement*, 56(3), pp.918-923.
- Hatziargyriou, N., Milanovic, J., Rahmann, C., Ajarapu, V., Canizares, C., Erlich, I., Hill, D., Hiskens, I., Kamwa, I., Pal, B. and Pourbeik, P., (2020). “Definition and classification of power system stability–revisited and extended.” *IEEE Transactions on Power Systems*, 36(4), pp.3271-3281.
- Jiang, T., Li, X., Bai, L. and Li, F., (2019), October. “Synchrophasor measurement-based modal analysis in power grids.” In *2019 North American power symposium (NAPS)* (pp. 1-5). IEEE.
- IEEE Power Engineering Society (2005)IEEE Standard for Synchrophasors for Power Systems, in IEEE Std C37.118-2005 (Revision of IEEE Std 1344-1995) , vol., no., pp.1-65, 22 March 2006, doi: 10.1109/IEEESTD.2006.99376.



IEEE Standard Association, (2011). IEEE standard for synchrophasor measurements for power systems. IEEE Std C37. 118.1-2011, pp.1-61.

IEEE Standard Association, (2014). IEEE Standard for Synchrophasor Measurements for Power Systems—Amendment 1: Modification of Selected Performance Requirements. IEEE Std C37. 118.1 a-2014 (Amendment to IEEE Std C37. 118.1-2011), 2014, pp.1-25.

IEC/IEEE 60255-118-1, (2018). IEEE/IEC International Standard—Measuring Relays and Protection Equipment—Part 118-1: Synchrophasor for Power Systems—Measurements.

IEEE Power and Energy Society, (2013). “IEEE guide for synchronization, calibration, testing, and installation of phasor measurement units (PMUs) for power system protection and control.” *IEEE Standards Association*.

IEEE Standard for Synchrophasor Data Transfer for Power Systems, (2011). “IEEE Std C37. 118.2-2011 (Revision of IEEE Std C37. 118-2005).”

IEEE Power and Energy Society, (2013). “IEEE guide for synchronization, calibration, testing, and installation of phasor measurement units (PMUs) for power system protection and control.” IEEE Standards Association.

Ivanković, I. and Brnobić, D., (2021). “Distance protection based on the synchrophasor data in control room.” In Istanbul, Turkey: *9th European Conference on Renewable Energy Systems*.

Jafarpisheh, B., Madani, S.M., Parvaresh, F. and Shahrtash, S.M., (2018). “Power system frequency estimation using adaptive accelerated MUSIC.” *IEEE Transactions on Instrumentation and Measurement*, 67(11), pp.2592-2602.

Jin, T. and Zhang, W., (2020). “A novel interpolated DFT synchrophasor estimation algorithm with an optimized combined cosine self-convolution window.” *IEEE Transactions on Instrumentation and Measurement*, 70, pp.1-10.

Kamwa, I., and R. Grondin, R.(1991). “Fast Adaptive Schemes for tracking Voltage Phasor and Local Frequency in Power Transmission and Distribution Systems,” *Proceedings of the 1991 IEEE Power Engineering Society Transmission and Distribution Conference*

- Kamwa, I., Samantaray, S.R and Wide, G.J., (2014). “Wide Frequency Range Adaptive Phasor and Frequency PMU Algorithms,” *IEEE Transactions On Smart Grid* Vol. 5, No. 2
- Khodaparast, J., Fosso, O. and Molinas, M., (2022). “Phasor Estimation by EMD-Assisted Prony.” *IEEE Transactions on Power Delivery*.
- Kim, Y.H., Son, K.J., Kang, S.H. and Chang, T.G., (2020). “Improved frequency estimation algorithm based on the compensation of the unbalance effect in power systems.” *IEEE Transactions on Instrumentation and Measurement*, 69(12), pp.9880-9892.
- Kim, D.I., Chun, T.Y., Yoon, S.H., Lee, G. and Shin, Y.J., (2015). “Wavelet-based event detection method using PMU data.” *IEEE Transactions on Smart grid*, 8(3), pp.1154-1162.
- Kirkham, H., Dickerson, W. and Phadke, A., (2018), “ Defining power system frequency.” In *2018 IEEE Power and Energy Society General Meeting (PESGM)* (pp. 1-5). IEEE.
- Kulkarni, A.M. (2014). “Wide area frequency measurement system.” IIT Bombay, Mumbai, India, URL: <http://www.ee.iitb.ac.in/~peps>.
- Kulkarni, A.R. and Ballal, M.S., (2020). “Ultra mega power plant disturbance related oscillation detection in Indian grid using PMU data.” *International Journal of Emerging Electric Power Systems*, 21(4).
- Kumar, R., Dewal, M.L. and Saini, K., (2010). “Utility of SCADA in power generation and distribution system.” In *2010 3rd International Conference on Computer Science and Information Technology* (Vol. 6, pp. 648-652). IEEE.
- Kumar, B.R., Mohapatra, A. and Chakrabarti, S., (2020). “Combined Two-Point and Three-Point Interpolated DFT for Frequency Estimation.” In *2020 21st National Power Systems Conference (NPSC)* (pp. 1-6). IEEE.
- Kundur, P. (1994). *Power system stability and control*, McGraw-Hill, New York.
- Kutz, J.N., (2013). “Data-driven modeling and scientific computation: methods for complex systems and big data. Oxford University Press.”

- Lavand, S.A. and Soman, S.A., (2016). “Predictive analytic to supervise zone 1 of distance relay using synchrophasors”. *IEEE Transactions on Power Delivery*, 31(4), pp.1844-1854.
- Li, J., Teng, Z., Wang, Y., You, S., Liu, Y. and Yao, W., (2019 ). “A fast power grid frequency estimation approach using frequency-shift filtering.” *IEEE Transactions on Power Systems*, 34(3), pp.2461-2464.
- Liu, X., Lavery, D.M., Best, R.J., Li, K., Morrow, D.J. and McLoone, S., (2015). “Principal component analysis of wide-area phasor measurements for islanding detection—A geometric view.” *IEEE Transactions on Power Delivery*, 30(2), pp.976-985.
- Liu, H., Qi, Y., Zhao, J. and Bi, T., (2021). “Data-driven subsynchronous oscillation identification using field synchrophasor measurements.” *IEEE transactions on power delivery*, 37(1), pp.165-175.
- Liu, Z., Zhang, Y., Feng, K., Ma, H. and Li, T., (2014). “A wide area information based method of tracking power system’s oscillation center and its application.” *Power Syst. Technol.*, 38(6), pp.1694-1699.
- Liu, Y., Fan, R. and Terzija, V., (2016). “Power system restoration: a literature review from 2006 to 2016.” *Journal of Modern Power Systems and Clean Energy*, 4(3), pp.332-341.
- Louis, S.S., Feroz, F., Gajjar, G. and Kulkarni, A.M., (2021), December. “Wide Area Synchronous Disturbance Recording System.” In *2021 9th IEEE International Conference on Power Systems (ICPS)* (pp. 1-6). IEEE.
- Macci, D., Petri, D. and Zorat, A. (2011). “Accuracy of DFT-based synchrophasor estimators at off-nominal frequencies”, *Proc., 2011 Int. Workshop on Applied Measurements for Power Systems (AMPS)*, Aachen, Germany, 19–24.
- Maslennikov, S., Wang, B., Zhang, Q. and Litvinov, E., (2016). “A test cases library for methods locating the sources of sustained oscillations.” In *2016 IEEE Power and Energy Society General Meeting (PESGM)* (pp. 1-5). IEEE.
- Maharjan, S., Peng, J.C.H., Martinez, J.E., Xiao, W., Huang, P.H. and Kirtley, J.L., (2016). “Improved sample value adjustment for synchrophasor estimation at off-nominal power system conditions.” *IEEE Transactions on Power Delivery*, 32(1), pp.33-44.

- Mallat, S.G., (1989). "A theory for multiresolution signal decomposition: the wavelet representation". *IEEE transactions on pattern analysis and machine intelligence*, 11(7), pp.674-693.
- Mallat, S., (2008). "A Wavelet Tour of Signal Processing: The Sparse Way, 805 p."
- Manousakis, N.M., Korres, G.N. and Georgilakis, P.S., (2011), September. "Optimal placement of phasor measurement units: A literature review." In 2011 *16th International Conference on Intelligent System Applications to Power Systems* (pp. 1-6). IEEE.
- Martin, K.E., Benmouyal, G., Adamiak, M.G., Begovic, M., Burnett, R.O., Carr, K.R., Cobb, A., Kusters, J.A., Horowitz, S.H., Jensen, G.R. and Michel, G.L., (1998). "IEEE standard for synchrophasors for power systems." *IEEE Transactions on Power Delivery*, 13(1), pp.73-77.
- Martin, K.E., (2015). "Synchrophasor measurements under the IEEE standard C37. 118.1-2011 with amendment C37. 118.1 a." *IEEE Transactions on Power Delivery*, 30(3), pp.1514-1522.
- Martinez, E.V. and Serna, J.A., (2015). "Smart grids part 1: Instrumentation challenges." *IEEE Instrumentation and Measurement Magazine*, 18(1), pp.6-9.
- McDonald, M., Tziouvaras, D. and Apostolov, A., (2005). "Power swing and out-of-step considerations on transmission lines". *IEEE PSRC WG D6*, p.2005.
- Meng, W., Wang, X., Wang, Z. and Kamwa, I., (2017). "Impact of causality on performance of phasor measurement unit algorithms." *IEEE Transactions on Power Systems*, 33(2), pp.1555-1565.
- Misiti, M., Misiti, Y., Oppenheim, G. and Poggi, J.M., (1996). "Wavelet toolbox. The MathWorks Inc., Natick, MA, 15, p.21."
- Milano, F. and Manjavacas, Á.O., (2020). *Frequency Variations in Power Systems: Modeling, State Estimation, and Control*. John Wiley and Sons.
- Monti, A., Muscas, C. and Ponci, F., (2016). "Phasor measurement units and wide area monitoring systems." Academic Press.

- Moore, P.J., Carranza, R.D. and Johns, A.T., (1994). “A new numeric technique for high-speed evaluation of power system frequency.” *IEEE Proceedings-Generation, Transmission and Distribution*, 141(5), pp.529-536.
- Musleh, A.S., Muyeen, S.M., Al-Durra, A., Kamwa, I., Masoum, M.A. and Islam, S., (2018). “Time-delay analysis of wide-area voltage control considering smart grid contingences in a real-time environment.” *IEEE Transactions on Industrial Informatics*, 14(3), pp.1242-1252.
- Nam, S.R., Kang, S.H. and Kang, S.H., (2014 ). “Real-time estimation of power system frequency using a three-level discrete fourier transform method.” *Energies*, 8(1), pp.79-93.
- Narduzzi, C., Bertocco, M., Frigo, G. and Giorgi, G., (2018). “Fast-TFM—Multifrequency phasor measurement for distribution networks.” *IEEE Transactions on Instrumentation and Measurement*, 67(8), pp.1825-1835.
- Nazari-Heris, M. and Mohammadi-Ivatloo, B., (2015). “Application of heuristic algorithms to optimal PMU placement in electric power systems: An updated review.” *Renewable and Sustainable Energy Reviews*, 50, pp.214-228.
- North American Electric Reliability Corporation (NERC), (2010). “Real-Time Application of Synchrophasors for Improving Reliability.”, 116-390 Village Blvd, Princeton, NJ, October 2010.
- Novak, R., (2021). “Three-Point Synchrophasor Estimator With Better Off-Nominal Frequency Leakage Reduction.” *IEEE Access*, 9, pp.50126-50137.
- North American Electric Reliability Corporation (NERC), (2013). “ Protection System Response to Power Swings”, System Protection and Control Subcommittee. 1–61. <http://www.nerc.com>
- Padiyar, K.R. (2008). *Power system dynamics - stability and control*, BS Publications, Hyderabad, India.
- Padiyar, K.R. and Kulkarni, A.M. (2019). *Dynamics and control of electric transmission and microgrids*, John Wiley and Sons, Inc., USA.

- Padiyar, K.R. and Krishna, S., (2005). “Online detection of loss of synchronism using energy function criterion.” *IEEE Transactions on Power Delivery*, 21(1), pp.46-55.
- Pandey, S., Srivastava, A.K. and Amidan, B.G., (2020). “A real time event detection, classification and localization using synchrophasor data.” *IEEE Transactions on Power Systems*, 35(6), pp.4421-4431.
- Petri, D., Fontanelli, D. and Macii, D.,(2014). “A frequency-domain algorithm for dynamic synchrophasor and frequency estimation.” *IEEE Transactions on Instrumentation and Measurement*, 63(10), pp.2330-2340.
- Phadke, A.G., Thorp, J.S. and Adamiak, M.G. (1983). “A new measurement technique for tracking voltage phasors, local system frequency, and rate of change of frequency.” *IEEE Trans. Power App. Syst.*, 102(5), 1025–1038.
- Phadke, A.G., Thorp, J.S. and Karimi, K.G. (1986). “State estimation with phasor measurements.” *IEEE Trans. Power Syst.*, 1(1), 233–238.
- Phadke, A.G. (1990). “Synchronized phasor measurements - a historical overview.” *IEEE Trans. Power Syst.*, 5(1), 476–479.
- Phadke A.G. and Thorp J.S. (2010). *Synchronized phasor measurements and their applications*, Springer, New York, USA.
- Phadke, A.G and Thorp, J.S (2009). “Computer Relaying for Power Systems”, Second edition, WILEY publications.
- Power Grid Corporation of India (2012), “Unified Real Time Dynamic State Measurement (URTDSM)” *A Report by Power Grid Corporation of India Ltd*, Gurgaon, February 2012. Available at: <http://www.cea.nic.in>.
- Power System Relaying Committee of the IEEE Power Engineering Society (1995)IEEE Standard for Synchrophasors for Power Systems, in IEEE Std 1344-1995(R2001) , vol., no., pp.i-, 1995, doi: 10.1109/IEEESTD.1995.93278.
- Premarlani, W., Kasztenny, B. and Adamiak, M., (2007). “Development and implementation of a synchrophasor estimator capable of measurements under dynamic conditions.” *IEEE Transactions on Power Delivery*, 23(1), pp.109-123.

- Proakis, J.G. and Manolakis, D.G. (2007). *Digital signal processing*, Prentice Hall, Upper Saddle River, New Jersey, USA.
- Radulović, M., Zečević, Ž. and Krstajić, B.,(2019). “Dynamic phasor estimation by symmetric Taylor weighted least square filter.” *IEEE Transactions on Power Delivery*, 35(2), pp.828-836.
- Rahmann, C. and Castillo, A., (2014). “Fast frequency response capability of photovoltaic power plants: The necessity of new grid requirements and definitions.” *Energies*, 7(10), pp.6306-6322.
- Raj, A. and Soman, S.A., (2020) “A graph theoretic approach to accelerate natural cutset prediction during an out-of-step condition.”, *International Journal of Electrical Power and Energy Systems*, 123, p.106278.
- Raj, A., Gajjar, G. and Soman, S.A., (2019). “Controlled islanding of transmission system using synchrophasor measurements.” *IET Generation, Transmission and Distribution*, 13(10), pp.1942-1951.
- Rao, K. and Shubhanga, K.N. (2017). “A comparison of power system signal detrending algorithms.”, *Proc. 2017 7th Int. Conf. on Power Systems (ICPS)*, Pune, India, Dec. 2017, 404–409.
- Rao, K. and Shubhanga, K.N. (2018). “MAPE - an alternative fitness metric for Prony analysis of power system signals.”, *Int. J. Emerging Electric Power Syst.*, 19(6).
- Reza, M.S., Ciobotaru, M. and Agelidis, V.G., (2014). “A modified demodulation technique for single-phase grid voltage fundamental parameter estimation.” *IEEE Transactions on Industrial Electronics*, 62(6), pp.3705-3713.
- Ree, J.D.L., Centeno, V., Thorp, J.S., and Phadke, A.G., (2010). “Synchronized Phasor Measurement Applications in Power Systems,” *IEEE Transactions on Smart Grid* Vol 1, No 1
- Reza, M.S., Ciobotaru, M. and Agelidis, V.G., (2014 ). “Accurate estimation of single-phase grid voltage parameters under distorted conditions.” *IEEE Transactions on Power Delivery*, 29(3), pp.1138-1146.

- Romano, P. and Paolone, M., (2014). “Enhanced interpolated-DFT for synchrophasor estimation in FPGAs: Theory, implementation, and validation of a PMU prototype.” *IEEE Transactions on Instrumentation and Measurement*, 63(12), pp.2824-2836.
- Roscoe, A.J., Abdulhadi, I.F. and Burt, G.M., (2013). “P and M class phasor measurement unit algorithms using adaptive cascaded filters.” *IEEE transactions on power delivery*, 28(3), pp.1447-1459.
- Roscoe, A.J., Dickerson, B. and Martin, K.E., (2015). “Filter design masks for C37. 118.1 a-compliant frequency-tracking and fixed-filter M-class phasor measurement units.” *IEEE Transactions on Instrumentation and Measurement*, 64(8), pp.2096-2107.
- Roy, B.K.S., Sinha, A.K. and Pradhan, A.K., (2013). “Synchrophasor-assisted prediction of stability/instability of a power system.” *International Journal of Emerging Electric Power Systems*, 14(1), pp.1-8.
- Rubeša, R., Ivanković, I., Rekić, M., Brnobić, D., Grudenić, V. and Holjevac, N., (2020), October. “On line electromechanical oscillations detection in transmission network with synchrophasor.” In *2020 3rd international colloquium on intelligent grid metrology (SMAGRIMET)* (pp. 114-120). IEEE.
- Salunkhe, K. and Kulkarni, A.M., (2015 ). “Reconstruction of transient waveforms from phasors sampled at the fundamental frequency.” In *2015 IEEE Eindhoven PowerTech* (pp. 1-6). IEEE.
- Salunkhe, K.A., Gajjar, G., Soman, S.A. and Kulkarni, A.M., (2014), July. “Implementation and applications of a wide area frequency measurement system synchronized using network time protocol.” In *2014 IEEE PES General Meeting| Conference & Exposition* (pp. 1-5). IEEE.
- Sarkar, N., Rao, K. and Shubhanga, K.N., (2018). “A comparative study between Prony and eigensystem realization algorithm for identification of electromechanical modes.” In *2018 20th national power systems conference (NPSC)* (pp. 1-6). IEEE.
- Seo, W.S. and Kang, S.H., (2017). “A novel frequency estimation algorithm based on DFT and second derivative.” *Journal of International Council on Electrical Engineering*, 7(1), pp.69-75.



- Seyedi, H. and Sanaye-Pasand, M., (2012). “A new time-domain based power system frequency estimation algorithm.” *European Transactions on Electrical Power*, 22(4), pp.433-448.
- Sharma, R.B. and Dhole, G.M., (2016). “Synchrophasor measurement network and its applications in Indian grid”. In *2016 International Conference on Emerging Trends in Electrical Electronics and Sustainable Energy Systems (ICETEESES)* (pp. 30-34). IEEE.
- Sharma, C. and Tyagi, B.,(2014). “Fuzzy type-2 controller design for small-signal stability considering time latencies and uncertainties in PMU measurements.” *IEEE Systems Journal*, 11(2), pp.1149-1160.
- Shaik, A.G. and Mahela, O.P., (2018). “Power quality assessment and event detection in hybrid power system.” *Electric power systems research*, 161, pp.26-44.
- Shahraeini, M and Javidi, M.H (2012). “Wide Area Measurement Systems”, *Advanced Topics in Measurements*, Golestan University and Ferdowsi University of Mashhad, Iran.
- Shi, J., Foggo, B., Kong, X., Cheng, Y., Yu, N. and Yamashita, K., (2020). “Online event detection in synchrophasor data with graph signal processing.” In *2020 IEEE International conference on communications, control, and computing technologies for smart grids (SmartGridComm)* (pp. 1-7). IEEE.
- Shubhanga, K.N. (2018). *Power system analysis - a dynamic perspective*, Pearson India Education Services Pvt. Ltd., Noida, India.
- Shaw, P. and Jena, M.K., (2020). “A Novel Event Detection and Classification Scheme Using Wide-Area Frequency Measurements”. *IEEE Transactions on Smart Grid*, 12(3), pp.2320-2330.
- Sreenivasachar, K., (2021). “Out-of-step detection on transmission lines using apparent impedance differential method”. *IEEE Transactions on Power Delivery*.
- Stahlhut, J.W., Browne, T.J., Heydt, G.T. and Vittal, V., (2008). “Latency viewed as a stochastic process and its impact on wide area power system control signals.” *IEEE Transactions on Power Systems*, 23(1), pp.84-91.
- Sun, J., Aboutanios, E., Smith, D.B. and Fletcher, J.E., (2019). “Robust frequency, phase, and amplitude estimation in power systems considering harmonics.” *IEEE Transactions on Power Delivery*, 35(3), pp.1158-1168.

- Thilakarathne, C., Meegahapola, L. and Fernando, N., (2017). “Improved synchrophasor models for power system dynamic stability evaluation based on IEEE C37. 118.1 reference architecture.” *IEEE Transactions on Instrumentation and Measurement*, 66(11), pp.2937-2947.
- Thorp, J.S., Phadke, A.G., Horowitz, S.H., and Begovic, M.M., (1988). “Some applications of phasor measurements to adaptive protection”, *IEEE Transactions on Power Systems* Vol 3, No 2
- Thomas, A., Koshy, S. and Sunitha, R., (2020), December. “Machine Learning Based Detection and Classification of Power System Events.” In *2020 International Conference on Power, Instrumentation, Control and Computing (PICC)* (pp. 1-6). IEEE.
- Thomas, M.S., Senroy, N. and Rana, A.S., (2014), December. “Analysis of time delay in a wide-area communication network.” In *2014 6th IEEE Power India International Conference (PIICON)* (pp. 1-6). IEEE.
- Tziouvaras, D.A. and Hou, D., (2004), April. “Out-of-step protection fundamentals and advancements.” In *57th Annual Conference for Protective Relay Engineers, 2004* (pp. 282-307). IEEE.
- Usman, M.U. and Faruque, M.O., (2019). “Applications of synchrophasor technologies in power systems.” *Journal of Modern Power Systems and Clean Energy*, 7(2), pp.211-226.
- Vaz, R., Moraes, G.R., Arruda, E.H., Terceiro, J.C., Aquino, A.F., Decker, I.C. and Issicaba, D., (2021). “Event detection and classification through wavelet-based method in low voltage wide-area monitoring systems.” *International Journal of Electrical Power and Energy Systems*, 130, p.106919.
- Verma, A.K., Subramanian, C., Jarial, R.K., Roncero-Sánchez, P. and Rao, U.M., (2020). “A robust Lyapunov’s demodulator for tracking of single-/three-phase grid voltage variables.” *IEEE Transactions on Instrumentation and Measurement*, 70, pp.1-11.
- Vejdan, S., Sanaye-Pasand, M. and Malik, O.P., (2015 ). “Accurate dynamic phasor estimation based on the signal model under off-nominal frequency and oscillations.” *IEEE Transactions on Smart Grid*, 8(2), pp.708-719.

- Von Meier, A., Stewart, E., McEachern, A., Andersen, M. and Mehrmanesh, L.,(2017). “Precision micro-synchrophasors for distribution systems: A summary of applications.” *IEEE Transactions on Smart Grid*, 8(6), pp.2926-2936.
- Wang, S., Dehghanian, P. and Li, L., (2019). “Power grid online surveillance through PMU-embedded convolutional neural networks.” *IEEE Transactions on Industry Applications*, 56(2), pp.1146-1155.
- Wang, W., Yin, H., Chen, C., Till, A., Yao, W., Deng, X. and Liu, Y.,(2020). “Frequency disturbance event detection based on synchrophasors and deep learning.” *IEEE Transactions on Smart Grid*, 11(4), pp.3593-3605.
- Wang, S., Meng, X. and Chen, T., (2011). “Wide-area control of power systems through delayed network communication.” *IEEE Transactions on Control Systems Technology*, 20(2), pp.495-503.
- Xia, Y., He, Y., Wang, K., Pei, W., Blazic, Z. and Mandic, D.P., (2015). “A complex least squares enhanced smart DFT technique for power system frequency estimation.” *IEEE Transactions on Power Delivery*, 32(3), pp.1270-1278.
- Xia, Y., Wang, K., Pei, W., Blazic, Z. and Mandic, D.P., (2016), “A least squares enhanced smart DFT technique for frequency estimation of unbalanced three-phase power systems.” In *2016 International Joint Conference on Neural Networks (IJCNN)* (pp. 2762-2766). IEEE.
- Xia, Y., Blazic, Z. and Mandic, D.P., (2014 ). “Complex-valued least squares frequency estimation for unbalanced power systems.” *IEEE Transactions on Instrumentation and Measurement*, 64(3), pp.638-648.
- Xia, Y., Douglas, S.C. and Mandic, D.P., (2012). “Adaptive frequency estimation in smart grid applications: Exploiting non-circularity and widely linear adaptive estimators.” *IEEE Signal Processing Magazine*, 29(5), pp.44-54.
- Xia, T. and Liu, Y., (2009). “Single-phase phase angle measurements in electric power systems.” *IEEE Transactions on Power Systems*, 25(2), pp.844-852.
- Xie, L., Chen, Y. and Kumar, P.R., (2014). “Dimensionality reduction of synchrophasor data for early event detection: Linearized analysis.” *IEEE Transactions on Power Systems*, 29(6), pp.2784-2794

- Xia, Y., Douglas, S.C. and Mandic, D.P., (2012). “Adaptive frequency estimation in smart grid applications: Exploiting noncircularity and widely linear adaptive estimators.” *IEEE Signal Processing Magazine*, 29(5), pp.44-54.
- Xu, T. and Overbye, T., (2015), November. “Real-time event detection and feature extraction using PMU measurement data.” In 2015 *IEEE International Conference on Smart Grid Communications (SmartGridComm)* (pp. 265-270). IEEE.
- Yadav, R., Pradhan, A.K. and Kamwa, I., (2018). “Real-time multiple event detection and classification in power system using signal energy transformations.” *IEEE Transactions on Industrial Informatics*, 15(3), pp.1521-1531.
- Yadav, R., Raj, S. and Pradhan, A.K., (2019). “Real-time event classification in power system with renewables using kernel density estimation and deep neural network.” *IEEE Transactions on Smart Grid*, 10(6), pp.6849-6859.
- Yuill, W., Edwards, A., Chowdhury, S. and Chowdhury, S.P., (2011), July. “Optimal PMU placement: A comprehensive literature review.” In 2011 *IEEE Power and Energy Society General Meeting* (pp. 1-8). IEEE.
- Zarifakis, M., Coffey, W.T., Kalmykov, Y.P., Titov, S.V., Byrne, D.J. and Carrig, S.J., (2019). “Active damping of power oscillations following frequency changes in low inertia power systems.” *IEEE Transactions on Power Systems*, 34(6), pp.4984-4992.
- Zečević, Ž., Krstajić, B. and Popović, T., (2016). “Improved frequency estimation in unbalanced three-phase power system using coupled orthogonal constant modulus algorithm.” *IEEE Transactions on Power Delivery*, 32(4), pp.1809-1816.
- Zhang, S. and Zhang, Y., (2016). “A novel out-of-step splitting protection based on the wide area information.” *IEEE Transactions on Smart Grid*, 8(1), pp.41-51.
- Zhan, L., Liu, Y. and Liu, Y., (2016). “A Clarke transformation-based DFT phasor and frequency algorithm for wide frequency range.” *IEEE Transactions on Smart Grid*, 9(1), pp.67-77.
- Zhan, L. and Liu, Y., (2014), “Improved WLS-TF algorithm for dynamic synchronized angle and frequency estimation.” In 2014 *IEEE PES General Meeting| Conference and Exposition* (pp. 1-5). IEEE.

Zhang, F., Cheng, L., Gao, W. and Huang, R., (2018). “Synchrophasors-based identification for subsynchronous oscillations in power systems.” *IEEE Transactions on Smart Grid*, 10(2), pp.2224-2233.

Zhu, K., Song, J., Chenine, M. and Nordström, L., (2010), May. “Analysis of phasor data latency in wide area monitoring and control systems.” In *2010 IEEE international conference on communications workshops* (pp. 1-5). IEEE.

---

## Publications based on the thesis

### Journals

1. Mir Khadim Aalam and K. N. Shubhanga, “Power system event detection and localization—A new approach,” *Electric Power Systems Research* (2023), Volume 223, October 2023, 109553  
<https://doi.org/10.1016/j.epsr.2023.109553>
2. Mir Khadim Aalam and K. N. Shubhanga, “An integrated PMU architecture for power system applications,” *International Journal of Emerging Electric Power Systems* (2021), Vol 23  
<https://doi.org/10.1515/ijeeps-2021-0151>.
3. Under review “Frequency Estimation Using Signal Reconstruction Approach”, 2nd revision submitted to *Electric Power Systems Research*.

### Conferences

1. Mir Khadim Aalam and K. N. Shubhanga, “Synchrophasor Measurement Standard Comparison and Testing of an FF-based PMU,” *I4Tech 2020*, Vishwakarma Institute of Technology, Pune, India, 13-15, February 2020.  
10.1109/I4Tech48345.2020.9102672
2. Mir Khadim Aalam and K. N. Shubhanga, “EMD-based Detrending of Non-Linear and Non-Stationary Power System Signals,” *INDICON 2021*, IIT Guwahati, India, 19-21, December 2021.  
10.1109/INDICON52576.2021.9691539



## CURRICULUM VITAE

Full Name: Mir Khadim Aalam  
Date of Birth: 21-11-1991  
E-mail: mkaalam7@gmail.com  
Mobile: +91-9481079031



### **Address**

Research Scholar,  
Department of Electrical & Electronics Engineering,  
National Institute of Technology Karnataka (NITK),  
Surathkal,  
Srinivasnagar P.O.,  
Surathkal, Mangalore-575 025, INDIA.

### **Educational Qualification**

Degree	Specialization	Institute/University	Year
B.E.	Electrical and Engineering	MIET Jammu (University of Jammu)	2010-2014
M.Tech	Power Systems	University B. D. T College of engineering	2015-2017
Pursuing Ph.D.	Power System Engineering	NITK-Surathkal	2017-till date

### **Research Interests :**

- Power System operation and control
- Power System dynamics
- Wide Area Measurement Systems (WAMS)
- Phasor Measurement Units (PMU)
- Event Detection and Postmortem analysis
- Power system measurements

### **Society Memberships**



- Student Member of IEEE

### **Software and Computer Proficiency**

- Operating Systems: Windows and Linux.
- Simulation Packages: MATLAB/Simulink, SCILAB/XCOS.

### **Interest and Activities**

- Football
- Music